Studying multiplicity and rapidity dependence of K* production and probing initial conditions of high energy collisions with ALICE at the LHC energies

By

DUKHISHYAM MALLICK

PHYS11201604011

National Institute of Science Education and Research, Bhubaneswar

A thesis submitted to
the Board of Studies in
Physical Sciences

In partial fulfillment of requirements
For the Degree of

DOCTOR OF PHILOSOPHY
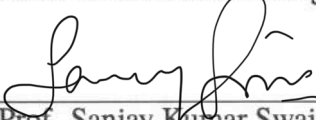*of*

HOMI BHABHA NATIONAL INSTITUTE

December, 2022

ii

Homi Bhabha National Institute

Recommendations of the Viva Voce Committee

As members of the Viva Voce Committee, we certify that we have read the dissertation prepared by **Dukhishyam Mallick** entitled **"Studying multiplicity and rapidity dependence of K* production and probing initial conditions of high energy collisions with ALICE at the LHC energies"** and recommend that it may be accepted as fulfilling the thesis requirement for the award of Degree of Doctor of Philosophy.

Chairman - Prof. Sanjay Kumar Swain   Date: 9/3/2023
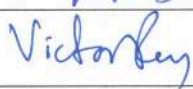
Guide / Convener - Prof. Bedangadas Mohanty   Date: 9/08/2023

Co-guide - NA   Date:

Examiner 1 - Dr. Santosh Kumar Das   Date: 14/03/2023

Examiner 2 -   Date:

Member 1 - Dr. Amaresh Kumar Jaiswal   Date: 13/03/2023

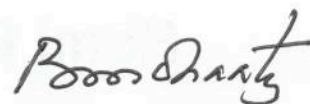Member 2 - Dr. Victor Roy   Date: 14-03-23

Member 3 - Dr. Aruna Kumar Nayak   Date: 14/03/2023

Final approval and acceptance of this thesis is contingent upon the candidate's submission of the final copies of the thesis to HBNI.

I hereby certify that I have read this thesis prepared under my direction and recommend that it may be accepted as fulfilling the thesis requirement.

Date : 09/03/2023
Place : NISER

(Co-guide)   **(Prof. Bedangadas Mohanty)**

STATEMENT BY THE AUTHOR

This dissertation has been submitted in partial fulfillment of requirements for an advanced degree at Homi Bhabha National Institute (HBNI) and is deposited in the library to be made available to borrowers under rules of the HBNI.

Brief quotations from this dissertation are allowable without special permission, provided that accurate acknowledgement of source is made. Requests for permission for extended quotation from or reproduction of this manuscript in whole or in part may be granted by the Competent Authority of HBNI when in his or her judgment the proposed use of the material is in the interests of scholarship. In all other instances, however, permission must be obtained from the author.

Date : 09/03/2023
Place : NISER

Dukhishyam Mallick

(DUKHISHYAM MALLICK)

vi

DECLARATION

I hereby declare that the investigation presented in the thesis has been carried out by me. The work is original and has not been submitted earlier as a whole or in part for a degree/diploma at this or any other Institution/University.

Date : 09/03/2023
Place : NISER

Dukhishyam Mallick

(DUKHISHYAM MALLICK)

List of publications and presentations

Journal

Published

1. $K^*(892)^0$ and $\phi(1020)$ production at midrapidity in pp collisions at $\sqrt{s}$= 8 TeV, ALICE Collaboration, Primary contributors: Dukhishyam Mallick, Raghunath Sahoo, Arvind Khuntia, Sushanta Tripathy, Anders Garritt Knospe, arXiv:1910.14410, Phys. Rev. C 102 (2020) 024912.

2. $K^*(892)^0$ and $\phi(1020)$ production at midrapidity in p–Pb collisions at $\sqrt{s_{NN}}$= 8.16 TeV, ALICE Collaboration, Primary contributors: Dukhishyam Mallick, Ranbir Singh, Bedangadas Mohanty, Sandeep Dudi, Lokesh Kumar, arXiv:2110.10042, Accepted in Phys. Rev. C (PRC).

3. Multiplicity and rapidity dependence of $K^*(892)^0$ and $\phi(1020)$production in p–Pb collisions at $\sqrt{s_{NN}}$ = 5.02 TeV, ALICE Collaboration, Primary contributors: Dukhishyam Mallick, Bedangadas Mohanty, Sandeep Dudi, Lokesh Kumar, arXiv:2204.10263, Accepted in European Physical Journal C (EPJC).

4. Study of charged particle multiplicity, average transverse momentum and azimuthal anisotropy in Xe+Xe collisions at $\sqrt{s_{\mathrm{NN}}}$ = 5.44 TeV using AMPT model, Sourav Kundu, Dukhishyam Mallick and Bedangadas Mohanty, Eur. Phys. J. A 55, 157 (2019).

Conferences

Conference/Proceedings

1. Mesonic Resonance Production in p−Pb, Pb−Pb and Xe−Xe Collisions with ALICE at the LHC, MDPI Proc. 10 (2019) 1, 23.

2. Energy and system size dependence of hadronic resonance production with ALICE at the LHC, DAE Symp. Nucl. Phys. 63 (2018), 928.

3. Recent results on hadronic resonance production with ALICE at the LHC, DAE Symp. Nucl. Phys.64 (2019) 706.

4. Latest results on hadronic resonance production with ALICE at the LHC, XXIV DAE-BRNS HEP SYMPOSIUM, Springer Proceedings in Physics, 365-368, 2022.

5. Latest results of hadronic resonance production with ALICE at the LHC, PoS PANIC2021, PoS(PANIC2021)226.

6. Search for higher mass resonances via KK decay channel in pp collisions with ALICE at the LHC, QM-2022, Acta Phys.Polon.Supp. 16 (2023) 1, 153, arXiv:2211.10606.

7. Exploring the hadronic phase of relativistic heavy-ion collisions with resonances in ALICE, SQM-2022, EPJ Web Conf. 276 (2023) 04005.

ALICE Analysis notes

1. Measurements of K^{*0} production in pp collisions at $\sqrt{s}=$ 7 TeV, Dukhishyam Mallick, Ranbir Singh and Bedangadas Mohanty, ID number: ANA-833, https://alice-notes.web.cern.ch/node/833.

2. K^{*0} resonance production in p-Pb collisions at $\sqrt{s_{\mathrm{NN}}}=$8.16 TeV, Dukhishyam Mallick, Ranbir Singh and Bedangadas Mohanty, ID number: ANA-777, https://alice-notes.web.cern.ch/node/777.

3. Rapidity dependence studies of K^{*0} resonance production in p-Pb collisions at $\sqrt{s_{\mathrm{NN}}}=$5.02 TeV, Dukhishyam Mallick, Ranbir Singh and Bedangadas Mohanty, ID number: ANA-968, https://alice-notes.web.cern.ch/node/968.

4. $K^{*\pm}$ resonance production in p-Pb collisions at $\sqrt{s_{\mathrm{NN}}}=$5.02 TeV, Dukhishyam Mallick, Sudipan De and Bedangadas Mohanty, ID number: ANA-926, https://alice-notes.web.cern.ch/node/926.

5. Spin alignment of vector mesons ($K^{*0,\pm}$ and ϕ) in heavy-ion collisions at $\sqrt{s_{\mathrm{NN}}}=$ 5.02 TeV in ALICE at the LHC, Dukhishyam Mallick, Ranbir Singh and Bedangadas Mohanty, ID number: ANA-1340, https://alice-notes.web.cern.ch/node/1340.

Conference presentations

1. Exploring the hadronic phase of relativistic heavy-ion collisions with resonances in ALICE, The 20th International Conference on Strangeness in Quark Matter 13-17th, June 2022, Bussan, Republic Korea.

2. Search for higher mass resonances via KK decay channel in pp collisions with AL-ICE at the LHC, 29th International conference on ultrarelativistics nucleus-nucleus collsions, April 4-10th, 2022, Krakow, Poland.

3. Hadronic resonance production in small colliding systems with ALICE at the LHC, The 8th Asian Triangle Heavy-Ion Conference (ATHIC 2021),05-09th November, 2021, Inha University, Incheon, South Korea.

4. Latest results of hadronic resonance production with ALICE at the LHC, PANIC 2021, 5-10th, September, 2021, Lisbon, Portugal.

5. Exploring the magnetic field in heavy-ion collisions through spin alignment measurements at ALICE, VI International conference on Initial Stages of high-energy nuclear collisions (IS2021), 10–15th January, 2021, Weizmann Institute of Science, Rehovot (Israel).

6. Latest results on hadronic resonance production with ALICE at the LHC, XXIV DAE-BRNS HEP SYMPOSIUM-2020, 14-18th, December, 2020, NISER, Odisha, India.

7. Recent results on hadronic resonance production with ALICE at the LHC, 64th DAE International Symposium on Nuclear Physics, 23-27 December, 2019, Lucknow, India.

8. Hadronic resonance production in asymmetric collisions with ALICE at the LHC, Quark Matter 2019-the XXVIIIth International Conference on Ultra-relativistic Nucleus-Nucleus Collisions, 3-9 November, 2019, Wanda Reign Wuhan Hotel, China.

9. Measurement of $K^{*\pm}$ in p-Pb collisions with ALICE at the LHC, The 18th International conference on Strangeness in Quark Matter (SQM 2019), 10-15th June, 2019, Bari (Italy).

10. Energy and system size dependence of hadronic resonance production with ALICE at the LHC, 63th DAE International Symposium on Nuclear Physics, December 10-14th, 2018, BARC, Mumbai, India.

11. Mesonic Resonance Production in p–Pb, Pb–Pb and Xe–Xe Collisions with ALICE at the LHC, Presented at Hot Quarks 2018-Workshop for Young Scientists on the Physics of Ultrarelativistic Nucleus-Nucleus Collisions, Texel, The Netherlands, 7-14th September 2018.

12. Measurement of neutral $K^*(892)^0$ and $\phi(1020)$ production in p–Pb collisions at center-of-mass energy per nucleon $\sqrt{s_{NN}} = 8.16$ TeV with ALICE at the LHC(Poster), QM-2018, 14-19th, May 2018, Lido de Venezia, Italy.

Date : 09/03/2023

Place : NISER

Dukhishyam Mallick

(DUKHISHYAM MALLICK)

Dedicated to

my family, friends and teachers,
specially to my late Grandparents and Aunty

ACKNOWLEDEGEMENT

The work of this thesis would not have been completed without the support of many people. The journey of completion of a Ph.D. is a long one. Along the way, I learned a lot of invaluable things from my teachers, collaborators, and friends that helped me fulfill this dream and the overall growth in my professional and personal life. I want to extend a heartfelt thank you to everyone, and accept my apologies if I left anyone out who deserved to be recognized.

First and foremost, I would like to express sincere gratitude to my supervisor, prof. Bedangadas Mohanty for his continuous guidance, support, and advice throughout my Ph.D. His dedication, sincerity, and generosity inspired me and gave me the strength to reach this stage. His constructive criticism and suggestions are essential for research work and remind me about other responsibilities for the growth of yourself and the community. He has provided all the necessary resources for my research work. I greatly appreciate all the opportunities he gave me to attend several national and international conferences, workshops, and schools.

I would like to thank Prof. Sudhakar Panda (Director of NISER) for providing all the support required to complete my PhD. I am thankful to all my doctoral committee members prof. Sanjay Kumar Swain, Dr. Victor Roy, Dr. Amaresh Kumar Jaiswal and Dr. Aruna Kumar Nayak for their support and motivation. I would like to thank all the faculty and staff memebers, medical, hostel and canteen staffs of NISER for their support. I am very grateful to the School of Physical Sciences, NISER for providing me with all the required resources. Specially thanks to Sabyasachi, Prakash, Dhiren for their help during my Ph.D.

I thank to all people at the high energy physics group (RL-202) at NISER for constructive physics discussions, company and all the fun time we had spent throughout my PhD. It

during my visiting period.

I would like to thank to ALICE-Indi Juniors (JRs) representatives committe such Suman Deb, Baidyanath Sahoo, Pranjal Sarma, and Shreyasi Acharya. We worked as a team to organize monthly journal clubs, collect the suggestions or opinions from the juniors to present in front of ALICE-India CB members to solve the issue. I also thanks to all the juniors and seniors members from ALICE-STAR-INDIA. We helped each other directly and indirectly. I would like express gratitute to Prof. Nu Xu, Prof. Chitrasen Jena and Prof. Santosh Das gave value suggestions that provide the betterment of the thesis. I would also like to thank the conference committee chairs of ALICE collaboration for giving me opportunities to represent ALICE collaboration on multiple occasions in international/national conferences. I would like to thank all the engineers and technicians for their invaluable contributions to the construction of the ALICE experiment and the CERN accelerator teams for the outstanding performance of the LHC complex. I gratefully acknowledge the resources and support provided by the Grid computing facilities at CERN, VECC and NISER. I also acknowledge HBNI, DAE-BRNS and NISER for their financial support during my PhD.

I am particularly grateful for a bunch of people and helpful friends at NISER. My Ph.D classmates (specially Jagannath), Milan, Rik, Ankit, Soumya, Akshya, Deepak, Malaya, Shakti, Situn, Prafulla, Jobin, Sujit NS, Lakshmikant, Chandi Bhai, Bharat Bhai, Rajat Bhai and Beda Bhai from their constant support, love, help and good wishes making NISER life as a memorable one. The time that I have spent with you all are very special and will always remain close to my heart. I also bleesed with group of friends they always stand whenever I need their assistance. I would like thank Basu Bhai, Kunu Di, Tanim Di, Rashmi Di, Deepika Di,Snigdha Di, Sushanta Bhai, Tapas, Sahil, Sarmil, Bubu, Twinkle, Manisha, Rajesh, Sikan, Pravakar, Neelakantha, Pooja, Lipan, Mukesh, Nimish, Aswini,

Tribhubana, Prabhupada, Srinivas, Inderjit, Amrit, Surya, Sonu, Vijay, Anand, Darshan, Bharat, Ganesh, Lakshman, Lipu and Priya for keeping in touch and offering insightful assistance during my Ph.D program.

Finally, I am thankful to my school, college and university teachers for their guidance because of which I am able to reach this stage. Most importantly, I would like to express my respect, gratitude and humbleness to my parents, my brother and sister, and all my family members for their blessings, constant support and encouragement throughout my life. I thank the almighty God for his blessings to complete my research successfully.

Abstract

Quantum chromodynamics (QCD) is the theory of strong interaction that describes the basic building blocks of nature. The QCD predicts a new state of strongly interacting matter at a very high temperature and/or density known as Quark-Gluon-Plasma (QGP), in which quarks and gluons are in a free state. It is believed that such a state of matter was present in the microsecond after the Big-Bang. To recreate such a primordial state of QCD matter in the laboratory and study its properties, ultra-relativistic heavy-ion collisions are carried out at Large Hadron Collider (LHC) facility and the data recorded using the ALICE detector. The present study aims to understand the properties of QCD matter and the different stages formed in ultra-relativistic high-energy collisions through hadronic resonance production. Hadronic resonances are short-lived (a few fm/c) in nature and decay via the strong interaction. These resonances are sensitive probes of the hadronic phase and the particle production mechanism. The yield, mass, and width of resonances are expected to be modified due to their decay daughters interaction within the hadronic phase via rescattering and regeneration processes. $K^{*0,\pm}$ is suitable for this purpose because of its very short lifetime (~ 4 fm/c), which is comparable to the hadronic phase lifetime. We have measured the

$K^{*0,\pm}$ production in the rapidity interval $-0.5 < y < 0$ for proton-nucleus (p–Pb) collisions at $\sqrt{s_{NN}} = 5.02$ and 8.16 TeV for various multiplicity classes. The p_T spectra, p_T-integrated yield, $\langle p_T \rangle$, x_T-scaling, resonance to stable particle yield ratio, and nuclear modification factor (R_{pPb}) are discussed.

The p–Pb is an asymmetric and intermediate collision system compared to the pp and Pb-Pb collisions. It plays a vital role in disentangling initial cold nuclear matter effects from final state effects of hot dense matter produced in heavy-ion collisions. In the p-Pb collisions, one expects the mechanism of particle production to be different in forward (p-going) and backward (Pb-going) rapidities. The partons from the p-going side are expected to undergo multiple scattering while traversing the Pb-nucleus. Those on the Pb-side are likely to be affected by the properties of the nucleus. Thus, the rapidity dependence measurement of K^{*0} production in p–Pb collisions at $\sqrt{s_{NN}} = 5.02$ TeV is interesting. We have measured the K^{*0}, production in the rapidity interval $-1.2 < y < 0.3$ for p–Pb at $\sqrt{s_{NN}} = 5.02$ TeV for four multiplicity classes. The p_T spectra, p_T-integrated yield, $\langle p_T \rangle$, rapidity yield asymmetry (Y_{asym}), and nuclear modification factor (Q_{CP}) are presented.

The high p_T region of K^{*0} production obeys an interesting x_T-scaling behaviour for the LHC energies. K^{*0}/K ratio decreases with increasing event multiplicity which suggests that the rescattering effect dominates over regeneration. No significant energy dependence in R_{pPb} is observed, and values are consistent with unity within the uncertainties for K^{*0} and other light flavor hadrons at $p_T > 8$ GeV/c, confirming the absence of QGP-like effects in p–Pb collisions. The rapidity asymmetry has been observed at low p_T and Cronin-like enhancement seen in the Q_{CP} at the intermediate p_T suggests that nuclear effects play an important role in p–Pb collisions.

In non-central relativistic heavy-ion collisions, where two nuclei collide with a nonzero impact parameter, a large orbital angular momentum ($\vec{L}$) of O(10^{6-7} $\hbar$), and magnetic field

($|\vec{B}|$) of O(10^{18} Gauss) are expected to be created. In the presence of large initial angular momentum, vector mesons (spin = 1) can be polarized due to the spin-orbital interaction of the QCD. The spin-orbit coupling could lead to a polarization of quarks that is followed by a net-polarization of vector mesons along the direction of angular momentum. Recently, the spin alignment of vector mesons at LHC energy was found to be surprisingly large compared to the polarisation measured for hyperons at RHIC and LHC energies. Theoretical studies have suggested that the local polarisation (where polarisation axes are chosen as a beam direction or along the momentum of vector meson) can also lead to the spin alignment of vector mesons and hyperons. It is exciting and challenging to extend such type of measurements to understand the contribution coming from global and local polarization. We have presented new measurements of spin alignment of vector mesons ($K^{*0,\pm}$, and ϕ) using different polarisation axes in Pb–Pb collisions at $\sqrt{s_{\mathrm{NN}}}$ = 5.02 TeV with high statistics Run-2 data. The spin alignment of vector mesons is observed at low p_{T} for mid-central collisions, whereas no spin alignment at high p_{T}. No significant energy dependence is observed. K^{*0} and $K^{*\pm}$ show similar spin alignment.

Contents

List of Figures

List of Tables

Introduction

The curiosity to know the unknown inspires us to explore and understand the universe. High energy physics community, both theorists and experimentalists, have a significant role in understanding the fundamental constituents of matter, which makes up the whole universe and knowledge about the possible origin and evolution of the universe. In 1911, the atomic nucleus was uncovered through an experiment involving the scattering of alpha particles against a thin gold foil by E. Rutherford [1]. This changed the view of atoms. It was predicted that the core of the atom is concentrated with positively charged nucleus and negatively charged electrons surrounding it. Subsequently, proton [2], and neutron [3] were discovered, which helps to understand the constituents of the nucleus and the basic nuclear properties. Deep-Inelastic Scattering (DIS) experiment confirmed the first evidence of the composite structure of the proton and that it consists of partons (quarks or gluons, where gluons are the carrier of strong interaction). Quarks were found to have fractional charges [4, 5]. In 1979, DESY experiment in Germany, revealed the existence of gluons from e^+e^- annihilation [6].

As per the current understanding, the fundamental building blocks of nature are leptons,

quarks, and force carriers the gauge bosons (photons, W, Z bosons, and gluons). The standard model (SM) is a theoretical framework proposed by Glashow [7], Salam [8], and Weinberg [9], which describes three interactions (electromagnetic, weak, and strong) out of four fundamental interactions (except gravity) that constitutes the building blocks of nature. Experimentally, the measurements of W and Z bosons [10] verified the predictions of the SM. The recent discovery of the Higgs boson [11, 12, 13] provides information on how the particles get their mass. This discovery is also consistent with the SM predictions. The SM is the theory that describes the interaction of elementary particles. Experimentally, ultra-relativistic heavy-ion collisions is one of the tools to understand the nature of strong interaction and help us to probe the matter formed in extreme conditions such as high temperature and high energy density.

This thesis discusses the formation of strongly interacting Quantum Chromodynamics (QCD) matter and its novel properties in high energy collisions at high temperature and/or density. This chapter provides a brief overview of the QCD and the Quark-Gluon Plasma (QGP), followed by an introduction to heavy-ion collisions and the signatures of formation of QGP medium in heavy-ion collisions. The relevance of hadronic resonance production in high-energy collisions is also discussed. The final section discusses motivation of this thesis.

1.1   Quantum chromodynamics (QCD)

The QCD is a theory of strong interaction that describes the interaction between quarks and gluons. It is characterized by color quantum numbers similar to electric charge playing a role in quantum electrodynamics (QED). The quarks and gluons carry color charge with self interactions being allowed. The massless gluons act as mediators in the strong interaction,

similar to photon in the QED. The gluon has eight kinds of color charge states, which makes the QCD different from the QED. Free quarks have never been observed experimentally; they are bound inside hadrons by the strong interaction. Color-neutral hadrons (mesons or baryons) are composed of quarks and gluons. The mesons consist of a quark and anti-quark, whereas three quarks bind to form baryons. The potential form of QCD interaction ($V_{\text{QCD}}(r)$) is expressed as

$$V_{\text{QCD}}(r) = -\frac{4}{3}\frac{\alpha_s}{r} + kr \tag{1.1}$$

Where α_s is coupling constant that gives strength of the strong interaction, k is color string tension constant. The distance between two interacting partons (quarks or gluons) is denoted as "r". The strong coupling constant (α_s) depends on the momentum transfers between partons, it is expressed as

$$\alpha_s(Q^2) = \frac{12\pi}{(11N_c - 2N_f)\ln\left(\frac{Q^2}{\Lambda_{QCD}^2}\right)} \tag{1.2}$$

Where N_c is the number of color charge and N_f is the number of color flavors. Λ_{QCD} is a scale parameter in QCD calculations, which is about ~ 200 MeV [14]. Figure 1.1 shows α_s as a function of Q. Figure 1.1 and Eq. 1.1 provide an understanding of two novel properties of QCD; color confinement and asymptotic freedom. The QCD potential mentioned in Eq. 1.1 suggests that quarks exhibit the property of color confinement i.e., isolated quarks can not be found. First term of Eq. 1.1 is similar to Coulomb potential form in QED and it dominates at small r. As the distance between two quarks increases, then the linear term starts to dominate. Thus, nearly infinite energy is required to get a free quark. When separation between two quarks increases, the color field lines between them, forms flux tubes. After that, it reaches a threshold energy creating a quark anti-quark pair instead of

two free quarks. The coupling α_s is not a constant, depends on the momentum transfer as given in Eq. 1.2; hence α_s is known as the running coupling constant. From Fig. 1.1, it is observed that at small momentum transfer ($Q^2 << \Lambda_{QCD}$) or large distance scales, the strength of running coupling constant of QCD becomes large. As a result, quarks and gluons are bound inside the hadrons instead of being free. This property of QCD is known as the quark or color confinement. It is the regime, where non-perturbative QCD is applicable. Similarly, at large momentum transfer ($Q^2 >> \Lambda_{QCD}$) or small distance scales, the QCD coupling constant becomes weaker. If Q^2 tends to infinity, the quarks and gluons become free inside the QCD vacuum. This property of the QCD is known as the asymptotic freedom. As the running coupling strength is small, in this regime perturbative QCD is applicable. Figure 1.1 shows the good agreement between the QCD bases model predictions and experimental results obtained from different systems for the QCD running coupling constant in a wider range of momentum transfer. The asymptotic freedom was discovered in the year 1973 by David Gross [16] and Frank Wilczek [17], and independently research carried by David Politzer [18] in the same year, for which they were awarded nobel prize in the year 2004.

1.2   QCD phase transition and QGP

A phase transition is commonly known as a change of matter from one state to another with a given set of order parameters. The order parameters are variables; that can distinguish two different phases (or orders). The phase transition of different states possible in the QED sector is well understood as an example of the water phase diagram [19]. Similarly, phase transition is expected in the QCD sector, where the transition is defined between a bound state of hadrons to a deconfined state of quarks and gluons. As the QCD is asymptotically
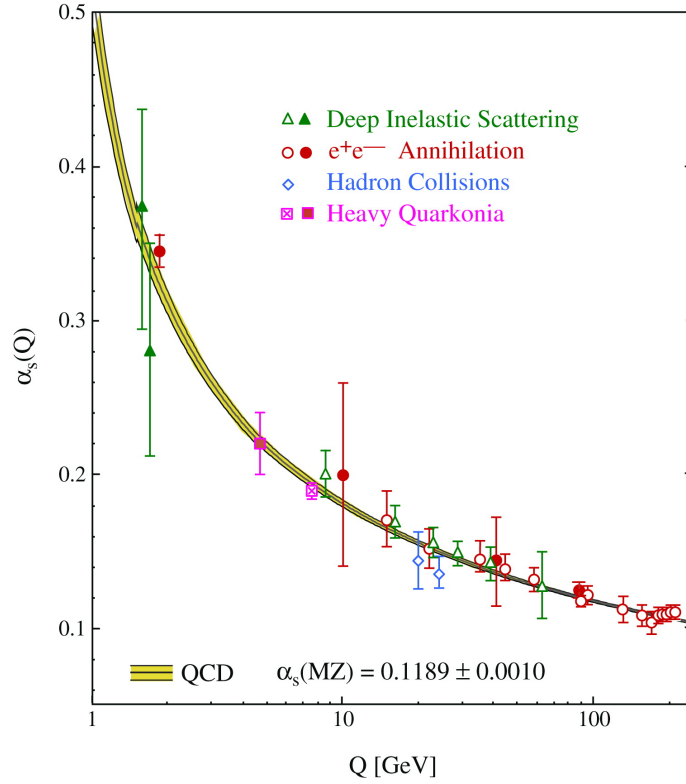
FIGURE 1.1: Strength of the QCD running coupling constant (α_s) as a function of momentum transfer (Q), compared with different experimental measurements. This figure is taken from [15].

free at large momentum transfer or small distance scale, it suggests that at high energies or temperatures, the interaction between quarks or gluons becomes weaker [16, 17]. In the year 1974, T. D. Lee [20], J. C. Collins and M. J. Perry [21] argued that by having high energy density, it is possible to create a dense nuclear matter of asymptotically free quarks or gluons [20]. Such a dense nuclear matter of free quarks or gluons over volumes larger than typical nucleonic sclaes is known as the QGP. Theoretically, lattice QCD calculations suggested the possibility of QGP medium at high temperature [22, 23, 24, 25]. Figure 1.2 shows energy density (ϵ/T^4), pressure density ($3p/T^4$) and entropy density ($3s/4T^3$) as a function of temperature from LQCD calculation for (2+1) quark flavors at zero baryon

chemical potential ($\mu_B = 0$). The μ_B measures how the energy of a system changes due to change in the number of baryons. The energy density shows a rapid increase around a critical temperature, $T_c = 156.5 \pm 1.5$ MeV [22], which indicates an increase in the number of degrees of freedom. This suggests a transition from the hadronic matter to the phase where the quarks and gluons are free.
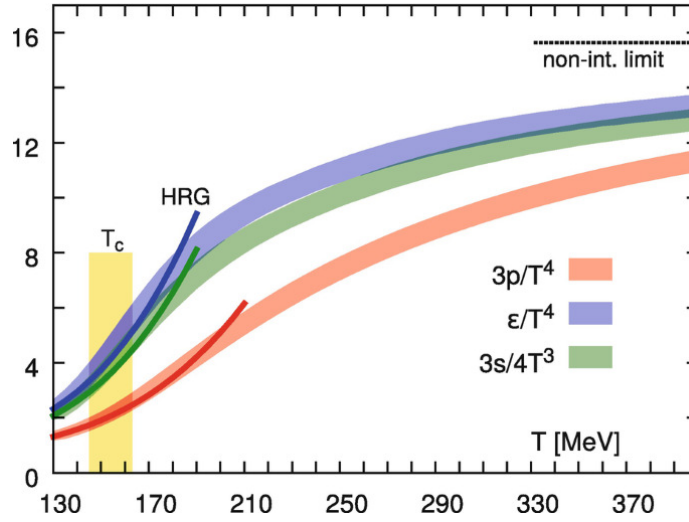
FIGURE 1.2: Normalised energy density(ϵ/T^4), pressure density($3p/T^4$), entropy density($3s/4T^3$) as a function of temperature from Lattice QCD calculation of (2+1) flavor at zero baryon chemical potential ($\mu_B = 0$), as represented by different color bands. At low temperature, the solid line of different color represents results from hadron resonance gas (HRG) and dash lined at high temperature represents non-interaction hardon resonance gas, it is also known as the regime of Stefan-Boltzman ideal gas limit. This figure is taken from [22].

Figure 1.3 shows the conjectured phase diagram (which is not fully established in both theoretically and experimentally) of strongly interacting matter. The QCD phase diagram is usually represented as the temperature (T) vs. the baryon chemical potential (μ_B). The baryon number (B) is a conserved quantity similar to electric charge (Q) and strangeness (S) in the QCD. The μ_B value is found relatively large compared to μ_Q and μ_S in high energy collisions [26, 27]. Different phases of the nuclear matter can be achieved by varying the

temperature (T) and chemical potential (μ_B). Normal nuclear matter is shown at T = 0 and

$\mu_B \sim 925$ MeV. At low T and μ_B, the quarks and gluons are confined inside the hadrons.

At low $\mu_B \sim 0$ and high T, there is a smooth cross over transition between hadronic phase

to QGP phase, it is also predicted by the lattice QCD [28]. At finite T and large μ_B,

several QCD based model calculations suggest the phase transitions to be first order [29].

The neutron star or color superconductive like phases are expected at high μ_B and low

T [30, 31]. Experimentally, the different phases of QCD diagram are studied by varying the
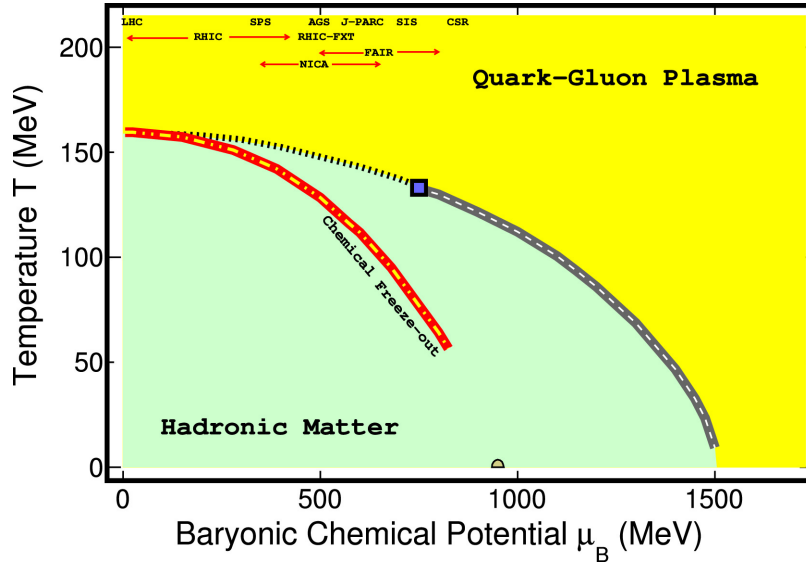
FIGURE 1.3: Schematically a conjectured QCD phase diagram is shown as the temperature (T)
verus the baryon chemical potential (μ_B). This figure is taken from [22]. Black solid
line represents the first-order phase transition line separating the hadronic phase and
quark-gluon phase at large μ_B. The end point of the first order phase transition line
is called the critical point (shown in solid square marker). The red-yellow dotted
line corresponds to the chemical freeze-out inferred from particle yields in heavy-ion
collisions using a thermal model. At T = 0 and $\mu_B \sim 925$ MeV, the ground state of
nuclear matter is shown in the x-axis. This figure is taken from [26].

collision energy ($\sqrt{s_{NN}}$) and different species of colliding system of heavy-ion collisions, as

both T and μ_B depend on $\sqrt{s_{NN}}$ [32]. The various heavy-ion programme at the Relativistic

Heavy Ion Collider (RHIC), the Large Hadron collider (LHC), and future experiments at

the Nuclotron based Ion Collider fAcility (NICA), and the Facility for Anti-proton and Ion Research (FAIR) aim to explore the phase diagram of QCD.

1.3   Relativistic Heavy-Ion Collisions

The relativistic heavy-ion collisions provide the necessary conditions, such as very high temperature and energy density, to create a deconfined state of quarks and gluons in the laboratory and study its properties. Experimentally, to understand the QGP and study its properties that is formed in heavy-ion collisions, several facilities at RHIC, LHC, and NICA and future experiments at FAIR are built. One such facility is A Large Ion Collider Experiment (ALICE) at the LHC, which allows the forming of a primordial state of QCD matter; it is believed that such a state of matter was present in the microsecond old universe of the Big Bang. In this following subsections about geometrical aspects of heavy-ion collisions, space-time evolution of the QCD matter produced in heavy-ion collisions, and an introduction to basic kinematics variables used in high energy physics are discussed.

1.3.1   Geometrical aspects of heavy-ion collisions

Figure 1.4 shows a geometrical picture of collision of two symmetric heavy-ions. The projectile and target beams collide at ultra-relativistic energies, so they are Lorentz contracted along the direction of motion (generally taken as z-axis). The perpendicular distance between the centre of two colliding nuclei is called the impact parameter ("b"), which determines the overlap region of collisions and tells information about the centrality of collision. The nucleons that participate in the collisions are in the overlap region and are called as participant nucleons (N_{part}). Those nucleons that do not take part in the collisions are called as "spectators" ($N_{spectator}$ = 2A - N_{part}, A is the mass number of nucleus). The

impact parameter value varies from 0 fm (corresponding to head collisions) to about twice the radius of the nucleus (corresponding to most peripheral collisions). Experimentally, the impact parameter "b" cannot be measured directly; the number of charged particles produced in collisions is used to characterize the geometry of collisions, referred to as centrality or multiplicity. Most central collisions are defined as having a large number of participating nucleons, small impact parameters, or a large number of charged particles produced. In contrast, a low number of participating nucleons or larger value of impact parameter, or a less number of final charged particles produced in a collision, is called peripheral collisions. The detailed discussion of centrality or multiplicity determination using the number of charged particles produced in a collision is given in Section 3.2.1 of Chapter 3.
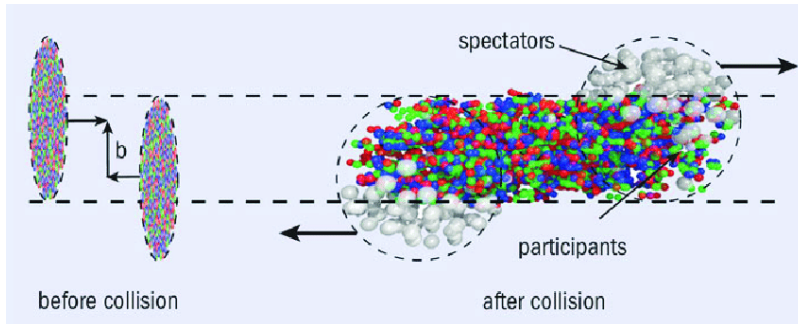
FIGURE 1.4: A schematic picture of geometry of ultrarelativistic heavy-ion collisions. This figure is taken from [33].

1.3.2 Space-Time evolution

Figure 1.5 shows a schematic view of space-time evolution of heavy-ion collisions. When two nuclei moving towards each other with velocity (v) nearly equal to the velocity of light (c), they are Lorentz contracted, along the direction of the motion. At proper time $\tau = 0$, the collision between two Lorentz contracted nuclei takes place. The space-time evolution

of ultra-relativistic heavy-ion collisions has been divided into mainly 3 stages: i) initial stage: Pre equilibrium stage ii) intermediate stage: QGP stage, and iii) final stage: hadron gas and freeze-out.
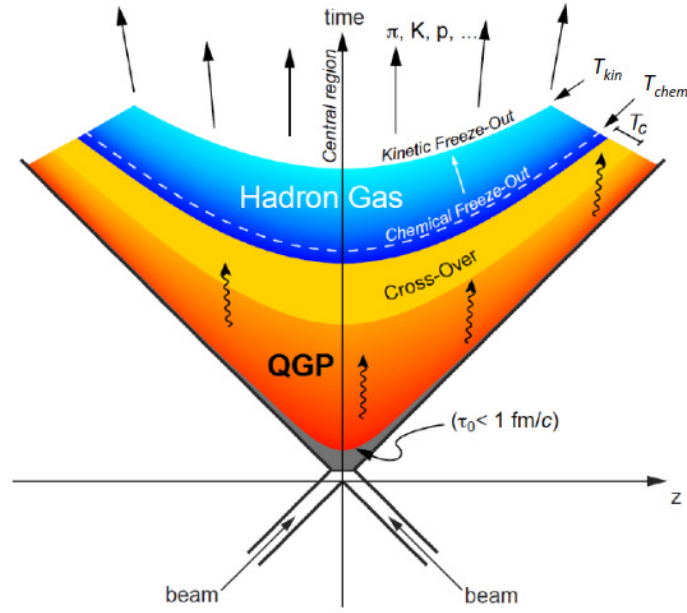
FIGURE 1.5: A schematic diagram of space-time evolution of a system created in heavy-ion collisions at ultra-relativistic energies. This figure is taken from [34].

Pre equilibrium stage

After the collisions, a large amount of kinetic energy is deposited in the overlap region between two colliding nuclei within a small volume and a short time interval. If energy density is sufficiently high enough such that it is expected to create a deconfined state of quarks or gluons, the produced deconfined states may not be in thermal equilibrium at $\tau <$ 1 fm/c. Particles with very high momentum are produced in this stage due to the interaction among the partons.

QGP stage

After the pre-equilibrium stage, when the deconfined state of quarks and gluons reaches above a critical energy density or temperature, it attains a local thermal equilibrium due to the interaction among the constitutes. After that free quarks and gluons to form the QGP medium. According to the Lattice QCD predictions, the QGP formation is required above the critical energy density 1 GeV/fm^3 or critical temperature. The evolution of the QGP medium in this stage is assumed to behave like a hydrodynamic fluid. The QGP matter starts expanding and cools down with time; it reaches a temperature at which quarks and gluons combine to form hadrons.

Hadron gas phase and freeze-out stage

Hadrons stay in the hardon gas phase, interacting with each other elastically and inelastically after harmonization. It expands further and the inelastic interactions among them stop at a temperature. This temperature is known as chemical freeze-out temperature (T_{chem}), at which the chemical composition of hadrons and relative abundance of the stable particle yields are fixed. But still, hadrons interact elastically; when the distance between two hadrons is greater than the mean free path, the interaction among the hadrons stop. The temperature at which elastic collisions cease is known as kinetic freeze-out temperature (T_{kin}), where the shape of transverse momentum spectra gets fixed. After that, hadrons fly freely towards the detector.

1.3.3 Kinematics variable

In relativistic heavy-ion collisions, kinematic variables are commonly used because they are invariant quantities or can be expressed in the simple form under the Lorentz transformation

from one frame of reference to another. This section briefly discusses the kinematics variables used in high-energy collision experiments.

Natural units

In ultra-relativistic high-energy collisions, all physical quantities of the experimental observables are expressed in natural units for simplicity of calculation. In natural units, the planck's scale ($\hbar$), speed of light (c) and boltzmann constant (k_B) are taken as unity, and length and time scale are expressed in GeV^{-1} and mass or energy in GeV. The observables in SI units can be converted to the natural units by using the conversion factor $\hbar c = 0.1975$ GeV fm.

Center-of-mass energy

In a two body colliding system, the center of mass of incoming particles is defined as a square of the sum of four momentum of two incoming particles. It is a Lorentz invariant quantity and expressed in terms of Mandelstam variable "s", which is defined as

$$s = (\mathbf{p}_1 + \mathbf{p}_2)^2 = (E_1 + E_2)^2 - (\vec{p_1} + \vec{p_2})^2 = (E_1 + E_2)^2 \qquad (1.3)$$

Where $\mathbf{p}_1$ and $\mathbf{p}_2$ are four momentum of colliding particles, E_1, E_2, $\vec{p_1}$, $\vec{p_2}$ are the energy and momentum vector of incoming particles, respectively. In center-of-mass frame, total momentum of colliding beams vanishes, hence $\vec{p_1} = - \vec{p_2}$ as the mass of colliding particles are identical mass. Therefore, center-of-mass energy ($\sqrt{s}$) can be expressed as

$$\sqrt{s} = E_1 + E_2 = 2E \qquad (1.4)$$

In heavy-ion collisions at LHC, the Lead (Pb) nuclei accelerate at 2760 GeV/nucleon, and the estimation of total center-of-mass energy involved in most central (head-on, b=0) Pb–Pb

collisions is = 2×2760 GeV $\times 208$ nucleons = 1.15×10^6 GeV. It shows that a very large amount of energy is available in a small volume.

Transverse momentum

The total momentum (p) of a particle has three components p_x, p_y and p_z. The momentum component along beam direction i.e., z-axis corresponds to the longitudinal component. The other two components p_x and p_y are transverse components of p. The transverse momentum (p_T) is invariant under the Lorentz transformation and is defined as

$$p_T = \sqrt{p_x^2 + p_y^2} \tag{1.5}$$

Rapidity

The rapidity is expressed as,

$$y = \frac{1}{2} \ln \left(\frac{E + p_z}{E - p_z} \right), \tag{1.6}$$

where E and p_z energy and longitudinal momentum of a produced particle. In non-relativistic limit ($p \leq$ m , where m is rest mass), the rapidity of a particle is equivalent to velocity. In high-energy collisions, the advantage of using kinematic variable rapidity (y) due to it is additive under Lorentz transformation in the relativistic limit.

Pseudorapidity

Experimentally, mass of particles cannot be measured directly, generally momentum information of particles are measured. Therefore, simultaneous measurements of energy and momentum are difficult in the experiment. In this situation, one uses another kinematic variable over rapidity called as pseudorapidity. The pseudorapidity is defined as

$$\eta = \frac{1}{2} \ln \left(\frac{p + p_z}{p - p_z} \right) = - \ln \tan(\theta/2), \tag{1.7}$$

where $\theta = \cos^{-1}(p_z/p)$ is the angle between the particle emitted with respect to the beam direction. In the relativistic limit, $p >> $ m, E $\approx$ p, then pseudorapidity is equivalent to rapidity.

Particle multiplicity

The number of particles produced in an event or a single collision is called multiplicity. In experiment, the term multiplicity generally refers to the total charged particle multiplicity.

Invariant yield

In high energy collisions, the yield of produced particles is measured by a quantity known as invariant yield. It is invariant under the Lorentz transformation. The invariant yield is obtained by integrating over azimuthal angle (ϕ), where ϕ is defined as $\tan^{-1}(p_y/p_x)$ and is expressed as

$$E\frac{d^3N}{dp^3} = E\frac{d^3N}{dp_x dp_y dp_z} = E\frac{d^3N}{p_T dp_T d\phi dp_z} = \frac{d^3N}{p_T dp_T d\phi dy} = \frac{d^2N}{2\pi p_T dp_T dy} \qquad (1.8)$$

The expression is simplified using the relations, $dp_x dp_y = dp_T$ and $dy = dp_z/$E. Experimentally, the invariant is expressed in terms of transverse momentum (p_T) or transverse mass ($m_T = \sqrt{p_T^2 + m^2}$), as

$$E\frac{d^3N}{dp^3} = \frac{d^2N}{N_{evt} 2\pi p_T dp_T dy} = \frac{d^2N}{N_{evt} 2\pi m_T dm_T dy} \qquad (1.9)$$

where N_{evt} stands for the number of events and N is the number of produced particles.

1.4 Experimental probes and signature of QGP

In this section, we discuss a few experimental signatures indicating the presence of QGP phase in heavy-ion collisions.

1.4.1 Jet quenching

High-energy nucleon-nucleon or nucleus-nucleus collisions produce highly energetic partons (quarks or gluons) through initial hard scattering processes. These partons fragment into the number of collimated spray of hadrons, it is called as jets. The study of jet physics is interesting because it is produced in early stages of collisions well before the formation of the QGP. It carries information on the entire space-time evolution of collisions, thus helping to probe the hot and dense medium of the QGP. When a highly energetic patron traverses through the hot and dense medium of QGP, it interacts with other patrons inside the medium. As a result, the initial parton loses its energy before the formation of hadrons. This phenomenon is known as jet quenching. Experimentally, the jet quenching is measured using two observables; azimuthal correlation between two high-momentum hadrons, known as di-hardons azimuthal correlation, and suppression in the yield of high p_T hadrons, by measuring the nuclear modification factor (R_{AA}). The most hard scattering processes are two body scatterings, which results in di-jets are produced back to back ($\Delta\phi = 180°$) due to momentum conservation. Figure 1.6 illustrates the jets formation in pp and heavy-ion collisions (i.e., Pb–Pb), one of the jets can be produced in the edge of created medium, known as near-side ($\Delta\phi = 0$) jet and other jet is produced at same point as the near-side jet but it travels inside the medium, known as away-side ($\Delta\phi = \pi$) jet. The away-side jet traverses more path inside the medium than the near-side jet. As a result, the produced away-side jet is more quenched than near-side jet in heavy-ion collisions.

Figure 1.7 shows di-hadron azimuthal correlation of high p_T particles for pp (black line), d–Au (red marker), and Au–Au (blue marker) collisions from the STAR experiment. It is observed that two peaks have been seen at near-side ($\Delta\phi = 0$ radians) and away-side ($\Delta\phi = \pi$ radians) for pp and d–Au collisions. However, the away-side peak is suppressed
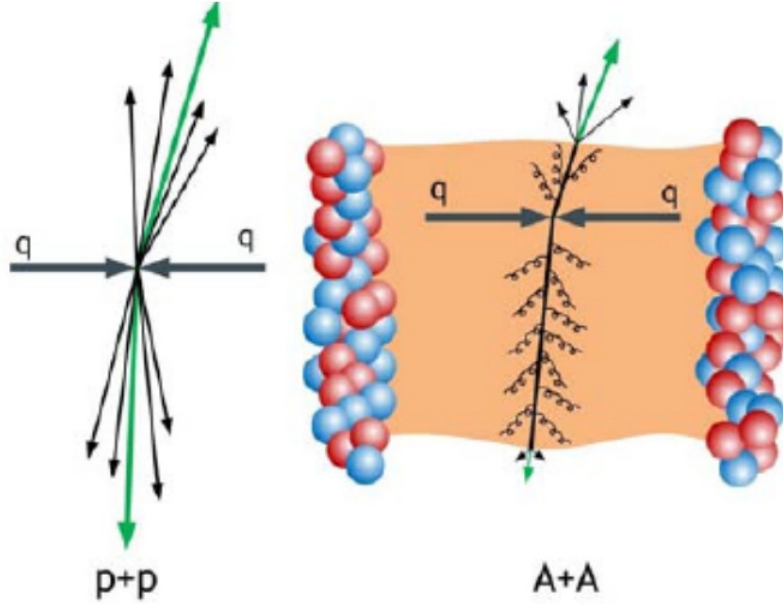
FIGURE 1.6: Illustration of jets formation in pp and heavy-ion collisions. This figure is taken from [35].

compared to the near-side peak in central Au–Au collisions. This suppression of away side peak in central Au-Au collisions suggests the presence of jet quenching effects. It provides a clear signature of the hot and dense medium of the QGP, however jet quenching effect is absent in small colliding systems.

Another experimental observable used to characterize jet quenching is the nuclear modification factor (R_{AA}), it is defined as

$$R_{AA}(p_T) = \frac{d^2 N_{AA}/dp_T dy}{\langle T_{AA} \rangle d^2 \sigma_{pp}^{INEL}/dp_T dy}, \tag{1.10}$$

where $d^2 N_{AA}/dp_T dy$ is the yield in A–A collisions and $d^2 \sigma_{pp}^{INEL}/dp_T dy$ is the invariant yield cross section in inelastic pp collisions. $\langle T_{AA} \rangle = \langle N_{coll} \rangle / \sigma^{INEL}$ (σ^{INEL} is nucleon–nucleon inelastic cross section) is the average nuclear overlap function, which accounts for
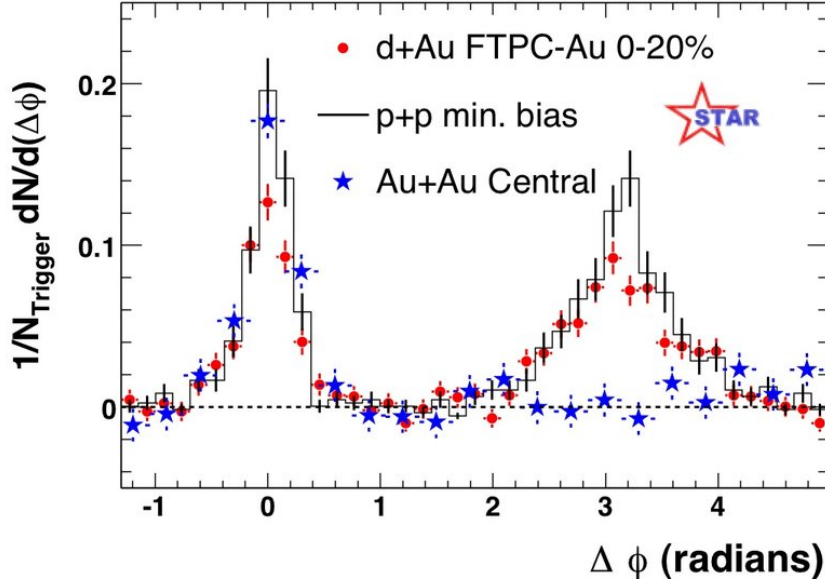
FIGURE 1.7: The di-hadron azimuthal correlation distributions for high p_T charged particles for pp, d–Au and Au–Au collisions. This figure is taken from [36].

the nuclear collision geometry, it is obtained from a Glauber model [37]. If $R_{AA} = 1$, it suggests that the A–A collisions is a simple superposition of pp collisions. Any deviation of R_{AA} from unity implies the presence of effect caused by the medium. Figure 1.8 shows the nuclear modification factor as a function of p_T for four different center-of-mass energies ($\sqrt{s_{NN}} = 0.017$, 0.2, 2.76 and 5.02 TeV) of different species such as neutral pions (SPS, RHIC), charged pions (SPS), and inclusive charged hadrons (h$^\pm$) (RHIC, LHC) for central heavy-ion collisions. The suppression of high p_T yield suggests that jet quenching is observed at both RHIC and LHC energies in heavy-ion collisions.

1.4.2 J/ψ suppression

J/ψ is a flavor neutral meson consisting of c and $\bar{c}$ quark pairs. Heavy quarks like c and $\bar{c}$ are produced early in the collisions from hard scattering. They see the full evolution
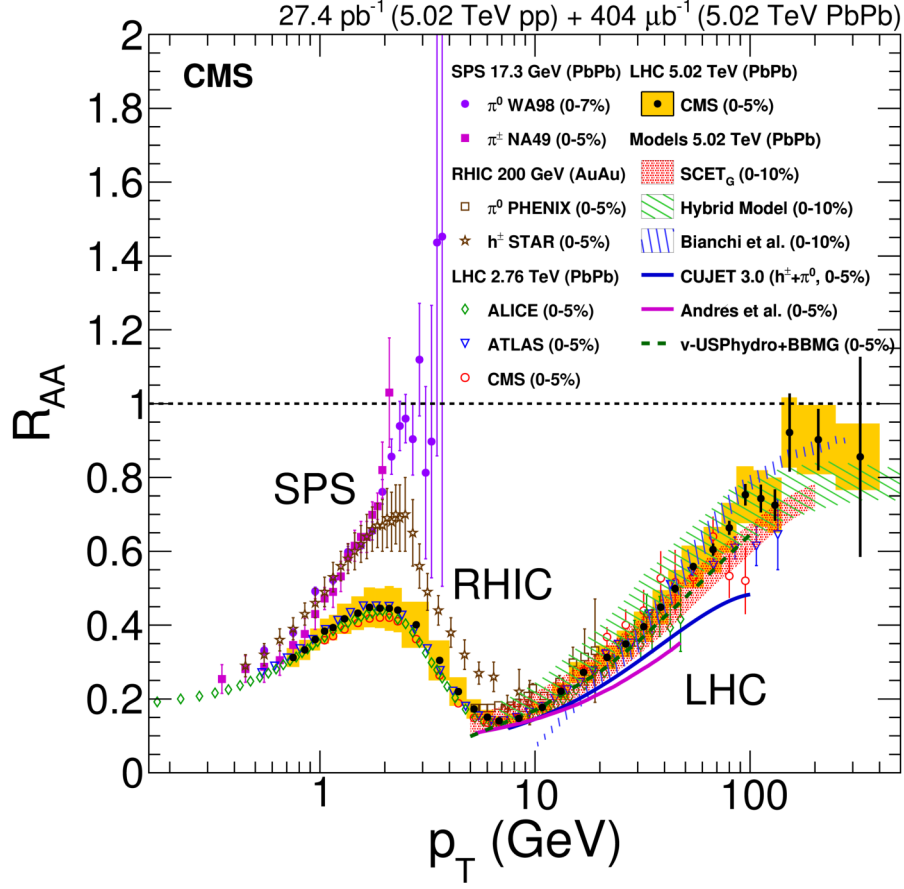
FIGURE 1.8: Nuclear modification factor as a function of p_T for central heavy-ion collisions at four different center-of-mass energies, for neutral pions (SPS, RHIC), charged pions (SPS), and inclusive charged hadrons ($h^\pm$) (RHIC, LHC). Measurements are compared to the predictions of four models for Pb–Pb collisions at $\sqrt{s_{NN}} = 5.02$ TeV. This figure is taken from [38].

of the produced system and are good candidates to probe the deconfined state of quarks and gluons and its novel properties. In QED, the strength of potential between charged particles is reduced due to the presence of surrounding charges. This effect is known as Debye screening or shielding. Similarly, the modification of heavy-quark pair potential is expected due to the presence of color charge in hot and dense medium formed in heavy-ion

collisions. The potential ($V(r)$) between $c\bar{c}$ pair in QCD vacuum is expressed as

$$V(r) = \frac{a}{r} + kr \qquad (1.11)$$

where a is coulombic interaction coupling constant and k is the string tension, respectively. The "r" is the distance between the c and $\bar{c}$. The second term of Eq. 1.11 vanishes for the QGP medium when temperature of the system reaches T_c. Due to presence of QGP medium, the potential between $c\bar{c}$ pair is modified, it is expressed as

$$V(r) = \frac{a}{r} e^{-(\frac{r}{\lambda_D})} \qquad (1.12)$$

Where λ_D is Debye length and it depends on T. In the year 1986, Matsui and Satz first proposed that the Debye length could become smaller than the size of the J/ψ radius in the QGP medium [39]. As a result, the bound state of $c\bar{c}$ can not occur. This leads to suppression of J/ψ production in heavy-ion collisions due to presence of QGP medium. Experimentally, first signature of J/ψ suppression was seen at the SPS [40], subsequently confirmed by the RHIC [41, 42] and later at the LHC [43, 44]. Figure 1.9 (left panel) shows nuclear modification factor as a function of p_T for Pb–Pb collisions at $\sqrt{s_{NN}}$ = 2.76 and 5.02 TeV for centrality 0-20%. The suppression of J/ψ production is observed in the measured p_T region. However, the suppression is stronger at high p_T and also a weak energy dependence is observed. The transport model predictions [45] fairly describes the data whereas the statistical model [46] fails to describe the data. The R_{AA} of J/ψ as a function of $\langle N_{part} \rangle$ at RHIC and LHC is shown in right panel of the Fig. 1.9. The higher value of $\langle N_{part} \rangle$ corresponds to central collisions and lower value to the peripheral collisions. The value of R_{AA} at LHC is higher than RHIC at central collisions. At the same time, at LHC, energies favor the production of more c and $\bar{c}$ pairs is that followed by recombination processes to enhance J/ψ production. The $R_{AA} < 1$, indicating the clear suppression in J/ψ production
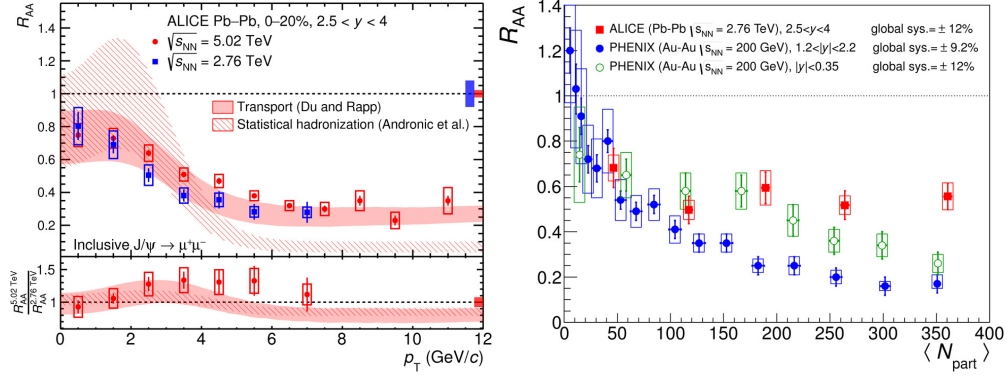
FIGURE 1.9: Nuclear modification factor of J/ψ as a function of p_T (left) and $\langle N_{part} \rangle$ (right) for heavy-ion collisions (Au–Au collisions at $\sqrt{s_{NN}}$ = 200 GeV, and Pb–Pb collisions at $\sqrt{s_{NN}}$ = 2.76 and 5.02 TeV). These figures have been taken from [43, 44].

at both RHIC and LHC energies. These observations are compatible with the formation of the QGP that suppresses the J/ψ production.

1.4.3   Strangeness enhancement

One of the primary signatures of the formation of QGP medium is to see the enhancement of strange particle production in heavy-ion collisions, it was proposed by J. Rafelski and B. Muller [47]. Enhanced production of particles having the strange quark in the QGP medium created in heavy-ion collisions relative to the pp collisions is known as strangeness enhancement. As nucleus-nucleus (A–A) or nucleon-nucleon (pp) collisions, at initial colliding system have no valence strange quarks (s, $\bar{s}$), so the production of strange quarks are only by product after the collisions. The strange quarks are produced by hard scattering processes such as flavor creation ($gg \rightarrow s\bar{s}$, $q\bar{q} \rightarrow s\bar{s}$), and flavour excitation ($gs \rightarrow gs$, $qs \rightarrow qs$) and also via gluon splittings ($g \rightarrow s\bar{s}$). In the presence of QGP medium or gluon rich system, the production of s$\bar{s}$ from gluon (g) channel dominates over the quark (q) and anti-quark ($\bar{q}$) annihilation [48]. As a result, it enhanced the strange

hadron production for the QGP medium compared to pp collisions. In addition to the QGP medium, the hadrons consists of strange quark can be formed in hadronic phase via some reaction as $\pi + \pi \rightarrow K + K$, $N + N \rightarrow N + \Lambda + K$ etc. Another explanation of strangeness enhancement according to canonical picture is that in small colliding systems (like pp, p–Pb), the hadrons having strange content (K, K_S^0, ϕ, Λ) may be suppressed, as results, it leads to enhancement in yield ratios (the ratio between particle yield measured in heavy-ion collisions to pp collisions). As the ϕ meson consists of s and $\bar{s}$ pair and net strangeness is zero, the measurements of ϕ meson along with strange baryons can provide further understanding of strangeness enhancement. Experimentally, the observable used for quantifying the strangeness enhancement is defined as

$$\varepsilon = \frac{2}{\langle N_{\text{part}} \rangle} \frac{\frac{\mathrm{d}N^{\text{AA}}}{\mathrm{d}y}}{\frac{\mathrm{d}N^{\text{pp}}}{\mathrm{d}y}} \tag{1.13}$$

Figure 1.10 shows strangeness enhancement factor (ε) as a function of $\langle N_{part} \rangle$ for strange mesons (K$^-$, ϕ) and baryons ($\overline{\Lambda}$, Ξ) in Au–Au and Cu–Cu collisions at $\sqrt{s_{\text{NN}}} = 200$ GeV. Strangeness enhancement is observed for all species as a function of centrality, energy, and quark content of strangeness. The enhancement of ϕ meson observed for both Au–Au and Cu–Cu collisions suggests that enhanced strange quark production indicates the presence of the QGP medium formed in heavy-ion collisions. Recent high multiplicity measurements of strange and multi-strange particle in small colliding system (pp, p–Pb) have shown similar behavior of strangeness enhancement as that have been observed in heavy-ion collisions [49]. In the year 2017, ALICE reported the enhancement of strange and multi-strange production relative to pions in high multiplicity pp and p–Pb collisions is shown in Fig. 1.11 showing the possible hint of formation of QGP like medium in high multiplicity small colliding systems at LHC energies. The pQCD inspired models fail to describe the measurements. Further, exploration is ongoing to understand the high
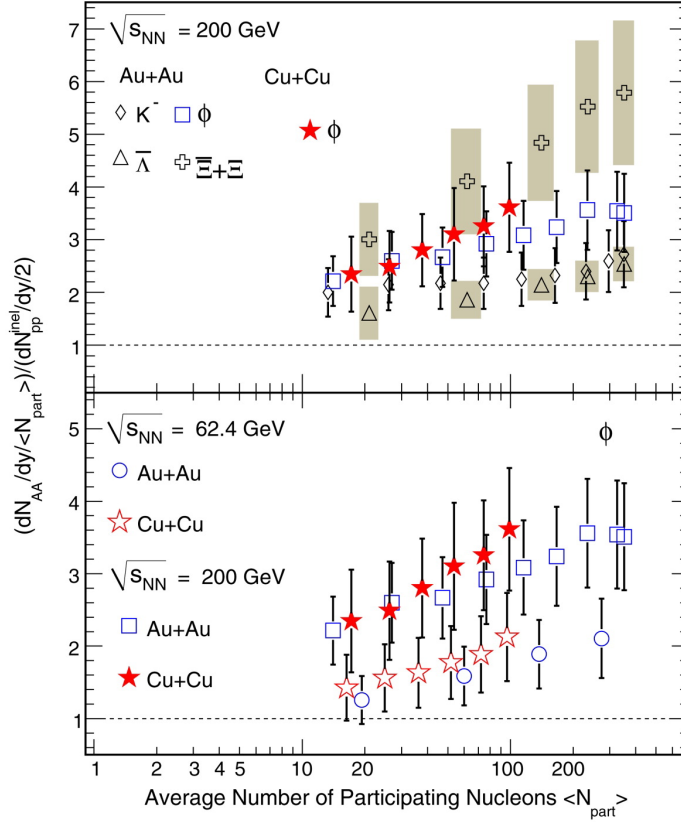
FIGURE 1.10: ε as a function of $\langle N_{part} \rangle$ for K$^-$ (S=1), ϕ (S =0), $\bar{\Lambda}$ (S = 1) and Ξ (S =2) for Au–Au and Cu–Cu collisions at $\sqrt{s_{NN}}$ = 200 GeV. This figure is taken from [50].

multiplicity collisions at LHC energies.

1.4.4   Azimuthal anisotropy

In non-central heavy-ion collisions, the interaction volume of two colliding nuclei has an almond shape. The initial spatial anisotropy of the almond shape is converted to momentum anisotropy of final state hadrons due to the interaction among constituents via large pressure gradient. The momentum anisotropy leads to anisotropy in the azimuthal angle (ϕ) of a produced particle with respect to the reaction plane, this is known as azimuthal anisotropy. The reaction plane is defined as the plane containing impact parameters and beam direction.
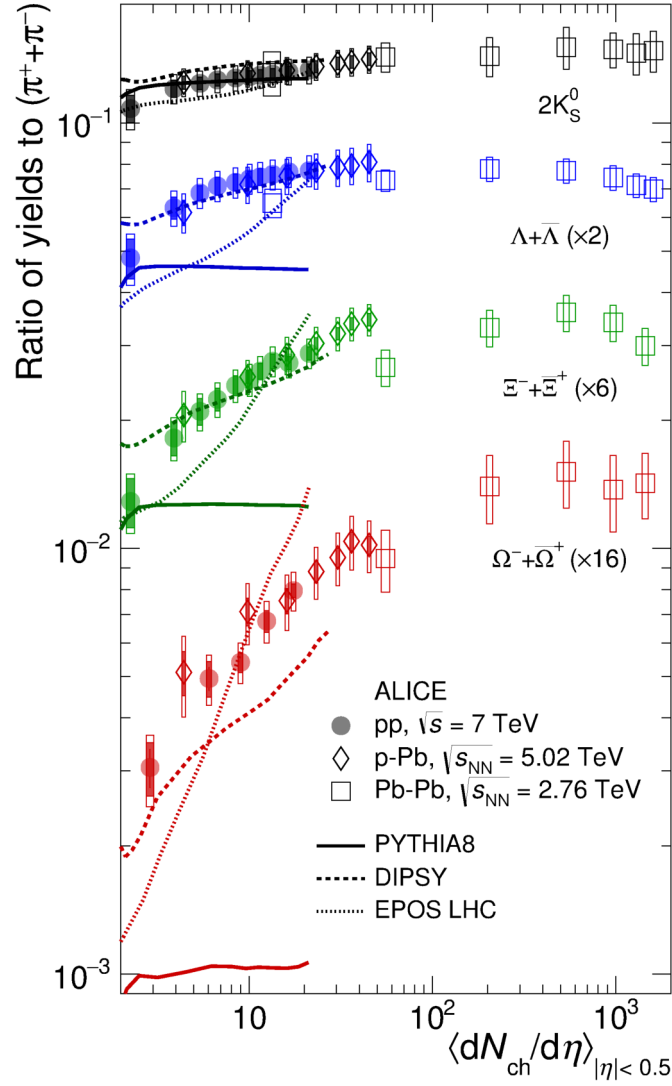
FIGURE 1.11: The yield ratios of strange and multi-strange particles to pion in pp, p–Pb and Pb–Pb collisions as a function of charged particle multiplicity ($\langle dN_{ch}/d\eta \rangle_{|\eta|<0.5}$). This figure is taken from [48].

Experimentally, the azimuthal distribution of produced particle can be expressed in terms of Fourier expansion [51] as

$$E\frac{d^3N}{d^3p} = \frac{d^2N}{2\pi p_T dp_T dy}\left(1 + \sum_{n=1}^{\infty} 2v_n \cos(n\phi)\right), \qquad (1.14)$$

where the second-order flow harmonic coefficient v_2 is known as the elliptic flow. The elliptic flow is sensitive to the early stage of heavy-ion collisions because the spatial anisotropy vanishes, due to the hot and dense medium produced in such collisions expands quickly. Figure 1.12 (left panel) shows elliptic flow as a function of p_T for identified particles (π, K, K_S^0, p, ϕ, Λ and Ω) in Au–Au collisions at $\sqrt{s_{NN}}$ = 200 GeV measured by STAR and PHENIX Collaboration [52, 53, 54]. At low p_T (< 2 GeV/c), v_2 increases with p_T and a clear mass dependence is observed. The measurements are fairly well reproduced by the hydrodynamical model calculation as shown in solid and dashed lines [55]. At high p_T, v_2 of baryons and mesons show a different trend and model predictions fail to describe and overestimate the data. This suggests a different mechanism of particle production (i.e., quark coalescence/recombination [12]) above $p_T \gtrsim 2$ GeV/c compared to the lower p_T region. Similar behavior observed for v_2 (right panel) as a function of p_T for identified particles (π, K, p, ϕ, and Λ) in Pb–Pb collisions at $\sqrt{s_{NN}}$ = 5.02 TeV by ALICE Collaboration [12].
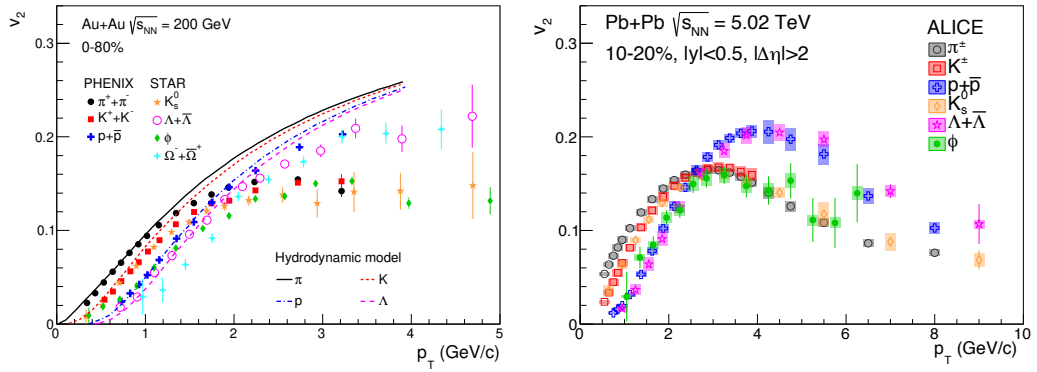
FIGURE 1.12: Left: v_2 as a function of p_T for $\pi^\pm$, $K^\pm$, K_S^0, $p(\bar{p})$, ϕ, $\Lambda(\bar{\Lambda})$, and Ω in Au+Au collisions at $\sqrt{s_{NN}}$ = 200 GeV from the STAR and PHENIX experiments [52, 53, 54]. Solid and dashed curves show the prediction of the hydrodynamic model [55]. Right: v_2 as a function of p_T for $\pi^\pm$, $K^\pm$, K_S^0, $p(\bar{p})$, ϕ, and $\Lambda(\bar{\Lambda})$ in Pb–Pb collisions at $\sqrt{s_{NN}}$ = 5.02 TeV from the ALICE [12]. .

It has been observed that a clear mass dependence in v_2 and values are similar in order at low p_T for both RHIC and LHC energies. The hydrodynamical model with the initial conditions of the QGP explains the data, it indicates the flow is developed at partonic level and formation of the QGP medium in heavy-ion collisions.

1.5   Resonance production in high energy collisions

Resonances are short-lived particles having lifetime of the order a few fm/c ($\sim 10^{-23}$ sec) and decay via the strong interaction. Due to their short lifetime, they are sensitive probes to characterize the hadronic phase created in high energy collisions, it is the phase between chemical freeze-out (when inelastic collisions among the constituents cease) and kinetic freeze-out (when elastic collision ceases). The decay products of the resonance can elastically interact with other hadrons and change their momentum in the hadronic phase. As a result, the parent resonance can not be reconstructed back and it leads to a suppression in the final yield of resonance. This process is known as a rescattering effect. Similarly, another process is that the hadrons inside the hadronic phase can re-generate a resonance via pseudo-elastic interaction (for example: $K\pi \rightarrow K^{*0} \rightarrow K\pi$). This effect is known as a regeneration, it leads to enhancement in the final measured resonance yield relative to primary production. Several resonances have been measured experimentally to understand the rescattering and regeneration effects due to the presence of the hadronic phase. The detailed properties such as mass, decay products (branching ratios), and lifetimes of hadronic resonances are shown in Table 1.1. The schematic view for the rescattering and regeneration processes for K^{*0} in the hadronic phase is demonstrated in Fig. 1.13.

The interplay between the rescattering and regeneration effects are studied by measuring

TABLE 1.1: Experimentally measured hadronic resonances in high energy collisions by the ALICE, arranged according to their lifetime. BR = branching ratio.

Resonance(MeV/c^2)	Decay channel (BR %)	Lifetime (fm/c)
$\rho(770)$	$\pi^+\pi^-$ (100)	1.1
$K^{*0}(892)$	$K^\pm\pi^\mp$ (66.6)	4.2
$K^{*\pm}(892)$	$K^0_S\pi^\mp$ (33.3)	4.0
$f_0(980)$	$\pi^+\pi^-$ (46)	$\sim$ 5-10
$\Sigma^{*\pm}(1385)$	$\Lambda\pi$ (87)	$\sim$ 5-6
$\Lambda(1520)$	Kp (22.5)	12.6
ϕ (1020)	K^+K^- (49.2)	46.2
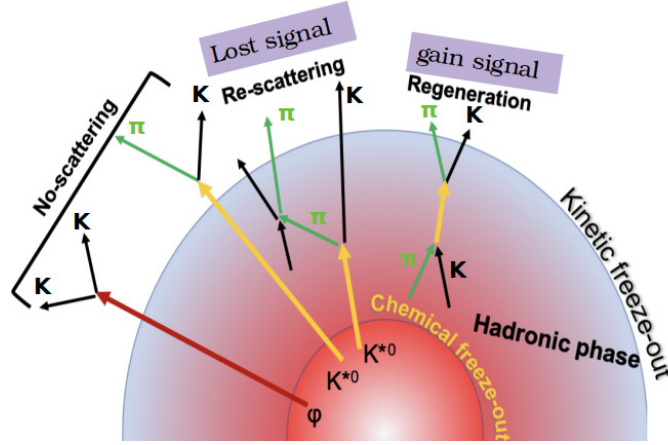
FIGURE 1.13: Schematic view of rescattering and regeneration processes in the hadronic phase.

the ratio of the resonance to stable hadron yield with similar quark content. Figure 1.14 shows the particle ratios (K^{*0}/K, ϕ/K) as a function of average charged particle multiplicity ($\langle dN_{ch}/d\eta \rangle^{1/3}_{|\eta|<0.5}$ is a proxy as system size) for Pb–Pb collisions at $\sqrt{s_{NN}}$ = 2.76 and 5.02 TeV, for p–Pb at $\sqrt{s_{NN}}$ = 5.02 TeV and minimum bias pp collisions at $\sqrt{s_{NN}}$ = 5.02 TeV [57, 58, 59], and results are compared with model predictions. The K^{*0}/K ratios decreases from peripheral to central collisions (large value of $\langle dN_{ch}/d\eta \rangle^{1/3}_{|\eta|<0.5}$ corresponds to central collisions, whereas lower value corresponds to peripheral collisions). The K^{*0}/K

value in central Pb–Pb collision is significantly lower than the value measured in minimum bias pp collisions and the thermal model predictions. This suppression in K^{*0}/K ratio in most central collisions indicates the decay product of K^{*0} has been modified by rescattering effects. The rescattering effects dominates over regeneration effects. However, ϕ/K ratios show remains constant and show similar value as a function of $\langle dN_{ch}/d\eta \rangle_{|\eta|<0.5}$ for all colliding systems. It is expected because the lifetime of ϕ (46.2 fm/c) is larger compared to the lifetime of K^{*0} (4.2 fm/c).
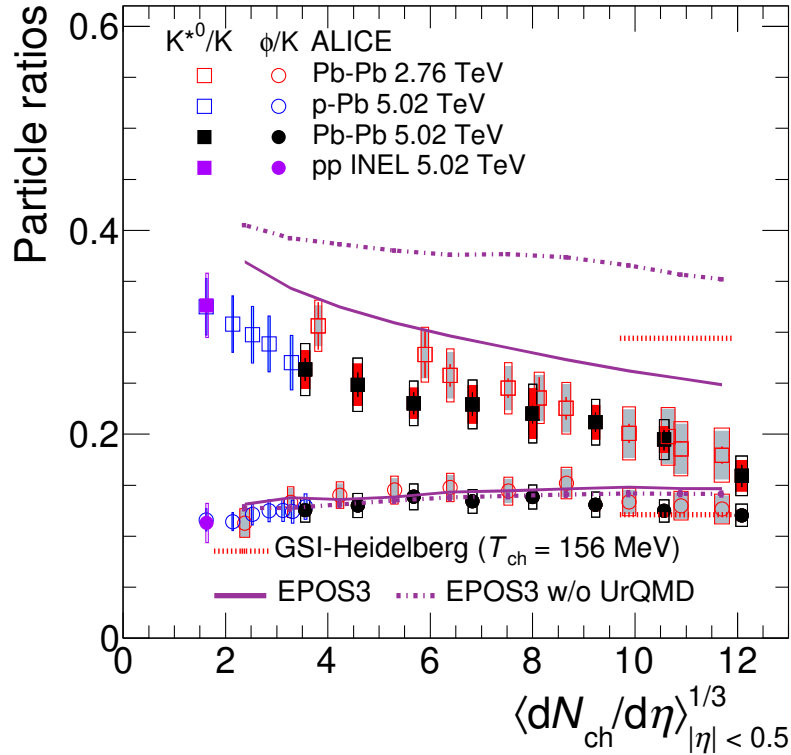
FIGURE 1.14: Particle ratios (K^{*0}/K, ϕ/K) as a function of $\langle dN_{ch}/d\eta \rangle_{|\eta|<0.5}^{1/3}$ for Pb–Pb collisions at $\sqrt{s_{NN}}$ = 2.76 and 5.02 TeV , for p–Pb at $\sqrt{s_{NN}}$ = 5.02 TeV and minimum bias pp collisions at $\sqrt{s_{NN}}$ = 5.02 TeV and results are compared with model predictions. This figure is taken from [58].

The measurements are also compared with model predictions from EPOS3 with and

without hadronic phase modeled by UrQMD [60]. The EPOS3 with UrQMD fairly describes the observed trend of the measurements. A similar decrease trend in K^{*0}/K and modification of the resonance yields in the hadronic phase through rescattering and regeneration processes have been discussed at lower energy by STAR [61, 62]. Measurements of various hadronic resonances having different lifetime, mass, quark content, and quantum numbers have been studied. They provide information about the understanding of the mechanisms that influence the shape of particle momentum spectra, lifetime of the hadronic phase, strangeness production, parton energy loss, rapidity yield asymmetry and collective effects. In addition, the vector meson (spin =1) resonances (K^{*0}, $K^{*\pm}$,ϕ) have been used to explore initial conditions of heavy-ion collisions. The system produced in non-central collisions have generated a large angular momentum ($\vec{L} \sim 10^{6-7}\hbar$) and magnetic field ($|\vec{B}| \sim 10^{18}$ Gauss). Due to spin orbit coupling in the strong interaction, the produced vector mesons resonance can be aligned along the direction of $\vec{L}$ or $\vec{B}$. Measurements of hadronic resonances not only important to probe the hadronic phase, where final state effects are dominant but also explore the initial condition of heavy-ion collisions through spin alignment measurement.

1.6 Thesis motivation

This thesis is based on the study of resonances production with ALICE at LHC. The first part of the thesis mainly discusses on understanding the final state effect, and the initial state effects arising from the nuclear processes in high energy collisions have been studied by measuring the $K^{*0,\pm}$ production in pp and p–Pb collisions. The second part of the thesis focuses on studying the initial conditions of heavy-ion collisions by measuring the angular distribution of vector mesons ($K^{*0,\pm}$, ϕ) in Pb-Pb collisions at $\sqrt{s_{\mathrm{NN}}}$ = 5.02 TeV.

1.6.1 Multiplicity dependence of $K^{*0,\pm}$ production in p–Pb collisions

Recent measurements in high multiplicity p–Pb collisions have shown similar striking features that have been observed in heavy-ion collisions. Observation in the enhancement of multi-strange hadrons [15] (shown in left panel of the Fig. 1.15), non-zero value of elliptic flow (v_2) [11] (shown in right panel of Fig. 1.15), near and away side ridge structure in two particle angular correlation [13, 14], mass ordering in hadron p_T spectra and enhancement in baryon-to-meson ratios [16] indicate that collective-like phenomena are present in p–Pb collisions at the LHC energies. A smooth transition of hadron yield as a function of
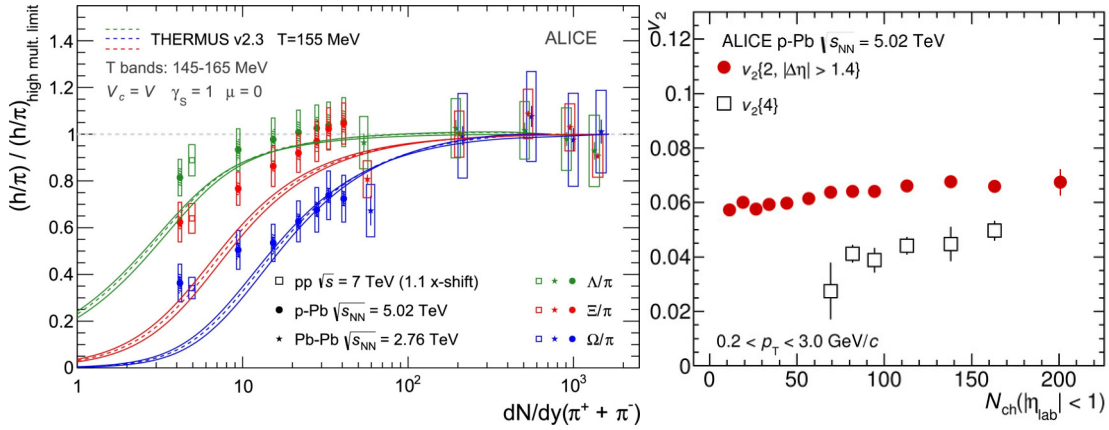
FIGURE 1.15: Left : Double ratio of hyperon (Λ, Ξ and Ω) to pion ratio as a function of pion yield for pp, p–Pb and Pb–Pb collisions at LHC energies. The measurements are compared with THERMUS model predictions [68]. This figure is taken from [15]. Right : v2 as a function of charged particle multiplicity, $N_{ch}(|\eta_{lab}| < 1)$ in p–Pb collisions at $\sqrt{s_{NN}}$ = 5.02 TeV.

charged particle multiplicity is observed for pp , p–Pb and Pb–Pb collisions. For a given charged particle multiplicity ($\langle dN_{ch}/d\eta\rangle_{|\eta|<0.5}$), the yield of produced hadrons scaled with $\langle dN_{ch}/d\eta\rangle_{|\eta|<0.5}$ show similar value irrespective of colliding systems and energies, which suggest that a common underlying mechanism govern the particle productions [58, 59, 69]. K^{*0}/K ratios decreases with $\langle dN_{ch}/d\eta\rangle_{|\eta|<0.5}$ in p–Pb collisions [19], similar to that observed

in Pb–Pb collisions [9].   The origin of these phenomena in the p–Pb is not yet fully understood [15, 11, 14, 19]. Hence, multiplicity dependent measurements play improtant role to understanding these phenomena. The measurements in p–Pb collisions also play a crucial role in disentangling initial cold nuclear matter effects from final state effects of hot dense matter produced in heavy-ion collisions.

We have studied K^{*0} production at the highest center-of-mass energy per nucleon, $\sqrt{s_{NN}}$ = 8.16 TeV and measurement of $K^{*\pm}$ at $\sqrt{s_{NN}}$ = 5.02 TeV in p–Pb collisions in the rapidity interval -0.5 < y < 0 with ALICE at the LHC, the data collected in the year 2016. It allows a higher multiplicity and a larger p_T coverage as compared to previous measurements in p−Pb collisions [19].   In this thesis, we have reported the measurements of transverse momentum (p_T) distribution, p_T-integrated yield (dN/dy), average transverse momentum ($\langle p_T \rangle$), particle ratios (resonance to stable hadron yield with similar quark content) as a function of charged particle multiplicity and nuclear modification factor (R_{pPb}) in p−Pb collisions.   In addition, for the first time, x_T-scaling is tested for resonances in p–Pb collisions at LHC energies. Measurements are also compared with model predictions such as HIJING [72], DPMJET [73] and EPOS-LHC [74].

1.6.2   Rapidity dependence of K^{*0} production in p–Pb collisions

p–Pb is an asymmetric and intermediate colliding system compared to the pp and Pb–Pb collisions (shown in Fig. 1.16). One expects the mechanism of particle production to be different in forward (p−going) and backward (Pb−going) rapidities [75, 76, 77]. The partons from the p−going side are expected to undergo multiple scattering while traversing the Pb-nucleus. Those on the Pb−side, are likely to be affected by the properties of the nucleus. Different effects such as nuclear modification of the parton distribution functions (nuclear shadowing) and possible parton saturation, multiple scattering, and radial flow [78,

79, 80, 24] are expected to depend on the rapidity of the produced particle. Hence, particle

production may be influenced by these effects. The previous measurements at RHIC [75, 76]
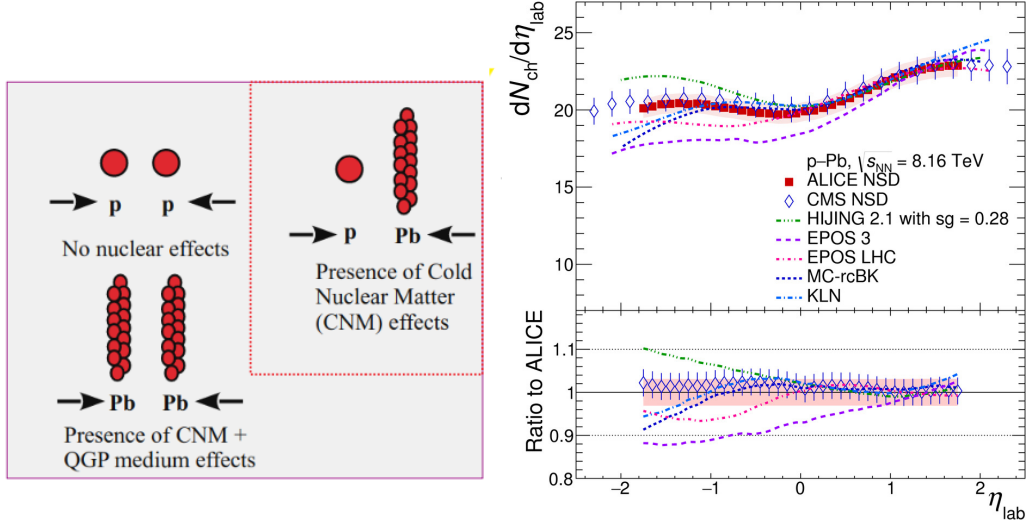
FIGURE 1.16: Left: Schematic view of collision system. Right: Pseudorapidity distribution in p–Pb collisions at $\sqrt{s_{NN}}$ = 8.16 TeV. Dashed lines are theoretical predictions from different models. This figure is taken from [82]

and the recent results at LHC [77] showed that rapidity yield asymmetry (particle yield

asymmetry in forward and backward rapidities, as shown in Fig. 1.17) [75, 76], flat behavior

of average transverse momentum [77], rapidity evolution of nuclear modification factor [83]

have been observed. Theoretical predictions on rapidity dependence of these observables

$\langle p_T \rangle$, v_2 and v_3 have been discussed in [79, 80].

In addition, the p−Pb collisions at Large Hadron Collider (LHC) energies enable probing

the parton distribution functions in nuclei at very small values of the Bjorken x variable,

where gluon saturation effects may occur [75, 83, 84]. In this thesis, we reported the

first measurement of the rapidity dependence of K^{*0} meson production in p–Pb collisions

at $\sqrt{s_{NN}}$ = 5.02 TeV by the ALICE experiment at the LHC. The large size of the data

sample collected in the year of 2016 and the excellent particle identification using ALICE
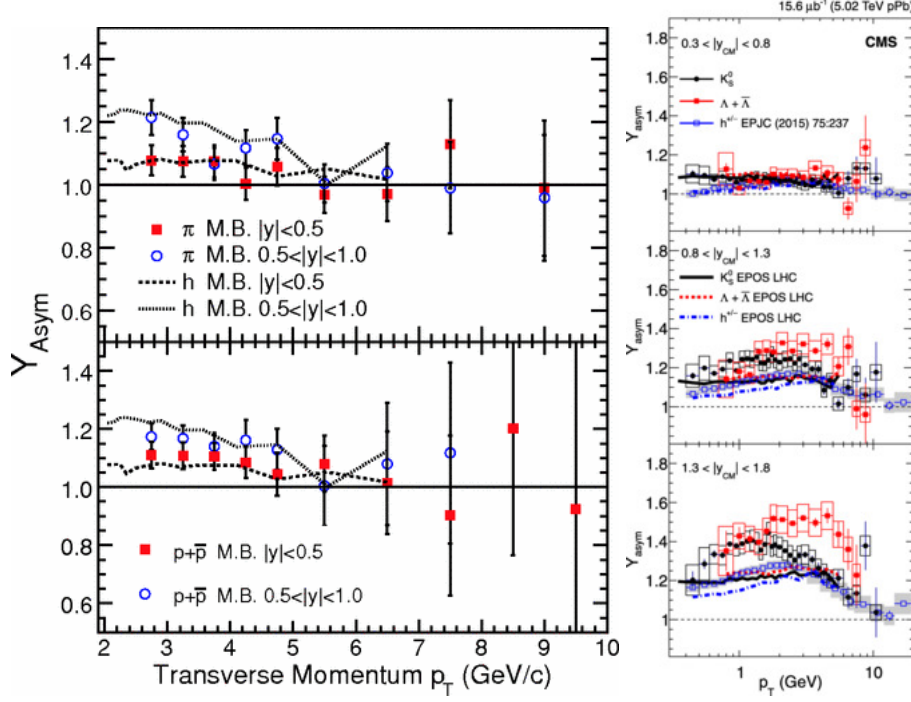
FIGURE 1.17: Left: rapidity yield asymmetry (Y_{asym}) as a function of transverse momentum (p_T) for d–Au collisions at $\sqrt{s_{NN}} = 200$ GeV for identified particle (π, h and p($\bar{p}$)). Right: Y_{asym} as a function of p_T for multi-strange hadrons (K_S^0, Λ) and inclusive charged hadrons in p–Pb collisions at $\sqrt{s_{NN}} = 5.02$ TeV. This figure is taken from [75, 76].

detectors provide an opportunities to extend these measurements in a wider rapidity interval and multiplicity classes compared to earlier midrapidity measurements [19, 85, 86]. The p_T spectra, dN/dy and $\langle p_T \rangle$ and their ratios have studied in the rapidity range -1.2 < y < 0.3 and four multiplicity classes. In addition to understanding the asymmetry of particle production in forward and backward rapidity, a ratio is measured, known as the rapidity asymmetry (Y_{asym}). The Y_{asym} is calculated as the ratio of the particle yield between Pb−and p-going directions. The Y_{asym} is measured as a function of p_T in the rapidity interval 0.0 < |y| < 0.3 for four multiplicity classes. Experimentally, it is a good observable because systematic uncertainties cancel out in the ratio. Hence, it can help better discriminate between rapidity-dependent effects by comparing the results from various models to the

measurement. Further, to investigate the quantum evolution of nuclear effect, the nuclear modification factor (Q_{CP}) as a function of p_T for various rapidity intervals is measured. The Q_{CP} is calculated as the ratio of yields of particle normalized to the corresponding number of binary collisions ($\langle N_{coll} \rangle$) in high multiplicity (central) and low multiplicity (peripheral) collisions. Measurements are also compared with different model predictions.

1.6.3 K^{*0} production in pp collisions

K^{*0} production in minimum-bias pp collisions at $\sqrt{s}$ = 7 TeV have also been studied. It is an improved and extended measurement of the transverse momentum spectrum up to p_T = 20 GeV/c compared to the previous study [64]. It includes the p_T-distribution, dN/dy, $\langle p_T \rangle$, p_T-integrated particle ratios of inelastic pp collisions. Measurements help to understand the particle production mechanism in high energy pp collisions. The results are compared with other collisions energies. The pp measurement acts as reference for the measurements in p–Pb and Pb–Pb collisions.

1.6.4 Spin alignment of vector mesons in heavy-ion collisions

In ultra-relativistic high energy collisions, spin polarization studies have drawn much attention in both theory and experiment to understand the initial condition of collisions, as spin degree of freedom provides us a unique opportunity to probe the QGP at a quantum level [88]. In non-central relativistic heavy-ion collisions (shown in left of the Fig. 1.18), when two nuclei collide with a nonzero impact parameters, a large orbital angular momentum ($\vec{L}$) of O(10^{6-7} $\hbar$) [89], and magnetic field ($|\vec{B}|$) of O(10^{18} Gauss) [90] are expected to be created (shown in right of the Fig.1.19). As the angular momentum is a conserved quantity, its effect could be present throughout the evolution of the system, whereas the magnetic field is transient in nature. In the presence of large initial angular momentum,
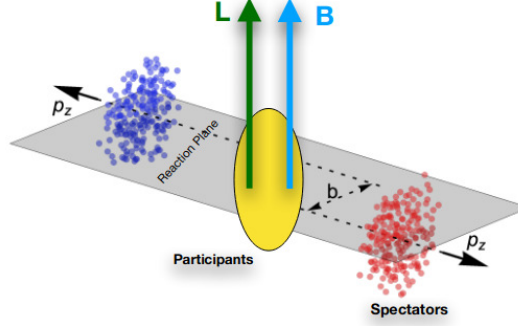
FIGURE 1.18: Schematic view of non-central heavy-ion collisions

vector mesons (spin = 1) can be polarized due to the spin-orbital interaction of the QCD. The net-polarization of vector mesons in the direction of angular momentum may occur after the polarization of quarks brought on by the spin-orbit interaction. Subsequently, it is transferred to hadronic degrees of freedom through recombination. Recently, the measured spin alignment of vector mesons at LHC energy was found to be surprisingly large compared to the polarisation measured for hyperons at RHIC and LHC energies [88]. Experimentally, these effects can be studied by measuring the angular distribution of decay daughters of vector mesons. Spin alignment of vector meson is described by a spin-density matrix ρ, which is a 3×3 hermitian matrix having unit trace. A deviation of the diagonal elements ρ_{mm} (m = -1, 0, 1) from 1/3 signals hints at the presence of net spin alignment. The diagonal elements $\rho_{-1,-1}$ and $\rho_{1,1}$ are degenerate and so the independent observable is ρ_{00}. The angular distribution of decay products of vector mesons is described by the equation [91]

$$\frac{dN}{d\cos\theta^*} = N_0 \times [(1 - \rho_{00}) + (3\rho_{00} - 1)\cos^2\theta^*] \qquad (1.15)$$

where N_0 is the normalization constant and θ^* is the angle between the quantization axis and the momentum direction of a daughter particle in the rest frame of the vector meson.
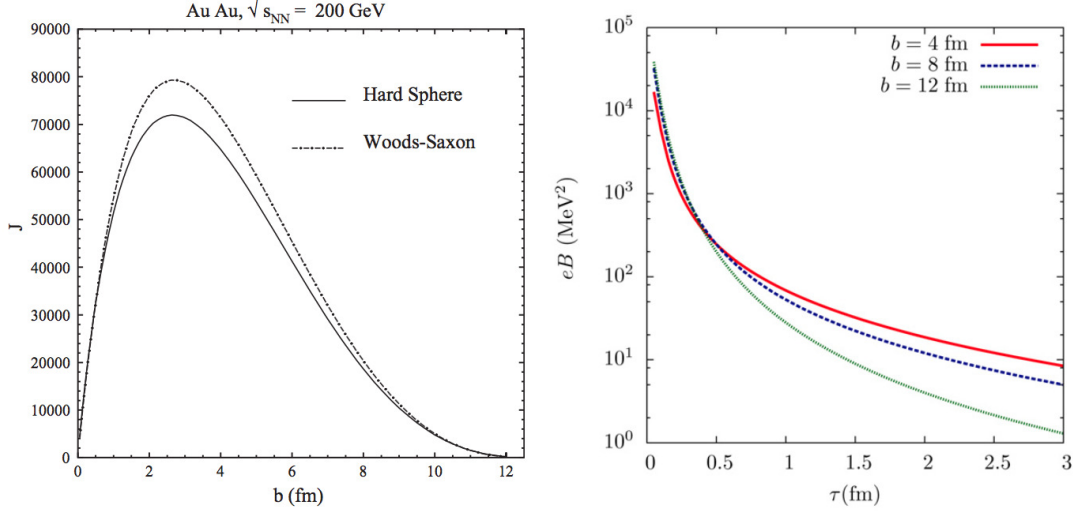
FIGURE 1.19: Left: angular momentum ($\vec{L}$) [89] as a function impact parameter (b) for two different nucleon distributions, Hard Sphere and Woods-Saxon. Right: magnetic field ($|\vec{B}|$) [90] as a function of time (τ in fm) for various impact parameters (b). This calculation is for Au–Au collisions at $\sqrt{s_{\text{NN}}}$ = 200 GeV [89, 90].

This quantization axis can be the normal to the production plane (plane subtended by the momentum vector of resonance and the beam axis) or normal to the reaction plane (defined by the impact parameter and the beam axis) of the system (shown in Fig. 1.20).

In the absence of spin alignment, ρ_{00}= 1/3, which makes the angular distribution uniform. The ρ_{00} deviates from 1/3 leads to a non uniform angular distribution, and is considered as the experimental signature of the spin alignment. Recently, the spin alignment of vector mesons (K^{*0}, ϕ) have been observed at low p_{T} in non-central heavy-ion collisions at $\sqrt{s_{\text{NN}}}$ = 2.76 TeV [88]. In this thesis, measurement of spin alignment of vector mesons ($K^{*0,\pm}$, ϕ) in Pb-Pb collisions at $\sqrt{s_{\text{NN}}}$ = 5.02 TeV at the Large Hadron Collider (LHC) are reported. The focus of the present study is on precise and energy dependence measurement of ρ_{00} for $K^{*0,\pm}$, ϕ. The spin alignment of $K^{*\pm}$ may provide information about the initial magnetic field due to the different magnetic moments between K^{*0} and $K^{*\pm}$. The
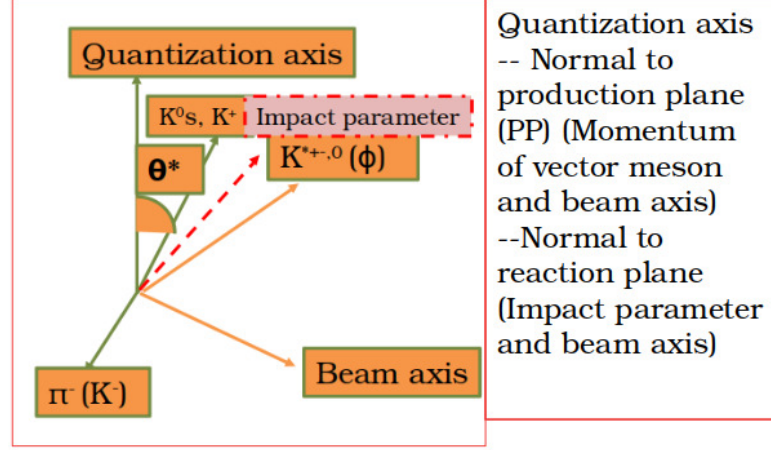
FIGURE 1.20: Sketch of angular distribution of decay products of vector meson in different quantization axes.

magnetic momentum of $K^{*\pm}$ is 7 times higher than magnetic momentum of K^{*0}. The polarization measurements are considered as global polarization or transverse polarisation, if polarization axes are chosen along $\vec{L}$ or $\vec{B}$. Theoretical studies have suggested that local polarisation (i.e, longitudinal polarisation where polarisation axes are chosen as beam momentum direction or direction along the momentum of vector meson) can also lead to the spin alignment of vector mesons and hyperons. The quark and anti-quarks can be polarized due to helicity charge and local vorticity generated from the anisotropic expansion of the system formed in non-central heavy-ion collisions [92, 93]. It is also interesting to extend such types of measurements to understand the contribution coming from global and local polarization [92, 93]. The spin alignment of vector mesons (K^{*0}, ϕ) are explored using the helicity frame (quantization axis is taken as momentum vector of resonance) [93] in Pb–Pb collisions at $\sqrt{s_{NN}}$ = 5.02 TeV.

Bibliography

[1] E. Rutherford, Phil. Mag., Ser. 6, Vol. 21, 669-688, (1911).

[2] E. Rutherford, Phil. Mag., Ser. 6, Vol. 37, 581, (1919).

[3] J. Chadwick, Nature 129, 312, (1932).

[4] E. D. Bloom et al., Phys. Rev. Lett. 23, 930, (1969).

[5] M. Breidenbach et al., Phys. Rev. Lett. 23, 935, (1969).

[6] R. Brandelik et al., [TASSO Collaboration], Phys. Lett. B 86, 243, (1979).

[7] S. L. Glashow, Nucl. Phys. 22, 579, (1961).

[8] A. Salam et al., Phys. Lett. 13, 168, (1964).

[9] S. Weinberg, Phys. Rev. Lett. 19, 1264, (1967).

[10] S. van der Meer, Rev. Mod. Phys. 57,689, (1985).

[11] J. Woithe et al., Phys. Educ. 52, 034001, (2017).

[12] G. Aad et al., [ATLAS collaboration], Phys. Lett. B 716, 1, (2012).

[13] W. Adam et al., [CMS collaboration], Phys. Lett. B 716, 30, (2012).

[14] M. Göckeler et al., Phys. Rev. D73:014513, (2006).

[15] S. Bethke, Prog. Part. Nucl. Phys. 58, 351, (2007).

[16] D. J. Gross et al., Phys. Rev. Lett. 30, 1343, (1973).

[17] D. J. Gross et al., Phys. Rev. D 8, 3633, (1973).

[18] H. D. Politzer, Phys. Rev. Lett. 30, 1346, (1973).

[19] L. Glasser et al., J. Chem. Education. 86 (5): 566, (2009).

[20] T. D. Lee et al., Phys. ReV. D 9, 2291. (1974).

[21] J.C.Collins et al., Phys. Rev. Lett. 34, 1353. (1974).

[22] H. Ding et al., Int. J. Mod. Phys. E 24, 1530007, (2015).

[23] F. Karsch et al., Prog. Theor. Phys. Suppl. 153, 106, (2004).

[24] R. C. Hwa et al., vol. 3, World Scientific, (2004).

[25] R. V. Gavai et al., Phys. Rev. D 71, 114014, (2005).

[26] A. Pandav et al., Progress in Particle and Nuclear Physics 125, 103960, (2022).

[27] B.I.Abelev et al., [STAR Collaboration], Phys. ReV.C 79, 034909, (2009).

[28] Y. Aoki et al., Nature 443, 675, (2006).

[29] S. Ejiri, Phys. Rev. D 78, 074507, (2008).

[30] M.G. Alford et al., Mod. Phys. 80,1455, (2008).

[31] K. Rajagopal et al., arXiv:0011333[hep-ph], (2000).

[32] P.B.Munzinger et al., Nature 448, 302-309,(2007).

[33] R Snellings, I. Phys. G 41, no.12, 124007, (2014).

[34] J. D. Bjorken, Phys. Rev. D 27, 140, (1983).

[35] G.Y. Qin et al., IJMP E Vol. 24, No. 11, 1530014, (2015).

[36] J. Adams et al., [STAR Collaboration], Phys. Rev. C 72, 014904, (2005).

[37] C. Loizides et al., Phys. Rev. C 99 1, 019901, (2019).

[38] V. Khachatryan et al., [CMS Collaboration], JHEP 04, 039, (2017).

[39] T. Matsui et al., Phys. Lett. B 178, 416, (1986).

[40] R. Arnaldi et al., [NA60 Collaboration], Nucl. Phys. A 783, 261, (2007).

[41] A. Adare et al., [PHENIX Collaboration], Phys. Rev. Lett. 98, 232301, (2007).

[42] A. Adare et al., [PHENIX Collaboration], Phys. Rev. C 84, 054912, (2011).

[43] B. Abelev et al., [ALICE Collaboration], Phys. Rev. Lett. 109, 072301, (2012).

[44] S. Acharya et al., [ALICE Collaboration], JHEP 02, 041, (2020).

[45] X. Zhao et al., Nucl. Phys. A 859, 114, (2011).

[46] A. Andronic et al., Phys. Lett. B 797, 134836, (2019).

[47] J. Rafelski, Phys. Rev. Lett. 48, 1066, (1982).

[48] J. Adam et al., [ALICE Collaboration], Nature Phys 13, 535âĂŞ539, (2017).

[49] B. B. Abelev et al., [ALICE Collaboration], Phys. Lett. B 734, 409-410, (2014).

[50] B. I. Abelev et al., [STAR Collaboration], Phys. Lett. B 673, 183, (2009).

[51] S. Voloshin et al., Z. Phys. C. 70, 665âĂŞ672, (1996).

[52] J. Adam et al., [STAR Collaboration], Phys. Rev. Lett. 92, 052302, (2004).

[53] L.Adamczyk et al., [STAR Collaboration], Phys. Rev. Lett. 116 6, 062301, (2016).

[54] A. Adare et al., [PHENIX Collaboration], Phys. Rev. Lett. 98, 162301, (2007).

[55] P. Huovinen et al., Phys. Lett. B 503, 58-64, (2001).

[56] S. Acharya, et al., [ALICE Collaboration], JHEP. 09, 006, (2018).

[57] J. Adam et al., [ALICE Collaboration], Phys. Rev. C 95, 064606, (2017).

[58] S. Acharya et al., [ALICE Collaboration], Phys. Lett. B 802, 135225, (2020).

[59] S. Acharya et al., [ALICE Collaboration], Phys. Rev. Lett. 125, 012301, (2020).

[60] A. G. Knospe et al., Phys. Rev. C93 no. 1, 014911, (2016).

[61] B. I. Abelev et al., [STAR Collaboration], Phys. Rev. C 78, 044906, (2008).

[62] M. M. Aggarwal et al., [STAR Collaboration], Phys. Rev. C 84, 034909, (2011).

[63] J. Adam et al., [ALICE Collaboration], Phys. Lett. B 758, 389-40, (2016).

[64] B. B. Abelev et al., Phys. Rev. C 90, 5, 054901, (2014).

[65] S. Chatrchyan et al., [CMS Collaboration], Phys. Lett. B 718, 795-814, (2013).

[66] B. Abelev et al., [ALICE Collaboration], Phys. Rev. C 90(5), 054901, (2014).

[67] B. Abelev et al., [ALICE Collaboration], Phys. Lett. B 728, 25-38, (2014).

[68] S. Wheaton et al., Comput. Phys. Commun. 180, 84âĂŞ106, (2009).

[69] S. Acharya et al., [ALICE Collaboration], Phys. Rev. C 99, 024906, (2019).

[70] J. Adam et al., [ALICE Collaboration], Eur. Phys. J. C 76, 245, (2016).

[71] S. Acharya et al., [ALICE Collaboration], Phys. Lett. B 802, 135225, (2020).

[72] Miklos Gyulassy et al., Comput. Phys. Commun. 83, 307, (1994).

[73] S. Roesler et al., ICAMCRP, PTSA, hep-ph/0012252, (2000).

[74] T. Pierog et al., Phys. Rev. C 92 3, 034906, (2015).

[75] B. I. Abelev et al., [STAR Collaboration], Phys. Rev. C 76, 054903, (2007).

[76] A. M. Sirunyan et al., [CMS Collaboration], Phys. Rev. C 101 no. 6, 064906, (2020).

[77] V. Khachatryan et al., [CMS Collaboration], Phys. Lett. B 768, 103-129, (2017).

[78] Zhong-Bo Kang et al., Phys. Lett. B 718, 482âĂŞ487, (2012).

[79] P. Bozek et al., Phys. Lett. B 748, 301âĂŞ305, (2015).

[80] P. Bozek et al., Phys. Lett. B 728, 662âĂŞ665, (2014).

[81] B. B. Abelev et al., [ALICE Collaboration], Phys. Lett. B 728, 25-38, (2014).

[82] S. Acharya et al., [ALICE Collaboration], Eur. Phys. J. C, 79: 307, (2019).

[83] I. Arsene et al., [BRAHMS Collaboration], Phys. Rev. Lett. 93:242303, (2004).

[84] J. Breitweg et al., [ZEUS Collaboration], Phys. Lett. B 407, 432âĂŞ448, (1997).

[85] J. Adam et al., [ALICE Collaboration], Phys. Lett. B 768, 203âĂŞ217, (2017).

[86] S. Acharya et al., [ALICE Collaboration], http://arxiv.org/abs/2110.10042, (2021).

[87] B. Abelev et al., [ALICE Collaboration], Eur. Phys. J. C72, 2183, (2012).

[88] S. Acharya et al.,[ALICE Collaboration], Phys. Rev. Lett. 125, 012301, (2020).

[89] F. Becattini et al., Phys. Rev. C 77, 024906, (2008).

[90] A. Ayala et al., Phys. Lett. B 682, 408, (2010).

[91] K. Schilling et al., Nucl. Phys. B18, 332, (1970).

[92] X.L. Xia et al., Phys. Lett. B 817, 136325, (2021).

[93] Jian-Hua Gao, Phys. Rev. D 104, 076016, (2021).

A Large Ion Collider Experiment (ALICE)

at the LHC

Large Hadron Collider (LHC), a marvel of engineering, it is already constructed and running for more than 10 years at the European Council for Nuclear Research (CERN), in Geneva, Switzerland, to investigate the nature of primordial matter of the microsecond-old universe. Presently, the LHC accelerator is the world's largest and most powerful particle accelerator. One of the major experiments of the LHC is A Large Ion Collider Experiment (ALICE). ALICE is a dedicated experiment to study the physics of strongly interacting matter at extreme temperatures and/or energy densities. It started collecting data on hadronic and nuclear collisions from the year 2009. This chapter discusses the overviews of the LHC and its major experiments. A brief description of the experimental setup in the ALICE and its sub-detectors is given. It is followed a short discussion on sub-detectors used for tracking and particle identification along with online and offline computing systems.

2.1   The Large Hadron Collider Experiment (LHC)

The Large Hadron Collider (LHC) at the CERN is situated on the Switzerland and France border with a 26.7 km long tunnel at a depth of about 50-150 m. The LHC consists of two rings of superconducting magnets where two beams of particles rotate in opposite directions. The CERN accelerator complex consists of various accelerator systems, such as the Linear Accelerator (LINAC2, LINAC3), the Proton Synchrotron Booster (PSB), the Proton Synchrotron (PS), the Super Proton Synchrotron (SPS) as systematically shown in Fig. 2.1. A number of acceleration set ups used to boost the energy of beam particles along the way. Each machine in the accelerator systems sequentially boosts the energy of a beam of particles before the beam finally being injected into the main LHC ring. For pp collisions, proton source is achieved from a simple bottle of hydrogen gas. Electrons from the hydrogen is removed by applying an electric field. The proton beam starts its acceleration from LINAC2 reaching an energy of 50 MeV. Then the protons are injected into PSB, PS, and SPS to push the energy of the beam particle up to 450 GeV. The beam is finally transferred to LHC rings in both clockwise and anticlockwise directions, where energy is ramped up to the desired energy of collisions. Similarly, the lead (Pb) ion beam is prepared from a vapour of lead atoms obtained by heating a 2 cm long, 500 mg pure lead sample to 500 °C. An electric field is used to remove a few electrons from Pb atom, and the newly created Pb ions are accelerated by a LINAC 3 up to the energy of 4.2 MeV per nucleon. In LINAC 3, further electrons are removed from the Pb ions. In the next step, the ions are accelerated to 72 MeV per nucleon in the Low Energy Ion Ring (LEIR). These first three stages are unique for heavy-ions collisions. The Pb ions are subsequently accelerated in the PS and SPS. In the PS, the energy of Pb ions is boosted up to 5.9 GeV per nucleon, and then the remaining electrons are eliminated from the Pb ions. In the SPS,
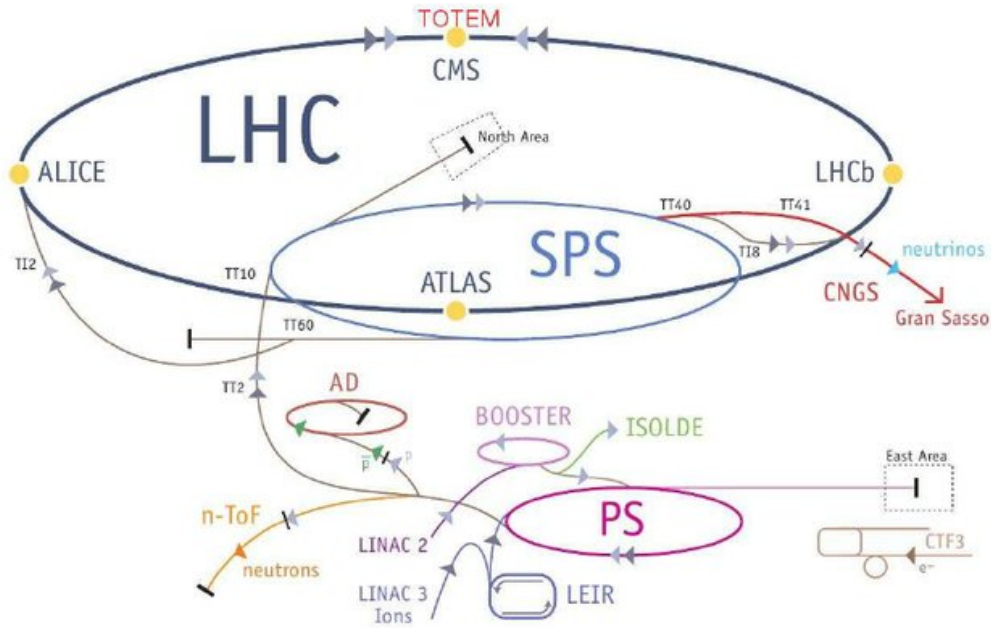
FIGURE 2.1: CERN accelerator complex and the locations of the four major LHC experiments: ALICE, ATLAS, CMS and LHCb along the LHC ring [1]

the Pb beam is accelerated up to 177 GeV per nucleon and injected in two directions into the LHC ring. Points 2 and 8 in Fig. 2.2 are used to inject particles into the LHC ring in two different directions. The beam is accelerated at point 4 using the Radio Frequency (RF) mechanism. The four primary experiments, A Toroidal LHC Apparatus (ATLAS), ALICE, Compact Muon Solenoid (CMS), and Large Hadron Collider beauty (LHCb) [1], are situated at positions 1, 2, 5, and 8 where two beams cross. The collimation system cleans the beam at points 3 and 7 by removing the beam bunches, which have a wide spatial spread from the bunch centre, after the beam dumps at point 6. The LHC operation points are schematically laid out in Fig. 2.2. With the present accelerator facilities at the LHC, the maximum center of mass energy that can be reached is 14 TeV for pp collisions and 5.5 TeV per nucleon for heavy-ion collisions.
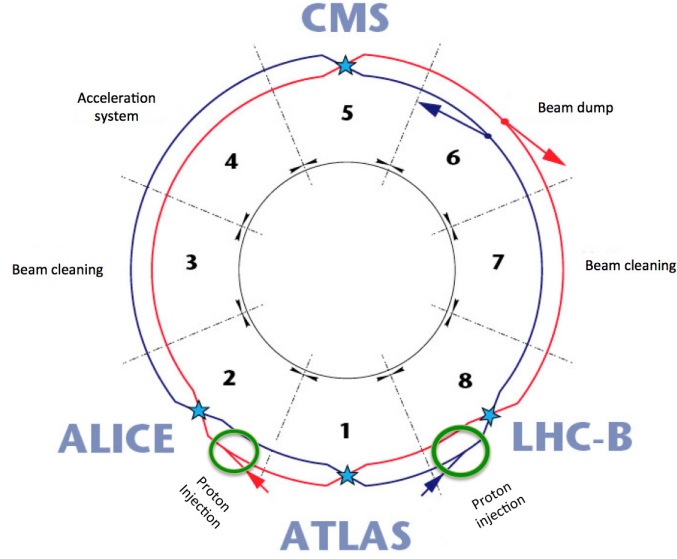
FIGURE 2.2: Schematic view of LHC accelerator complex [2]

2.2   The ALICE experiment at LHC

ALICE is one of the four main detector systems at the LHC. It is situated at point 2 of the LHC accelerator complex, about 56 m underground in the village of St Genis-Pouilly at Switzerland-France border. It is a dedicated experiment to understand nuclear matter under extreme temperature and/or energy density. It has excellent tracking and particle identification (PID) capabilities over a broad momentum range (10^{-2} - 10^2 GeV/c) that allows for studying various topics from soft physics to jets and high-p_{T} particle production. It is also designed to handle the high charged particle multiplicity densities ($\langle \mathrm{d}N_{\mathrm{ch}}/\mathrm{d}\eta \rangle >$ 1500) at midpseudorapidity in central Pb–Pb collisions. The ALICE detector has a size of $26 \times 16 \times 16$ m^3 and a total weight of 10,000 tones. The ALICE coordinate system is chosen as the standard right-handed Cartesian coordinate system, where the origin (0,0,0) of the coordinate system is the interaction point of collisions, which is nominally taken as
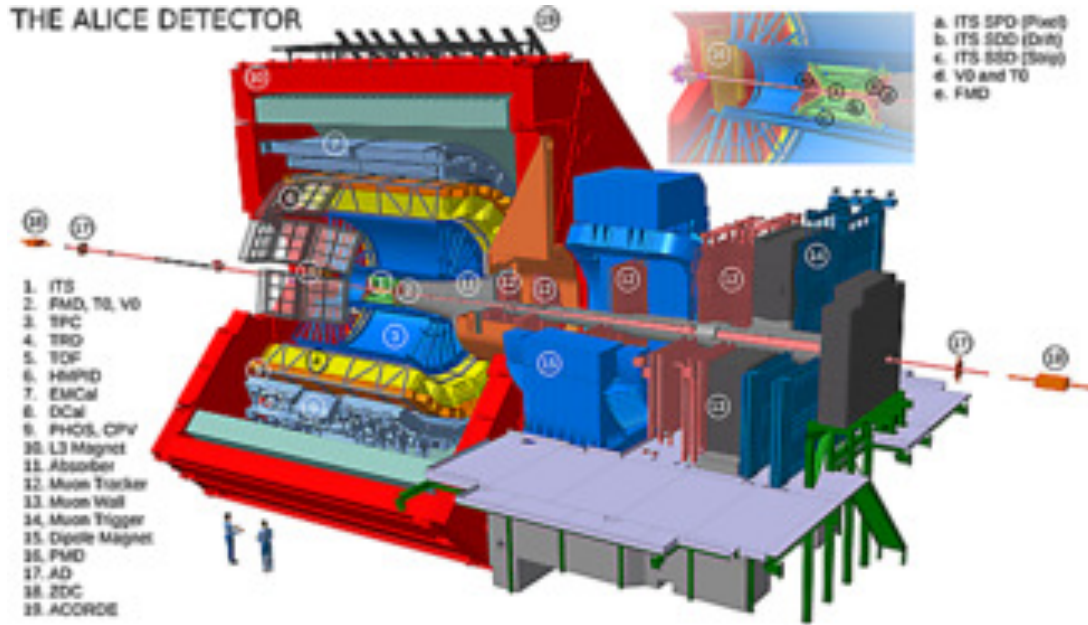
FIGURE 2.3: Schematic diagram for the ALICE detector systems [3]

the center of the ALICE detector system. The direction opposite to the muon spectrometer is taken as the positive z-axis of the ALICE coordinate system. The x and y axes are perpendicular to the z-axis, where the x-axis is pointing towards the centre of the LHC ring, and the y-axis is vertically upward. The ALICE detector systems are divided mainly into three parts such as central barrel, forward, and muon spectrometers. The ALICE detector consists of 19 detector subsystems, as shown in Fig. 2.3. The positions of η, and ϕ acceptances and purposes of ALICE detector subsystems are summarized in Tab. 2.1. The heart of the ALICE is the central barrel detectors that cover the midpseudorapidity region ($|\eta| < 0.9$). They are housed in the L3 solenoid magnet that provide a uniform magnetic field of a maximum of 0.5 T along the beam direction. The central detectors are mainly used for tracking, vertex reconstruction, particle identification, and measurement of track momentum. The central barrel detectors are ITS, TPC, TOF, and V0. They are extensively

TABLE 2.1: Summary of the positions, η and ϕ acceptances and purposes of ALICE detector subsystems [4]

Detector	Position (in cm)	η acceptance	ϕ acceptance (in °)	Purpose
Central barrel detector:				
SPD	$r = 3.9$	$|\eta| < 2.0$	$0° < \phi < 360°$	tracking, vertex
	$r = 7.6$	$|\eta| < 1.4$	$0° < \phi < 360°$	tracking, vertex
SDD	$r = 15.0$	$|\eta| < 0.9$	$0° < \phi < 360°$	tracking, particle identification
	$r = 23.9$	$|\eta| < 0.9$	$0° < \phi < 360°$	tracking, particle identification
SSD	$r = 38.0$	$|\eta| < 1.0$	$0° < \phi < 360°$	tracking, particle identification
	$r = 43.0$	$|\eta| < 1.0$	$0° < \phi < 360°$	tracking, particle identification
TPC	$85 < r < 247$	$|\eta| < 0.9$	$0° < \phi < 360°$	tracking, particle identification
TRD	$290 < r < 368$	$|\eta| < 0.8$	$0° < \phi < 360°$	tracking, $e^{\pm}$ identification
TOF	$370 < r < 399$	$|\eta| < 0.9$	$0° < \phi < 360°$	particle identification
PHOS	$460 < r < 478$	$|\eta| < 0.12$	$220° < \phi < 320°$	photons
EMCAL	$430 < r < 455$	$|\eta| < 0.7$	$80° < \phi < 187°$	photons
HMPID	$r = 490$	$|\eta| < 0.6$	$1° < \phi < 59°$	particle identification
ACORDE	$r = 850$	$|\eta| < 1.3$	$30° < \phi < 150°$	cosmics
Forward detector:				
PMD	$z = 367$	$2.3 < \eta < 3.9$	$0° < \phi < 360°$	photons
FMD	$z = 320$	$3.6 < \eta < 5.0$	$0° < \phi < 360°$	charged particles
	$z = 80$	$1.7 < \eta < 3.7$	$0° < \phi < 360°$	charged particles
	$z = -70$	$-3.4 < \eta < -1.7$	$0° < \phi < 360°$	charged particles
V0	$z = 329$	$2.8 < \eta < 5.1$	$0° < \phi < 360°$	charged particles
	$z = -88$	$-3.7 < \eta < -1.7$	$0° < \phi < 360°$	charged particles
T0	$z = 370$	$4.6 < \eta < 4.9$	$0° < \phi < 360°$	time, vertex
	$z = -70$	$-3.3 < \eta < -3.0$	$0° < \phi < 360°$	time, vertex
ZDC	$z = \pm 11300$	$|\eta| > 8.8$	$0° < \phi < 360°$	forward neutrons
ZDC	$z = \pm 11300$	$6.5 < |\eta| < 7.5$	$|\phi| < 10°$	forward protons
ZDC	$z = \pm 730$	$4.8 < \eta < 5.7$	$|2\phi| < 32°$	photons
Muon spectrometer:				
MCH	$-1420 < z < -540$	$-4.0 < \eta < -2.5$	$0° < \phi < 360°$	muon tracking
MTR	$-1710 < z < -1610$	$-4.0 < \eta < -2.5$	$0° < \phi < 360°$	muon trigger

used for this thesis and details are discussed in the following sub-sections.

The Inner Tracking System (ITS)

The Inner Tracking System (ITS) is one of the main detectors of the ALICE [5]. It is used to reconstruct the interaction point of collisions (primary vertex) with a resolution better than 100 μm and separated vertices (secondary vertices), where particle decay took place. It has a unique capability of tracking and identification for very low momentum particles ($p_{\mathrm{T}} < 200$ MeV/c). It also allows for reconstructing the tracks of low momentum that do not reach the TPC or traversing the dead channels of the TPC. The ITS is an innermost detector system in a central barrel with a radius between 3.9 to 43 cm. It consists of

six cylindrical layers having three different types of silicon detector. It is surrounded by an 800 μm thick beryllium beam pipe, which has an outer diameter of 6 cm. A layout of the ITS detector systems is shown in Fig. 2.4. The η and ϕ acceptance for different layers of the ITS detector is shown in Tab. 2.1. The first two layers of the ITS are the Silicon Pixel Detectors (SPD). It consists of two-dimensional sensor matrices of silicon diodes of thickness $\sim$ 200 μm. The sensor matrices include 256 $\times$ 160 pixels/cells with each pixel measuring 50 μm ($r\phi \times$ 425 μm(z)). The spatial resolution of the SPD along the $r\phi$ plane and z-direction is 12 μm and 100 μm, respectively. It plays an important role in the determination of primary and secondary vertices. Due to the extremely fine segmentation of the SPD, the SPD can operate in a region with track density as high as 50 tracks/cm^3. It has full azimuthal coverage and pseudorapidity acceptance of $|\eta|$ < 2.0. Silicon Drift Detector (SDD) is the intermediate layers (3rd and 4th) of the ITS. These layers are assembled with ladders and modules to ensure full azimuthal coverage. It provides high precision of position information with a position resolution of 35 μm. It also provides information on the energy loss ($\mathrm{d}E/\mathrm{d}x$), which is used for the PID. Silicon Strip Detector (SSD), the outermost layer in the ITS, is crucial for matching the tracks in the ITS and TPC. It comprises 698 modules, each consisting of a 1536 strip, double-sided silicon sensor connected through an aluminum Kapton micro-cables to the front-end electronics. It provides a two-dimensional measurement of the track position along with the $\mathrm{d}E/\mathrm{d}x$ information. The SSD and SDD have analogous readouts, which have a large dynamic range that allows the particle identification (PID) via energy loss ($\mathrm{d}E/\mathrm{d}x$) for low momentum particles down to p_T = 100 MeV/c.
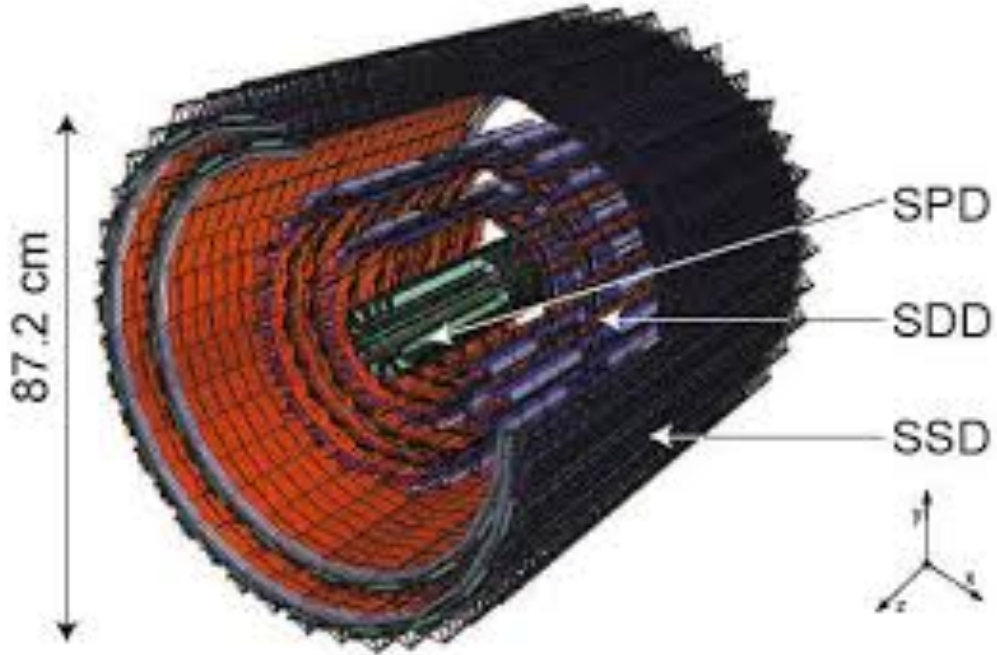
FIGURE 2.4: Schematic diagram for the ITS of ALICE detector [3]

The Time Projection Chamber (TPC)

The Time Projection Chamber (TPC) is the primary detector for particle identification via specific energy loss in the ALICE [6]. Figure 2.5 shows a schematic layout of the ALICE TPC. It covers full azimuthal angle with pseudorapidity coverage of $|\eta| < 0.9$. It is a cylindrical chamber of volume ~ 90 m^3. Its length is 5 m, and its inner and outer radii are 80 cm and 250 cm, respectively. It is filled with a gas mixture of 90% noble gas (Ne) and 10% of quenching gas (CO_2).

The TPC drift volume is divided into two parts using a cylindrical conducting electrode, that is placed at the center of the TPC. It acts as the cathode and generates a uniform axial electrostatics field of 400 V/cm in the two volumes. Multiwire proportional chamber (MWPC) based readout chambers are mounted at both ends of the TPC. Each of the end
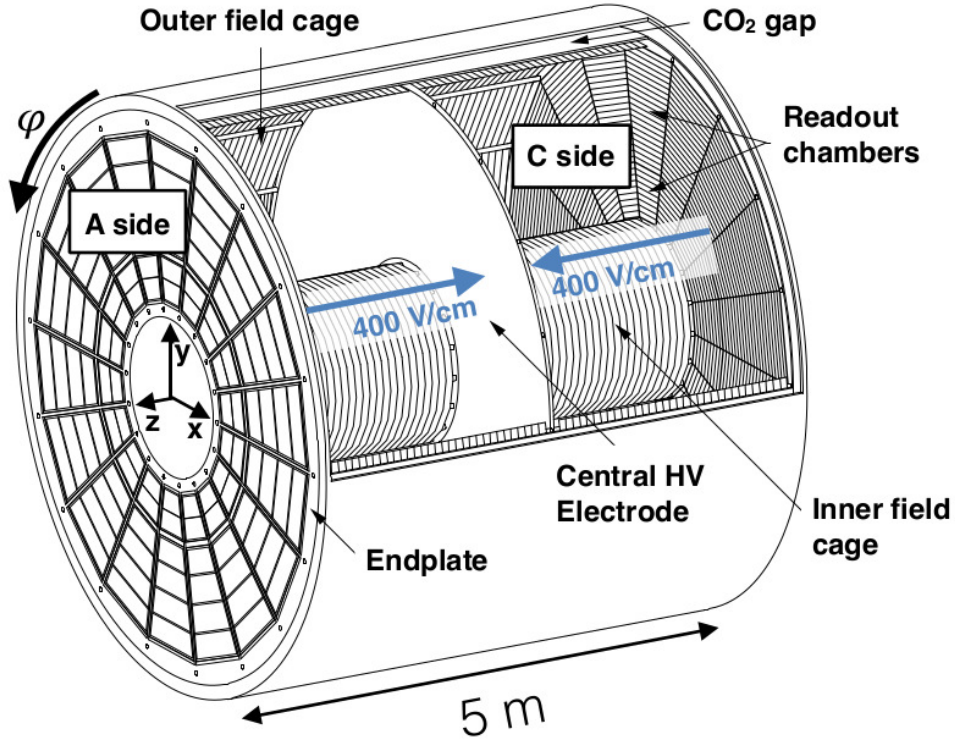
FIGURE 2.5: A schematic layout for the ALICE TPC [43]

plates has 36 readout chambers, which are arranged in 18 sectors. Each readout sector consists of an Outer Readout Chamber (OROC) and an Inner Readout Chamber (IROC). The TPC is a gaseous detector; it operates in the proportional region. Figure 2.6 shows the working principle of the TPC [7]. When a charged particle passes through the active gas volume, it excites and ionizes gas atoms along the trajectory of the track. As a result, the charged particle loses its energy per unit of track length, which is called specific energy loss (dE/dx), depending on the mass of the particle. Due to the electric field, ionised free electrons floated toward the end plates of the cylinder, while the ions drifted toward the high-voltage cathode positioned in the middle of the TPC.

The drifting of electrons is not affected by the external magnetic field as it is oriented

parallel to the electric field. At the end of the drift path around the anode wires, drifted electrons are amplified by an avalanche process. The hits on the anode pads at the end plates are used to rebuild the x and y positions of the recordings. The z-coordinates of the tracks are reconstructed based on the information of drift velocity and arrival time of the drift electrons at the anode plane. A uniform magnetic field of (nominal) 0.5 T or (low) 0.2 T is supplied, causing the particles to follow a helical path. The curvature of the path is used to calculate the particle momentum (p). The tracks are reconstructed from the 3D space points. Identification of charged particles in TPC is determined by specific energy loss
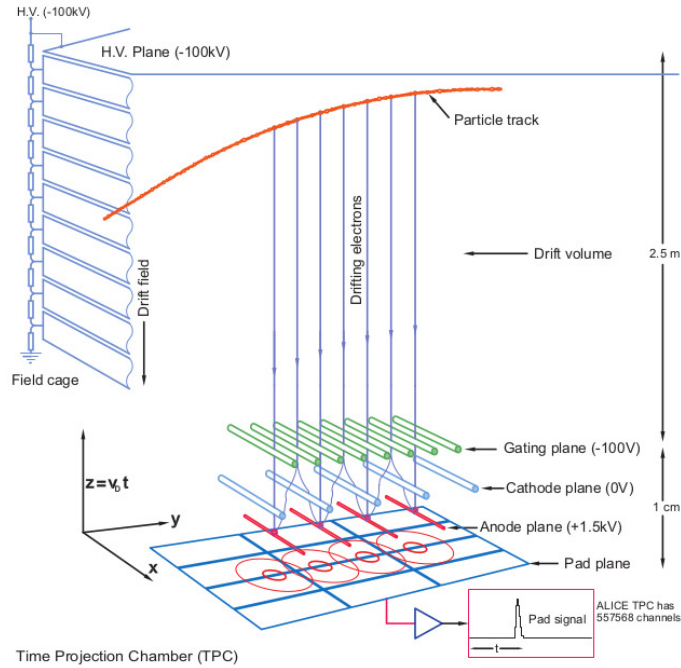
FIGURE 2.6: A schematic illustration of the working principle of the TPC [7]

(dE/dx) of charged particles traveling through a detector gas as a function of the momentum (p). The average energy loss of charged particles inside the TPC is parameterized by a modified Bethe-Bloch function, originally proposed by the ALEPH Collaboration [8], as

given in Eq. 2.1.

$$f(\beta\gamma) = \frac{p_1}{\beta^{p_4}}(p_2 - \beta^{p_4} - ln(p_3 + \frac{1}{(\beta\gamma)^{p_5}})) \qquad (2.1)$$

Here β and γ are the velocity and Lorentz factor for the track, respectively. The p_1 to p_5 fit parameters. Figure 2.7 shows energy loss per unit length (dE/dx) as a function of momentum (p) for charged particles as measured in ALICE TPC for p–Pb collisions at $\sqrt{s_{NN}} = 8.16$ TeV. The different band of dE/dx represents the particles that have different masses. For Run 2, the readout rate in central Pb–Pb collisions is limited by the TPC

ALI-PERF-337036
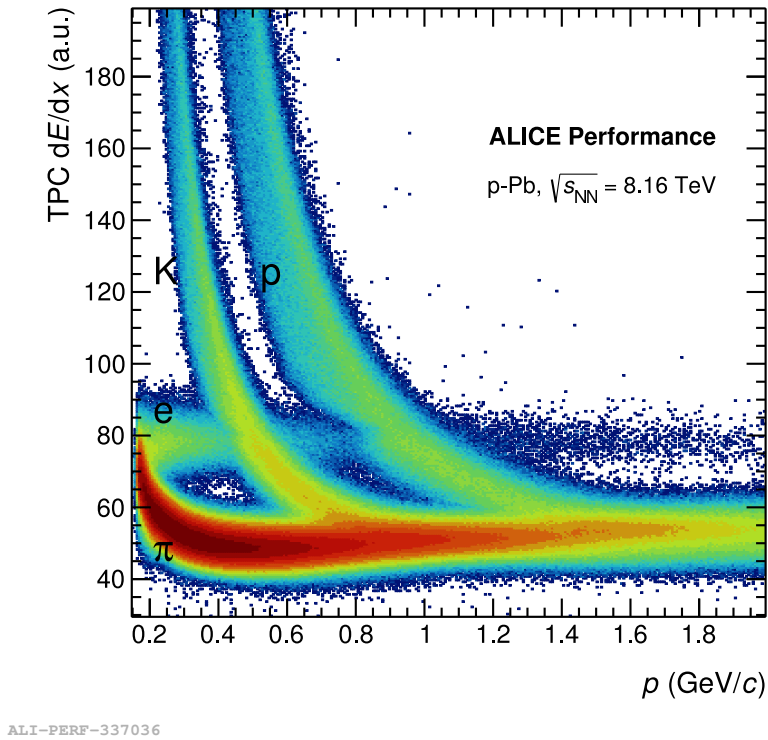
FIGURE 2.7: Energy loss per unit length as a function of momentum (*p*) in p–Pb collisions at $\sqrt{s_{NN}}$ = 8.16 TeV.

readout system with 500 Hz and 3.5 kHz for pp collisions. For upcoming LHC Run 3 and

Run 4, the readout electronics and readout chamber of ALICE TPC will be upgraded with GEM (Gas electron multiplier) based readout. The upgraded TPC will allow continuous data taking and is expected to achieve the readout rate of about 200 kHz for pp and p–Pb collisions and 50 kHz for central Pb–Pb collisions [9].

The Time Of Flight (TOF)

The Time Of Flight (TOF) detector is used for particle identification at the low and intermediate transverse momentum range. The TOF detector is a cylindrical gas detector consisting of a Multigap Resistive Plate Chamber (MRPC) [10]. It is placed around the Transition Radiation Detector (TRD), having an inner radius of 3.7m and an outer radius of 3.99m. It covers η and ϕ acceptance of $|\eta| < 0.9$ and 2π, respectively. A charged particle passes through the TOF detector and ionizes the gas. The avalanche electrons move towards the electrode, which is stopped due to the gap of resistive plates. The total signal is the sum of the signals from all the gaps of resistive plates. The TOF detector identifies particles from its time-of-flight. The time-of-flight (t) is the time a particle takes to travel from the interaction point to the TOF detector by covering a distance (L). The start time reference (t_0) is provided by the T0 detector, which sits both sides of the interaction point [4]. The time resolution of the ALICE TOF is $\sim$ 80 ps. Experimentally, the mass of the particle in the TOF detector is calculated using the information on time-of-flight from the TOF detector and the momentum (p) of particle obtained from the TPC, using the following Eq. 2.2.

$$m = p\sqrt{\frac{t^2}{L^2} - 1} \qquad (2.2)$$

The TOF β is defined as the ratio of the velocity of a particle with respect to that of light. The TOF β as a function of momentum is shown in Fig. 2.8 for different particles in p–Pb

collisions at $\sqrt{s_{NN}}$ = 8.16 TeV. The TOF identifies pion and kaon with a separation larger than 3σ up to p < 2.5 GeV/c and a separation better than 3σ up to p < 4.0 GeV/c for kaon and proton.
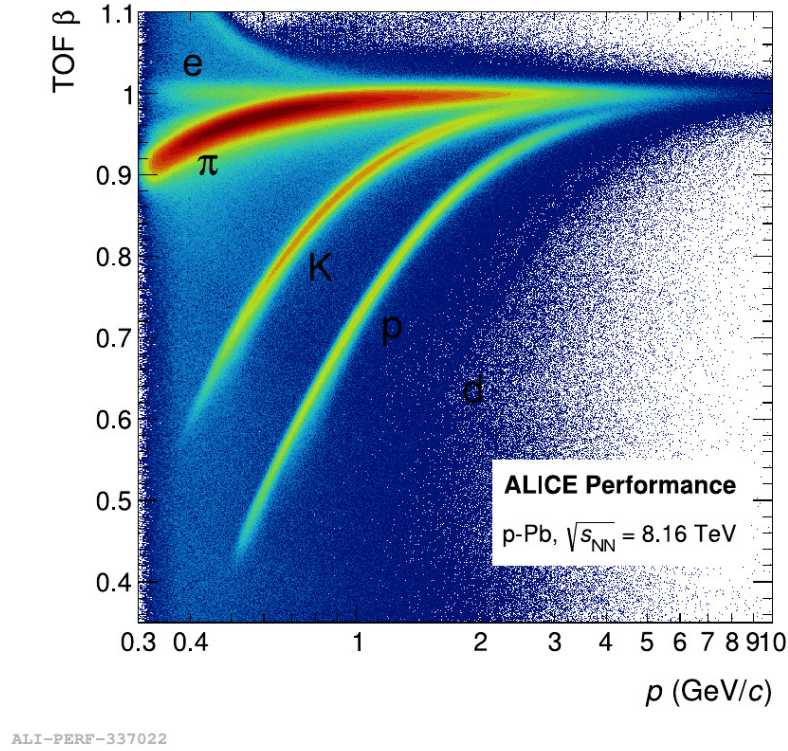
FIGURE 2.8: Distribution of β, measured by using TOF detector as a function of momentum of particles which reach the TOF detector in p–Pb collisions at $\sqrt{s_{NN}}$ = 8.16 TeV.

The VZERO (V0)

The VZERO (V0) detectors are plastic scintillator detectors situated asymmetrically on both sides of the interaction point [11]. The one in a forward direction is named VZERO-A (V0–A), and the one in a backward direction is named VZERO-C (V0–C), as shown in Fig. 2.9. They cover in the pseudorapidity range of 2.8 < η < 5.1 (V0–A) and -3.7 < η < - 1.7 (V0–C) with full azimuth coverage [40]. Both detectors consist of two arrays of

32 scintillator counters distributed in 4 rings. Each ring is further divided into 8 sectors. The V0 detectors are mainly used for triggering and rejecting beam gas events from their timing information.
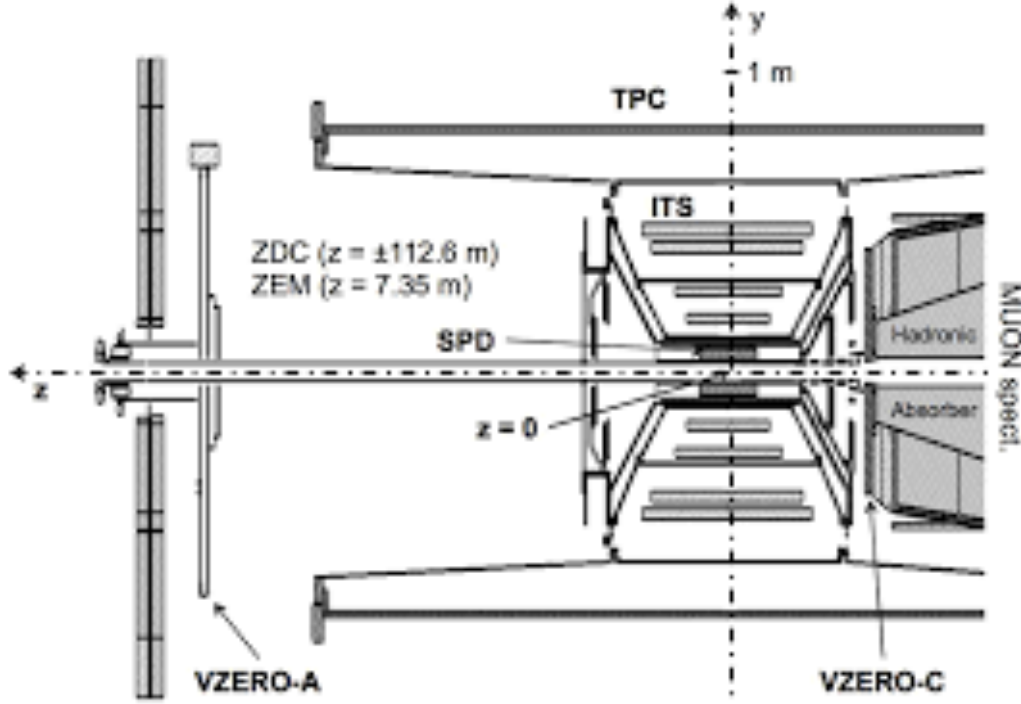
FIGURE 2.9: Position of the V0A and V0C detectors within the layout of the ALICE experiment [11]

The time resolution is about 1 ns. ALICE has dedicated detectors for a minimum bias trigger during data taking of pp, p–Pb, and heavy-ion collisions. The particles originating from the primary vertex of the collisions and secondary interactions in the vacuum chamber elements provide the trigger information for central barrel detectors. In addition, they are also used to determine the collision centrality in heavy-ion collisions and multiplicity estimation for pp and p–Pb collisions.

Details of centrality and multiplicity Selection 3.2.1 are described in Chapter 3.

2.3 Online and offline computing system

The data-taking activities are controlled by the central online systems. The Detector Control System (DCS) allows the operation of the detector hardware from a central interface. The configuration of the detectors during data collection is defined by the Data Acquisition (DAQ). The Trigger (TRG) and High-Level Trigger (HLT) systems are interfaced with it. The Experiment Control System (ECS) coordinates all the operations of the central systems (DAQ, TRG and HLT) [12]. The detectors can operate individually, it is known as standalone mode. Standalone mode is used to perform commissioning, calibration, and debugging activities. During the physics data taking, the detectors are grouped in partitions that can operate simultaneously with a given set of trigger inputs. The offline project is dedicated to the development of the framework of data processing. ALICE Grid and ALIEN data processing are distributed to several computing centers located worldwide. The distributed computing infrastructure, which is used in the LHC. The experimental program is managed under the Worldwide LHC Computing Grid (WLCG) project. The ALICE grid uses Models of networked analysis at regional centers (MONARC) model, which is classified into different stages and tiers. All real data originate from CERN, which is called Tier-0. Tier-1, which are large regional computing centers, share with CERN the role of safe storage of the data. Tier-2 are the smaller centers, which are logically clustered around Tier-1. ALICE Online project also develops ALIce Environment (ALIEN), which provides ALICE users to have transparent access to grid computing and storage resources.

Bibliography

[1] CERN Annuarl Report 2017, http://cds.cern.ch/record/2624296, (2017).

[2] Castillo et al., Morgan and Claypool Publishers, (2015).

[3] [ALICE Collaboration], https://alice-figure.web.cern.ch/node/11218, (2017).

[4] B. Abelev et al. [ALICE Collaboration], Int. J. Mod. Phys. A 29, 1430044, (2014).

[5] K. Aamodt et al., [ALICE Collaboration], JINST 5, P03003, (2010).

[6] J. Alme et al., [ALICE Collaboration], Nucl. Instrum. Meth. A 622, 316-367, (2010).

[7] A. Kalweit, https://cds.cern.ch/record/2119440, (2012).

[8] W. Blum et al., https://cds.cern.ch/record/1105920, (2008).

[9] S. Acharya et al., [ALICE Collaboration], arXiv:2211.02491, (2022).

[10] A. Akindinov et al., [ALICE Collabortaion], Eur. Phys. J. Plus 128, 44, (2013).

[11] E. Abbas et al., [ALICE Collaboration], J. Instrum. 8, P10016, (2013).

[12] CERN-LHCC-2015-006; ALICE-TDR-019, (2015).

Multiplicity dependence of K^* production in p–Pb collisions at LHC energies

3.1 Motivation

The primary goal of ultra-relativistic high-energy collisions is to investigate the formation of the strongly interacting matter of free quarks and gluons, called the QGP, and its novel properties produced in such collisions [1, 2, 3, 4]. The produced hot and dense medium cools as it expands. It reaches a certain temperature, called a critical temperature after which hadronization takes place, where free quarks and gluons combine to form hadrons. After that, hadrons continue to interact elastically and inelastically among themselves. As the temperature of the system falls further below, the inelastic collisions among the constituents cease, and the yield of relative abundance of primarily produced particles gets fixed, that temperature is called chemical freeze-out temperature. Further, hadrons continue to interact elastically. When the mean free path among the constituents exceeds the distance

between them, the elastic interaction stops. Then hadrons free stream to the detectors. This freeze-out temperature is known as kinetic freeze-out. At this stage, the shape of the transverse momentum spectra of produced particles gets fixed. Hadronic phase is defined here as the phase between chemical and kinetic freeze-out. This is because the chemical freeze-out temperature and critical temperature are of similar values at LHC energies. The properties of the hadronic phase can be probed through resonances. Resonances are short-lived hadrons that decay via the strong interaction. The decay products of resonances inside the hadronic phase take part in two processes called regeneration and rescattering effects through elastic or pseudo-elastic scatterings, which leads to the modification of the yields of resonances. Experimentally, several resonances measurements have been studied with varying mass, lifetime, quark contents in heavy-ion collisions at RHIC and LHC [5, 6, 7, 8, 9, 10]. These measurements provide the evidence that in the hadronic phase, where the hadrons interact via rescattering and regeneration processes [5, 6, 7, 8, 9, 10]. Similar measurement in p–Pb collisions play an important role because it is an intermediate collision system between pp and heavy-ion collisions, in terms of produced charged particle multiplicity and size of the colliding system. It also acts as the reference colliding system to interpret the heavy-ion collisions.

Recent measurements in high–multiplicity pp, p–Pb collisions show a number of effects that are qualitatively similar to those seen in heavy-ion collisions for various observables [11, 12, 13, 14, 15, 16, 17, 18, 19]. This includes non-zero value of elliptic flow (v_2) [11, 12], near and away side ridge structure in two particle angular correlation [13, 14], mass ordering in hadron p_T spectra and enhancement in baryon-to-meson ratios at the intermediate p_T[16] and the enhancement of multi-strange hadrons [15]. The decreasing trend of K^{*0}/K ratios are seen for high multiplicity pp and p–Pb collisions with respect to minimum bias pp collisions [18, 19]. These measurements provide the challenge

to intriguing the question of whether these observations that arose similar to heavy-ion collisions were due to the formation of a hot and dense medium or instead involved other physical mechanisms. The origin of these phenomena are yet understood completely. Several theoretical approaches and models have been tested to explain these QGP-like effects in small systems considering multiple parton interactions (MPI) [20], string shoving [21], or rope hadronization [22]. However, these models cannot explain the measured non-zero elliptic flow [11, 12]. In this thesis, we report on the multiplicity dependence of K^{*0} production at the highest center-of-mass energy, $\sqrt{s_{NN}} = 8.16$ TeV, reached at the LHC in p–Pb collisions. This provides an opportunity to extend the previous measurement in p–Pb collisions at $\sqrt{s_{NN}} = 5.02$ TeV [19], to a higher multiplicity reach and a larger p_T coverage. In addition, the new $K^{*\pm}$ measurements in p–Pb collisions at $\sqrt{s_{NN}} = 5.02$ TeV have been discussed. The transverse momentum spectra of light–flavor hadrons have shown a clear evolution with multiplicity in high energy pp and p–Pb collisions [18, 19, 23, 24], similar to that observed in Pb–Pb collisions [25, 9, 10], where in the latter case the effect is usually attributed to a collective expansion of the system. The slope of the p_T spectra increases with multiplicity in the low–p_T region of the spectrum. It is attributed to the radial flow. The observation of increasing the average transverse momentum $\langle p_T \rangle$ with multiplicity also supports the presence of the radial flow effect. In contrast to the yields dN/dy, which evolve smoothly as a function of multiplicity for different collision systems, the $\langle p_T \rangle$ of light–flavor hadrons as well as resonances (i.e., K^{*0}) rises faster as a function of multiplicity in pp and p–Pb collisions than in Pb–Pb collisions, as discussed in Refs. [18, 19].

The high–p_T particle production is analyzed within the framework of perturbative Quantum Chromodynamics (pQCD) which features a nearly scale-invariant behavior of elementary parton–parton hard-scattering processes [26, 27]. The convolution of hard scattering cross sections with the parton distribution functions (PDFs) of incident hadrons

and fragmentation functions (FFs) leads to the observed scaling of the inclusive invariant cross section $E\mathrm{d}^3\sigma/\mathrm{d}p^3$ as p_T^{-n} at fixed transverse x, $x_\mathrm{T} = 2p_\mathrm{T}/\sqrt{s}$ [28, 29]. The exponent n can be related to the scattering processes in which high–p_T hadrons are produced. If hadrons are produced by leading twist (LT) 2 $\rightarrow$ 2 hard subprocesses, n $\sim$ 4 and for higher twist (HT) processes, $n \sim 8$. It has been observed that the exponent value decreases with increasing collision energy, which suggests that the contribution of higher twist processes on high–p_T hadron production is reduced as a function of energy. The transverse momentum distributions of different particle species at high p_T are observed to satisfy a universal x_T scaling over a wide energy range up to $\sqrt{s}$ = 13 TeV. This scaling behavior was observed by the CDF [30, 31, 32] and UA1 [33] Collaborations in p($\overline{\mathrm{p}}$) collisions, and by the STAR [34], ALICE [35] and CMS [36] Collaborations in pp collisions. In this thesis, the x_T scaling of K^{*0} meson is tested in p–Pb collisions at LHC energies. The transverse momentum distributions of the particles in p–Pb collisions are compared to those in pp collisions using the nuclear modification factor (R_pPb). The measurement of R_pPb acts as a control experimental observable in p–Pb collisions [37] in the context of the observed high–p_T hadron suppression in Pb–Pb collisions [38, 8, 9]. R_pPb measurements of K^{*0} in p–Pb collisions at $\sqrt{s_\mathrm{NN}}$ = 5.02 and 8.16 TeV, and compared with other available hadron measurements in p–Pb collisions at $\sqrt{s_\mathrm{NN}}$ = 5.02 TeV. In this thesis, the particle species and collision energy dependence of R_pPb have been studied for p–Pb collisions at LHC energies.

Throughout this thesis, the results for K^{*0} (K^{*+}) and $\overline{\mathrm{K}}^{*0}$ (K^{*-}) are averaged and denoted by the symbol K^{*0} (K$^{*\pm}$). The chapter is organized as follows. In Section 3.2 and 3.3 include the analysis details such as data sample, event and track selection criteria, multiplicity estimation, the analysis techniques, the procedure of extraction of the yields and efficiency $\times$ acceptance. The corrected p_T spectra and systematic uncertainties are discussed in

Section 3.4 and Section 3.5, respectively. In Section 3.6 the results on transverse momentum (p_T) spectra, dN/dy, $\langle p_T \rangle$, x_T-scaling, and R_{pPb} in p–Pb collisions are discussed. Finally, the results are summarized in Section 3.7.

3.2 Analysis details

The analysis is carried out on the data collected in the year 2016 for p–Pb collisions. Measurements of K^{*0} and $K^{*\pm}$ have been performed at centre-of-mass energy per nucleon-nucleon $\sqrt{s_{NN}}$ = 8.16 and 5.02 TeV, respectively. Measurements of K^{*0} and $K^{*\pm}$ production have performed using the minimum bias-triggered events of the data samples of 30 and 240 million. The K^{*0} and $K^{*\pm}$ are reconstructed from their decay products. The decay channels are $K^{*0} \rightarrow \pi^{\pm} K^{\mp}$ having branching ratios (BR) of 66.6 % [19] and $K^{*\pm} \rightarrow \pi^{\pm} K_S^0$ with BR of 33.3 % [39], respectively.

3.2.1 Event selection

A minimum bias trigger criteria is used to select events by requiring at least a coincidence signal in both the V0A and V0C detectors [40]. The V0 consists of two arrays of 32 scintillator detectors, one on each side of the interaction point covering the full azimuthal angle in the pseudorapidity regions $2.8 < \eta < 5.1$ (V0A) and $-3.7 < \eta < -1.7$ (V0C). The minimum bias p–Pb collision events are collected with a solenoidal magnetic field of B = 0.5 T. The background events due to beam–gas interaction and other machine-induced background collisions are rejected using the timing information from the V0 and the Zero Degree Calorimeter (ZDC) [41]. The primary vertex of a collision is determined using charged tracks reconstructed in the ITS [42] and the TPC [43]. The events are selected whose primary vertex position along the beam axis (v_z, z is the longitudinal direction)

within ± 10 cm from the nominal interaction point. Pile-up events from the triggered

bunch crossing are rejected if multiple collision vertices are identified in the SPD, which is

the innermost detector of the ITS [42]. In p–Pb configurations, the ^{208}Pb beam circulates

towards the positive z–direction in the ALICE laboratory frame, while the proton beam

circulates in the opposite direction. Due to the asymmetric system, the center-of-mass

frame is shifted in the rapidity by $\Delta y = -0.465$ in the direction of the proton beam with

respect to the laboratory frame. For centrality selection in p–Pb collisions have similar

geometrical meaning to that in Pb–Pb collisions, where it indicates how two nuclei overlap

at the moment of collide. Figure 3.1 illustrates the examples of p–Pb collisions, which are

quantified by a geometrical impact parameter (b), a variable used as indicative for centrality.

The impact factor, b is defined as the perpendicular distance between the centre of two

interacting particles. The maximum b value is obtained for p–Pb collisions is equivalent

to the radius of Pb-nucleus, $R_{Pb} = 6.62 \pm 0.06$ fm [44].
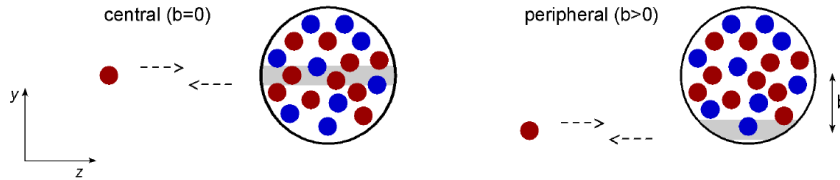
FIGURE 3.1: Example of sketch of geometrical collisions of most central (left) and peripheral (right) p–Pb system. In central collisions, the incident proton interact with larger number of nucleons and large number of particle are produced. Peripheral collisions seems to smaller number of particle produced that lead to smaller multiplicity. This figure is taken from [44].

A pure geometrical Monte-Carlo simulation Glauber model [45] is used to describe the

high energy nuclear (A–A and p–Pb) collisions. It considers A–A and p–Pb interactions

as the superposition of individual nucleon-nucleon interactions. The aim is to provide

the statistical basis of the geometrical configuration of A–A and p–Pb collisions relative to the simpler pp collisions. Assumptions are considered in this model as nucleons are followed a straight trajectory and are entirely transparent to previous interactions. The nucleon-nucleon interaction cross section remains unchanged for subsequent collisions of the same proton. N-N cross section is assumed to be the same regardless of whether it occurs in vacuum (pp-like collisions) or inside nuclear matter (A–A and p–Pb).For p–Pb collisions, the Monte Carlo generates simulation of Pb ions consists of 208 nucleons randomly distributed within in a sphere defined by the radius of Pb-nucleus (R_{Pb}), separated by a distance no smaller than a hard sphere exclusion separation of 0.4 fm. They follow a density profile is described by Woods-Saxon parameterizations [45].

$$\rho_{Pb} = \frac{\rho_N}{1 + \exp^{(r-R_{Pb})/a}} \tag{3.1}$$

where r is the radial position of nucleon inside the ion, ρ_N and a is density and skin thickness of the nucleus. The collisions are simulated randomly changing values for b and satisfy the condition as given $b_{NN} < \sqrt{\frac{\sigma_{NN}^{inel}}{\pi}}$. The σ_{NN}^{inel} corresponds to inelastic cross section. The number of N-N collisions (N_{coll}) and number of participate nucleons ($N_{part} = N_{coll} + 1$) are counted in event by event simulation to determine their dependence on the impact parameter [46].

Multiplicity as an indicator of centrality

The "b" can not be measured directly in experiment, the obtained quantity N_{coll}, and N_{part} from simulation are mapped onto the measured quantity. In ALICE p–Pb collisions, the measurable quantity is the V0A amplitude that is proportional to number of charged particle produced in the collisions. This is the energy deposited in V0-detector on the A-side (the direction in which Pb-beam travels) of the experiment and situated at higher η, the selection

of charged particle in this η avoids the self-correlation effects with central η regions where the actual measurements of resonances are made. The minimum bias events are divided into various multiplicity classes, according to the total charge deposited in the forward V0A detector [40], as shown in Fig. 3.2.
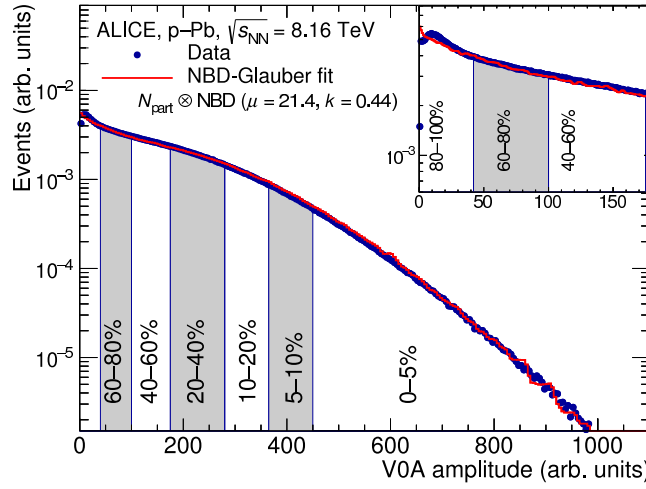
FIGURE 3.2: V0A amplitude distribution measured in p–Pb collisions are divided in various multiplicity classes. The distribution is fitted with a Gluaber model function [45].

The yield of K*0 is measured in the rapidity interval $-0.5 < y < 0$ for the following event multiplicity classes, 0–5%, 5–10%, 10–20%, 20–40%, 40–60%, 60–80% and 80–100% along with multiplicity integrated 0–100%. Similarly, K*± measurements are performed in 5 multiplicity classes (0–20%, 20–40%, 40–60%, 60–80%, 80–100%) and also using a multiplicity-integrated sample (0–100%). The mean charged-particle multiplicity ($\langle dN_{ch}/d\eta \rangle$) corresponding to each multiplicity class that measured in the pseudorapidity interval $|\eta_{lab}| < 0.5$, is given in Table 3.1 taken from [46].

TABLE 3.1: Mean charged particle multiplicity densities ($\langle dN_{ch}/d\eta \rangle$) measured in pseudorapidity range $|\eta_{lab}| < 0.5$, corresponding to the various multiplicity classes defined using the V0A detector in p–Pb collisions at $\sqrt{s_{NN}}$ = 8.16 TeV [46].

V0A percentile (%)	$\langle dN_{ch}/d\eta \rangle_{|\eta_{lab}|<0.5}$
0–5	53.22 ± 1.38
5–10	42.40 ± 1.10
10–20	35.49 ± 0.92
20–40	26.89 ± 0.70
40–60	18.39 ± 0.48
60–80	10.97 ± 0.29
80–100	4.47 ± 0.14

3.2.2   Track selection

The charged tracks coming from the primary vertex are selected in the pseudorapidity interval $|\eta| < 0.8$ with $p_T > 0.15 \, GeV/c$. This ensures the uniform acceptance for the central barrel detectors. The high quality tracks are chosen based on selection criteria as done previously in Ref. [19]. The K^{*0} and $K^{*\pm}$ mesons are reconstructed from the charged tracks which have crossed at least 70 out of maximum 159 horizontal segments along the transverse readout plane of the TPC. The contamination from secondary particles originating from weak decays and beam background events are reduced by applying a selection on the distance of closest approach to the primary vertex in the transverse plane (DCA_{xy}) and along the longitudinal direction (DCA_z). A p_T-dependent cut of $DCA_{xy}(p_T) < (0.0105 + 0.035 \, p_T^{-1.1})$ cm, with p_T in GeV/c, is used, which is less than 7 times its resolution. The track DCA_z is required to be less than 2 cm.

3.2.3   Particle identification (PID)

The decay daughters (pions, kaons) of K^{*0} and $K^{*\pm}$ are identified by measuring the specific ionization energy loss (dE/dx) in the detector gas of the TPC [43] and their time-of-flight

information using the TOF [47]. The dE/dx resolution of the TPC is denoted as $n\sigma_{\text{TPC}}$ and the charged tracks are identified as pions and kaons if the mean specific energy loss measured by the TPC is within $6\sigma_{\text{TPC}}$, $3\sigma_{\text{TPC}}$ and $2\sigma_{\text{TPC}}$ from the expected $\langle dE/dx \rangle$ values in the momentum range $p < 0.3 \,\text{GeV}/c$, $0.3 < p < 0.5 \,\text{GeV}/c$ and $p > 0.5 \,\text{GeV}/c$, respectively. In addition to the TPC, if the TOF information is available, the charged tracks are identified by requiring the time-of-flight values within $|n\sigma_{\text{TOF}}| < 3$ of the expected values for the full momentum range. The $n\sigma_{\text{TPC}}$ is defined as

$$n\sigma_{\text{TPC}} = \frac{\langle dE/dx \rangle_{measured} - \langle dE/dx \rangle_{expected}}{\sigma_{\text{TPC}}} \tag{3.2}$$

Where $\langle dE/dx \rangle_{\text{measured}}$ is the measured average energy loss of tracks present inside the TPC, $\langle dE/dx \rangle_{\text{expected}}$ is the theoretical predictions of average energy loss of a pion (corresponds $n\sigma_{\text{TPC}}$ for pion) or kaon (corresponds to $n\sigma_{\text{TPC}}$ kaon) track, obtained from the parameterization of modified Bethe-Bloch function [48]. The $\langle dE/dx \rangle$ is calculated from the truncated mean of 60% of the measured cluster to avoid the fluctuation arise due to ionization and TPC edge effects. The σ_{TPC} is the PID resolution of the TPC and the typical values are $\sim 5.2\%$ for pp collisions and $\sim 6.5\%$ for central 0–5% of A–A collisions. The TOF detectors is able to identify a particle by combining the information of the flight time of particle measured in the TOF detector and its momentum information from ITS and TPC detectors. The start time of the flight is assumed to be the collision time. It is obtained for each event from the T0 detector [49]. The $n\sigma_{\text{TOF}}$ is defined as

$$n\sigma_{\text{TOF}} = \frac{t_{measured} - t_{expected}}{\sigma_{\text{TOF}}} \tag{3.3}$$

Where t_{measured} is the flight time of a particle measured in the TOF detector and t_{expected} is the expected time obtained form the track length and its momentum. The σ_{TOF} is the PID resolution of the TOF and value is $\sim 56 \,\text{ps}$ [47]. The details of quality assurance plots

for identification of decay daughter of K^{*0} are shown in Fig. A.1, Fig. A.2, Fig. A.3 and Fig. A.4 in the Appendix. The secondary vertex reconstructed particle (using V shaped topology), K_S^0 is identified from its decay daughter of π^+ and π^- having branching ratio of 69.2%. Similar selection criteria have been taken for K_S^0 as used in Ref. [39].

3.3   Signal extraction

The production K^{*0} at $\sqrt{s_{NN}} = 8.16$ TeV and $K^{*\pm}$ at $\sqrt{s_{NN}} = 5.02$ TeV in p–Pb collisions have been measured by using invariant mass method from their hadronic decay products. The invariant mass distribution of πK and πK_S^0 pairs are expressed as

$$M_{\pi K(K_S^0)} = \sqrt{(E_\pi + E_{K(K_S^0)})^2 - (\vec{p}_\pi + \vec{p}_{K(K_S^0)})^2} \tag{3.4}$$

Where E and $\vec{p}$ are energy, and momentum of decay products of resonances, respectively. Figure 3.3 shows invariant mass distribution of πK and πK_S^0 pairs that are obtained from the same event, which gave a peak over a combinatorial background. This distributions is shown for a given transverse momentum (p_T) range $1.4 \le p_T < 1.6$ GeV/c in p–Pb collisions for minimum bias (0-100%) events at $\sqrt{s_{NN}} = 8.16$ TeV (for K^{*0}) and $\sqrt{s_{NN}} = 5.02$ TeV (for $K^{*\pm}$), respectively. The combinatorial background distributions are estimated using event-mixing technique. For reconstruction of event-mixing pairs, 5 events are mixed, whose z-vertex difference is within 1 cm and multiplicity difference within 5, to reduce the statistical uncertainty of the combinatorial background distributions (invariant mass distribution πK pairs before combinatorial background subtraction for various p_T intervals for multiplicity classes 0–100% are shown in Fig. A.5 and Fig. A.6 in the Appendix). After the event-mixing, the invariant mass distribution of combinatorial backgrounds have 5 times higher statistics than the invariant distribution obtained from the same event pairs.

The mixed-event combinatorial background distributions are normalized in the mass region more than 5 Γ (Γ is full width at half maximum of the resonance) away from the signal mass peak position. The mixed event backgrounds (red markers) for both πK and πK$_S^0$ pairs are normalized in the region of invariant mass of 1.1 to 1.15 GeV/c^2 is shown in Fig. 3.3. The signal of K^{*0} and K$^{*\pm}$ distributions are obtained after subtraction of the normalized mixed event invariant mass distribution from same event invariant mass distributions. After the subtraction of combinatorial background distribution, the remaining background
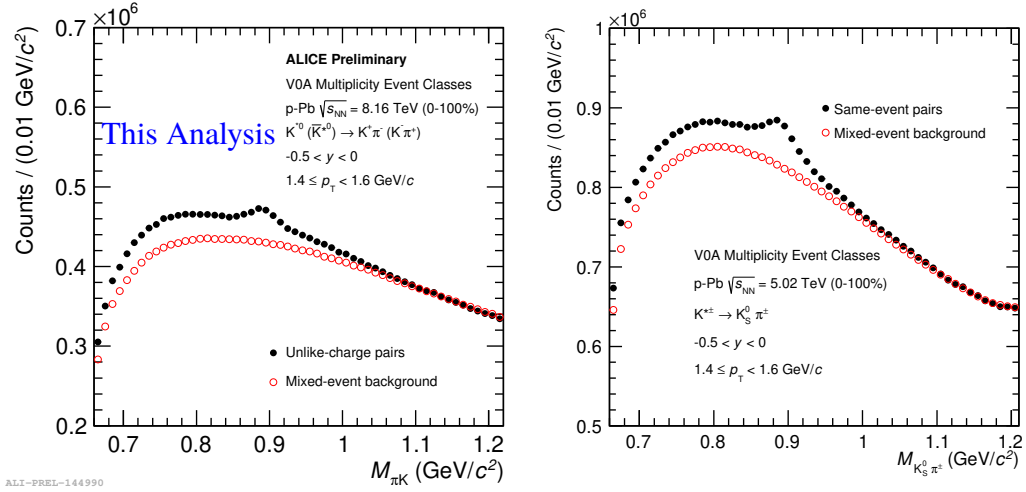
FIGURE 3.3: Invariant mass distributions of πK (left) and πK$_S^0$ (right) from same event pair (black markers) for p_T interval $1.4 \leq p_T < 1.6$ GeV/c in minimum bias (0-100%) p–Pb collisions. The normalized mixed-event distributions are shown in red markers.

present is known as residual background. The source of the residual background mainly originate from correlated decay products from decay of higher mass resonances (i.e., $K_1(1400) \rightarrow K\rho \rightarrow K\pi\pi$, $K^*(1410) \rightarrow K\rho \rightarrow K\pi\pi$, $K_2(1770) \rightarrow K\pi\pi$) and misidentified of decay products. The combinatorial background subtracted invariant mass distributions from πK, and πK$_S^0$ pair are fitted with the combination of the Brest-Wigner function for the signals. For describing residual background, the polynomial function of second order

(for K^{*0}) and the combination exponential plus polynomial function of second order(for $K^{*\pm}$) are used. The distributions after combinatorial subtraction and fitted with signal plus residual background function is shown in Fig. 3.4 (Invariant mass distribution πK pairs after combinatorial background subtraction for various p_T intervals for multiplicity class 0–100% are shown in Fig. A.7 and Fig. A.8 in the Appendix). The fit functions used for K^{*0} and $K^{*\pm}$ are given in Eq. 3.5 and Eq. 3.6, respectively.

$$\frac{Y}{2\pi} \frac{\Gamma_0}{(M_{\pi K} - M_0)^2 + \frac{\Gamma_0^2}{4}} + AM_{\pi K}^2 + BM_\pi K + C \tag{3.5}$$

$$\frac{Y}{2\pi} \frac{\Gamma_0}{(M_{\pi K_S^0} - M_0)^2 + \frac{\Gamma_0^2}{4}} + (M_{\pi K_S^0} - (m_\pi + m_{K_S^0}))^n \exp(AM_{\pi K_S^0}^2 + BM_{\pi K_S^0} + C) \tag{3.6}$$

Where M_0 and Γ_0 are PDG mass and width of resonances, respectively. $M_{\pi K}$ and $M\pi K_S^0$ are pair mass of decay products of K^{*0} and $K^{*\pm}$, respectively. A, B, C and n are fit parameters. The parameter Y is the area under the Breit-Wigner distribution that gives raw yield of K^{*0} and $K^{*\pm}$ signal, respectively. During the fitting of K^{*0} and $K^{*\pm}$, the width of Breit-Wigner distributions are fixed to the PDG value of 47.3 ± 0.5 MeV/c^2 [50] (the measured mass as a function of p_T for K^{*0}, using both data and Monte Carlo (MC) is shown in Fig. A.9 in the Appendix) and 50.8 ±0.9 MeV/c^2 [50], respectively. The K^{*0} and $K^{*\pm}$ yield are extracted for different p_T intervals and multiplicity classes from the minimum bias collisions (the signals for various p_T intervals are shown in Fig. A.10 and Fig. A.11 in the highest multiplicity (0–5%) and low multiplicity (80–100%) classes for K^{*0} in the Appendix).
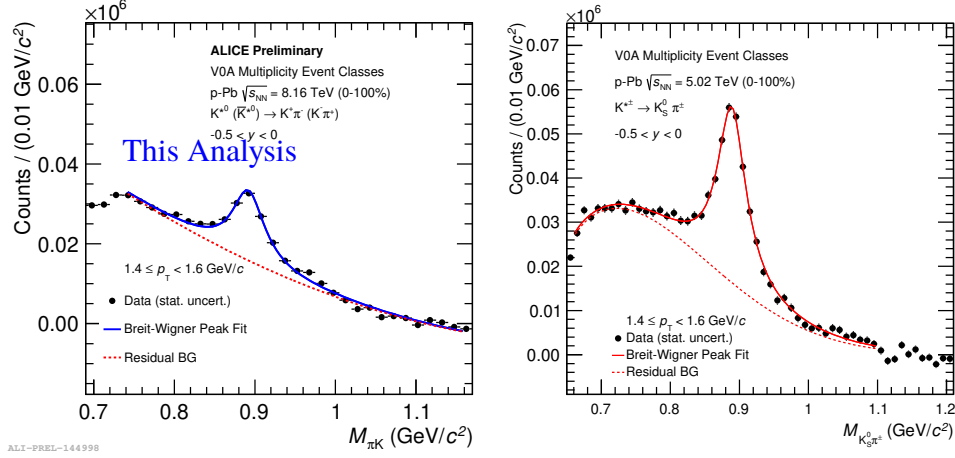
FIGURE 3.4: Invariant mass distributions of πK (left) and πK_S^0 (right) in the p_T interval $1.4 \leq p_T$ < 1.6 GeV/c after combinatorial background subtraction fitted with a combination of Breit-Wigner function for signal, and polynomial function of second order for K^{*0} and exponential plus polynomial function of second order for $K^{*\pm}$ are used as the residual background function in p–Pb collisions for rapidity interval -0.5 < y < 0. The solid line is the result of the fit functions of Eq. 3.5 for K^{*0} and Eq. 3.6 for $K^{*\pm}$. The dashed line represents the residual background function.

3.3.1 Raw yield extraction

The raw yield of K^{*0} and $K^{*\pm}$ are calculated by two methods; bin counting and functional integral method. The yield extraction by bin counting method is taken as default, whereas functional integral method is used for systematic study. In bin counting method, the raw yield (N_{count}) is estimated by integrating invariant mass histogram after subtraction of normalized mixed-event background in the mass range: M_0 - 2Γ to M_0 + 2Γ, where M_0 and Γ are PDG mass and width of resonances (K^{*0} and $K^{*\pm}$). The contribution due to residual background is estimated from the integral of residual background fit function (N_{res}) in the same mass interval as used for calculate the N_{count}. After that raw yield (N_{raw}) is obtained after subtraction of N_{res} from N_{count}, as expressed in Eq. 3.7.

$$N_{\text{raw}} = N_{\text{counts}} - N_{\text{res}} \tag{3.7}$$

To the N_{raw} is further added two tail correction terms. The tail correction terms are given in Eq. 3.8 and Eq. 3.9, respectively.

$$N_{low} = \int_{M_\pi + M_K (M_\pi + M_{K_S^0})}^{M_0 - 2\Gamma} fit(m_{inv}) dm_{inv} \tag{3.8}$$

$$N_{high} = \int_{M_0 + 2\Gamma}^{\infty} fit(m_{inv}) dm_{inv} \tag{3.9}$$

Where fit(m_{inv}) is signal fit function of the Breit-Wigner distributions for K^{*0} and $K^{*\pm}$. The final yield due to bin count method is

$$Y_{BC} = N_{\text{raw}} + N_{\text{low}} + N_{\text{high}} \tag{3.10}$$

In function integral method, yield is extracted by integrating the signal function (Breit-Wigner) over the mass range $M_\pi + M_K$ $(M_\pi + M_{K_S^0}) < m_{inv} < \infty$ for K^{*0} ($K^{*\pm}$). The yield of K^{*0} and $K^{*\pm}$ are extracted as a function of p_T for minimum bias and also various multiplicity classes. The raw p_T spectra are corrected with corresponding number of accepted events.

3.3.2 Efficiency × Acceptance

Particle production and decay are simulated using a DPMJET [51] based event generator (for K^{*0}) and an EPOS-LHC [52]event generator (for $K^{*\pm}$), while particle interactions with the ALICE detector are simulated using GEANT3. The same event selection and track quality cuts are used for both the real and simulated data. The particles produced by the event generator (without any detector effects) are referred to as the generated particles. These particles are the input for the GEANT3 detector simulation and the track and signal reconstruction algorithms. The tracks identified by the reconstruction algorithms and pass the track selection and PID cuts are referred to as reconstructed tracks. The K^{*0} and $K^{*\pm}$ mesons are known as reconstructed mesons if they have reconstructed from their reconstructed decay daughters. The K^{*0} and $K^{*\pm}$ reconstruction efficiency × acceptance (ϵ_{rec}) is ratio of the number of reconstructed K^{*0} ($K^{*\pm}$) mesons having decay products of $\pi^{\pm}K^{\pm}$ ($\pi^{\pm}K^0_S$) that passes through the track cuts which are used in real data to the number of generated K^{*0} ($K^{*\pm}$) in the same rapidity range -0.5 < y < 0.

$$\epsilon_{rec} = \frac{N_{reconstructed}}{N_{generated}} \tag{3.11}$$

Efficiency×acceptance as a function of p_T for minimum bias p–Pb collisions at $\sqrt{s_{NN}}$ = 8.16 TeV shown in left panel of the Fig. 3.5 and similarly right panel of figure show same for $K^{*\pm}$ in p–Pb collisions at $\sqrt{s_{NN}}$ = 5.02 TeV. This indicates that the efficiency of K^{*0} and $K^{*\pm}$ has a strong dependence on transverse momentum at low p_T.

The uncertainty in ϵ_{rec} is calculated using the Bayesian approach described in [53]. The standard deviation in an efficiency ϵ_{rec} = k/n, where the numerator k is a subset of the denominator n, is
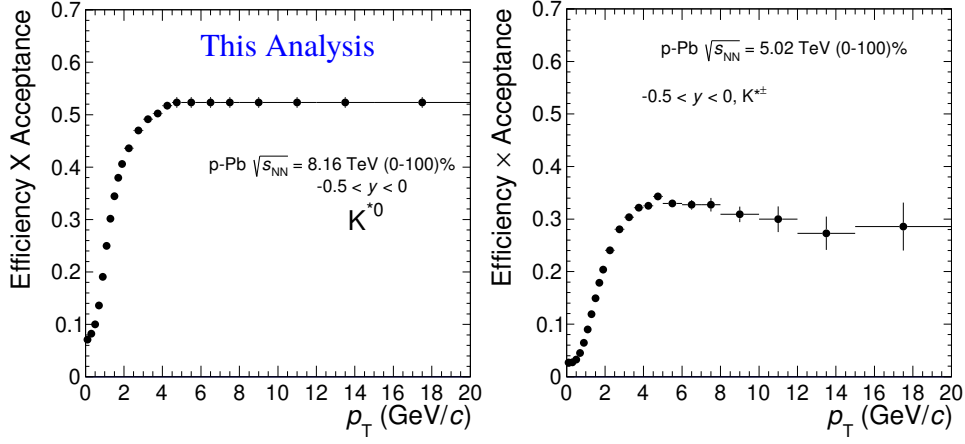
FIGURE 3.5: Efficiency × acceptance as a function of p_T for K^{*0} (left) at $\sqrt{s_{NN}}$ = 8.16 TeV and for $K^{*\pm}$ (right) at $\sqrt{s_{NN}}$ = 5.02 TeV in the rapidity interval -0.5 < y < 0 for minimum bias (0-100%) p–Pb collisions.

$$\sigma_\epsilon = \sqrt{\frac{k+1}{n+2}\left(\frac{k+2}{n+3} - \frac{k+1}{n+2}\right)} \tag{3.12}$$

The efficiency × acceptance as a function of p_T for various multiplicity classes is shown in Fig. A.12 in the Appendix. No multiplicity dependence on efficiency × acceptance as a function of p_T is seen for K^{*0} [54] and $K^{*\pm}$ [55] in p–Pb collisions. The minimum bias efficiency × acceptance is used for different event multiplicity classes.

3.3.3 Re-weighted Efficiency × Acceptance

The shape of the simulated p_T distribution is different from the measured p_T distribution; therefore, a re-weighting procedure is used, in which the generated distribution is weighted to match the measured distribution. Fig. 3.6 shows the generated and reconstructed K^{*0} spectra plotted with the (corrected) measured K^{*0} spectrum and the Lévy-Tsallis fit [56] of that measured spectrum. An iterative procedure is performed to determine the correct

weighting (and, therefore, the correct ϵ_{rec}).

1. The unweighted ϵ_{rec} is calculated.

2. This ϵ_{rec} is used to correct the measured $K^{*0} p_T$ spectrum.

3. The corrected K^{*0} spectrum is fitted with Lévy-Tsallis function.

4. This fit is used to weight the MC generated K^{*0} spectra. A p_T dependent weight is applied to the generated K^{*0} spectrum so that it follows the fit. The same weight is applied to the reconstructed K^{*0} spectrum.

5. The (weighted) ϵ_{rec} is calculated.

6. Steps 2-5 are repeated (with the weighted ϵ_{rec} from step 5 used as the input for step 2) until the ϵ_{rec} values are observed to change by $< 0.1\%$ (relative) between iterations. It is observed that two iterations is sufficient to converge this process. The correction factor is defined as the ratio of efficiency x acceptance after re-weighted to unweighted efficiency x acceptance after two iterations, is shown in Fig. 3.7.

The effect of the weighting procedure is very small.
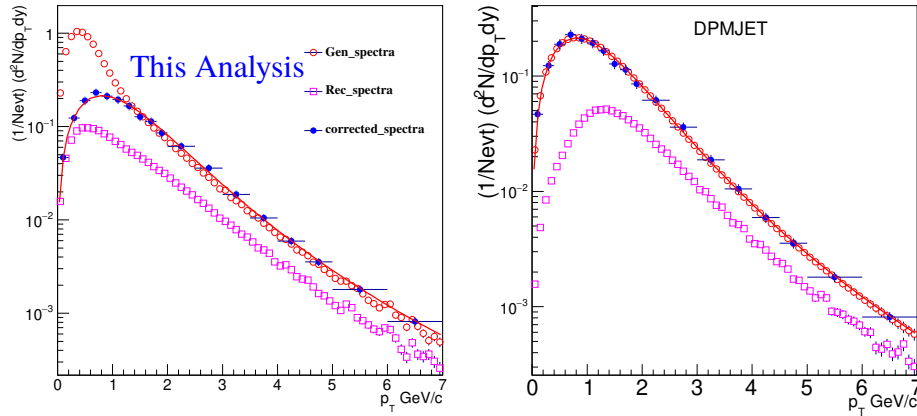
FIGURE 3.6: Corrected K^{*0} spectrum (blue) with Lévy-Tsallis fit (red curve). Also shown are the unweighted generated (red) and reconstructed (magenta) K^{*0} meson spectra for minimum bias p-Pb collisions at $\sqrt{s_{NN}} = 8.16$ TeV. Generated K^{*0} spectra: unweighted (red) and 2 iterations of weighting (blue, magenta) for minimum bias p-Pb collisions at $\sqrt{s_{NN}} = 8.16$ TeV.
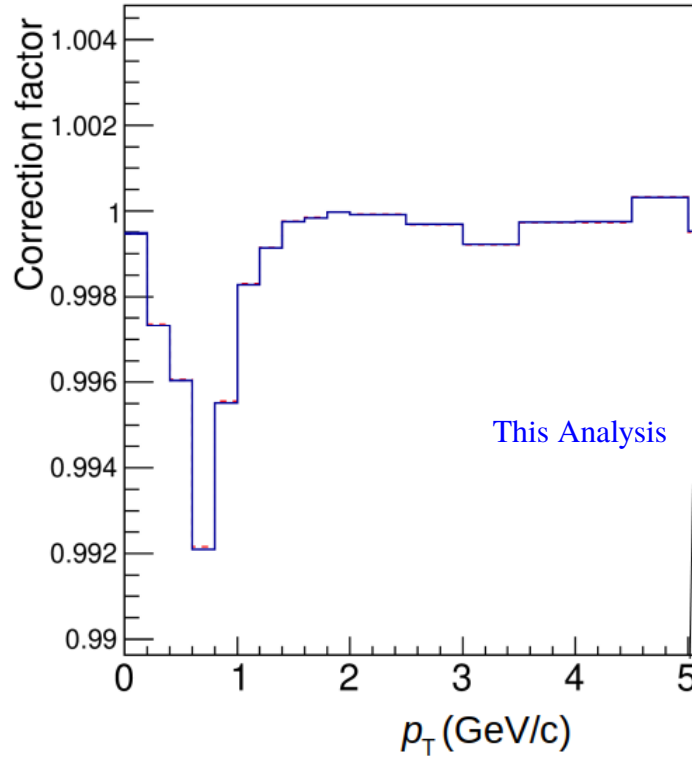
FIGURE 3.7: Ratio of K^{*0} re-weighted to unweighted efficiency $\times$ acceptance after two iteration for minimum bias p–Pb collisions at $\sqrt{s_{NN}}$ = 8.16 TeV.

3.4 Corrected p_T spectra

The raw p_T spectra are corrected for efficiency $\times$ acceptance (ϵ_{rec}), branching ratio. The normalized corrected spectra are obtained using the following formula:

$$\frac{d^2N}{dp_T dy} = \frac{N_{raw}}{2 \times N_{evt} \times BR \times dp_T \times dy \times \epsilon_{rec}} \times f_{norm} \times f_{SL} \times f_{vtx} \qquad (3.13)$$

Where N_{raw} is raw yield of K^{*0} or $K^{*\pm}$. BR is the branching ratio, 0.66 for K^{*0} and 0.33 for $K^{*\pm}$. Where dy = 0.5 and a factor 2 is used yield average over K^{*0} and $\overline{K^{*0}}$ (K^{*+} and

K^{*-}). The factor f_{norm} is normalized correction for NSD events. The value is found to be 0.992 [54]. The f_{vtx} correction is the ratio between the number of trigger events and the number of events at which the primary vertex is found (i.e., it satisfies the vertex quality criteria without the selection criteria of z-position of the vertex). The factor f_{SL} is known as signal loss correction factor. The signal loss correction gives information about fraction signal lost due to event and trigger selection criteria. This correction factor depends on p_T and the effect is seen at low p_T. The signal-loss correction factor for K^{*0} in p–Pb collisions is calculated following steps.

Different event selection cut is used for calculating signal loss correction in minimum bias(NSD) and various multiplicity classes. Three event section criteria are assigned names as A, B, and C, respectively.

where A : apply cut only generated $|v_z, Gen| < 10$ cm (no other cuts).

B: cut on trigger selection and generated v_z within $\pm$ 10 cm (no other cuts).

C: standard default event-selection cuts.

The signal loss correction factors for minimum bias and various multiplicity classes are calculated as the ratio between two generated p_T spectra.

For minimum bias, 0-100% (NSD) is p_T dependant ratio:

Numerator : particle p_T spectrum obtained with event selection A.

Denominator: particle p_T spectrum obtained with event selection C.

For various multiplicity classes is p_T dependant ratio:

Numerator:particle p_T spectrum obtained with event selection B.

Denominator: particle p_T spectrum obtained with event selection C.

The signal loss correction is obtained by taking the ratio between particle generated p_T spectra with event selection A and C. The generated p_T of each event selection is normalized with the corresponding number of events. The signal loss correction is shown for 0–100%

in Fig. 3.8. A constant function is fitted p_T up to 2 GeV/c, and extracted value is taken as the signal loss correction factor. The error on this correction factor is calculated as $\frac{|1-constantvalue|}{2}$.
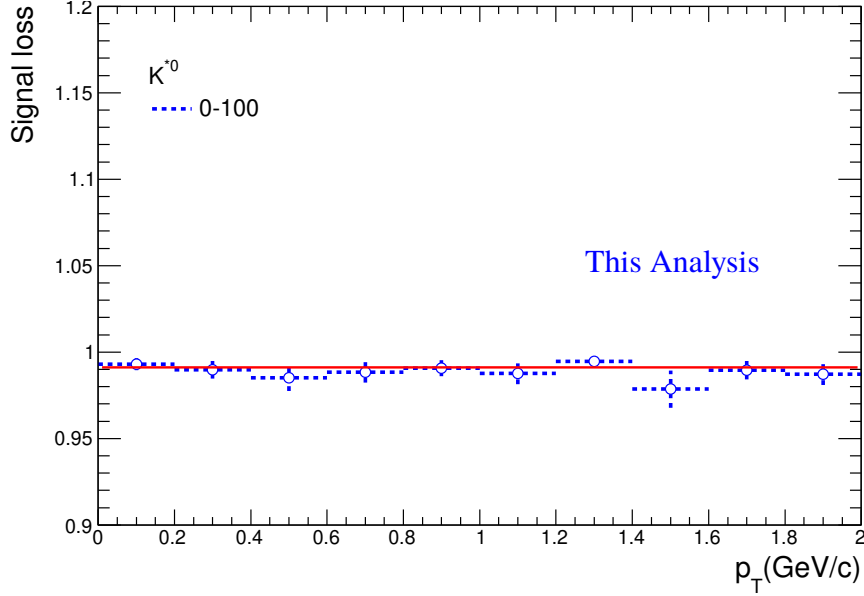
FIGURE 3.8: Signal loss correction for minimum bias (0–100%) in p–Pb collisions at $\sqrt{s_{NN}}$ = 8.16 TeV. The red line represents the a constant fit function.

The signal loss correction factor for various multiplicity classes have been calculated (plots are shown in Fig. A.13 in the Appendix). The values are found to be consistent with unity. The correction factors are negligible and consistent with unity for minimum bias and multiplicity classes.

3.5 Systematic uncertainties

The measurements have been repeated for the systematic study by varying one selection criteria and others same as the default selection criteria. A Barlow check has been performed for each measurement to verify whether it is due to a systematic effect or a statistical

fluctuation. The procedure of Barlow criteria [57] is calculated in the following steps. Let us consider two cases: one measurement is due to the default settings, and another is due to the alternative systematic measurements (i.e., fitting range variations, etc.). Let us denote the yield in the default case as y_{def} with statistical error σ_{def} and yield in the systematic case as y_{sys} with statistical error σ_{sys}. Then the difference between the yields is denoted as $\Delta = y_{def}$ - y_{sys} and the quadrature difference of their statistical error is $\sigma = \sqrt{\sigma_{def}^2 - \sigma_{sys}^2}$. Then it is defined as a factor $n = \Delta/\sigma$. This n is calculated for each p_T bin, and the distribution of n or Δ/σ is shown in Fig. A.14 in the Appendix. In general, if two measurements are consistent, it is expected that the distribution of n would have a mean near 0, a standard deviation near 1 and that 68% (95%) of the entries would lie within $|\Delta/\sigma| <$ 1 ($|\Delta/\sigma| < 2$). For this study, a source is considered the systematic if $|\Delta/\sigma|$ distribution of that source having standard deviation > 1. The source of systematic uncertainties consists of the contribution coming from variation due to signal extraction, track selection criteria, particle identification, global tracking efficiency, the hadronic interaction cross section and uncertainty in the material budget of the detector material. For systematic study, a similar approach is adopted that was used for p–Pb collisions at $\sqrt{s_{NN}}$ = 5.02 TeV [19]. The uncertainties due to signal extraction include variations in fitting range, normalization region of mixed-event invariant mass distribution, variations in the width of resonances, choice of a residual background function, and combinatorial background. The fitting range is varied by ~ 50 MeV/c^2 on each side of the signal peak of resonances. The normalization range of the invariant mass distribution is varied by approximately 150 MeV/c^2 with respect to the default value. The width of the resonances is fixed for the default fit, whereas it is kept free for systematic studies. The residual background is fitted with a first-order and third-order polynomial function for the systematic studies of the signal extraction. The systematic effects due to the track selection have been studied

by varying default track selection criteria. This includes the variation of distance of the closest approach from primary along the longitudinal and transverse directions, variation in the number of TPC crossed rows, variations of χ^2 per cluster value obtained from fitting of TPC and ITS cluster during track reconstruction and variation in the ratio of crossed rows to findable cluster in TPC. In addition, topological track selection criteria have been used for K_S^0 selection. The topological criteria variation includes the cosine angle, proper lifetime, decay radius, distance of closest approach to secondary vertex point in longitudinal and transverse directions, variation in decay radius, mass tolerance, and PID selection for decay products of K_S^0. For the PID systematic uncertainty, the TPC and TOF selection criteria are varied. Three variations are taken where one is a momentum-dependent PID selection of $5\sigma_{TPC}$ ($0 < p < 0.3$), $2.5\sigma_{TPC}$ ($0.3 < p < 0.5$), $1.5\sigma_{TPC}$ ($p > 0.5$) with $3\sigma_{TOF}$, and two momentum-independent selection; $2\sigma_{TPC}$ with $3\sigma_{TOF}$ and $2\sigma_{TPC}$ only. The global tracking uncertainty, due to the uncertainty in ITS-TPC matching, is included in the systematic study. This uncertainty arises due to the ITS-TPC tracking matching efficiency in data and MC. It is calculated as the ratio between tracks matched in TPC to tracks reconstructed in ITS for both data and MC. This tells the matching probabilities of tracks present in ITS and TPC. The systematic uncertainty from material budget arises due to the imperfect description of the material budget. In the ALICE detector setup, the material budget is known with an uncertainty of 7% in terms of radiation length, which is determined on the basis of γ conversion measurements [58]. The systematic uncertainty due to material budget is calculated varying the amount of material by ± 7% in the Monte Carlo simulation. The material budget systematic uncertainties for resonances are estimated using the p_T dependent material budget uncertainty of their decay products. The decay products of resonances interact with detector materials and have hadronic interactions. Therefore, the uncertainties due to material budget and hadronic interactions are estimated

from the corresponding uncertainty contributions of the single charged particles (their decay products) according to the decay kinematics. The systematic uncertainties of the material budget and the hadronic interaction cross section were taken from [19], and single tracking uncertainty was taken from [59]. The summary of systematic uncertainties contribution from different sources for minimum bias (0–100%) is shown in left of Fig. 3.9 for K^{*0} in p–Pb collisions at $\sqrt{s_{NN}}$ = 8.16 TeV and right of Fig. 3.9 for $K^{*\pm}$ at $\sqrt{s_{NN}}$ = 5.02 TeV. The total systematic uncertainties vary from 10–15% for both K^{*0} and $K^{*\pm}$. The systematic uncertainties for various multiplicity classes for K^{*0} have been evaluated (plots are shown in Fig. A.15 of the Appendix). It is found that systematic uncertainty variations are similar for all multiplicity classes. Therefore, the systematic uncertainty of minimum bias is used for all multiplicity classes.
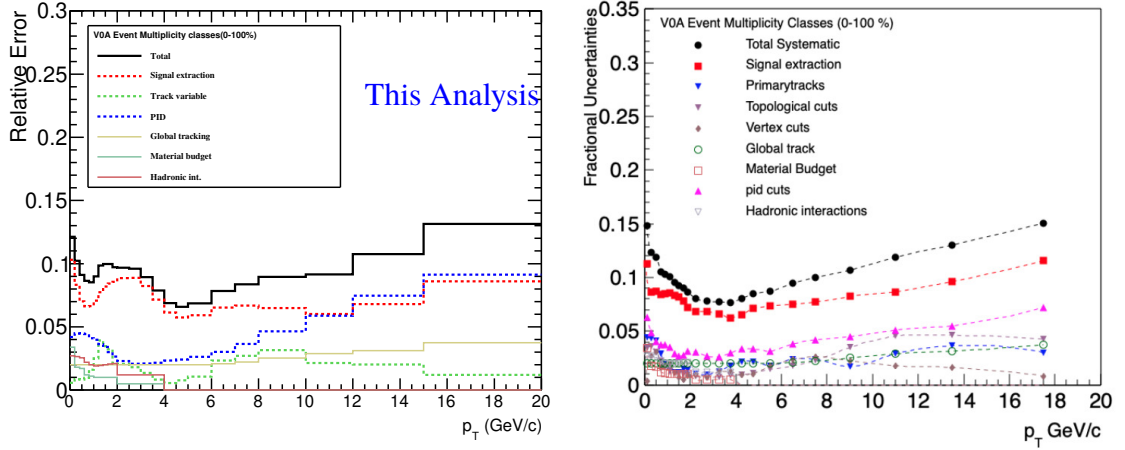
FIGURE 3.9: Left figure:summary of relative uncertainties from different source of systematics for K^{*0} in 0–100% multiplicity class in p–Pb collisions at $\sqrt{s_{NN}}$ = 8.16 TeV. Right figure : summary of fractional uncertainties from different source of systematic uncertainties for $K^{*\pm}$ in in p–Pb collisions at $\sqrt{s_{NN}}$ = 5.02 TeV.

3.5.1 Multiplicity uncorrelated systematic uncertainties

We have estimated multiplicity uncorrelated systematic uncertainties because systematic uncertainties across different multiplicity are correlated. The aim is to separate the uncorrelated part of uncertainty from total uncertainty. The idea is to compare the spectra for each source of systematic in each multiplicity class and look for its variation with respect to minimum bias. Suppose the variation in particular systematic selection criteria between any multiplicity class and minimum bias, the shift in the measurement is in a particular direction, and it observes the same amount of shit in all multiplicity classes. In that case, there is a correlation between the systematic error. If the points fluctuate about the default value, then the error is uncorrelated over the multiplicity classes. The uncorrelated systematic uncertainties are estimated by using "R" method. It is calculated as

$$R = 1 - \frac{\frac{Y^{variation}_{multiplicity\ class,i}}{Y^{default}_{multiplicity\ class,i}}}{\frac{Y^{variation}_{minimumbias}}{Y^{default}_{minimumbias}}} \tag{3.14}$$

Where Y stands for yield of K^{*0} and "i" represents the different multiplicity classes. The measurements with default selection and source of systematic variation is denoted as "default" and i "variation", respectively. Similar procedure was used in previously for K^{*0} measurements in p–Pb collisions at $\sqrt{s_{NN}}$ = 5.02 TeV [19]. The uncorrelated systematic uncertainty due to various multiplicity classes is shown in Fig. 3.10.
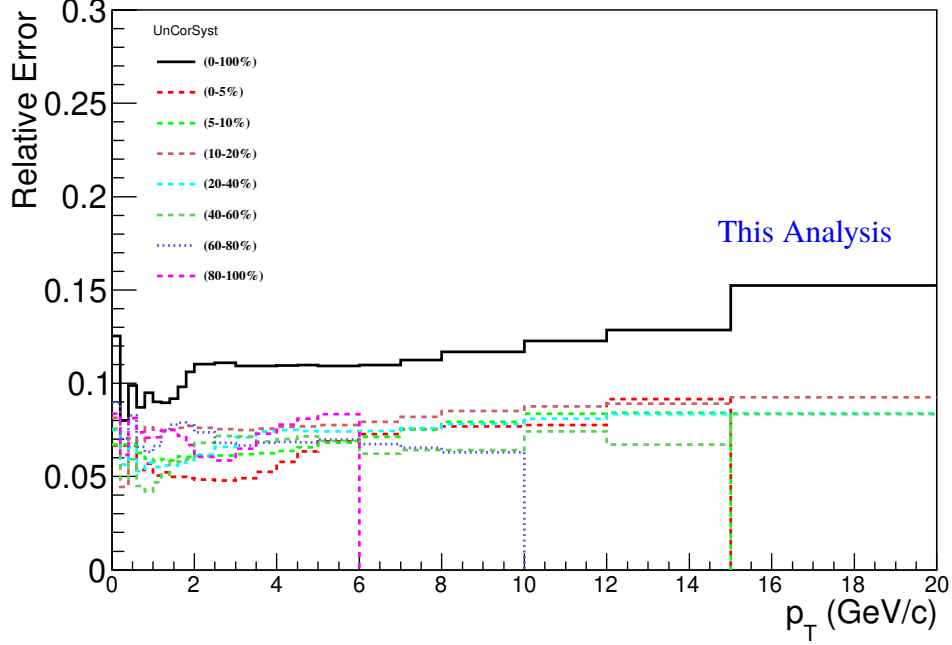
FIGURE 3.10: Summary of uncorrelated systematic uncertainties for various multiplicity classes is shown different color lines in p–Pb collisions at $\sqrt{s_{NN}}$ = 8.16 TeV.

The source of signal extraction and PID are considered for calculating uncorrelated systematic uncertainties across multiplicity classes. These two sources are expected to be uncorrelated in multiplicity and p_T bins. The track variables, global tracking efficiency, material budget, and the hadronic interactions are correlated for minimum bias and multiplicity classes. These sources have not considered for calculating the multiplicity uncorrelated systematic uncertainties.

3.6 Results

3.6.1 Transverse momentum spectra

The measurement of K^{*0} production has been performed in the rapidity interval $-0.5 < y < 0$ up to p_T = 20 GeV/c in p–Pb collisions at $\sqrt{s_{NN}}$ = 8.16 TeV. Figure 3.11 (left) shows

the p_T spectrum of K^{*0} for minimum bias non-single diffractive (NSD) events. Measured p_T spectrum is compared with the predictions from EPOS-LHC [52, 60, 61], DPMJET [51] and HIJING [62] models. Among the model predictions, EPOS-LHC model gives a good description in the measured p_T spectrum comparison to other models DPMJET and HIJING. The EPOS Monte Carlo event generator is a hadronic interaction parton model based on Gribov's Reggeon field theory formalism, which includes the feature of collective hadronization and the core-corona mechanism from pp to A–A collisions [61]. DPMJET is a QCD-inspired dual parton model based on the Gribov-Glauber approach that treats the soft and hard scattering interaction processes differently. HIJING combines the perturbative QCD process with soft excitation, the production of multiple minijets, the interactions of jets in dense hadronic matter, and nuclear shadowing of parton distribution functions.
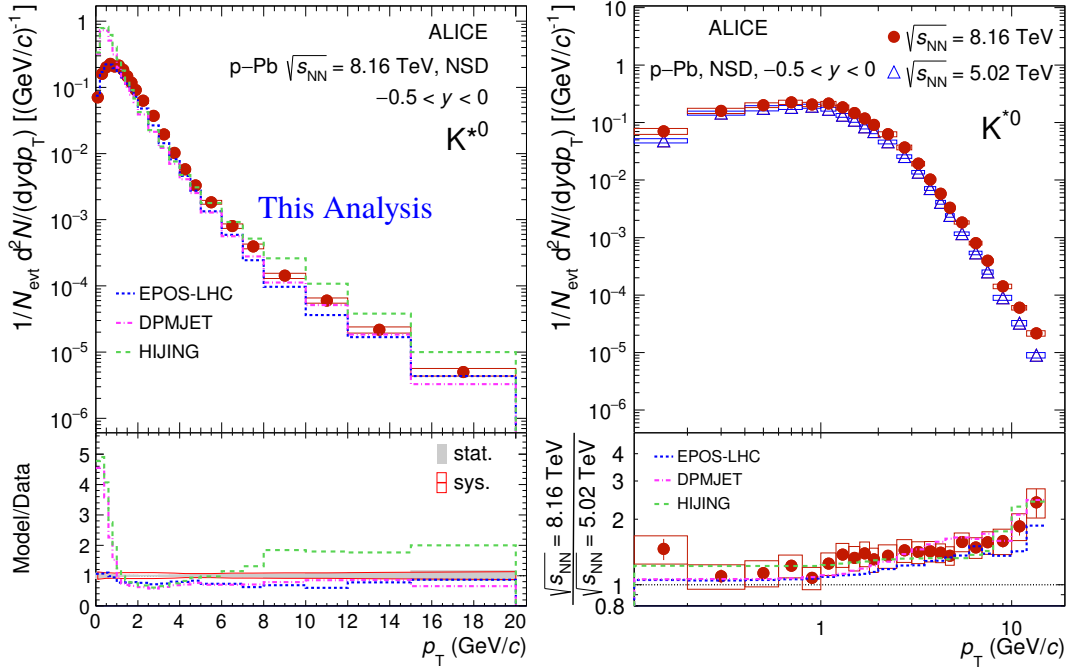
FIGURE 3.11: Left figure: Upper panel shows p_T spectrum of K^{*0} for the NSD events, measured in the rapidity interval $-0.5 < y < 0$ in p–Pb collisions at $\sqrt{s_{NN}}$ = 8.16 TeV. Lower panel shows the ratios of p_T spectra from model to data. The shaded bands around unity describe the statistical and systematic uncertainties of the data point. Right figure: upper panel shows the comparison of energy dependence p_T spectra of K^{*0} as a function of p_T for the NSD events in the p–Pb collisions at $\sqrt{s_{NN}}$ = 5.02 and 8.16 TeV. Lower panels: the ratio of p_T spectrum at $\sqrt{s_{NN}}$ = 8.16 TeV to the p_T spectrum at $\sqrt{s_{NN}}$ = 5.02 TeV. The NSD p_T spectrum and energy dependence p_T spectra are compared with the predictions from EPOS-LHC [52], DPMJET [51] and HIJING [62]. The statistical and systematic uncertainties are shown as bars and boxes, respectively. This figure is taken from [54].

Energy ($\sqrt{s_{NN}}$) evolution of the transverse momentum spectra of K^{*0} for NSD events in p–Pb collisions is shown in the right panel of Fig. 3.11. The upper panel of the right Fig. 3.11 shows the comparison of the p_T spectra of K^{*0} at $\sqrt{s_{NN}}$ = 5.02 and 8.16 TeV. The lower panel shows the ratio of the p_T-differential spectra at $\sqrt{s_{NN}}$ = 8.16 to 5.02 TeV and their model comparisons results obtained from [52, 51, 62]. The uncertainties of the ratios are obtained as the sum in quadrature of the uncertainties of the spectra at the two energies,

which are largely uncorrelated. Up to p_T =1 GeV/c, the ratio seems to be independent of p_T, and consistent with unity within uncertainties.

It suggests that the particle production in the soft scattering region is not strongly dependent on collision energy. For $p_T \gtrsim 1$ GeV/c, the p_T-differential yield ratio increases as a function of p_T and collision energy. This indicates that hard-scattering contributions on production of K^{*0} increase with p_T and collision energy. Similar behavior is also observed for resonances (K^{*0}, ϕ) in pp collisions as discussed in Ref. [63]. The energy dependence p_T differential yield ratios obtained from EPOS-LHC, DPMJET, and HIJING are found to reproduce well and consistent with the measurements within the systematic uncertainties for p–Pb collisions. Figure 3.12 shows comparison of K^{*0} and $K^{*\pm}$ in p–Pb collisions for minimum bias NSD events at $\sqrt{s_{NN}}$ = 5.02 TeV. It is observed that both spectra are consistent with unity within uncertainties, suggesting that the production of K^{*0} and $K^{*\pm}$ are similar, irrespective of quark content and different decay channels. The model predictions from EPOS-LHC better describe the p_T spectrum than HIJING. Figure 3.13 shows the transverse momentum distributions of K^{*0} (left) and $K^{*\pm}$ (right) in various multiplicity classes for p–Pb collisions. The ratios of p_T spectra in various multiplicity classes to the p_T spectrum for NSD events is shown in the bottom panels of Fig. 3.13. The shape of the p_T spectra changes, and slopes increase from low to high multiplicity classes for p_T < 4 GeV/c, whereas the spectral shapes are similar at high p_T for all multiplicity classes. This indicates that processes like radial flow, which lead to a change in the shape of the p_T spectra for various multiplicity classes, dominate mainly at low p_T. A similar behavior was also observed for K^{*0} and other light flavor hadrons in pp and p–Pb collisions at LHC energies [8, 9, 19, 18].
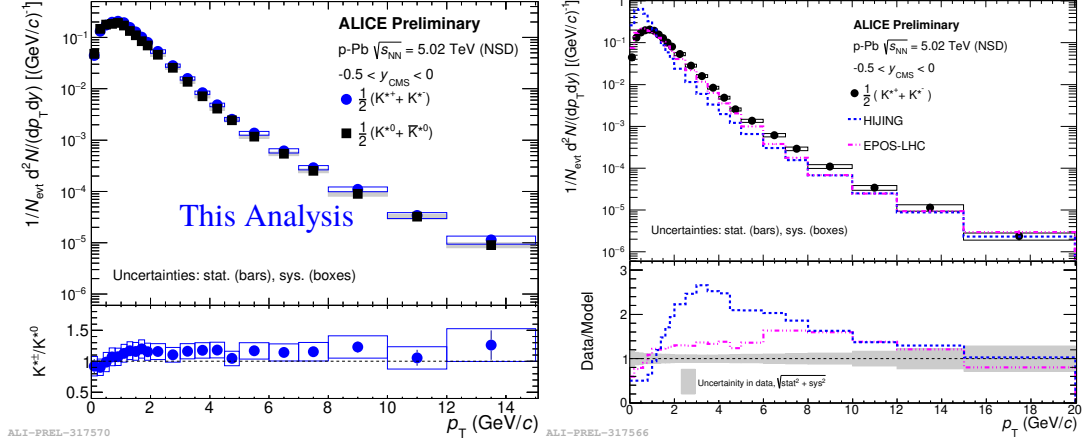
FIGURE 3.12: Left figure: Upper panel shows comparison on p_T spectrum of K^{*0} and $K^{*\pm}$ in p–Pb collisions at $\sqrt{s_{NN}}$ = 5.02 TeV. The lower panel shows the ratio of p_T spectrum of $K^{*\pm}$ to K^{*0} at the same collision energy. Right figure : Upper panel shows comparison on p_T of $K^{*\pm}$ in p–Pb collisions at $\sqrt{s_{NN}}$ = 5.02 TeV and its model predictions from EPOS-LHC [52], and HIJING [62] shown in dotted lines. Lower panels show data to model ratios of p_T spectrum of $K^{*\pm}$ in p–Pb collisions at $\sqrt{s_{NN}}$ = 5.02 TeV. This figure is taken from [55].

3.6.2 Integrated particle yield and mean transverse momentum

The p_T-integrated yields (dN/dy) are obtained by integrating the spectrum in the measured range and extrapolating to zero p_T and to higher p_T with the fitted Lévy-Tsallis function.

$$\frac{1}{N_{evt}}\frac{d^2N}{dydp_T} = p_T\frac{dN}{dy}\frac{(n-1)(n-2)}{nT[nT + m(n-2)]}(1 + \frac{\sqrt{m^2 + p_T^2} - m}{nT})^{-n} \qquad (3.15)$$

where n is the exponent parameter, inverse slope parameter T, and m for mass of the particle, respectively. This function describes both the exponential shape of the spectrum at low p_T and the power law at high p_T. The dN/dy is defined as:

$\frac{dN}{dy} = I_{hist} + I_{extrapolated}$, where $I_{hist} = \sum 2\pi p_T f(p_T, y)dp_T$ in the measured range and

$I_{extrapolated} = \int 2\pi f(p_T, y)p_T dp_T$ in the extrapolated region.

Similarly, the mean transverse momentum ($\langle p_T \rangle$) is defined as:

$\langle p_T \rangle = (\sum 2\pi p_T^2 f(p_T, y)dp_T + \int 2\pi p_T^2 f(p_T, y)dp_T)/(I_{hist} + I_{extrapolated})$,
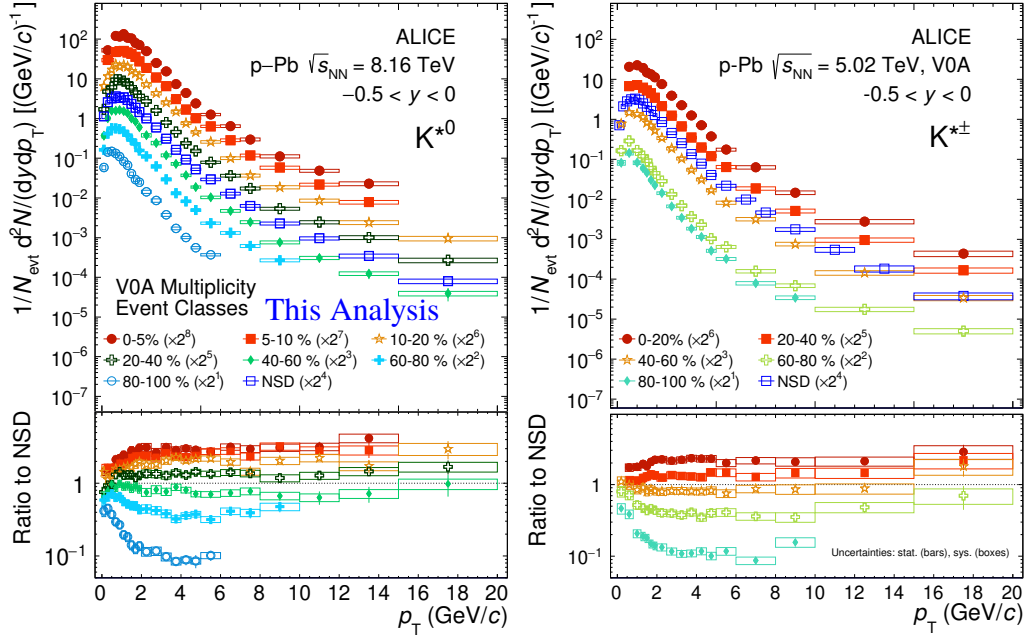
FIGURE 3.13: Top panels: The transverse momentum spectra of K^{*0} at $\sqrt{s_{NN}}$ = 8.16 TeV (left) and K$^{*\pm}$ at $\sqrt{s_{NN}}$ = 5.02 TeV (right) for various multiplicity classes, measured in the rapidity interval $-0.5 < y < 0$ for p–Pb collisions. Bottom panels: The ratios of p_T spectra of given event multiplicity classes to the NSD spectra is shown. The statistical and systematic uncertainties are shown as bars and boxes, respectively.

where $f(p_T, y)$ is the invariant yield.

The measured spectra are fitted with Lévy-Tsallis function [56]. The fit range is from 0 to 20 GeV/c. The final values of dN/dy and $\langle p_T \rangle$ and their statistical uncertainties are calculated from the Lévy-Tsallis fits made on the p_T spectrum including statistical uncertainties only. The systematic uncertainties have two parts: one coming from systematic uncertainties of the spectra and second caused by the extrapolation of the spectra to the unmeasured regions. The first part of the systematic uncertainties are calculated by re-fitting the data while moving the points up and down within the errors assuming that the uncertainties are full uncorrelated in the p_T bins. The maximum difference from the default value is assigned as the uncertainties. The systematic uncertainty due to the second part is not required in

this analysis as the K^{*0} spectra are measured from $p_T = 0$, so low–p_T extrapolation is not needed. The contribution of the extrapolated fraction of the yield is negligible for $p_T > 20$ GeV/c. The values of dN/dy and $\langle p_T \rangle$ of K^{*0} for various multiplicity classes is shown in Fig. 3.14. The dN/dy increases linearly with multiplicity ($\langle dN_{ch}/d\eta \rangle_{|\eta_{lab}|<0.5}$.), whereas $\langle p_T \rangle$ increases and seems to be saturated at higher $\langle dN_{ch}/d\eta \rangle_{|\eta_{lab}|<0.5}$. Figure 3.15 shows
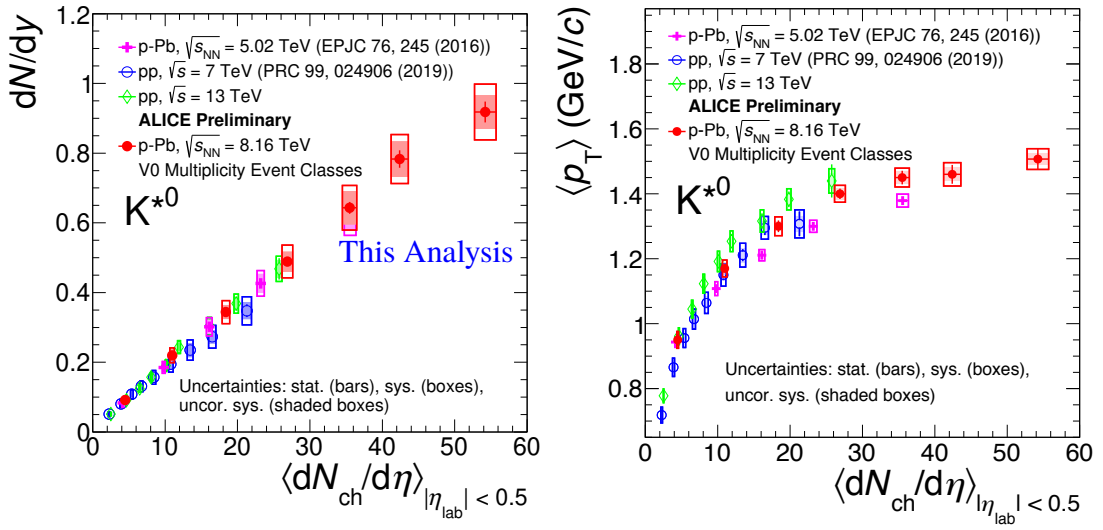
FIGURE 3.14: Comparison of dN/dy (left panel) and $\langle p_T \rangle$ (right panel) as function of average charge particle multiplicity ($\langle dN_{ch}/d\eta \rangle_{|\eta_{lab}|<0.5}$) of K^{*0} in different colliding systems and energies are shown. The red markers represent the results of new measurement in p–Pb collisions at $\sqrt{s_{NN}} = 8.16$ TeV. The uncertainties shown include statistical (bars) and systematic (boxes), uncorrelated systematic (shaded band) uncertainties.

comparison of dN/dy (left) and $\langle p_T \rangle$ (right) for K^{*0} and $K^{*\pm}$ in p–Pb collisions at $\sqrt{s_{NN}} = 5.02$ TeV. Results for both particles are consistent with each other within uncertainties. The multiplicity-scaled integrated yields ($dN/dy/\langle dN_{ch}/d\eta \rangle_{|\eta|<0.5}$) is shown in the upper panels of Fig. 3.16 as a function of $\langle dN_{ch}/d\eta \rangle_{|\eta|<0.5}$ for K^{*0}. These results are compared with other ALICE measurements in pp collisions at $\sqrt{s} = 7$ and 13 TeV [18, 64], in p–Pb collisions at $\sqrt{s_{NN}} = 5.02$ TeV [19], and in Pb–Pb collisions at $\sqrt{s_{NN}} = 2.76$ and 5.02 TeV [8, 9].
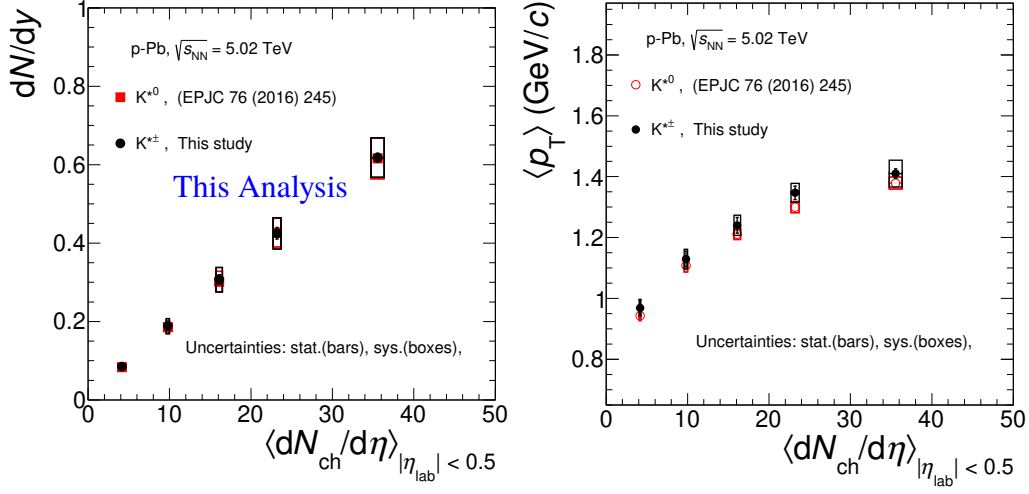
FIGURE 3.15: Comparison of dN/dy (left panel) and $\langle p_T \rangle$ (right panel) as function of average charge particle multiplicity ($\langle \mathrm{d}N_{\mathrm{ch}}/\mathrm{d}\eta \rangle_{|\eta_{lab}|<0.5}$) of K^{*0} (red markers) and K$^{*\pm}$ (black markers) at $\sqrt{s_{NN}}$ = 5.02 TeV. The uncertainties shown include statistical (bars) and systematic (boxes) uncertainties.
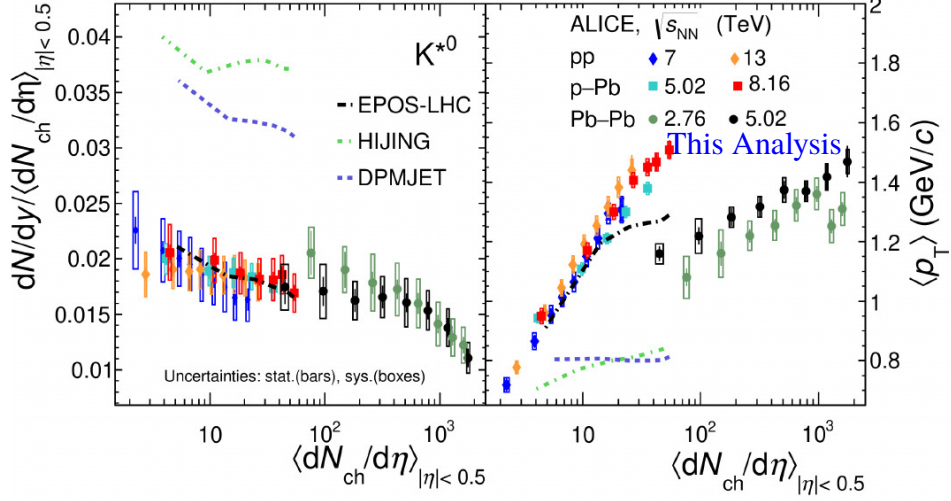
FIGURE 3.16: The multiplicity-scaled integrated yield (dN/dy/$\langle \mathrm{d}N_{\mathrm{ch}}/\mathrm{d}\eta \rangle_{|\eta|<0.5}$) (left panels) and mean transverse momentum ($\langle p_T \rangle$) (right panels) for K^{*0} as a function of $\langle \mathrm{d}N_{\mathrm{ch}}/\mathrm{d}\eta \rangle_{|\eta|<0.5}$ measured in the ALICE central barrel in pp collisions at $\sqrt{s}$ = 7, 13 TeV, in p–Pb collisions at $\sqrt{s_{NN}}$ = 5.02, 8.16 TeV and Pb–Pb collisions at $\sqrt{s_{NN}}$ = 2.76 , 5.02 TeV. Measurements are compared with the predictions from EPOS-LHC [52], DPMJET [51] and HIJING [62] for p–Pb collisions at $\sqrt{s_{NN}}$ = 8.16 TeV. Statistical uncertainties are represented as bars, boxes indicate total systematic uncertainties.

The scaled integrated yields evolve smoothly as a function of multiplicity from pp, p–Pb to Pb–Pb collisions. For similar $\langle dN_{ch}/d\eta \rangle_{|\eta|<0.5}$, these values are consistent within uncertainties for different colliding systems and at various LHC energies. This indicates that event multiplicity drives the resonance production, irrespective of the colliding systems and energies [18, 19, 8, 9]. The scaled integrated yields of K^{*0} show a slight decrease with multiplicity for all three collision systems, and the total decrease is 12% with a 1.8σ significance for p–Pb collisions at $\sqrt{s_{NN}} = 8.16$ TeV. The significance is calculated using statistical and multiplicity uncorrelated systematic uncertainties, added in quadrature. The model comparison with the p–Pb data shows that EPOS-LHC describes the scaled integrated yields, whereas HIJING overestimates the data for all multiplicities.

The $\langle p_T \rangle$ exhibits an increasing trend as a function of $\langle dN_{ch}/d\eta \rangle_{|\eta|<0.5}$ for K^{*0} in various colliding systems and energies as shown in the right panels of Fig 3.16. The increase in $\langle p_T \rangle$ is faster for pp and p–Pb than Pb–Pb and for a common multiplicity coverage, the values of $\langle p_T \rangle$ in pp and p–Pb are larger than Pb–Pb. At similar multiplicity ($\langle dN_{ch}/d\eta \rangle_{|\eta|<0.5} \sim$ 40), the difference in $\langle p_T \rangle$ values among Pb–Pb, p–Pb and pp collisions indicate that the geometry and dynamics of the collision systems are different, while the scaled integrated yields are similar for all colliding systems and energies. This indicates that the high multiplicity event sample in small collision systems has a dominantly large fraction of harder events. Similar studies are reported in Refs. [65], where the moderate increase of $\langle p_T \rangle$ in Pb–Pb collisions was related to collective flow. The strong increase of $\langle p_T \rangle$ with $\langle dN_{ch}/d\eta \rangle_{|\eta|<0.5}$ in small colliding systems. Systematic studies have been carried out in pp and p–Pb collisions for further investigation of $\langle p_T \rangle$ measurement by comparing the results from different models that incorporate processes like color reconnection, between strings produced in multi-parton interactions, different string fragmentation processes and the core-corona mechanism. It was observed in Ref. [18] that the PYTHIA8 [66] model with

color reconnection, which introduces a flow–like effect, and the EPOS-LHC model, which uses parameterized flow, is able to reproduce the increasing trend of $\langle p_T \rangle$ as a function of multiplicity for K^{*0} and ϕ in pp collisions at $\sqrt{s}$ = 13 TeV. The p–Pb measurements are important, as in Ref. [65], it is shown that the $\langle p_T \rangle$ of charged hadrons as a function of multiplicity shows a similar behavior as in pp collisions at low multiplicity whereas it seems to approach a similar but less prominent trend of saturation as in Pb–Pb collisions at high multiplicity. The model comparison with p–Pb data shows that EPOS-LHC describes the increasing trend of $\langle p_T \rangle$ with multiplicity. DPMJET and HIJING models fail to describe the observed trend in $\langle p_T \rangle$ and underpredict the data for all multiplicities.

3.6.3 Particle ratios

Figure 3.17 shows K^{*0}/K and ϕ/K as a function of $\langle dN_{ch}/d\eta \rangle^{1/3}_{|\eta|<0.5}$ for pp, p–Pb and Pb–Pb collisions and different collision energies measured by the ALICE. The $\langle dN_{ch}/d\eta \rangle^{1/3}_{|\eta|<0.5}$ is used as a proxy for the system size of the produced particles [9]. A smooth evolution of these ratios is seen as a function of multiplicity from pp to central Pb–Pb collisions. The K^{*0}/K ratio decreases with increasing $\langle dN_{ch}/d\eta \rangle^{1/3}$ is observed from pp to central Pb–Pb collisions. The decreasing of K^{*0}/K ratios with multiplicity can be understood as the decay products of K^{*0} undergo rescattering effects inside the hadronic phase. The EPOS model incorporates hadronic phase effect describes the measurements, whereas the thermal model predictions for central Pb–Pb collisions overestimate the measurement. This suggests that the rescattering effect dominates over regeneration in the hadronic phase.

Recently, high multiplicity pp [18] and p–Pb collisions in Fig. 3.17 show decreasing trend of K^{*0}/K ratios as a function of $\langle dN_{ch}/d\eta \rangle^{1/3}_{|\eta|<0.5}$. This indicates possible finite hadronic phase in high multiplicity small colliding systems. In other hand, ϕ/K ratios are nearly constant as a function of $\langle dN_{ch}/d\eta \rangle^{1/3}_{|\eta|<0.5}$ across all colliding systems and energies.
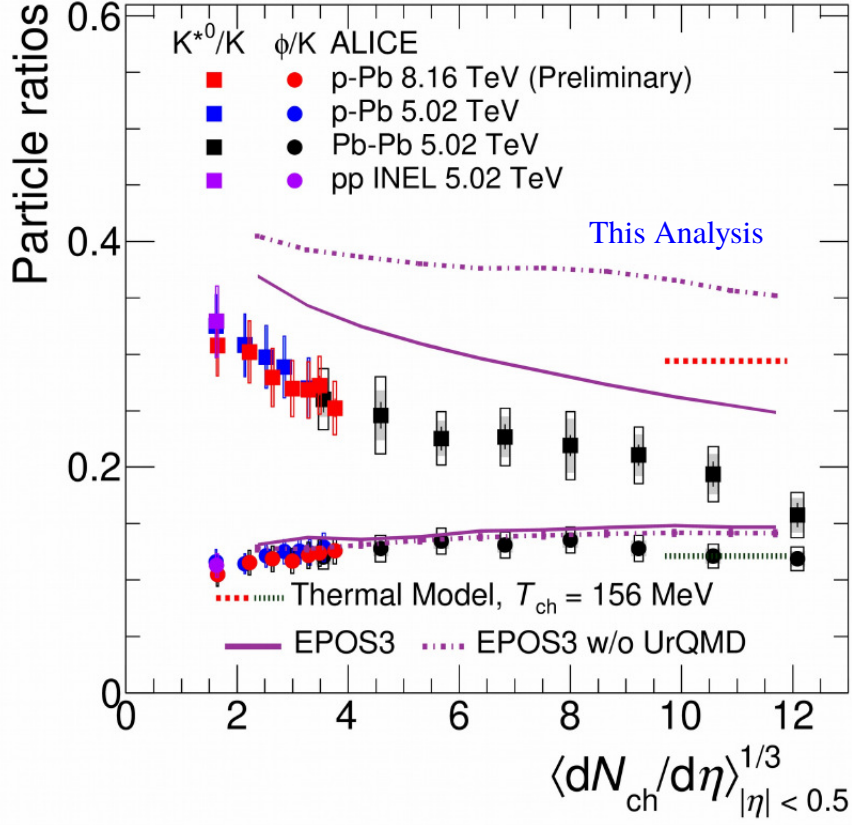
FIGURE 3.17: p_T-integrated yield ratios of resonances to their ground state particles (K*0/K, ϕ/K) as a function of $\langle dN_{ch}/d\eta \rangle^{1/3}$ in pp [9], p–Pb [19, 54] and Pb–Pb [9] collisions. Results from EPOS with UrQMD (solid line) and without UrQMD (dotted line) are shown for Pb–Pb at $\sqrt{s_{NN}}$ = 5.02 TeV. Thermal model predictions for central collisions are shown in dotted red and black lines, respectively. The kaon yield in p–Pb collisions at $\sqrt{s_{NN}}$=8.16 TeV is taken from [67].

The ϕ mesons yield is not affected inside the hadronic phase because its lifetime is 10 times higher than K*0. Results from EPOS with and without UrQMD and the central thermal model describe describe the ϕ/K ratios fairly well.

3.6.4 x_T **scaling**

Particle invariant production cross sections are known to follow a scaling behavior at high p_T of the transverse momentum spectrum for different collision energies. The scaling variable is $x_T = 2p_T / \sqrt{s_{NN}}$ [28, 29]. The invariant cross sections are calculated from the measured invariant yield as

$$E\mathrm{d}^3\sigma/\mathrm{d}p^3 = \sigma_{\mathrm{inel}} \times E\mathrm{d}^3N/\mathrm{d}p^3, \tag{3.16}$$

where $\sigma_{\mathrm{inel}} = (67.6 \pm 0.6)$ mb and (72.5 ± 0.5) mb [68] are the inelastic cross section at $\sqrt{s_{NN}} = 5.02$ and 8.16 TeV, respectively. At fixed x_T, the invariant cross section $E\mathrm{d}^3\sigma/\mathrm{d}p^3$ scales as p_T^{-n}, where the exponent of scaling n depends on x_T and $\sqrt{s_{NN}}$, and is calculated using the following equation

$$n(x_T, \sqrt{s_{NN1}}, \sqrt{s_{NN2}}) = \frac{ln(\sigma^{\mathrm{inv}}(x_T, \sqrt{s_{NN2}})/\sigma^{\mathrm{inv}}(x_T, \sqrt{s_{NN1}}))}{ln(\sqrt{s_{NN1}}/\sqrt{s_{NN2}})}, \tag{3.17}$$

Figure 3.18 shows the distributions of n as a function of x_T (left) for K^{*0} in p–Pb collisions at LHC energies. The n value increases with x_T at low x_T or p_T, where soft processes dominate the particle production. The n values seem to saturate at high x_T. The n values are obtained by fitting the n distribution with a constant function in the x_T range $1.3 \times 10^{-3} < x_T < 4 \times 10^{-3}$. The x_T spectra of K^{*0} are scaled by the corresponding $(\sqrt{s_{NN}}/\mathrm{GeV})^n$. The best scaling is obtained in the quoted fitting range with an exponent of $n = 4.94 \pm 0.10$ (sys.). The systematic uncertainties on the exponent n are calculated by changing the fit range in $n(x_T, \sqrt{s_{NN}})$ vs. x_T distribution. The maximum deviation of n value with respect to the default, is taken as a systematic uncertainty.
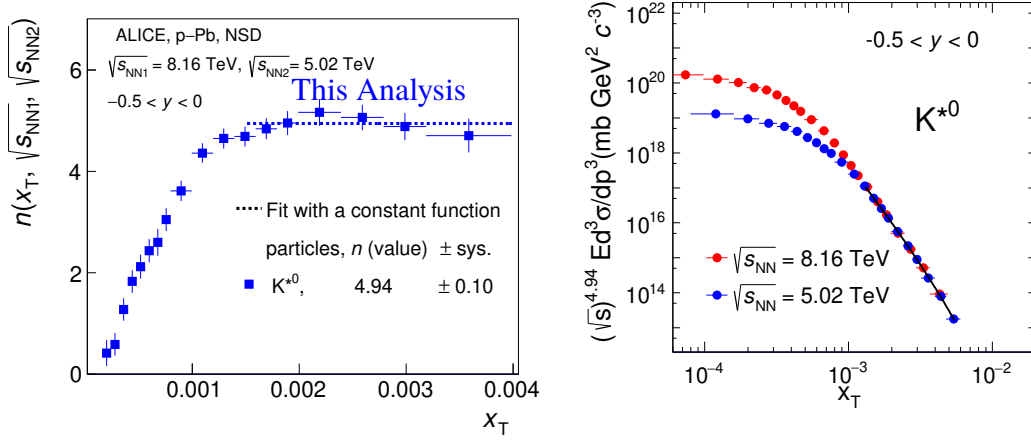
FIGURE 3.18: Left figurre: n as a function of x_T for K^{*0} in p–Pb collisions using at $\sqrt{s_{NN}}$ = 5.02 and 8.16 TeV. A constant fit function is shown in blue dotted lines. Right figure: Scaled invariant yield of K^{*0} as a function of $x_T = 2p_T/\sqrt{s_{NN}}$ in p–Pb collisions at different energies $\sqrt{s_{NN}}$ = 5.02 and 8.16 TeV. The power-law function of $a \times x_T^b \times (1+x_T)^c$ form is shown in balck solid line.

In this thesis, the validity of empirical x_T scaling is studied for K^{*0} measurements in p–Pb collisions at $\sqrt{s_{NN}}$ = 8.16 TeV and previous published measurement at $\sqrt{s_{NN}}$ = 5.02 TeV [19]. From this measurements, it is found that the K^{*0} yields follow a x_T scaling for $x_T \gtrsim 10^{-3}$ in p–Pb collisions at LHC energies. Similarly, x_T is calculated for ϕ in p–Pb collisions using $\sqrt{s_{NN}}$ = 5.02 and 8.16 TeV. The n value for ϕ is found $\sim$ 5 [54]. The n values for both K^{*0} and ϕ are consistent each other within the uncertainties, which suggests that the high p_T productions follow a common mechanism in p–Pb collisions at LHC energies.

A combined fit to the scaled differential cross sections of K^{*0} is performed with a power-law function of the form $a \times x_T^b \times (1+x_T)^c$ to verify the quality of the scaling behavior is shown in the right of Fig. 3.18. Here, a, b, and c are free parameters. The fitting is done in the region above $x_T \gtrsim 1.3 \times 10^{-3}$ (shown as black curve in Fig. 3.18), where the x_T scaling is observed. The χ^2/ndf value for K^{*0} is 0.16, which confirms the good quality of the fit. In the fitting region, the measurements agree with the combined power law fits

within $\approx 20\%$. The measurements at $\sqrt{s_{\mathrm{NN}}} = 8.16$ TeV are consistent, over the accessible x_{T} range $1.3 \times 10^{-3} < x_{\mathrm{T}} < 3 \times 10^{-3}$, with empirical x_{T} scaling and with measurements from p–Pb collisions at $\sqrt{s_{\mathrm{NN}}} = 5.02$ TeV. Similar studies were performed in pp collisions at LHC energies for identified hadrons ($\pi^{\pm}$, $K^{\pm}$, p ($\bar{\mathrm{p}}$) and K^{*0}) with ALICE [35] and for charged hadrons with CMS [36]. The n values obtained in pp collisions for all hadron species except the proton are comparable to those obtained for resonances (K^{*0} and ϕ) in p–Pb collisions [54]. In Ref. [35], the proton takes a larger value of the exponent n, which was discussed in the context of the decrease of the baryon-to-meson ratio with increasing p_{T} in contrast to the nearly constant behavior of meson-to-meson ratios. The n value obtained at LHC energies is also observed to be lower than at RHIC energies, which suggests an increasing contribution of hard processes at higher center-of-mass energies. This study further helps understand and distinguish the contributions of the soft and hard processes to particle production.

3.6.5 Nuclear modification factor (R_{pPb})

Nuclear modification factor (R_{pPb}) is an important observable that can provide information about parton energy loss in p–Pb collisions. It is calculated as :

$$R_{\mathrm{pPb}}(p_{\mathrm{T}}) = \frac{\mathrm{d}^2 N_{\mathrm{pPb}}/\mathrm{d}p_{\mathrm{T}}\mathrm{d}y}{\langle T_{\mathrm{pPb}}\rangle \mathrm{d}^2 \sigma_{\mathrm{pp}}^{\mathrm{INEL}}/\mathrm{d}p_{\mathrm{T}}\mathrm{d}y}, \tag{3.18}$$

where $\mathrm{d}^2 N_{\mathrm{pPb}}/\mathrm{d}p_{\mathrm{T}}\mathrm{d}y$ is the yield in p–Pb collisions and $\mathrm{d}^2 \sigma_{\mathrm{pp}}^{\mathrm{INEL}}/\mathrm{d}p_{\mathrm{T}}\mathrm{d}y$ is the invariant cross section in inelastic pp collisions. $\langle T_{\mathrm{pPb}}\rangle = \langle N_{\mathrm{coll}}\rangle/\sigma^{\mathrm{INEL}}$ is the average nuclear overlap function, which accounts for the nuclear collision geometry as obtained from a Glauber model [68]. If the nuclear modification factor is unity, no modification in transverse momentum spectra between pp and p–Pb collisions. The yield in nuclear collisions is the same as from an incoherent superposition of nucleon–nucleon collisions. Due to the

absence of K^{*0} measurement in pp collisions at $\sqrt{s}$ = 8.16 TeV, the reference p_T spectrum is obtained from the distributions measured in pp collisions at $\sqrt{s}$ = 8 TeV [63] scaled by the ratio between the p_T spectra at the two energies as obtained from PYTHIA 8.230 [66]. The comparison of p_T spectrum (left) and scale factor (right) are shown in the Fig. 3.19. For the systematic study, the reference pp spectra are also obtained using the measured p_T spectrum at $\sqrt{s}$ = 7 TeV [64]. The total systematic uncertainty of the pp reference spectrum is then calculated as the quadrature sum of the systematic uncertainties of the measured p_T spectrum at $\sqrt{s}$ = 8 TeV and the difference of the reference spectra obtained using the measured p_T spectra at $\sqrt{s}$ = 7 and 8 TeV. The systematic uncertainties of the reference p_T spectra of K^{*0} is 11.5% for the low p_T (< 4 GeV/c) and 15.5% for the high p_T (> 4 GeV/c) [63]. The systematic and statistical uncertainties of R_{pPb} are calculated as the quadrature sum of respective uncertainties of the p_T spectra in p–Pb and pp collisions. The value of the nucleon–nucleon inelastic cross section for the reference spectra at $\sqrt{s}$ = 8.16 TeV is (72.5±0.5) mb, taken from Ref. [68]. Figure 3.20 shows nuclear modification factor of K^{*0} and $K^{*\pm}$ as a function of p_T for $\sqrt{s_{NN}}$ = 5.02 and 8.16 TeV. It is observed that no suppression of the R_{pPb} at high p_T (> 8 GeV/c) for K^{*0} and $K^{*\pm}$, whereas suppression is observed in heavy-ion collisions [8, 9]. The R_{pPb} values are similar for energy, K^{*0}, and $K^{*\pm}$. No energy and species (K^{*0}, $K^{*\pm}$) dependence in R_{pPb} are observed.

The R_{pPb} measurements of K^{*0}, ϕ [19] and multi-strange baryon (Ξ and Ω) [69] in p–Pb collisions at $\sqrt{s_{NN}}$ = 5.02 TeV, and compared with K^{*0} and ϕ at $\sqrt{s_{NN}}$ = 8.16 TeV [54]. Figure 3.21 shows the particle species dependence of the nuclear modification factors in p–Pb collisions at $\sqrt{s_{NN}}$ = 5.02 and 8.16 TeV. Panels (a) and (b) show R_{pPb} of K^{*0} and ϕ at $\sqrt{s_{NN}}$ = 8.16 and 5.02 TeV, respectively. Previous measurements of π and K mesons at $\sqrt{s_{NN}}$ = 5.02 TeV [19] are also shown in panel (b). Panel (c) shows the R_{pPb} of multi-strange baryons (Ξ, Ω) at $\sqrt{s_{NN}}$ = 5.02 TeV [69]. To study the mass dependence of baryons and to
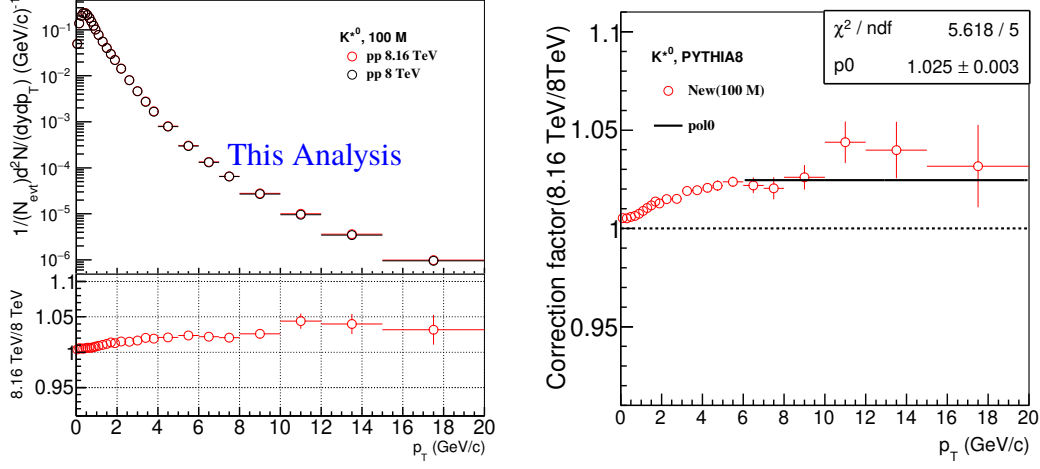
FIGURE 3.19: Left: Upper panel shows comparison of p_T spectra at $\sqrt{s_{NN}}$ = 8 and 8.16 TeV obtained from PYTHIA 8.230 for K^{*0} in pp collisions. Ratio of p_T spectra at 8.16 to 8 TeV is shown in lower panel. Right: Scale factor (ratio of p_T spectra at 8.16 to 8 TeV) as a function of p_T and fitted with a constant function.

compare baryons and mesons, the R_{pPb} of protons taken from [70] and that of ϕ mesons are also shown in panel (c). At low p_T (< 2 GeV/c), the R_{pPb} is less than unity for all hadrons.

The measurements of K^{*0} and ϕ at $\sqrt{s_{NN}}$ = 5.02 and 8.16 TeV are consistent with each other within uncertainties, no flavor dependence in R_{pPb} is observed. At intermediate p_T (2–8 GeV/c), the R_{pPb} of baryons shows a Cronin-like enhancement above unity [71]. The R_{pPb} shows a mass ordering and larger values are observed for the baryons with higher masses. A similar mass ordering for baryons in this p_T region is also reported by CMS in Ref. [72] and the results are consistent with a hydrodynamical expectation of the radial flow [52].

It is also observed that the R_{pPb} of ϕ meson is smaller than that of the proton in spite of their similar masses, which may indicate baryon-meson ordering. Therefore, along with the presence of a strong radial flow component, there are other effects like different production
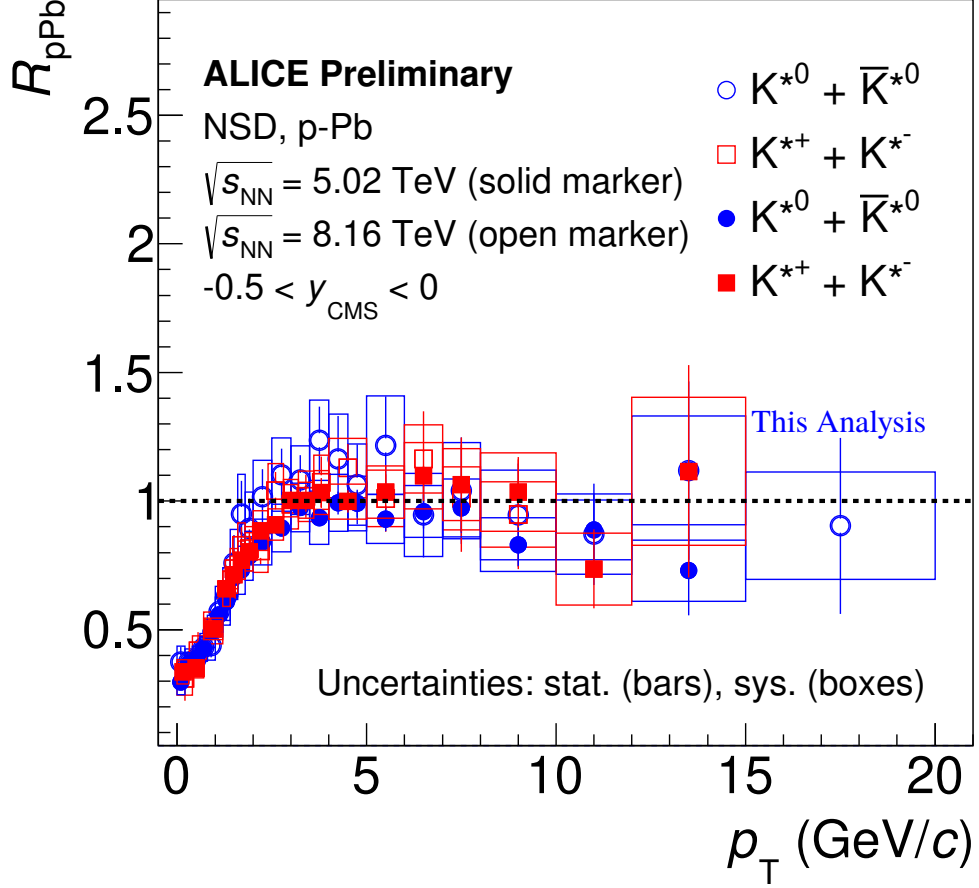
ALI-PREL-317599

FIGURE 3.20: Nuclear modification factor of K^{*0} and $K^{*\pm}$ as a function of p_T in p–Pb collisions at different energies $\sqrt{s_{NN}}$ = 5.02 (solid marker) and 8.16 (open marker) TeV. The statistical and systematic uncertainties are represented by vertical bars and boxes, respectively.

mechanism for baryons and mesons which affect the R_{pPb} in this p_T region. Similar behavior is also observed in Pb–Pb collisions in this p_T region [38, 10]. At high p_T (> 8 *GeV*/c), the R_{pPb} values of all particles are consistent with unity within the uncertainties in p–Pb collisions at $\sqrt{s_{NN}}$ = 5.02 and 8.16 TeV which suggests that there is no modification in R_{pPb} due to cold-nuclear matter effects for different particle species. Similar findings are
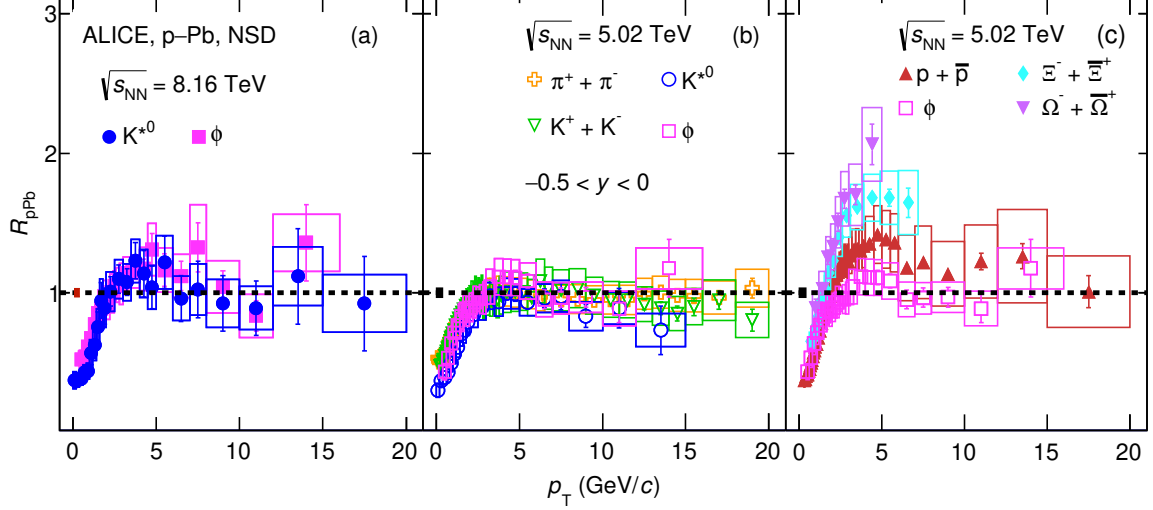
FIGURE 3.21: The nuclear modification factor R_{pPb} as a function of transverse momentum p_T for different particle species in p–Pb collisions at $\sqrt{s_{NN}} = 5.02$ and 8.16 TeV. For comparison the results for π, K, and p [25] are also shown. The statistical and systematic uncertainties are represented by vertical bars and boxes, respectively. The normalization uncertainties are shown in each panel as boxes around $R_{pPb} = 1$ near $p_T = 0$ GeV/c. This figure is taken from [54].

also reported for π^0 meson with p_T up to 200 *GeV*/c in p–Pb collisions at $\sqrt{s_{NN}} = 8.16$ TeV [73], for charged hadrons in p–Pb collisions at $\sqrt{s_{NN}} = 5.02$ TeV by ALICE [70, 37], and for strange hadrons by CMS in p–Pb collisions at p–Pb = 5.02 TeV [72] and by STAR in d–Au collisions at $\sqrt{s_{NN}} = 200$ GeV [74].

3.7 Summary

The production of K^{*0} as a function of p_T has been measured in the rapidity interval $-0.5 < y < 0$ for various multiplicity classes in p–Pb collisions at $\sqrt{s_{NN}} = 8.16$ TeV with the ALICE detector. The evolution of spectral shapes with multiplicity is observed for $p_T < 4$ GeV/c, with a pattern similar to that of Pb–Pb collisions, which can be attributed

to the collective radial expansion of the system. The spectral shapes are similar for all multiplicity classes at high p_T. At low p_T (1 < GeV/c), no collision energy dependence is observed for the p_T-differential ratio, where the soft process dominates the particle production. At high p_T the ratio increases with p_T and collision energy indicating that hard-scattering contribution on particle production increases with p_T and energy. The scaled p_T-integrated yields ($\mathrm{d}N/\mathrm{d}y/\langle \mathrm{d}N_{ch}/\mathrm{d}\eta \rangle_{|\eta|<0.5}$) as a function of multiplicity show a smooth evolution from small systems, pp and p–Pb, to Pb–Pb, and the values are similar for a given multiplicity, irrespective of the colliding systems and energies, suggesting that the hadrochemistry at LHC energies is mainly driven by the event multiplicity. The $\langle p_T \rangle$ values of K^{*0} increase as a function of multiplicity and follow a different trend for p–Pb and pp than Pb–Pb collisions. The EPOS-LHC model which includes parameterized flow gives a good description for NSD p_T distribution, collision energy dependence p_T-differential ratio, the scaled p_T-integrated yields and $\langle p_T \rangle$ values with multiplicity. The K^{*0}/K yield ratio shows a decreasing trend with multiplicity similar to that observed in Pb–Pb collisions. This suggests a possible finite hadronic phase in high multiplicity p–Pb collisions. An empirical x_T scaling holds within roughly 20% in the hard scattering region of the particle production. The obtained value of the exponent ($n \sim 5$) is lower than at RHIC energies which suggests an increasing contribution of hard scattering processes at higher $\sqrt{s_{NN}}$. Furthermore, the value of the exponent n in p–Pb collisions is compatible with those in pp collisions for $\pi^{\pm}$, $K^{\pm}$ and K^{*0} suggesting that the high–p_T particle production mechanism is similar in both colliding systems. No significant energy dependence in R_{pPb} is observed in p–Pb collisions at $\sqrt{s_{NN}}$ = 5.02 and 8.16 TeV. At intermediate p_T (2 < p_T < 8 GeV/c), R_{pPb} values for multi-strange baryon (Ξ and Ω) and the protons in p–Pb collisions at $\sqrt{s_{NN}}$ = 5.02 TeV show a Cronin-like enhancement and the values are found to be significantly larger than those for $\pi^{\pm}$, $K^{\pm}$, K^{*0} and ϕ. The R_{pPb} values are consistent with unity within

the uncertainties for all species at $p_T > 8$ GeV/c, which further confirms the absence of cold–nuclear matter effects in this p_T range.

Bibliography

[1] M. Gyulassy et al., Nucl. Phys. A 399 750, 30-63, (2005).

[2] J. Adams et al., Nucl. Phys. A 757, 102-183, (2005).

[3] J. Schukraft, Phil. Trans. Roy. Soc. Lond. A 370, 917-932, (2012).

[4] P. Braun-Munzinger et al., Phys. Rept. 621, 76âĂŞ126, (2016).

[5] J. Adams et al., [STAR Collaboration], Phys. Rev. C 71, 064902, (2005).

[6] M. M. Aggarwal et al., [STAR Collaboration], Phys. Rev. C 84, 034909, (2011).

[7] B. B. Abelev et al.,[ALICE Collaboration] Phys. Rev. C 91, 024609, (2015).

[8] J. Adam et al., [ALICE Collaboration], Phys. Rev. C 95, 064606, (2017).

[9] S. Acharya et al.,[ALICE Collaboration], Phys. Lett. B 802, 135225, (2020).

[10] S. Acharya et al.,[ALICE Collaboration], Phys. Rev. C 106 3, 034907, (2022).

[11] B. B. Abelev et al., [ALICE Collaboration], Phys. Rev. C 90 5, 054901, (2014).

[12] S. Acharya, et al., [ALICE Collaboration], JHEP. 09, 006, (2018).

[13] S. Chatrchyan et al., [CMS Collaboration], Phys. Lett. B 718, 795-814, (2013).

[14] B.Abelev et al., [ALICE Collaboration], Phys. Rev. C 90 (5), 054901, (2014).

[15] J. Adam et al., [ALICE Collaboration], Phys. Lett. B 758, 389-401, (2016).

[16] B. Abelev et al., [ALICE Collaboration], Phys. Lett. B 728, 25-38, (2014).

[17] S. Acharya et al., [ALICE Collaboration], JHEP 1811, 013, (2018).

[18] S. Acharya et al., [ALICE Collaboration], Phys. Lett. B 807, 135501, (2020).

[19] J. Adam et al., [ALICE Collaboration], Eur. Phys. J. C 76, 245, (2016).

[20] E. Cuautle et al., Eur. Phys. J. C 79, 7, 626, (2019).

[21] S. Chakraborty et al., PoS HardProbes2020, 134, (2021).

[22] C. Bierlich et al., EPJ Web Conf. 171, 14003, (2018).

[23] S. Acharya et al., [ALICE Collaboration], Eur. Phys. J. C 80, 8, 693, (2020).

[24] B. B. Abelev et al.,[ALICE Collaboration], Phys. Lett. B 728, 25-38, (2014).

[25] S. Acharya et al., [ALICE Collaboration], Phys. Rev. C 101, 044907, (2020).

[26] J. C. Collins et al., Adv. Ser. Direct. High Energy Phys. 5, 1-91, (1989).

[27] D. de. Florian et al., Phys. Rev. D 91 1, 014035, (2015).

[28] S. J. Brodsky et al., Phys. Lett. B 637, 58-63, (2006).

[29] F. Arleo et al., Phys. Rev. Lett. 105, 062002, (2010).

[30] F. Abe et al., [CDF Collaboration], Phys. Rev. Lett. 61, 1819, (1988).

[31] D. Acosta et al., [CDF Collaboration], Phys. Rev. D 65, 072005, (2002).

[32] T. Aaltonen et al., [CDF Collaboration], Phys. Rev. D 82, 119903, (2010).

[33] C. Albajar et al., Nucl. Phys. B 335, 261-287, (1990).

[34] J. Adams et al., Phys. Lett. B 637, 161-169, (2006).

[35] S. Acharya et al., [ALICE Collaboration], Eur. Phys. J. C 81 3, 256, (2021).

[36] S. Chatrchyan et al., [CMS Collaboration], JHEP 08, 086, (2011).

[37] S. Acharya et al., [ALICE Collaboration], JHEP 11, 013, (2018).

[38] S. Acharya et al., [ALICE Collaboration], Phys. Rev.C 101 4, 044907, (2020).

[39] S. Acharya et al., [ALICE Collaboration], Phys. Lett. B 828, 137013, (2022).

[40] E. Abbas et al., [ALICE Collaboration], J. Instrum. 8, P10016, (2013).

[41] B. B. Ablev et al., [ALICE Collaboration], Int. J. Mod. Phys. A 29, 1430044, (2014).

[42] K. Aamodt et al., [ALICE Collaboration], JINST 5, P03003, (2010).

[43] J. Alme et al., [ALICE Collaboration], Nucl. Instrum. Meth. A 622, 316-367, (2010).

[44] H. De Vries et al., Atom. Data Nucl. Data Tabl. 36, 495-536, (1987).

[45] M. L. Miller et al., Ann. Rev. Nucl. Part. Sci.,57:205-243, (2007).

[46] S. Acharya et al., [ALICE Collaboration], Eur. Phys. J. C, 79:307, (2019).

[47] A. Akindinov et al., [ALICE Collaboration], Eur. Phys. J. Plus 128, 44, (2013).

[48] W. Blum et al., https://cds.cern.ch/record/1105920, (2008).

[49] M. Bondila et al., IEEE Trans.Nucl.Sci. 52, 1705-1711, (2005).

[50] R.L.ÂăWorkmanÂăetÂăal., Prog. Theor. Exp. Phys. 2022, 083C01, (2022).

[51] S. Roesler et al., ICAMC for Radiation Physics, PTSA, hep-ph/0012252,(2000).

[52] T. Pierog et al., Phys. Rev. C 92 3, 034906, (2015).

[53] T. Ullrich et al., arXiv:physics/0701199, (2007).

[54] S. Acharya et al., [ALICE Collaboration], http://arxiv.org/abs/2110.10042, (2021).

[55] [ALICE Collaboration], https://alice-notes.web.cern.ch/node/926, (2019).

[56] Constantino Tsallis, Statist.Phys. 52, 479-487, (1988).

[57] R. Barlow, hep-ex/0207026, (2002).

[58] K. Aamodt et al., [ALICE Collaboration], Phys. Rev. Lett. 105, 072002, (2010).

[59] S. Acharya et al., [ALICE Collaboration, JHEP 92, (2019).

[60] K. Werner et al., Phys. Rev. C 89 6, 064903, (2014).

[61] K. Werner et al., Phys. Rev. Lett. 98, 152301, (2007).

[62] M. Gyulassy et al., Comput. Phys. Commun. 83, 307, (1994).

[63] S. Acharya et al., [ALICE Collaboration], Phys. Rev. C 102, 024912, (2020).

[64] B. B. Abelev et al., [ALICE Collaboration], Eur. Phys. J. C72, 2183, (2012).

[65] B. B. Abelev et al., [ALICE Collaboration], Phys. Lett. B 727, 371-380, (2013).

[66] P. Skands et al., Eur. Phys. J. C 74, 3024, (2014).

[67] [ALICE Collaboration], https://alice-notes.web.cern.ch/node/769, (2019).

[68] C. Loizides et al., Phys. Rev. C 99 1, 019901, (2019).

[69] J. Adam et al., [ALICE Collaboration], Phys. Lett. B 758, 389-401, (2016).

[70] J. Adam et al., [ALICE Collaboration], Phys. Lett. B 760, 720-735, (2016).

[71] B.Z. Kopeliovich et al., Phys. Rev. Lett. 88, 232303, (2002).

[72] A. M. Sirunyan et al., [CMS Collaboration], Phys. Rev. C 101 no. 6, 064906, (2020).

[73] S. Acharya et al., [ALICE Collaboration], Phys. Lett. B 827, 136943, (2022).

[74] B.I. Abelev et al., [STAR Collaboration], Phys. Rev. C 78, 044906, (2008).

Rapidity dependence of K^{*0} production in p–Pb collisions at $\sqrt{s_{\mathrm{NN}}}$ = 5.02 TeV

4.1 Motivation

The study of particle production in asymmetric collision systems such as proton-nucleus (p–A) and deuteron-nucleus (d–A) plays a vital role as control experiments, where the formation of the QGP is not expected. Measurements in these colliding systems act as a baseline to study the effects of cold nuclear matter (CNM) and disentangle the same from hot dense matter effects produced in heavy-ion collisions [1, 2, 3, 4, 5, 6]. In p–Pb collisions, the produced particle yields are expected to be different in forward (p-going) and backward (Pb-going) rapidities. Nuclear modification of the parton distribution functions (PDFs), parton saturation, multiple scattering, and radial flow effects have shown different behavior in forward and backward rapidities of hadron production [6, 7, 8, 9, 10, 11]. At Large Hadron Collider (LHC) energies, it provides an opportunity to access smaller values of the Bjorken x ($\sim \exp^{y}/\sqrt{s}$) variable, where gluon saturation effects may occur [5, 9].

113

Recent measurements in high-multiplicity pp, p–Pb collisions have shown features of strangeness enhancement, double-ridge structure, non-zero anisotropic flow harmonics, and suppression of K^{*0}/K relative to minimum bias pp collisions [12, 13, 14, 15, 16, 17]. All these observations have been seen in nucleus-nucleus collisions. However, the origin of these phenomena in small systems is not yet fully understood. The study of multiplicity and rapidity dependence yields of hadrons are important to understand the mechanism and the physics processes that contribute to particle production [8]. To probe the above mentioned physics effects experimentally, some observables are discussed here. The asymmetry of particle production is studied by the ratio of particle yields between Pb- and p-going directions, represented by the rapidity asymmetry (Y_{asym}) defined as:

$$Y_{\text{asym}}(p_{\text{T}}) = \frac{\left.\frac{\text{d}^2N}{\text{d}p_{\text{T}}\text{d}y}\right|_{-0.3<y<0}}{\left.\frac{\text{d}^2N}{\text{d}p_{\text{T}}\text{d}y}\right|_{0<y<0.3}} \tag{4.1}$$

where $\text{d}^2N/\text{d}p_{\text{T}}\text{d}y|_{-0.3<y<0}$ is the yield in the rapidity (y) interval $-0.3 < y < 0$, considered as the Pb-going direction, and $\text{d}^2N/\text{d}p_{\text{T}}\text{d}y|_{0<y<0.3}$ is the yield in the rapidity interval $0 < y < 0.3$, considered to be the p-going direction. Experimentally, the Y_{asym} is a good observable because systematic uncertainties cancel out in the ratio and hence it can better discriminate rapidity-dependent effects among models [4, 6].

The variation of nuclear modification factor ($Q_{\text{CP}}(p_{\text{T}})$) between central and non-central collisions with rapidity is defined as

$$Q_{\text{CP}}(p_{\text{T}}) = \left.\frac{\frac{\text{d}^2N}{\text{d}p_{\text{T}}\text{d}y}}{\langle N_{\text{coll}}\rangle}\right|_{\text{HM}} \bigg/ \left.\frac{\frac{\text{d}^2N}{\text{d}p_{\text{T}}\text{d}y}}{\langle N_{\text{coll}}\rangle}\right|_{\text{LM}}, \tag{4.2}$$

where $\langle N_{\text{coll}}\rangle$ is the average number of nucleon–nucleon collisions in low-multiplicity (LM) and high-multiplicity (HM) events, respectively. The $\langle N_{\text{coll}}\rangle$ values are obtained form Monte Carlo Glauber model [18]. In this thesis, we report the first measurements

of the rapidity dependence of K^{*0} production in p–Pb collisions at centre-of-mass energy per nucleon–nucleon collisions, $\sqrt{s_{NN}} = 5.02$ TeV by the ALICE experiment at the LHC. The large size of the data sample and the excellent particle identification (PID) particle identification ability of the ALICE detector provide opportunities to extend these measurements in a wider rapidity interval and multiplicity classes compared to earlier measurements [17, 19, 20]. Multiplicity dependence of K^{*0} production at midrapidity was studied in pp, p–Pb, and Pb–Pb collisions at LHC energies and reported in Refs. [16, 17, 19]. This measurement enables further investigation of the initial state effect due to the nuclear processes and multiplicity effect on the particle production in p–Pb collisions. The measurements are compared with various model predictions like EPOS-LHC [21], EPOS3 with and without UrQMD [22, 23], DPMJET [24], HIJING [25] and PYTHIA8/Angantyr [26]. For the results presented here, $K^{*}(892)^0$ and $\overline{K}^{*}(892)^0$ yields are averaged and denoted by the symbol K^{*0}. The chapter is organized as follows. The data sample, event and track selection criteria, the analysis techniques, the procedure of extraction of the yields are presented in Section 4.2 and 4.3, respectively. The study of the systematic uncertainties are discussed in Section 4.4. In Section 4.5, the results on the p_T spectra, the dN/dy, the $\langle p_T \rangle$, the Y_{asym} and the Q_{CP} in p–Pb collisions at $\sqrt{s_{NN}} = 5.02$ TeV are presented. Finally, the results are summarized in Section 4.6.

4.2 Analysis details

K^{*0} production is measured using data taken during the second LHC run (Run 2) in 2016 for p–Pb collisions at $\sqrt{s_{NN}} = 5.02$ TeV. The number of accepted events analyzed is about 640×10^6. The K^{*0} is reconstructed from its decay products by using invariant-mass method. The used decay channel is $\pi^{\pm} K^{\mp}$ having branching ratios (BR) of 66.6% [17]. The

K^{*0} measurement is studied in the rapidity range -1.2 < y < 0.3 (for five rapidity intervals of width 0.3 unit of rapidity) and three multiplicity classes (0–10%, 10–40 %, 40-100%) along with a multiplicity-integrated sample (0-100%).

4.2.1   Event selection

In p–Pb collision at center-of-mass energy per nucleon-nucleon collisions ($\sqrt{s_{NN}}$) = 5.02 TeV corresponds to the ^{208}Pb beam with energy of 1.58 TeV per nucleon colliding with a proton beam having an energy of 4 TeV in the laboratory frame [17]. The rapidity in the center-of-mass frame is shifted by $\Delta y = -0.465$ to the laboratory frame in the direction of the proton beam. Minimum bias trigger events are analyzed based on the coincidence signals in the pseudorapidity range 2.8 < η < 5.1 (V0A) and –3.7 < η < –1.7 (V0C) [27]. The events are selected for this study, whose reconstructed primary vertex position (v_z) is within ±10 cm from the center of the nominal interaction point along the beam direction (z-axis). A selection criterion is applied to reject pile-up events if multiple collision vertices are found [28].

4.2.2   Track selection and particle identification

The charged tracks with transverse momentum (p_T) > 0.15 GeV/c and having the pseudorapidity in the interval, $|\eta|$ < 0.8 are selected for this analysis. The selected charged tracks should have crossed at least 70 out of 159 horizontal segments along the transverse readout plane of the TPC. The DCA of the primary track to the primary vertex in the DCA_z is required to be less than 2 cm. In the transverse plane (xy), a p_T-dependent selection of DCA_{xy} (p_T) < 0.0105 + 0.035 $p_T^{-1.1}$ cm is applied. The minimum-bias events are further divided into three multiplicity classes according to the total charge deposited in the V0A detector [27]. The yield of K^{*0} is measured in five rapidity regions -1.2 < y < -0.9, -0.9

$< y <$ -0.6, -0.6 $< y <$ -0.3, -0.3 $< y <$ 0 and 0 $< y <$ 0.3 for the multiplicity classes 0–10%, 10–40%, 40–100% and the minimum bias events, 0–100%. The measurements are carried out with the ALICE central barrel detectors, which are utilized for tracking, the PID, and primary vertex reconstruction. It is housed inside a solenoidal magnet with a magnetic field of 0.5 T. The main detectors that are used for the analyses presented here are the ITS [28], the TPC [29], and the TOF [30] detectors. These detectors have full azimuthal coverage and have a common pseudorapidity coverage of $|\eta| < 0.9$. A detailed explanation of the ALICE detector setup and its performance can be found in Chapter 2. The PID procedure is similar to that described in Section 3.2.3 of Chapter 3. The decay daughter pions and kaons are identified by applying selection criteria on the measured $\langle dE/dx \rangle$ in the TPC $n\sigma_{\text{TPC}}$ (details are discussed in Section 3.2.3 of Chapter 3) from the expected $\langle dE/dx \rangle$ values for a given mass hypothesis, where σ_{TPC} is the $\langle dE/dx \rangle$ resolution of the TPC. The momentum-dependent (p) selection of $n\sigma_{\text{TPC}}$ is taken. The values are kept as $6\sigma_{\text{TPC}}$, $3\sigma_{\text{TPC}}$ and $2\sigma_{\text{TPC}}$ for momentum range $p < 0.3$ GeV/c, $0.3 < p < 0.5$ GeV/c and $p > 0.5$ GeV/c, respectively. If the TOF information is available for the tracks, selection criteria of $3\sigma_{\text{TOF}}$ are applied, and combined information of TPC and TOF is used, where the σ_{TOF} is the time-of-flight resolution of the TOF.

4.3 Signal extraction

The K^{*0} signal is obtained from its hadronic decay daughters using the invariant-mass method for various rapidity intervals, multiplicity classes, and p_{T} bins (details are given in Section 3.3 of Chapter 3). The invariant mass distribution of unlike-sign πK pairs from the same event in the transverse momentum range, $2.2 \leq p_{\text{T}} < 3.0$ GeV/c in the rapidity intervals -0.3 $< y <$ 0, and 0 $< y <$ 0.3 for multiplicity class 0–10% is shown (black markers) in left

panel of Fig. 4.1. The combinatorial background of invariant mass distribution of unlike-sign πK pairs are reconstructed using the mixed-event method (details are given in Section 3 of Chapter3). The mixed-event distributions (red markers) are normalized in the invariant mass region $1.1 < M_{\pi K} < 1.15$ GeV/c^2. After subtracting the normalized combinatorial background, K^{*0} signal peak sits on top of a residual background. The invariant mass distribution of πK pairs is fitted with a Breit-Wigner distribution for describing K^{*0} signal, whereas a second-order polynomial function is used for describing the residual background shape as shown in the right panel of Fig. 4.1.

The total fit function is,

$$\frac{Y}{2\pi} \frac{\Gamma}{(M_{\pi K} - M_0)^2 + \frac{\Gamma^2}{4}} + A M_{\pi K}^2 + B M_{\pi K} + C \qquad (4.3)$$

Where M_0 and Γ are PDG mass and width [31] of the K^{*0}. $M_{\pi K}$ is measured mass obtained from the fit function. The signal peak fit is performed in the mass range $0.75 < M_{\pi K} < 1.15$ GeV/c^2. During the fitting, the width parameter (Γ) is fixed to PDG value 47.4 MeV/c^2, whereas the mass (M$_0$) parameter is kept free. The parameter Y is the area under the Breit-Wigner distribution that gives raw yield or number of K^{*0}. The parameters A, B, and C are the co-efficient of second order polynomial function. Figure 4.2 shows the mass peak of πK invariant-mass distributions obtained from the fit as a function of p_T for 0–100% multiplicity class with different rapidity intervals in p–Pb collisions at $\sqrt{s_{NN}} = 5.02$ TeV. It is observed that the mass peak position deviates from the PDG mass at low p_T whereas consistent with the PDG mass at high p_T. The extracted mass as a function of p_T have similar dependence as reported earlier [16, 17, 32]. It is found that extracted mass is independent of both rapidity and multiplicity (Fig. B.1 shows extracted mass as a function of p_T for 0–10% in the Appendix).
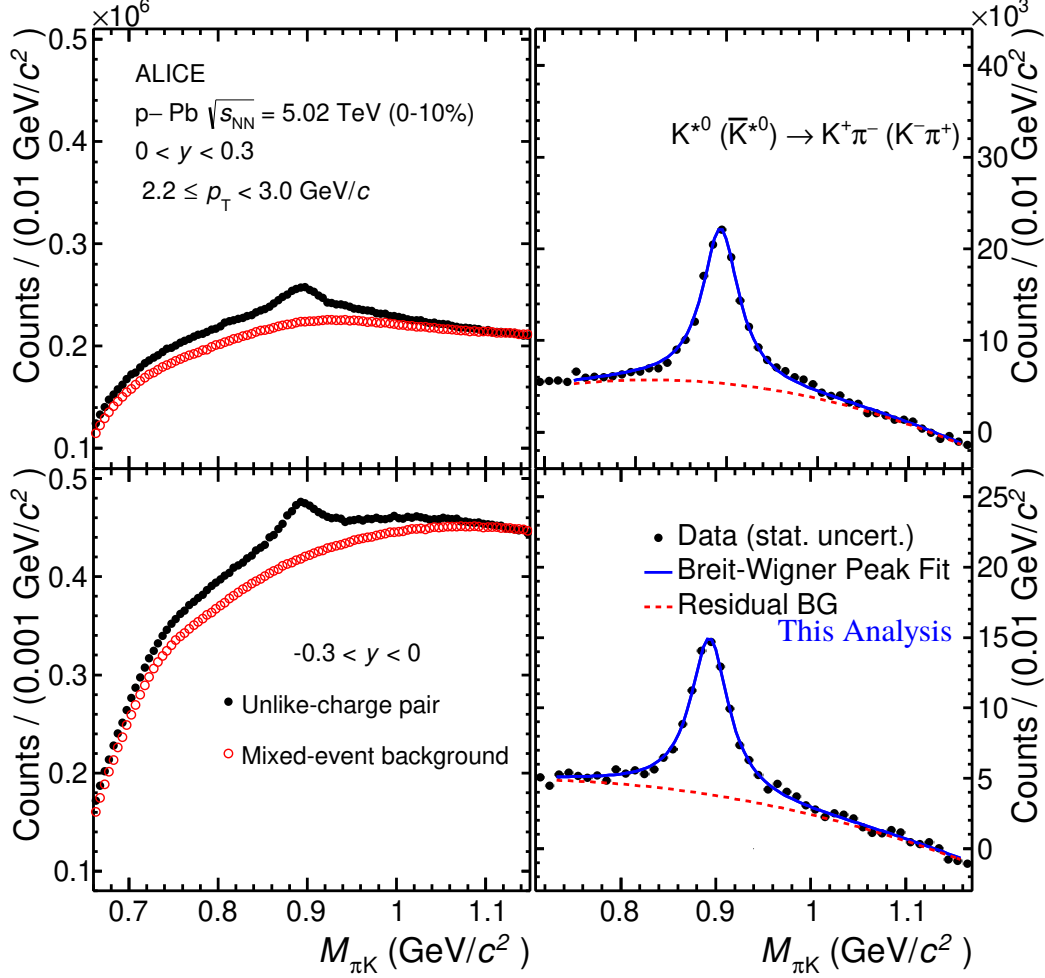
FIGURE 4.1: Left panel: Invariant mass distributions of unlike charged πK pairs from same events (black marker) and normalized mixed-event background (red-marker). Right panel: After subtraction of normalization mixed event background of πK invariant-mass distribution in the multiplicity class 0–10% and transverse momentum range $2.2 \leq p_T < 3.0$ GeV/c in the rapidity interval $0 < y < 0.3$ and $-0.3 < y < 0$. The signal peak is described by a Breit-Wigner function whereas the residual background is described by a polynomial function of order 2.

4.3.1 Raw p_T spectra

The raw p_T spectra for K^{*0} are extracted for five rapidity intervals and four multiplicity classes. The K^{*0} yield is extracted for 8 p_T bins: 0.8-1.5, 1.5-2.2, 2.2- 3.0, 3.0-4.0, 4.0-5.0,
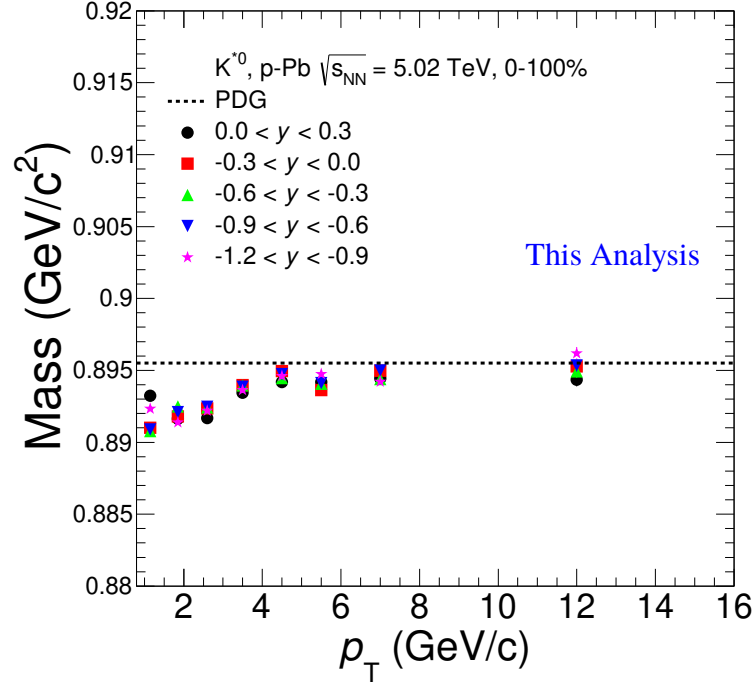
FIGURE 4.2: Extracted mass peak of πK invariant-mass distribution as a function of p_T for p–Pb collisions for 0-100% at $\sqrt{s_{NN}}$= 5.02 TeV. The black dashes line represents the PDG value of K^{*0} mass. The statistical uncertainty is shown only.

5.0-6.0, 6.0-8.0, 8.0-16.0 GeV/c, and in multiplicity classes 0–10%, 10–40%, 40–100% and 0-100%. Details of the yield extraction procedure are described in the Section 3.3 of Chapter 3. The raw p_T distribution of K^{*0} in 0–100% multiplicity class for various rapidity intervals is shown in the upper panel of Fig. 4.3. The lower panel shows the ratio of p_T spectra of various rapidity intervals to the p_T spectrum at $0.0 < y < 0.3$. It is observed that a rapidity dependence of K^{*0} production is seen at low p_T, whereas it is less pronounced at high p_T.
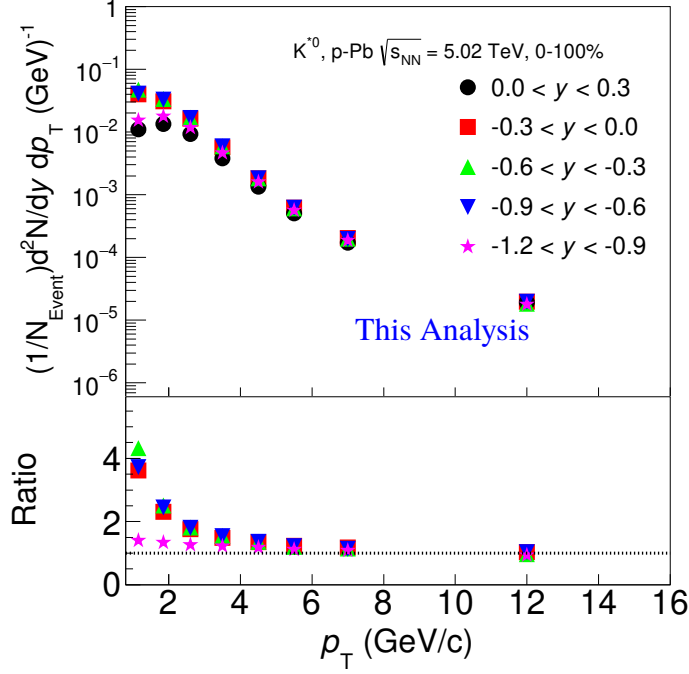
FIGURE 4.3: Upper panel shows raw transverse momentum p_T spectra in various rapidity range for multiplicity class 0-100% in p–Pb collisions at $\sqrt{s_{NN}}$ = 5.02 TeV. Below panel shows the ratio of p_T spectra for various rapidity intervals to p_T spectrum in rapidity $0.0 < y < 0.3$. Statistical uncertainties are shown only.

4.3.2 Acceptance × Efficiency

The $A \times \epsilon_{rec}$ is obtained from the Monte Carlo (MC) simulation based on DPMJET event generator [24] and the transport of the generated particles through the ALICE detector modeled using GEANT3 [33]. The $A \times \epsilon_{rec}$ is the ratio of reconstructed K^{*0} to generated K^{*0}, measured as a function of p_T for the same rapidity interval (details are discussed in Section 3.3.2 of Chapter 3). The track and the PID selection criteria are applied to the decay products of resonances in MC are identical to those used in the data. The shape of generated p_T distribution is different from the measured p_T distributions. Therefore, a re-weighting procedure is used, in which generated distributions are weighted to match the

measured distributions. Details of the procedure of calculation of re-weighted correction are already discussed in Section 3.3.3 of Chapter 3. Acceptance $\times$ Efficiency as a function of p_T in the rapidity ranges -1.2 < y < 0.3 for 0–100% multiplicity class is shown in Fig. 4.4. The lower panel shows the ratio of efficiency $\times$ acceptance for given rapidity intervals to the efficiency $\times$ acceptance in the rapidity 0.0 < y < 0.3. Significance rapidity dependence in efficiency $\times$ acceptance as a function of p_T is observed at low p_T whereas dependence is less pronounced at high p_T. The observed re-weighting factor also varies
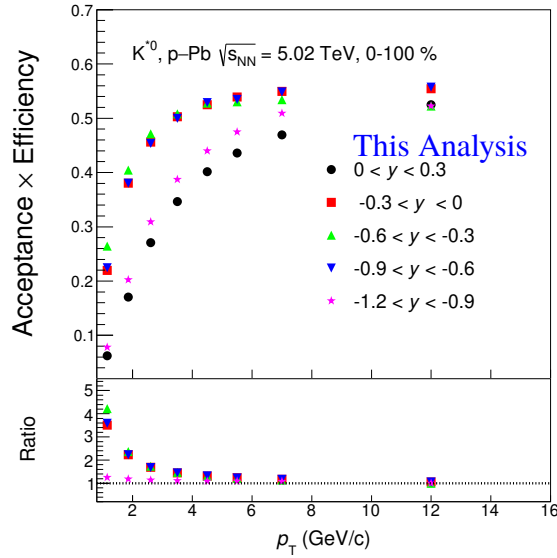
FIGURE 4.4: Upper panel shows acceptance $\times$ efficiency of K^{*0} meson as a function of p_T in the wider rapidity range -1.2 < y_{cms} < 0.3 for multiplicity class 0–100% in p–Pb collisions at $\sqrt{s_{NN}}$ = 5.02 TeV. Different color markers represents $A \times \epsilon_{rec}$ for different rapidity ranges. In lower panel, it is the ratio of $A \times \epsilon_{rec}$ in the various rapidity range to 0.0 < y < 0.3.

with rapidity at low p_T. The re-weighted $A \times \epsilon_{rec}$ is used to correct the raw p_T distribution. The $A \times \epsilon_{rec}$ is calculated for various rapidity intervals and multiplicity classes. The $A \times \epsilon_{rec}$ as a function of p_T shows a rapidity dependence for a given multiplicity class. However, no significant multiplicity dependence of $A \times \epsilon_{rec}$ is observed for a given rapidity interval. The

re-weighted correction factor as a function of p_T for various rapidity windows are shown in Fig. 4.5. The effect of the re-weighting on $A \times \epsilon_{rec}$ varies with p_T and amounts to $\sim 2 - 12\%$ at $p_T < 1.5$ GeV/c. At high p_T, the effect is negligible.
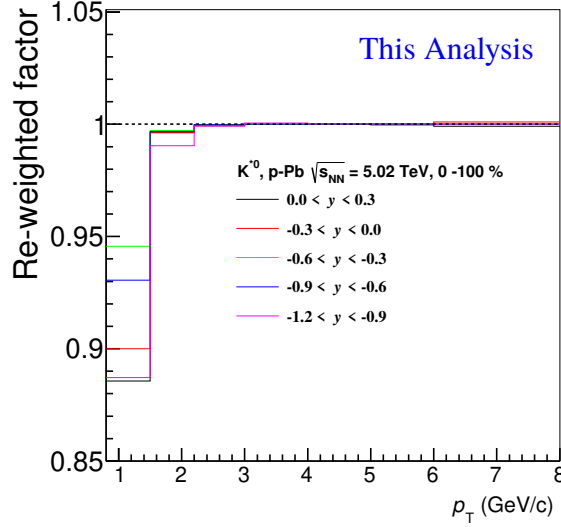
FIGURE 4.5: Figure shows re-weighted correction factors as a function of p_T for K^{*0} in the wider rapidity range -1.2 < y < 0.3 for multiplicity class 0–100% in p–Pb collisions at $\sqrt{s_{NN}}$ = 5.02 TeV. Different color line represents the results for the different rapidity intervals.

It is observed that there is no multiplicity dependence in $A \times \epsilon_{rec}$ as a function of p_T. For the multiplicity dependence studies, the minimum bias $A \times \epsilon_{rec}$ is used for various multiplicity classes to correct the raw transverse momentum spectra for different rapidity intervals.

4.3.3 Corrected p_T spectra

Raw transverse momentum spectra are corrected for $A \times \epsilon_{rec}$, branching ratio, and also with re-weighted correction factor. The corrected p_T spectra of K^{*0} in the multiplicity class 0–100% for various rapidity intervals are shown in Fig. 4.6.
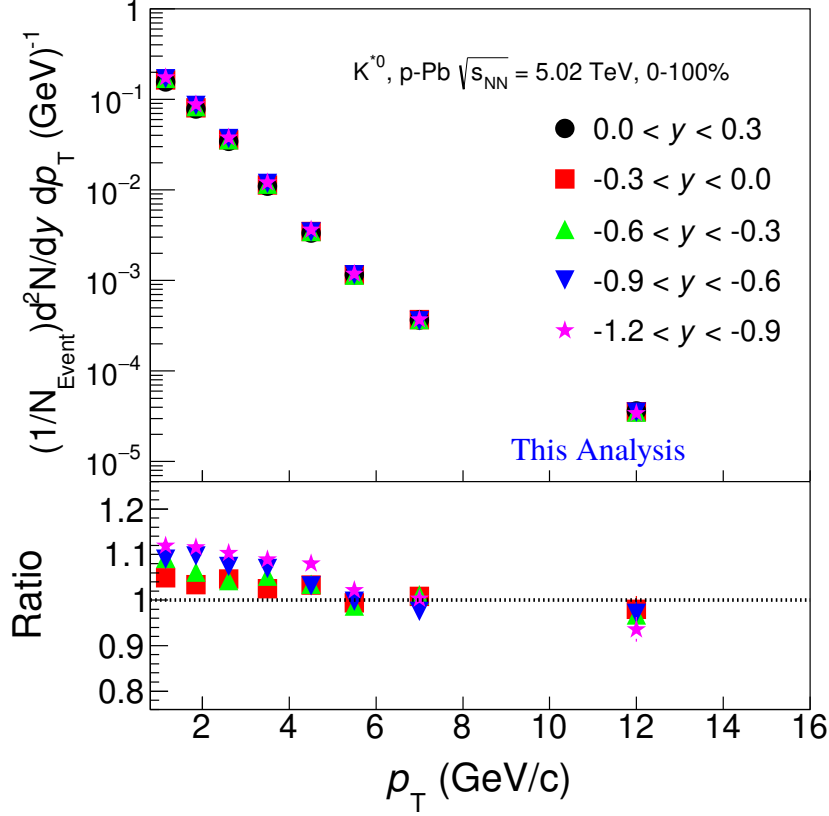
FIGURE 4.6: Top panel: The transverse momentum spectra of K^{*0} for five rapidity intervals within $-1.2 < y < 0.3$ and for multiplicity class 0–100% in p–Pb collisions at $\sqrt{s_{\mathrm{NN}}} = 5.02$ TeV. Bottom panel: The ratios of p_{T} spectra in various rapidity intervals to that in the interval $0 < y < 0.3$ for a given multiplicity class. The statistical and systematic uncertainties are shown as bars and boxes about the data points, respectively.

4.4 Systematic uncertainties

Systematic uncertainties of K^{*0} yields are extracted by varying the different selection criteria relative to the default one. The procedure to estimate the systematic uncertainties is similar as discussed in Section 3.5 of Chapter 3.

4.4.1 Systematic uncertainties on p_T spectra

The sources of systematic uncertainties on measured yields of K^{*0} are signal extraction, track selection criteria, particle identification, global tracking efficiency, uncertainty due to the imperfect description of the material budget of the ALICE detector and the hadronic interaction cross section in the detector material. The uncertainty due to signal extraction is inferred by varying the fitting range, width, mixed-event background, and choice of the residual background function to the default selection criteria. The systematic effects of charged track selection have been studied by varying selection criteria on track variables, it includes the number of crossed rows in the TPC, the ratio of TPC crossed rows to findable clusters, and the distance of the closest approach to the primary vertex of the collisions. For PID systematic uncertainty, two momentum-independent selection criteria, as $2\sigma_{TPC}$ with $3\sigma_{TOF}$ and $2\sigma_{TPC}$ only, are used by varying the TPC dE/dx and flight time measured in TOF for pions and kaons. The uncertainty due to global tracking efficiency, uncertainties in the detector's material budget, and the cross sections for hadronic interactions in the material are taken from [17]. The total systematic uncertainty is the quadratic sum of the contributions for all individual sources. A summary of relative uncertainties as a function p_T for K^{*0} in the rapidity range $0 < y < 0.3$ for multiplicity class 0–100% is shown in Fig. 4.7.

The systematic uncertainties on measured p_T spectra have been studied for different rapidity and multiplicity classes. No significant rapidity and multiplicity dependence effect is observed for the systematic studies. Therefore, the minimum bias relative systematic uncertainties in the rapidity interval $0 < y < 0.3$ is used for all rapidity intervals and multiplicity classes.
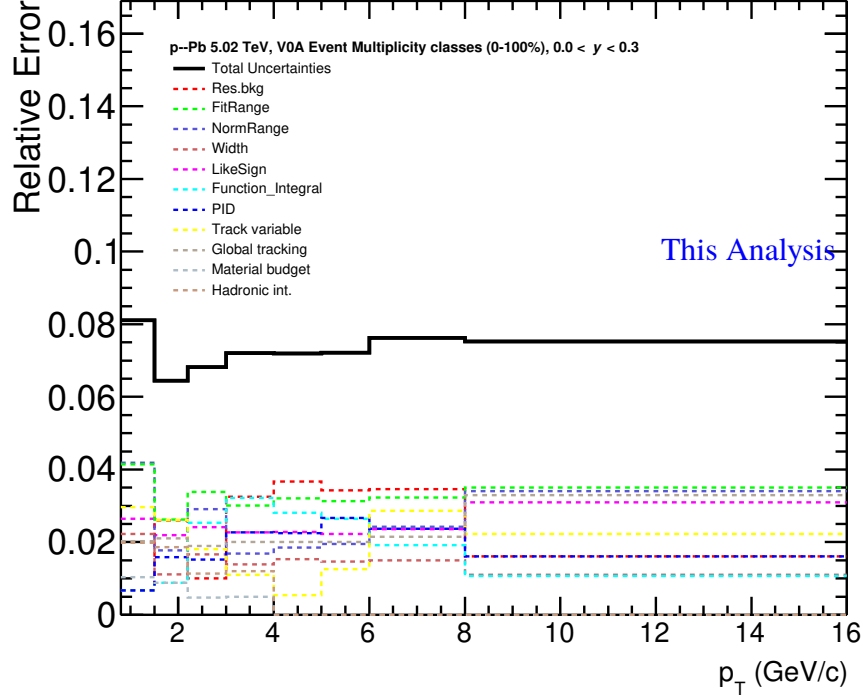
FIGURE 4.7: Summary of relative uncertainties as a function p_{T} for K^{*0} in the rapidity interval $0 < y < 0.3$ in the multiplicity class 0–100% in p–Pb collisions $\sqrt{s_{\mathrm{NN}}}$ = 5.02 TeV. Different color line represents the systematic uncertainties due to different sources.

4.4.2   Systematic uncertainties on Y_{asym} spectra

The systematic uncertainties on Y_{asym} are estimated by varying selection criteria to the default one, as it is a ratio of yields in the rapidity interval $-0.3 < y < 0$ to $0 < y < 0.3$. The same procedure and approach to obtain systematic uncertainity of p_{T} spectra are used for the observable Y_{asym}. For systematic uncertainties on the observable, Y_{asym}, it is found that the contribution from signal extraction and PID are uncorrelated among the different rapidity intervals. In contrast, sources such as track variables, global tracking uncertainties, material budget, and hadronic interactions are correlated among the various rapidity intervals; they would cancel out in the ratio. The variation of different selection criteria of the uncorrelated sources are taken, to estimate systematic contribution on the Y_{asym}. The total systematic

uncertainties on the Y_{asym} is the quadratic sum of the uncertainties due to each source; it is between 2–4% as shown in Fig. 4.8. No multiplicity and rapidity-dependent systematic
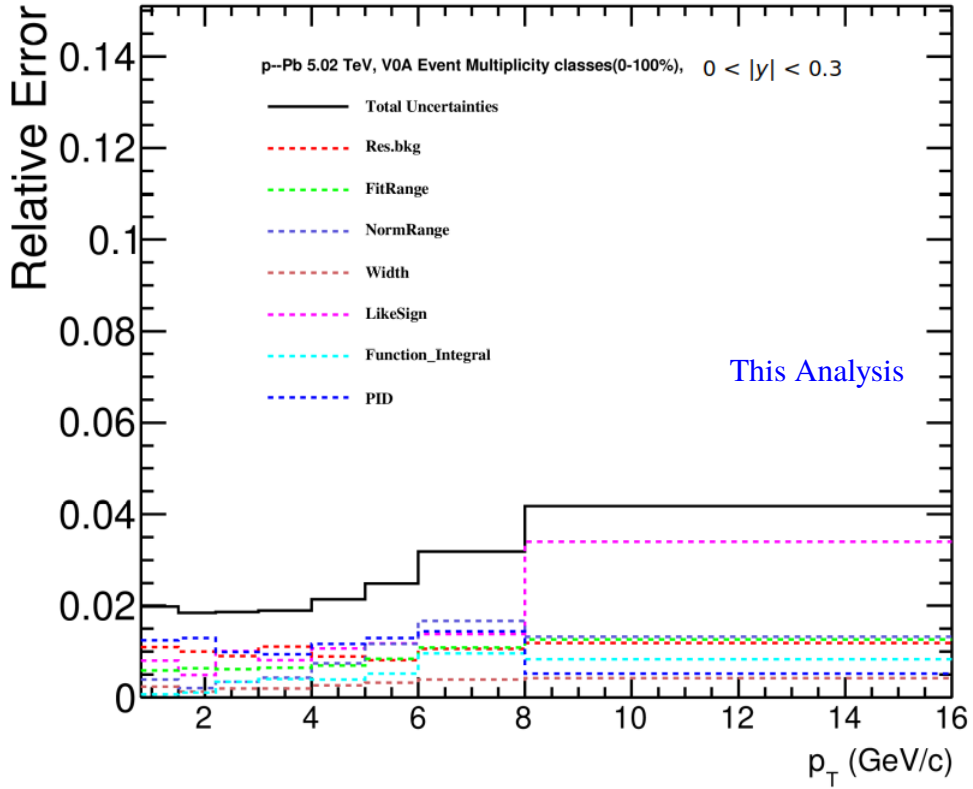
FIGURE 4.8: Summary of relative uncertainties as a function p_{T} in the rapidity interval $0 < |y| < 0.3$ for the multiplicity class 0–100% in p–Pb collisions for K^{*0} at $\sqrt{s_{\text{NN}}} = 5.02$ TeV. Different color line represents the systematic uncertainties due to different sources.

uncertainties in the Y_{asym} are found. Therefore, the relative systematic uncertainty for minimum bias events is assigned to the ratios of various rapidity interval and multiplicity classes.

4.4.3 Systematic uncertainties on ratios $(dN/dy)/(dN/dy)_{y=0}$ and $\langle p_T \rangle / \langle p_T \rangle_{y=0}$

Here, we discuss the procedure and method adopted to calculate the systematic uncertainties in the ratio observables, such as the p_T-integrated yield (dN/dy) and average transverse momentum $(\langle p_T \rangle)$ to the dN/dy and $\langle p_T \rangle$ at $y=0$ as a function of rapidity for a given multiplicity class. As it is ratio of the same quantity in two different rapidity interval, most of systematic uncertainties are canceled out. The sources of correlated systematic uncertainties, such as track variables, particle identification, global tracking efficiency, material budget, and hadronic interaction, are not considered in the systematic studies of these observables. The systematic uncertainties is calculated due to the variation of different sources of signal extraction criteria to the default. The systematic uncertainties on the ratios $(dN/dy)/(dN/dy)_{y=0}$ and $\langle p_T \rangle / \langle p_T \rangle_{y=0}$ as a function of rapidity are calculated in a similar way as for Y_{asym}. Figure 4.9 show the relative uncertainties in ratios of the dN/dy at given rapidity to the dN/dy at $y=0$ (left) and $\langle p_T \rangle$ at given rapidity to $\langle p_T \rangle$ at $y=0$ (right) as a function of rapidity for 0-100% multiplicity class for K^{*0} in p–Pb collisions at $\sqrt{s_{NN}}$ = 5.02 TeV. The systematic uncertainty on $(dN/dy)/(dN/dy)_{y=0}$ and $\langle p_T \rangle / \langle p_T \rangle_{y=0}$ of K^{*0} are 2.2 % and 1.2 %, respectively. It is observed that the relative uncertainties of these ratios as function of rapidity do not show significant rapidity dependent for 0–100% class. No multiplicity dependence is seen in relative uncertainties of these ratios. Therefore, the minimum bias relative uncertainties of these ratios are used for various multiplicity classes.

4.5 Results

4.5.1 Transverse momentum (p_T) spectra

The K^{*0} production has been studied for various rapidity interval and four multiplicity classes in p–Pb collisions at $\sqrt{s_{NN}}$ = 5.02 TeV. Figure 4.10 shows the p_T spectra of K^{*0} for
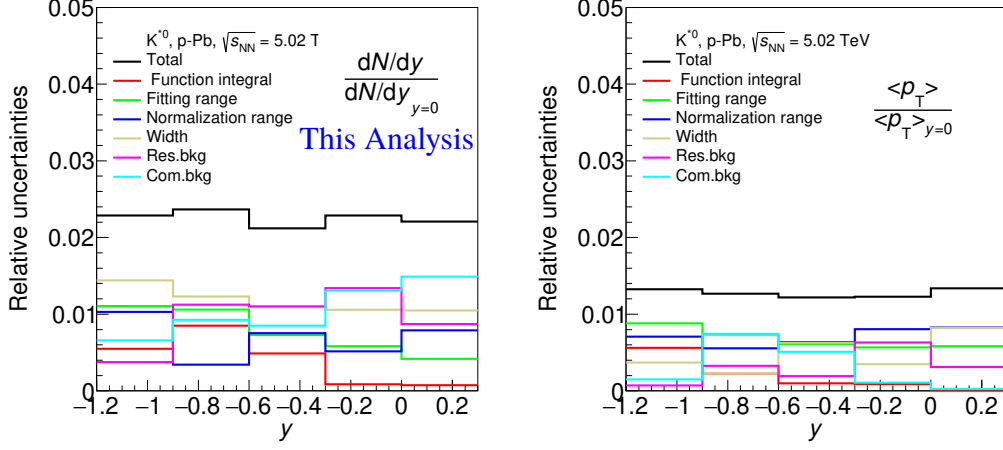
FIGURE 4.9: Left panel plot: relative uncertainties in ratio of dN/dy to dN/dy at y =0, right panel plot: relative uncertainties in ratio of $\langle p_T \rangle$ to $\langle p_T \rangle$ at y =0 of K^{*0} as a function of y for multiplicity class 0-100% in p–Pb collisions at $\sqrt{s_{NN}}$ = 5.02 TeV. Different lines represent relative uncerties of individual sources due to signal extraction. Black line represent total systematic uncertainties due to signal extractions

the five rapidity intervals within -1.2 < y < 0.3 and for two multiplicity classes 0–10% and 40–100%. The ratios of p_T spectra in different rapidity intervals to that in the interval, 0 < y <0.3 is shown in the bottom panels of Fig. 4.10. The measurements of p_T spectra for other multiplicity classes is shown in Fig. B.2 of the Appendix. The measured p_T spectra of K^{*0} shows a rapidity dependence at low p_T (< 5 GeV/c). It suggests that the production of K^{*0} is higher in Pb-going direction (y < 0) than in p-going direction (y > 0). This observation is more pronounced for higher multiplicity classes. For high p_T, no rapidity and multiplicity dependencies are observed.

4.5.2 Integrated particle yield and mean transverse momentum

The integrated yields (dN/dy) and mean transverse momenta ($\langle p_T \rangle$) are calculated from transverse momentum spectra in the measured range and using the fit function in the unmeasured region. The details of the procedure are already discussed in Section 3.6.2
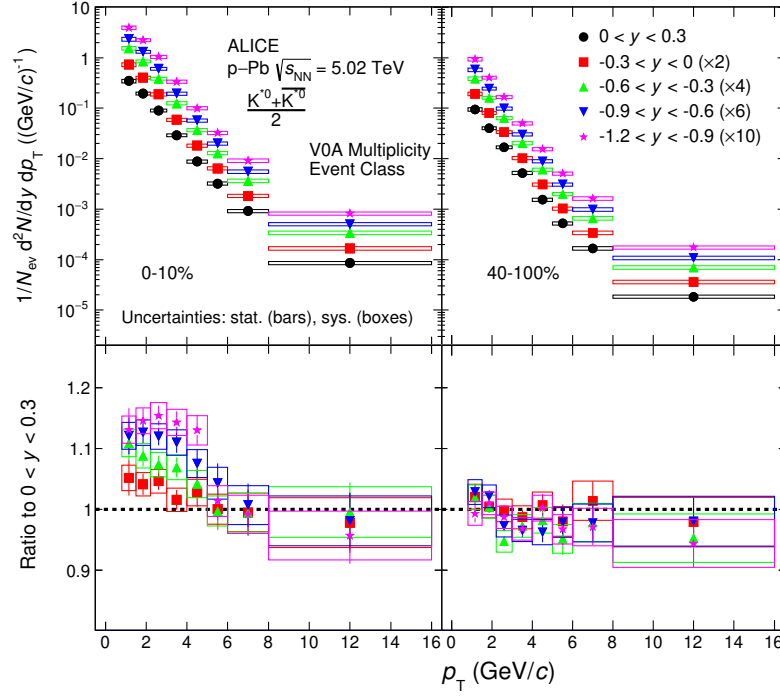
FIGURE 4.10: Top panels: The transverse momentum spectra of K^{*0} in the five rapidity intervals within $-1.2 < y < 0.3$ and for two multiplicity classes (0–10%, 40–100%) in p–Pb collisions at $\sqrt{s_{NN}} = 5.02$ TeV. The data for different rapidity intervals are scaled for better visibility. Bottom panels: The ratios of p_T spectra in various rapidity intervals to that in the interval $0 < y < 0.3$ for a given multiplicity class. The statistical and systematic uncertainties are shown as bars and boxes about the data points, respectively This figure is taken form [34].

of Chapter 3. A Lévy-Tsallis function [35] is used to fit the p_T spectrum. The fitting curve is extrapolated to the unmeasured region for $p_T < 0.8$ GeV/c. The integral of the extrapolated curve gives the contribution at low p_T accounting for 33% (39%) of the total yield in the 0–10% (40–100%) multiplicity class. The extrapolation contribution at low p_T is the same for all the rapidity intervals studied. The contribution of the extrapolated fraction of the yield is negligible for $p_T > 16$ GeV/c. The difference between the yield contribution at low p_T due to different fitting functions (i.e. m_T-exponential, Bose-Einstein and Boltzmann-Gibbs Blast-Wave function [16]) and that due to the default Lévy-Tsallis

function is included in the systematic uncertainties. Figure 4.11 shows the dN/dy (left) and $\langle p_T \rangle$ (right) of K^{*0} as a function of y for minimum bias events in p–Pb collisions at $\sqrt{s_{NN}}$ = 5.02 TeV. The dN/dy decreases slightly from rapidity interval $-1.2 < y < -0.9$ to $0 < y < 0.3$. The $\langle p_T \rangle$ remains constant as a function of rapidity. The model predictions from EPOS-LHC [21], EPOS with and without UrQMD [22, 23], DPMJET [24], HIJING [25], and PYTHIA8 (Angantyr) [26] are shown in the Fig. 4.11. The models show similar behavior as the data except EPOS with and without UrQMD for $\langle p_T \rangle$, which shows a decreasing trend with rapidity. The EPOS3 model incorporates production of hadronic resonances and their interaction in the partonic and hadronic medium, and the UrQMD model takes care of the description of the hadronic phase [22, 23]. Among all the model predictions shown in Fig. 4.11, EPOS-LHC provides the overall good description of the dN/dy and $\langle p_T \rangle$ measurements. The EPOS-LHC is a minimum-bias hadronic interaction event generator that includes flow parameterization based on LHC data. It incorporates multiple partonic scatterings based on Gribov's Reggeon field theory formalism, collective hadronization, and the core-corona mechanism from pp to A–A collisions.

The rapidity dependence of dN/dy and $\langle p_T \rangle$ for K^{*0} in the multiplicity class 0–100% is further studied by dividing the dN/dy and $\langle p_T \rangle$ values at a given y by the corresponding values at $y = 0$, as shown in Fig. 4.12. The ratio (dN/dy)/(dN/dy)$_{y=0}$ decreases with rapidity, whereas $\langle p_T \rangle / \langle p_T \rangle_{y=0}$ shows a flat behavior as a function of rapidity. The measurements are compared with various model predictions as shown in Fig. 4.12. It is observed that the model predictions from HIJING qualitatively reproduce the trend and are closer to the data. The predictions from PYTHIA8 (Angantyr), DPMJET, EPOS-LHC, EPOS with and without UrQMD show a similar trend but are lower than the data at lower rapidities. For $\langle p_T \rangle / \langle p_T \rangle_{y=0}$ as a function of y, EPOS with and without UrQMD overpredicts. The data is under predicted by PYTHIA8 (Angantyr), DPMJET, and EPOS-
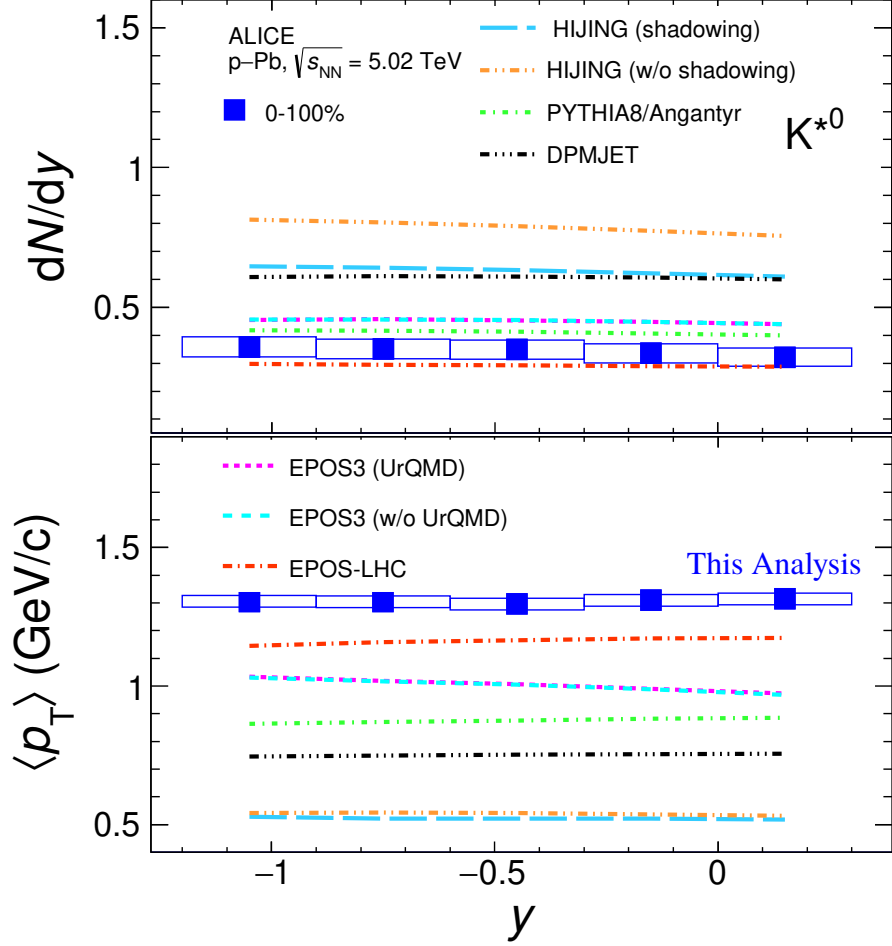
FIGURE 4.11: The p_T integrated yield, dN/dy (top) and mean transverse momentum, $\langle p_T \rangle$ (bottom) for K^{*0} as a function of y measured for multiplicity class 0-100% in p–Pb collisions at $\sqrt{s_{NN}}$ = 5.02 TeV. The predictions from EPOS-LHC [21], DPMJET [24], HIJING [25], PYTHIA(Angantyr) [26] and EPOS with and without UrQMD [22, 23] are also shown as different curves. The statistical uncertainties are represented as bars whereas the boxes indicate total systematic uncertainties.

LHC at lower rapidities. Figure 4.13 shows the multiplicity dependence of the dN/dy and $\langle p_T \rangle$ of K^{*0} as a function of y in p–Pb collisions at $\sqrt{s_{NN}}$ = 5.02 TeV. The dN/dy and the $\langle p_T \rangle$ increase with multiplicity for a given rapidity interval. The dN/dy shows a weak rapidity dependence with large uncertainties. This dependence is more pronounced for
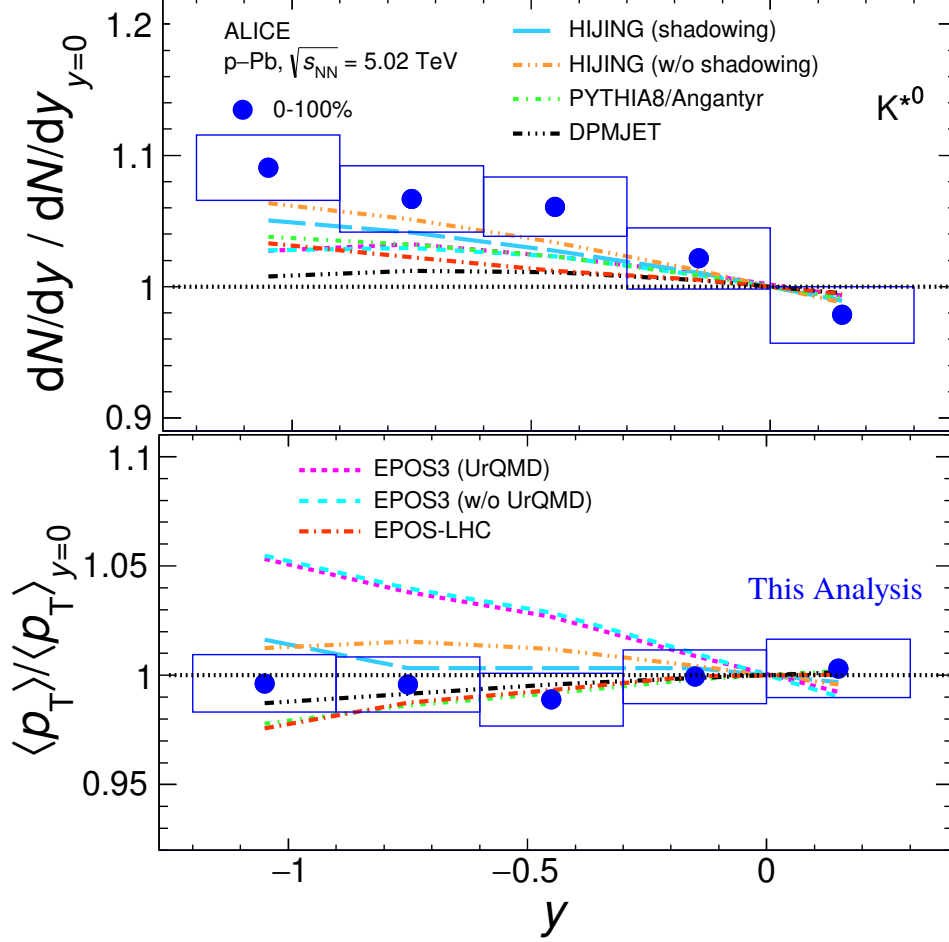
FIGURE 4.12: The p_T integrated yield (dN/dy) (upper panels) and mean transverse momentum ($\langle p_T \rangle$) (bottom panels) for K^{*0} as a function of y, divided by the dN/dy and $\langle p_T \rangle$ at $y = 0$ for the multiplicity class 0–100% in p–Pb collisions at $\sqrt{s_{NN}} = 5.02$ TeV. The predictions from EPOS-LHC [21], EPOS3 with and without UrQMD [22, 23], DPMJET [24], HIJING [25], and PYTHIA8/Angantyr [26] are shown as different curves. The statistical uncertainties are represented as bars whereas the boxes indicate total systematic uncertainties.

event with high multiplicity class (0–10%). The $\langle p_T \rangle$ shows a flat behavior as a function

of rapidity for all multiplicity classes in the measured rapidity interval. Similar behavior

in the average transverse kinetic energy as a function of rapidity for strange hadrons was

reported in Ref. [7]. These indicates that average transverse momentum of species does not change significantly with rapidity.
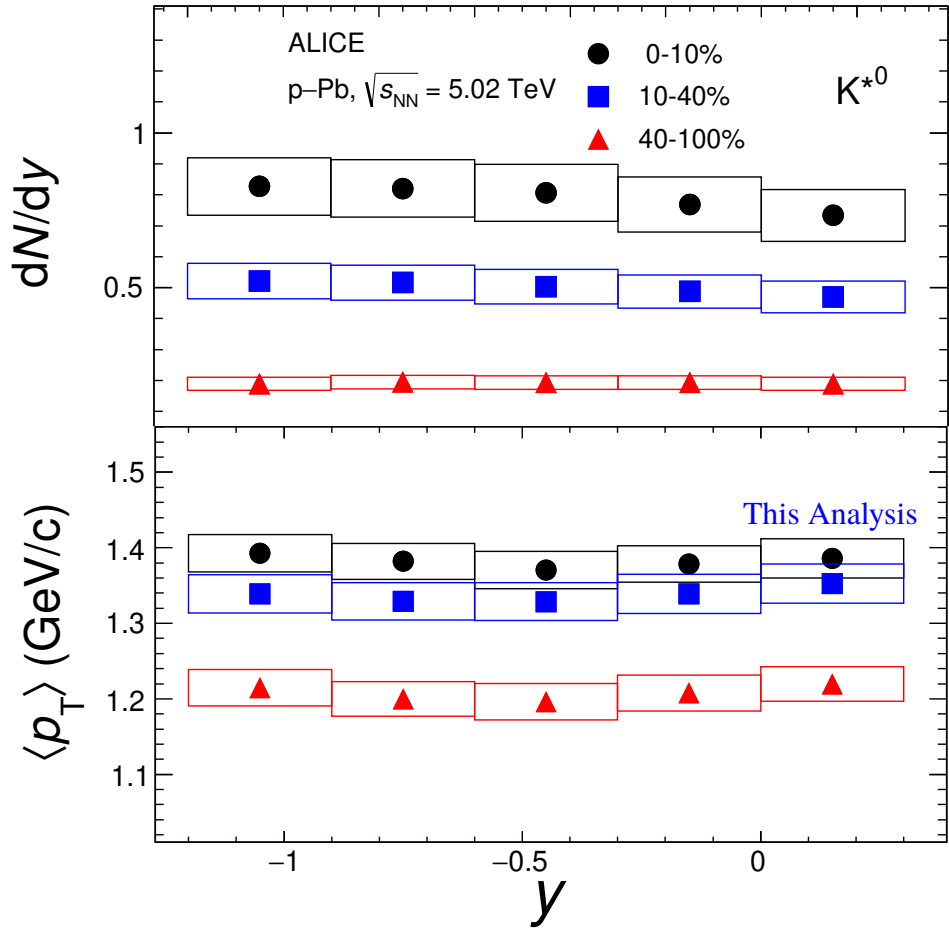
FIGURE 4.13: The dN/dy (top) and $\langle p_T \rangle$ (bottom) for K^{*0} as a function of y measured for the multiplicity classes 0–10%, 10–40% and 40–100% in p–Pb collisions at $\sqrt{s_{NN}} = 5.02$ TeV. The statistical uncertainties are represented as bars whereas boxes indicate the total systematic uncertainties on the measurements. This figure is taken form [34].

4.5.3 Rapidity asymmetry (Y_{asym})

The rapidity asymmetry (Y_{asym}) is defined by Eq. 4.1. Figure 4.14 shows the Y_{asym} of K^{*0} as a function of p_T in the rapidity interval $0.0 < |y| < 0.3$ for various multiplicity classes in p–Pb collisions at $\sqrt{s_{NN}}$ = 5.02 TeV. It is observed that the Y_{asym} deviates from unity at low p_T, suggesting the presence of nuclear effects. The deviations are more significant for events with high multiplicity. The Y_{asym} is consistent with unity at high p_T for all multiplicity classes, suggesting the absence of the nuclear effects at high p_T for the K^{*0} production in p–Pb collisions. The Y_{asym} of K^{*0} is also compared to ϕ [34]. Similar Y_{asym} is seen for both vector mesons within uncertainties. Figure 4.15 shows the comparison of
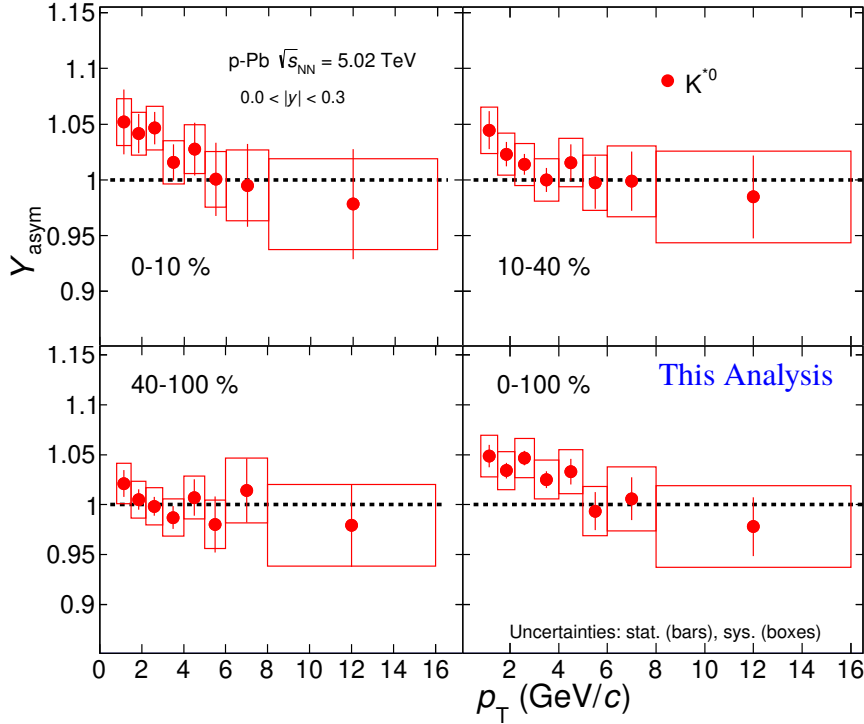
FIGURE 4.14: Rapidity asymmetry (Y_{asym}) of K^{*0} (red markers) as a function of p_T in the rapidity range $0.0 < |y| < 0.3$ for various multiplicity classes in p–Pb collisions at $\sqrt{s_{NN}}$ = 5.02 TeV. The statistical uncertainties are shown as bars whereas the boxes represent the systematic uncertainties on the measurements.

experimental results of Y_{asym} for K^{*0} as a function of p_{T} in the rapidity interval $0.0 < |y| <$

0.3 with the model predictions from EPOS-LHC, HIJING with and without shadowing,

DPMJET, PYTHIA8 (Angantyr) and EPOS with UrQMD and without UrQMD. These

models are not able to describe the Y_{asym} at low p_{T}. At high p_{T}, model predictions from

EPOS-LHC, PYTHIA8(Angantyr) and DPMJET fairly describe the data.
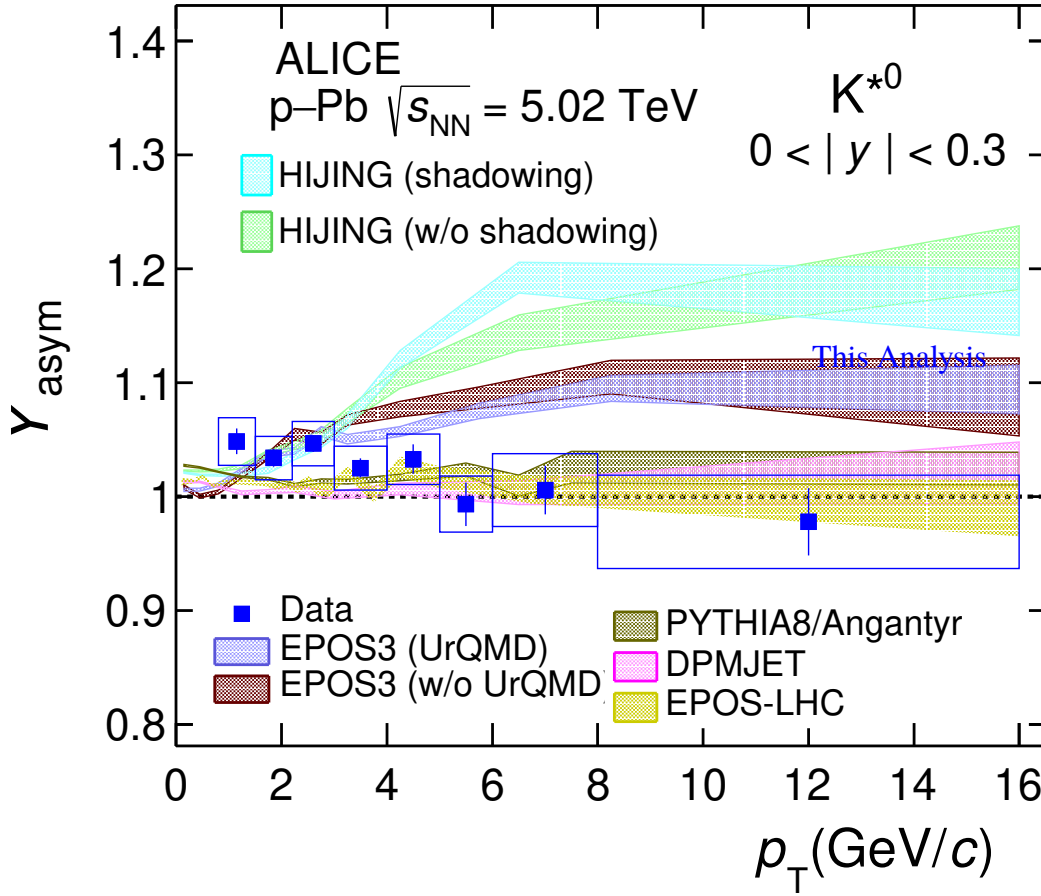
FIGURE 4.15: The comparison of experimental results of Y_{asym} for K^{*0} as a function of p_{T} in the rapidity range $0.0 < |y| < 0.3$ with the model predictions from EPOS-LHC, HIJING with and without shadowing, DPMJET, PYTHIA8 (Angantyr) and the EPOS with UrQMD and without UrQMD. Data points are shown with blue markers, and model predictions are shown by different color curves. The statistical uncertainties are represented as bars whereas the boxes indicate total systematic uncertainties.

4.5.4 Nuclear modification factor (Q_{CP})
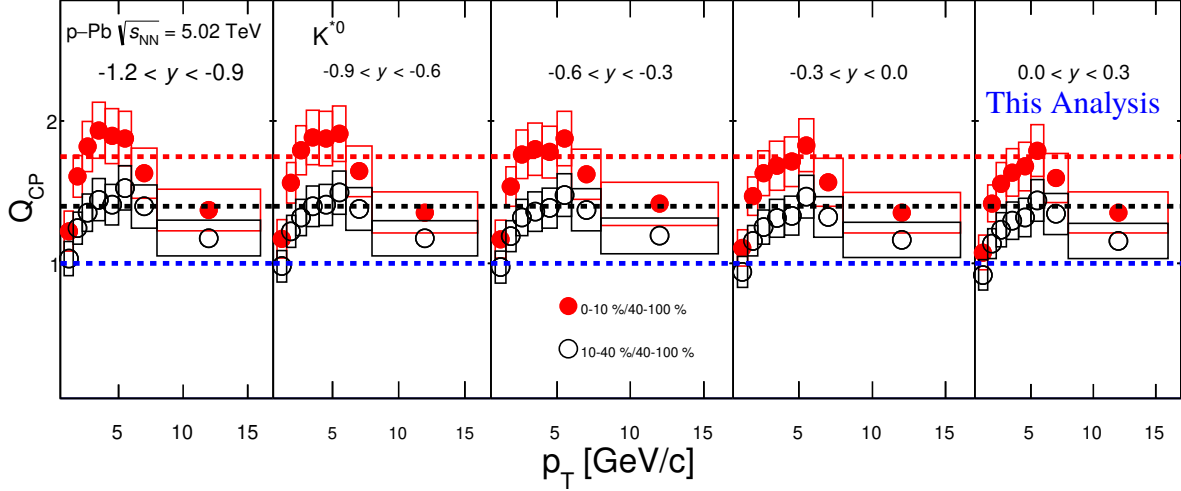
FIGURE 4.16: The Q_{CP} of K^{*0} as a function of p_T for 0–10%/40–100% (solid circle marker) and 10-40%/40-100% (open circle marker) in various rapidity intervals within the range $-1.2 < y < 0.3$ in p–Pb collisions at $\sqrt{s_{NN}}$ = 5.02 TeV. The statistical and systematic uncertainties are represented by vertical bars and boxes on the measurements, respectively.

The nuclear modification factor Q_{CP} is defined by Eq. 4.2. Figure 4.16 shows the Q_{CP} of K^{*0} as a function of p_T for 0–10%/40–100% (solid circle marker) and 10-40%/40-100% (open circle marker) in various rapidity intervals within the range $-1.2 < y < 0.3$ in p–Pb collisions at $\sqrt{s_{NN}}$ = 5.02 TeV. At intermediate p_T ($2.2 < p_T < 5.0$ GeV/c), the Cronin-like effects are observed for K^{*0}, which are more pronounced for higher rapidities and at high multiplicity classes. At high p_T (> 5 GeV/c), the Q_{CP} values are greater than unity and the ratios are consistent within uncertainties for all rapidity intervals. The rapidity dependence of Q_{CP} as a function of p_T is observed, which is more pronounced in the highest multiplicity class (0–10%). The Q_{CP} of ϕ [34] is found to be slightly higher than K^{*0} for the ratio of 0–10%/40–100%, however, they are consistent within uncertainties for

the ratio 10–40%/40–100% for all measured rapidity intervals.
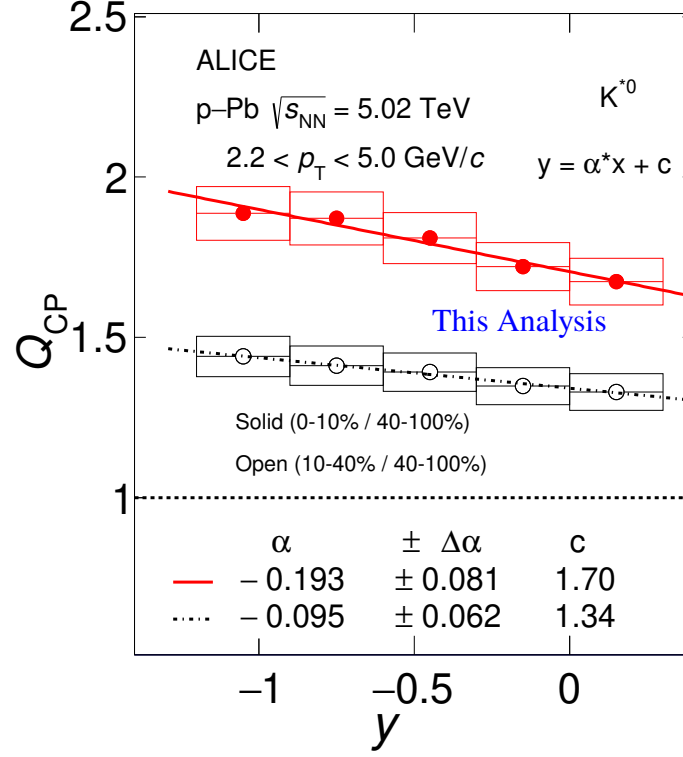
FIGURE 4.17: The Q_{CP} as a function of rapidity y of K^{*0} for 0–10 %/40–100% (solid markers) and 10–40%/40–100% (open markers) in p–Pb collisions at $\sqrt{s_{NN}} = 5.02$ TeV. The statistical and systematic uncertainties are represented by vertical bars and boxes on the measurements, respectively.

To quantify the rapidity dependence, the Q_{CP} values at the intermediate p_T ($2.2 < p_T < 5.0$ GeV/c) are plotted as a function of rapidity (y) in Fig. 4.17. The values of Q_{CP} at intermediate p_T ($2.2 < p_T < 5.0$ GeV/c) show a decreasing trend from the rapidity interval $-1.2 < y < -0.9$ to $0 < y < 0.3$ for 0–10%/40–100% compared to the 10-40%/40-100%, suggesting that the Cronin-like effects are more prominent for events with high multiplicity. The linear function fit to Q_{CP} as a function of y is shown in the Fig. 4.17. The slope parameter shows stronger rapidity dependence for 0–10%/40–100% than 10–40%/40–100%.

4.6 Summary

The transverse momentum (p_T) distribution of K^{*0} has been measured in the rapidity interval $-1.2 < y < 0.3$ for various multiplicity classes over the transverse momentum range $0.8 < p_T < 16.0$ GeV/c in p–Pb collisions at $\sqrt{s_{NN}} = 5.02$ TeV with the ALICE detector. The p_T spectra of K^{*0} exhibit the multiplicity and rapidity dependency at low p_T. The spectral shapes are similar for all multiplicity and rapidity intervals at high p_T (> 5 GeV/c) that indicating no significant effect due to multiplicity and rapidity. The measurement suggests that the soft and nuclear processes mainly control the particle production at low p_T in p–Pb collisions. The yields (dN/dy, $(dN/dy)/(dN/dy)_{y=0}$) decrease with rapidity whereas the average transverse momentum ($\langle p_T \rangle$) increases with multiplicity for a given rapidity. The $\langle p_T \rangle$ and ratio $\langle p_T \rangle / \langle p_T \rangle_{y=0}$ show a flat behavior as a function of rapidity for all multiplicity classes. The measured dN/dy, $\langle p_T \rangle$ and their ratios to the corresponding values at $y = 0$ are compared with model predictions for the minimum bias events. The EPOS-LHC model qualitatively describes the dN/dy and $\langle p_T \rangle$ whereas the HIJING predictions are closer to the data in the ratios of dN/dy and $\langle p_T \rangle$ than other models. The Y_{asym} as a function of p_T shows deviations from unity at low p_T for higher multiplicity class, however, their values are consistent with unity within uncertainties at high p_T in the measured multiplicity and rapidity interval. The Y_{asym} of K^{*0} and ϕ are found to be similar within uncertainties in the measured region. The observed Y_{asym} at low p_T suggests the presence of nuclear effects that depend on rapidity such as multiple scattering, and energy loss due to cold nuclear matter and nuclear shadowing. None of the models discussed here can adequately capture the Y_{asym} at low p_T. The Q_{CP} shows dependence on rapidity and multiplicity. At the intermediate p_T, the Cronin-like effects are seen in the Q_{CP} and are more prominent for higher rapidities and at high multiplicity class events. These measurements suggest that

nuclear effects play a significant role in particle production. The rapidity and multiplicity dependence effect on bulk observables have been observed. Future measurements using other hadron species and input from different event generators can constrain further the physical processes for particle production in asymmetric collision systems.

Bibliography

[1] J. Breitweg et al., [ZEUS Collaboration], Int. J. Mod. Phys. E 24, 10, 1530007, (2015).

[2] S. S. Adler et al., [PHENIX Collaboration], Phys. Rev. Lett. 91, 072303, (2003).

[3] I. Arsene et al.,[BRAHMS Collaboration], Phys. Rev. Lett. 93, 242303, (2004).

[4] B.I. Abelev et al.,[STAR Collaboration], Phys. Rev. C 76, 054903, (2007).

[5] B. Abelev et al., [ALICE Collabortaion], Phys. Rev. Lett. 110, 8, 082302, (2013).

[6] V. Khachatryan et al., [CMS Collaboration], Phys. Lett. B 768, 103-129, (2017).

[7] A. M. Sirunyan et al., [CMS Collaboration], Phys. Rev. C 101 no. 6, 064906, (2020).

[8] Z.B. Kang et al., Phys. Lett. B 718, 482-487, (2012).

[9] J. L. Albacete et al., Int. J. Mod. Phys. E 25, 9, 1630005, (2016).

[10] P. Bozek et al., Phys. Lett. B 748, 301-305,(2015).

[11] P. Bozek et al., Phys. Lett. B 728, 662-665, (2014).

[12] S. Chatrchyan et al., [CMS Collaboration], Phys. Lett. B 718, 795-814, (2013).

[13] J. Adam et al.,[ALICE Collaboration], Phys. Lett. B 758, 389-401, (2016).

[14] S. Acharya et al., [ALICE Collaboration], Phys. Rev. Lett. 123, 142301, (2019).

[15] ALICE Collaboration, B. B. Abelev et al., Phys.Lett.B 719, 29-41, (2013).

[16] S. Acharya et al., [ALICE Collabortaion], Phys. Lett. B 807, 135501, (2020).

[17] J. Adam et al.,[ALICE Collabortaion], Eur. Phys. J. C 76, 245, (2016).

[18] C. Loizides et al., Phys. Rev. C 99 1, 019901, (2019).

[19] S. Acharya et al.,[ALICE Collabortaion], Phys. Lett.B 802, 135225, (2020).

[20] J. Adam et al.,[ALICE Collabortaion], Phys. Lett. B 768, 203-217, (2017).

[21] T. Pierog et al., Phys. Rev. C 92 , 3, 034906, (2015).

[22] K. Werner et al., Phys. Rev. C 89, 6, 064903, (2014).

[23] A.G. Knospe et al., Phys. Rev. C 104, 5, 054907, (2021).

[24] S. Roesler et al., ICAMC PTSA, hep-ph/0012252, (2000).

[25] M. Gyulassy et al., Comput. Phys. Commun. 83, 307, (1994).

[26] C. Bierlich et al.,JHEP 10, 134, (2018).

[27] E. Abbas et al., [ALICE Collaboration], J. Instrum. 8, P10016 (2013).

[28] B. Abelev et al., [ALICE Collaboration], Int. J. Mod. Phys. A 29, 1430044, (2014).

[29] J. Alme et al., [ALICE Collaboration], Nucl. Instrum. Meth. A 622, 316-367, (2010).

[30] A. Akindinov et al., [ALICE Collabortaion], Eur. Phys. J. Plus 128, 44, (2013).

[31] R.L. Workman et al., Prog. Theor. Exp. Phys.2022, 083C01, (2022).

[32] S. Acharya et al., [ALICE Collabortaion], http://arxiv.org/abs/2110.10042, (2021).

[33] I. Hrivnacova et al.,[ALICE Collaboration], J. Phys. Conf. Ser. 331, 032016, (2011).

[34] S. Acharya et al., [ALICE Collaboration], http://arXiv:2204.10263, (2022).

[35] Constantino Tsallis, Statist. Phys. 52, 479-487, (1988).

CHAPTER 5

Measurement of K^{*0} production in minimum bias pp collisions at $\sqrt{s}$ = 7 TeV

5.1 Motivation

The study of hadronic resonances plays a crucial role in understanding particle production mechanisms. Both soft and hard scattering at LHC energies give rise to particle production. The bulk of the particles is produced due to soft interactions. It occurs at low p_T, where the particle production is governed by non-perturbative QCD processes. Understanding the non-perturbative domain necessitates the use of phenomenological model predictions because the production yield of low p_T particles cannot be determined from the basic principles of QCD. High p_T particles are generated through hard scatterings, followed by perturbative processes. By using perturbative QCD calculations, one can determine the yield and determine the origin of high-p_T particles [1]. In addition, the particle production

at low p_T follows a scaling behavior in transverse mass ($m_T = \sqrt{p_T^2 + m_0^2}$) spectra, where

m_0 is the rest mass of the particle. It was proposed by R. Hagedon [2]. The measurements

of m_T spectra of identified hadrons seem to fall on an approximately universal curve after

scaling with some arbitrary normalization factors. This behavior is known as m_T-scaling.

First, the m_T-scaling was seen at the ISR energies [3]. Later on, m_T-scaling observed by the

STAR Collaboration in pp collisions at $\sqrt{s} = 200$ GeV/c [4]. It is found that there is a clear

separation between baryons and mesons spectra at $p_T > 2$ GeV/c. The separation between

the baryons and mesons spectra seems to increase with m_T or p_T. This measurement in pp

collisions at $\sqrt{s} = 7$ TeV with the ALICE detector provides the opportunity to extend the

spectrum up to high p_T and m_T. Similarly, the high p_T region of transverse momentum(p_T)

spectra of different collision energies obey a scaling behavior known as x_T-scaling. The

detailed explanation of x_T-scaling is discussed in Section 3.6.4 of Chapter 3. The x_T-scaling

exponent parameter n provides information about the scattering processes at which high p_T

particles are produced. At high p_T, the invariant cross section of particle productions can

be calculated by the pQCD framework through convolution of the leading-twist (LT) $2 \rightarrow 2$

hard sub-process. The pQCD-based calculation with LT processes predicts $n = 4$, whereas

NLO pQCD calculation includes higher twist processes that lead to a maximum value of

$n = 8$ [5]. These predictions are tested using the measurements of identified hadrons and

resonances produced in minimum bias pp collisions at LHC energies. Measurements of

particle production in inelastic pp collisions provide input to tune the QCD-inspired Monte

Carlo (MC) event generators. Furthermore, the measurements in inelastic pp collisions

at $\sqrt{s} = 7$ TeV reported in this chapter, serve as reference data to study nuclear effects in

proton–lead (p–Pb) and lead–lead (Pb–Pb) collisions. K^{*0} is a vector meson consisting

of quark content of ds pair. It has a similar mass to the ϕ (s$\bar{s}$) but differs in strangeness

content by one unit. It also has lifetime a ~ 4 fm/c, whereas ϕ has a lifetime 42.6

fm/c. The measurements of K^{*0} and ϕ production may help understand the strangeness of production [6] and properties of the hadronic phase [7]. In this chapter, we report the K^{*0} production at midrapidity inelastic pp collisions at $\sqrt{s}$ = 7 TeV. is organized as follows. The data set, event, and track selection used in the analysis are briefly described in Section 5.2. In Section 5.3, the analysis techniques, the procedure for extraction of the yields, acceptance × efficiency, and the study of the systematic uncertainties are presented. In Section 5.4, the results on transverse momentum spectra (p_T), dN/dy, $\langle p_T \rangle$, empirical m_T and x_T-scaling are presented. Finally, the results are summarized in Section 5.5.

5.2 Analysis details

The data from pp collisions at centre-of-mass energy $\sqrt{s}$= 7 TeV, collected in 2010, are analyzed here. This analysis is based on a data sample of ∼ 45 million minimum bias-triggered events. The K^{*0} resonance is reconstructed from its decay products. The decay channel is K$^{*0} \rightarrow \pi^+$K$^-$ and its charge conjugate, having branching ratios (BR) of 66.6 % [8].

5.2.1 Event selection

A minimum bias trigger is required for at least one hit in the SPD or any of the two VZERO detectors (V0A and V0C). The minimum bias pp collision events are collected at a solenoidal magnetic field of B = 0.5 T. In addition, beam-induced background events are removed by the timing information in the VZERO detectors [9] and a selection of the position of the primary vertex reconstructed by the SPD [10]. Pile-up events are removed for the analysis by excluding events with multiple vertices reconstructed in the SPD. For the analysis, only those events are selected with a primary collision vertex are reconstructed in the SPD detector, and z position of the primary vertex (v_z) is within 10 cm along the beam

axis from the position of the collision vertex.

5.2.2 Track selection and particle identification

Invariant mass reconstruction of K^{*0} is performed with charged π and K tracks, which are coming from the primary vertex of the collisions, known as primary tracks. For this analysis, a set of high-quality track selection criteria is applied to maximize tracking efficiency, improve the PID by optimizing the dE/dx resolution and minimizing the contamination of weak decay contribution from secondary particles. Primary tracks are required to cross at least 70 out of 159 readout pad rows of the TPC. The tracks present at least one of the SPD layers. Primary tracks are selected within the kinematic acceptance of $p_T > 0.15$ GeV/c to maintain a good momentum resolution. Tracks are selected within $|\eta| < 0.8$ to ensure uniform acceptance by avoiding the edge of the TPC. To reduce the contamination from the secondary particles coming from weak decays and the interaction with detector material, a selection criterion on the DCA of the primary track to the primary vertex in the DCA$_{xy}$ is applied. The value of DCA$_{xy}$ is required to be less than the seven times its resolution: DCA$_{xy}(p_T) < 0.0105 + 0.035\, p_T^{-1.1}$ cm (p_T in GeV/c) and the distance of closest approach of the track to the primary vertex in the longitudinal direction (DCA$_z$) is required to be less than 2 cm. In addition, the ratio of the number of crossed rows to the number of findable clusters in the TPC is larger than 0.8, and rejection of track with kink decay (a track that decays to muon and neutrino) is also applied to ensure the good quality tracks. The PID procedure is similar to that described in Section 3.2.3 of Chapter 3. The PID is done using the TPC and the TOF. Both pions and kaons are selected by applying selection criteria of $|n\sigma_{TPC}| < 2.0$ with a TOF $|n\sigma_{TOF}| < 3.0$ as a veto. TOF veto criteria are applied only if track information is available in TOF [11].

5.3 K^{*0} signal extraction in pp collisions at $\sqrt{s} = 7$ TeV

The K^{*0} meson is reconstructed from their hadronic decay products by using the invariant-mass method [12]. In this chapter, the K^{*0} and $\overline{\text{K}}^{*0}$ are averaged i.e., (K^{*0} + $\overline{\text{K}}^{*0}$)/2 and denoted by the symbol K^{*0}. The K^{*0} is measured at midrapidity ($|y| < 0.5$) in pp collisions at $\sqrt{s} = 7$ TeV. The invariant mass distribution of decay daughter pairs of K^{*0} is constructed by taking unlike-sign pairs of π and K in the same event. The invariant mass distribution of unlike-sign pair of πK is shown (black marker) in Fig. 5.1 for transverse momentum range $1.0 \leq p_{\text{T}} < 1.2$ GeV/c. The shape of the uncorrelated combinatorial background is obtained via event mixing technique. The invariant-mass distribution is calculated from unlike-sign π and K pairs of different events, shown in the left (red marker) of the Fig. 5.1. In the event mixing technique, each event is mixed with other five events that satisfied similar event criteria, i.e., the only tracks from events with similar vertex positions ($|\Delta z| < 1$ cm) and track multiplicity ($|\Delta n| < 5$). The mixed-event distribution of decay pairs of K^{*0} is normalized in the mass region $1.1 < m_{\pi\text{K}} < 1.15$ GeV/c^2. This combinatorial background is subtracted from unlike-sign mass distribution in transverse momentum (p_{T}) interval $1.0 \leq p_{\text{T}} < 1.2$ GeV/c, is shown in right of Fig. 5.1. After subtracting the combinatorial background, the invariant-mass distribution consists of a resonance peak present over a background of correlated pairs, known as residual background, that can arise due to misidentified particle decays, or jets [12, 13]. The signal peak is fitted with a Breit-Wigner and a second-order polynomial function is used to describe the shape of the residual background. The fit function of K^{*0} is given by

$$\frac{dN}{dM_{\pi\text{K}}} = \frac{A}{2\pi} \frac{\Gamma_0}{(M_{\pi\text{K}} - m_0)^2 + \frac{\Gamma_0^2}{4}} + BM_{\pi\text{K}}^2 + CM_{\pi\text{K}} + D, \tag{5.1}$$
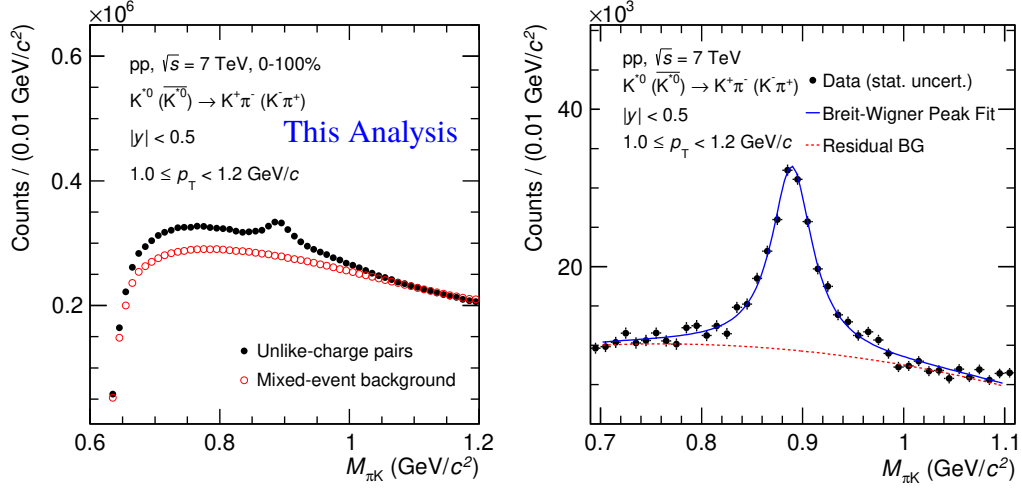
FIGURE 5.1: Invariant mass distributions after combinatorial background subtraction for K^{*0} for transverse momentum range $1.0 \leq p_T < 1.2$ GeV/c. The K^{*0} peak is described by a Breit-Wigner function. The residual background is described by a polynomial function of second order.

Here m_0 is the fitted mass pole of the K^{*0}, Γ_0 is the resonance width, and A is the yield of

the K^{*0} meson. B, C, and D are the fit parameters in the second-order polynomial. The fit

to the invariant-mass distribution is performed in the interval $0.75 < M_{\pi K} < 1.15$ GeV/c^2.

The widths of K^{*0} peaks is fixed to its known widths $\Gamma(K^{*0}) = 47.4 \pm 0.6$ MeV/c^2 [14].

The invariant-mass histogram is integrated over the region $0.75 < m_{\pi K} < 1.05$ GeV/c^2,

i.e., a range of three times the width around the nominal mass. The integral of the residual

background function in the same range is then subtracted. The resonance yields beyond the

histogram integration regions are found by integrating the tails of the signal fit function;

these yields are then added to the peak yield computed by integrating the histogram. The

raw yields of K^{*0} are extracted in the transverse momentum range from 0 to 20 GeV/c for

minimum bias pp collisions.

5.3.1 Efficiency × Acceptance

Generally, the detectors are not 100% efficient and full acceptance. It is necessary to apply correction factors like efficiency × acceptance to the measurements. From the real data, one cannot extract this information. So, a simulation is performed to get the efficiency × acceptance correction factor and to understand the real data. Efficiency × Acceptance (ϵ × A) as a function of p_T for K^{*0} in pp collisions is obtained from 70 million Monte Carlo (MC) simulated events. Particle productions and decays for this data set have been simulated by PYTHIA6 at $\sqrt{s} = 7$ TeV, while particle interactions with the ALICE detector are simulated by using GEANT3. The ϵ × A as a function of p_T in minimum bias pp collisions at $\sqrt{s} = 7$ TeV is shown in Fig. 5.2. For this study, we have used anchored Monte Carlo (MC) production having a period named LHC10d4 (PYTHIA 6 Perugia). The generated events are then passed through GEANT3 is a software package for geometry and tracking. A realistic description of the ALICE detector is used in GEANT3 to get the detector response. The simulated events are reconstructed in the same way as in the real data. The tracks identified by the reconstruction algorithms that pass the track selection and PID cuts are referred to as reconstructed tracks. The reconstruction efficiency(ϵ) × acceptance of a particle is defined as the ratio between the number of reconstructed particles to the number of generated particles within the rapidity interval $|y| < 0.5$. The ϵ × A is calculated for K^{*0} using πK decay pair. The ϵ × A as a function of p_T is shown in Fig. 5.2 for K^{*0} in minimum bias pp collisions at $\sqrt{s} = 7$ TeV, which indicates that the efficiency of K^{*0} has a strong dependence on transverse momentum at low p_T.

The uncertainty in ϵ × A is calculated using the Bayesian approach is described in Ref. [15]. The generated K^{*0} spectra may have different shapes than the measured K^{*0} spectra, so it is necessary to weigh the generated and reconstructed K^{*0} spectra in these simulations. A
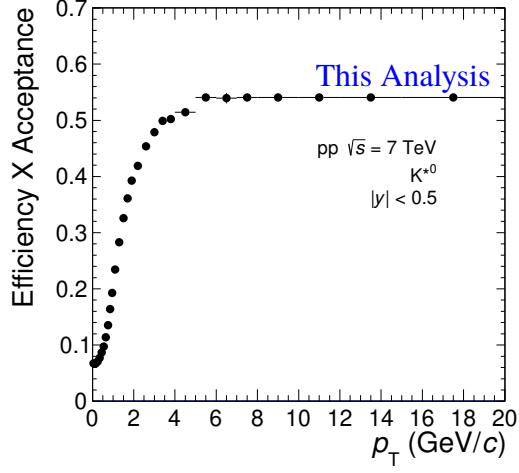
FIGURE 5.2: Efficiency × Acceptance as a function of p_T for minimum bias in pp collisions at $\sqrt{s}$ = 7 TeV. Errors shown in data points is statistical only, it is calculated using Bayesian approach described in [15].

re-weighting procedure is applied to match the generated p_T shapes to the measured ones. The effect of the re-weighting on $\epsilon \times A$ depends on p_T and amounts to ~ 1-2% at $p_T < 8$ GeV/c. The negligible effect is shown at the higher p_T in Fig. 5.3.
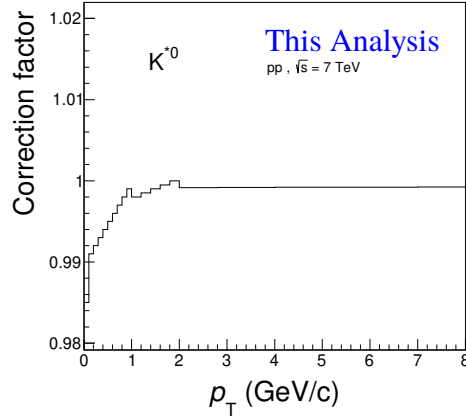
FIGURE 5.3: Ratio of K*⁰ re-weighted efficiency(ϵ_{rec}) × acceptance (A) to unweighted efficiency(ϵ_{rec}) × acceptance (A) after 2 iterations.

5.3.2   Corrected p_T spectra

The raw yields are normalized with a number of accepted events, detector reconstruction efficiency (ϵ) × Acceptance, branching ratio. Other correction factors also applied, such as vertex and normalization correction factor due to inelastic (INEL) events, to get the corrected transverse momentum (p_T) spectrum.

The corrected spectra is obtained using the following formula:

$$\frac{d^2N}{dp_Tdy} = \frac{Raw\ Counts}{N_{evt} \times BR \times dp_T \times dy \times \epsilon_{rec}} \times f_{norm} \times f_{vtx} \tag{5.2}$$

Here, BR (branching ratio) = 0.66, and the factor f_{norm} is applied in order to normalize the number of INEL events. The value for f_{norm} is $0.852^{+0.062}_{-0.03}$ [12]. The factor f_{vtx} = 0.9918 accounts for the requirement of a primary vertex to be reconstructed.

5.3.3   Source of systematic uncertainties

For the systematic study, each of the event selection criteria, PID selection criteria, track selection criteria, and signal extraction criteria are varied independently, and contributions from each of the sources are added in quadrature to get the total systematic uncertainties, considering them uncorrelated to each other. Sources of systematic uncertainties are the same as discussed in 3.5 of Chapter 3. The systematic uncertainty due to the global tracking efficiency, the detector material budget, and hadronic interactions in the material are taken from [12].
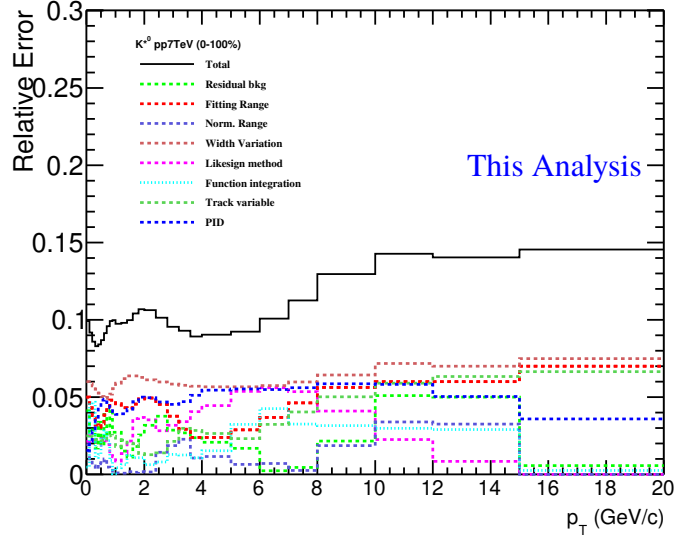
FIGURE 5.4: The summary of total relative uncertainties due to various sources in minimum bias pp collisions at $\sqrt{s}$ = 7 TeV for K^{*0}.

The total systematic uncertainty is the quadrature sum of all sources. For the systematic study, we repeat the measurement by varying one parameter at a time. A Barlow check has been performed for each measurement to verify whether it is due to a systematic effect or a statistical fluctuation. The yield extraction due to the bincount method and track variable χ^2/ITS satisfied Barlow criteria so that they are not included as a source of systematic uncertainties. Figure 5.4 shows the summary of total systematic uncertainties for K^{*0} in pp collisions at $\sqrt{s}$ = 7 TeV.

5.4   Results

5.4.1   Transverse momentum spectrum

The measurement of K^{*0} inelastic pp collisions at $\sqrt{s}$ = 7 TeV in the range up to p_T = 20 GeV/c at midrapidity is shown in the left panel of Fig.5.5. The new measurements of K^{*0} is good agreement with the previously published measurements [12]. The right of Fig. 5.5

shows the comparison of K^{*0} and ϕ spectrum at midrapidity and fitted with Lévy-Tsallis function [16]. The ratio of the measured data to the Lévy-Tsallis fit shows a good agreement between data and fit function within systematic uncertainties.
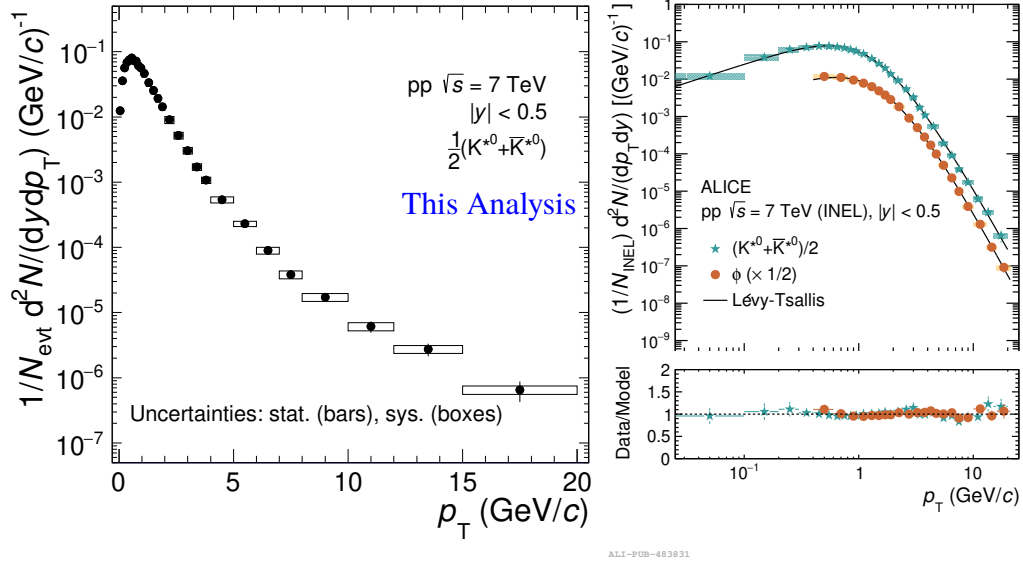
FIGURE 5.5: Left figure: measurement of K^{*0} p_T spectrum in p_T range up to 20 GeV/c at midrapidity in pp collisions at $\sqrt{s}$ = 7 TeV. The errors shown includes both statistical (bars) and systematic (boxes) uncertainties. Right figure: Upper panel comparison of p_T spectrum of K^{*0} and ϕ, is fitted with Lévy-Tsallis function in pp collisions at $\sqrt{s}$ = 7 TeV. Lower panel shows the ratio of data to the Lévy-Tsallis fit. Here, the bars show the systematic uncertainty.

Energy dependence of the transverse momentum spectra for K^{*0} is studied by measuring the ratio of p_T-differential yields for inelastic events at $\sqrt{s}$ = 7 and 8 TeV to those at $\sqrt{s}$ = 2.76 TeV [17]. This is shown in Fig. 5.6. It is found that the differential yield ratio is independent of p_T within systematic uncertainties up to about 1 GeV/c for various collision energies. This suggests that the particle production mechanism in soft scattering regions is independent of collision energy. An increase in slope of the p_T differential yield ratios is observed for $p_T > 1$-2 GeV/c.
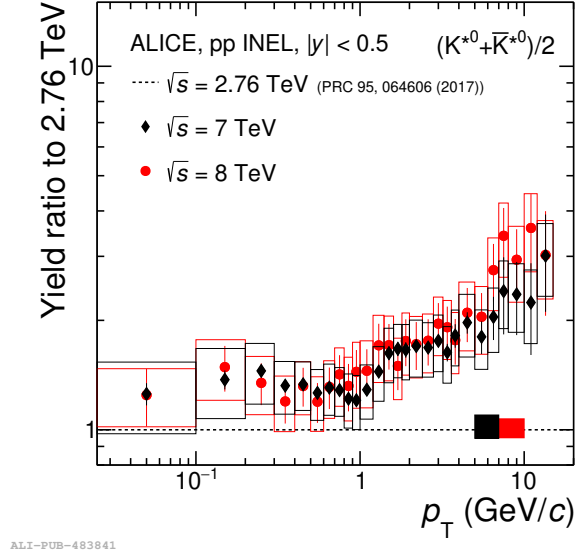
FIGURE 5.6: Collision energy dependence of p_T differential spectra ratio at $\sqrt{s}$ = 7 and 8 TeV to the p_T spectrum at $\sqrt{s}$ = 2.76 TeV for K^{*0}. The uncertainties are shown include both statistical (bars) and systematic (boxes).

5.4.2   Scaling properties of hadron production

Two types of universal scaling such as transverse mass (m_T) and x_T (= $2p_T$ /$\sqrt{s}$)-scaling have been studied for identified hadron production in high energy pp collisions. The m_T-scaling is expected to be observed in low p_T [3, 4, 18], whereas the the x_T scaling is observed at high p_T [5, 18]. Scaling properties of produced hadrons in pp collisions at $\sqrt{s}$ = 7 TeV have been discussed below.

Transverse mass (m_T)-scaling

The transverse mass spectrum is obtained from transverse momentum spectrum by using following relation , $m_T = \sqrt{p_T^2 + m^2}$, where m is rest mass of the hadrons. If the transverse mass (m_T) spectra as a function of m_T are calculated and scaled with proper normalisation factors for mesons and baryons, it is seen that all the hadrons fall in a single line that is

known as m_T-scaling. The scaled transverse mass spectra of charged kaon (reference for mesons) and proton (reference for baryons) are fitted separately with the modified Hagedorn function of the form, a $\times(e^{-bm_T} + m_T/c)^{-d}$, where a, b, c and d are fit parameters. The m_T spectra of other mesons are fitted with a parameterized fit function obtained form kaon spectra by keeping the normalization factors ("a") as a free parameter in the measured m_T and then scaled with appropriate normalisation factors so that their integral over measured m_T ranges match with integral over kaon fit function. Similarly, the baryon m_T spectra are normalized to match the integral of the proton fit function in the measured m_T range. The baryons further are scaled with normalization factors so that all m_T spectra have similar value at $m_T = 1$ GeV/c. The m_T spectra of identified hadrons in pp collisions at $\sqrt{s} = 7$ TeV is shown in the left panel of Fig. 5.7 and in the right panel of the same figure shows the ratios of scaled m_T spectra to kaon fit function.

ALI-PUB-499602   ALI-PUB-499612
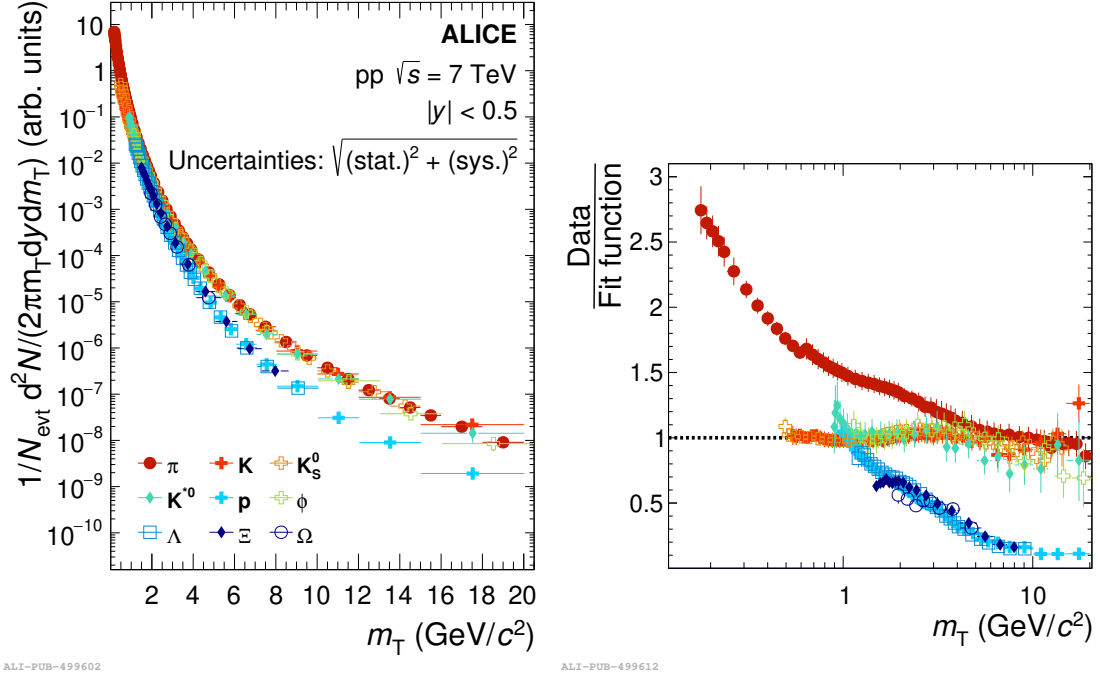
FIGURE 5.7: Left panel: Scaled m_T spectra for identified hadrons in pp collisions at $\sqrt{s}$ = 7 TeV [12, 18]. Right panel: Ratios of the scale m_T spectra to the function which fits the kaon m_T spectra.

It is observed that there are two types of scaling behavior: one for mesons and another for baryons. Clear separations in m_T spectra for mesons and baryons are found at $m_T > 2$ GeV/c. The different behavior in m_T spectra for mesons and baryons can be reflected as the production mechanism differs for mesons and baryons. Lund's hadronization model suggested that a meson is formed via the fragmentation of strings and requires the break up of a quark and ant-quark pair, while a baryon is by the diquark and anti-diquark pair [19, 20]. After $m_T > 10$ GeV/c, the separation between mesons and baryons trend becomes approximately constant. At low m_T, the pion m_T spectrum deviates from universal m_T scaling of other mesons. This deviation of pion m_T spectrum is likely considered due to feed-down contribution from resonance decay. Recent studies [21] suggest the measured primary π yield contains a significant contributions mostly form ρ and ω, which affects low

$p_T (< 1 \text{ GeV}/c)$ or low m_T spectrum. For this reason, the kaon m_T spectrum is considered as a reference for other mesons.

x_T scaling

The empirical x_T scaling for identified hadrons is studied using the invariant cross sections in pp collisions at $\sqrt{s} = 2.76, 7$, and 13 TeV. The high p_T region of the transverse momentum spectrum following a scaling behavior is known as x_T-scaling. The invariant cross section of particle production can be expressed by Eq. 3.16 in Section 3.6.4. The scaling exponent in Eq. 3.17 is calculated as the logarithm ratio of the invariant cross sections at two different collision energies, scaled by the logarithm ratio of the two collision energies. Figure 5.8 shows n values of K^{*0} as a function of x_T, obtained using K^{*0} transverse momentum spectrum in pp collisions at 7 and 13 TeV. The n value depends on both x_T and $\sqrt{s}$. It increases with the x_T or low (p_T)-region, where soft processes dominate the particle productions, and appear to saturate in the high x_T region. The comparison of x_T spectra of K^{*0} along with other hardons as a function of x_T is shown in Fig. 5.9. The scaling exponent "n" is estimated for 3 different combinations of collision energies: (2.76 TeV, 7 TeV), (2.76 TeV, 13 TeV), and (7 TeV, 13 TeV). The measured $n(x_T, \sqrt{s})$ distributions are fitted with a constant function in the x_T range $2 \times 10^{-3} < x_T < 6 \times 10^{-3}$ to get the respective n values for various energy combinations. The final n value is obtained for each hardon species by averaging the n values obtained in each combination. The uncertainties on the n values are taken as the maximum deviations from mean value of n to the n values obtained for 3 different combinations. The best scaling is achieved with exponent $\langle n \rangle = 5.04 \pm 0.02$ for pion, $\langle n \rangle = 5.02^{+0.21}_{-0.25}$ for kaon, $\langle n \rangle = 5.83 \pm 0.13$ for proton and $\langle n \rangle = 5.23 \pm 0.15$ for K^{*0}. It is found that identified hadrons follow the empirical x_T-scaling at high x_T or p_T region. The values of $\langle n \rangle$ for mesons such as π, K and K^{*0} are consistent with each

other within uncertainties. It is also observed that the value of $\langle n \rangle$ for protons is slightly higher compared to mesons. The NLO pQCD including higher twist processes predict a larger value of the exponent for baryons compared to mesons [5], which is in contrast to the observations based on the leading twist processes, where the exponent $\langle n \rangle$ has only a weak dependence on hadron species.
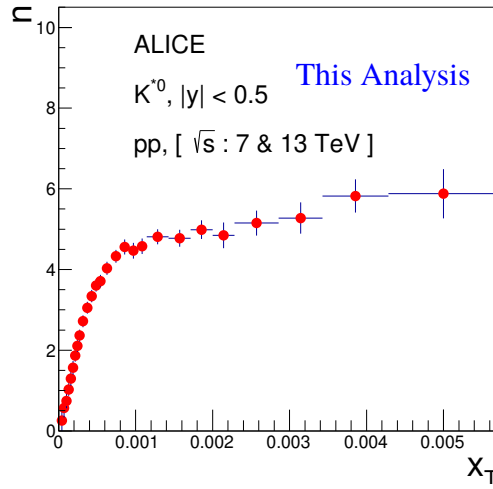
FIGURE 5.8: n as a function of x_{T} for K*⁰ is calculated using $\sqrt{s}$ = 7 and 13 TeV. The error in data points are quadrature sum of statistical and systematic uncertainties.

5.4.3 Integrated yield$(\mathrm{d}N/\mathrm{d}y)$ and mean transverse momentum ($\langle p_{\mathrm{T}} \rangle$)

The p_{T}-integrated yields ($\mathrm{d}N/\mathrm{d}y$) is calculated by integrating the p_{T} spectrum from 0 to 20 GeV/c. A comparison of $\mathrm{d}N/\mathrm{d}y$ (left) and $\langle p_{\mathrm{T}} \rangle$ (right) of K*⁰ in pp collisions at $\sqrt{s}$ = 2.76, 5.02, 7, 8, and 13 TeV is shown in Fig. 5.10. The $\mathrm{d}N/\mathrm{d}y$ and $\langle p_{\mathrm{T}} \rangle$ value increase with collision energy. In order to understand the dynamics of particle production, particle ratios are an interesting observable. Figure 5.11 (left) shows the K*⁰/K (resonance to stable hadron yield with same quark content) ratio as a function of centre-of-mass energy per nucleon for different collision systems. The K*⁰/K ratios are independent of energy and
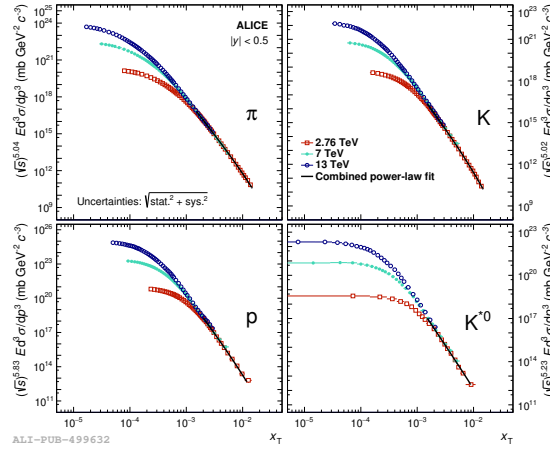
FIGURE 5.9: Comparison of scaled x_T spectra for identified hadrons in pp collisions at LHC energies [18].
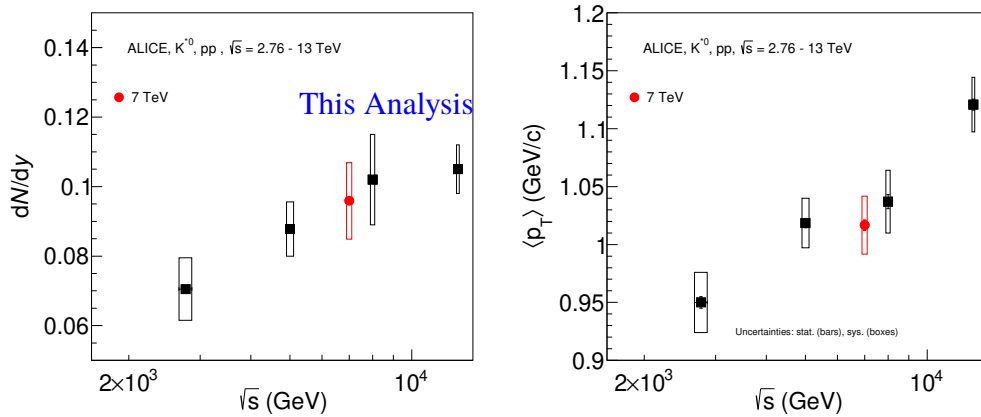
FIGURE 5.10: A comparison of dN/dy (left panel) and $\langle p_T \rangle$ of K^{*0} in pp collisions at $\sqrt{s} = 2.76$, 5.02, 7, 8, and 13 TeV. Bars represent for statistical uncertainties and boxes for systematic uncertainties.

consistent with thermal model predictions for small collisions. The K^{*0}/K ratios in central heavy-ion collisions show a suppression and value is lower than thermal model predictions; it attributes due to final state effects in the late hadronic stage [22, 23]. The ϕ/K^{*0} (particle having similar mass) ratio as a function of centre-of-mass energy is shown in right panel of Fig .5.11. The ratio seems to be independent of collision energy. The flat ratios suggest
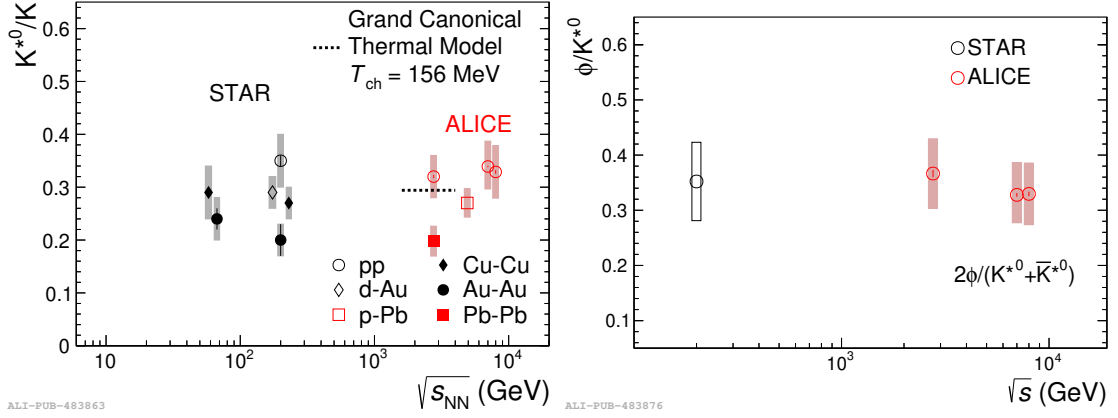
FIGURE 5.11: Left panel: particle ratios of K^{*0}/K in pp, high multiplicity p–Pb, central d–Au, and central A–A as a function of the collision energy. Bars represent statistical uncertainties. Boxes represent the total systematic uncertainties. The value given by a grand-canonical thermal model with a chemical freeze-out temperature of 156 MeV [24] is also shown. Right panel: Particle ratio ϕ/K^{*0} is presented for pp collisions as a function of the collision energy.

that the percentage increases of dN/dy for K^{*0} and ϕ as a function of the collision energy are similar from RHIC to LHC.

5.5   Summary

The measurement of K^{*0} production has studied in pp collisions at $\sqrt{s}$ = 7 TeV. It is an improved and extended measurement of the transverse momentum (p_T) spectrum up to p_T = 20 GeV/c. At low p_T ($\leq$ 1 GeV/c), the p_T spectrum between 7 and 13 TeV is consistent with unity, whereas it increases with p_T and collision energy at high p_T. This measurement indicates the high p_T particle production increase with collision energy due to the increased contribution of hard scattering processes. At $p_T > 2$ GeV/c, breaking of m_T scaling behavior is observed for mesons and baryons. The m_T spectrum of pion deviates at low m_T or low p_T from the universal m_T scaling of other mesons; it is likely due to feed-down from resonance decays. The x_T scaling holds fairly well for K^{*0} resonance and

other identified hadrons(π, K, and p) produced in pp collisions at the LHC energies. The exponent value is ~ 5, and the value for baryon is slightly higher than meson. No collision energy dependence in the p_T-integrated particle ratios (K^{*0}/K, ϕ/K, ϕ/K^{*0}) are observed in inelastic pp collisions. This indicates that there is no strangeness enhancement and energy dependence on the chemistry of the collision system. The pp measurements act as a reference for the measurements in p–Pb and Pb–Pb collisions.

Bibliography

[1]   D. de Florian et al., Phys. Rev. D 91, 014035, (2015).

[2]   R. Hagedorn, Nuovo Cimento, Suppl.3 no. CERN-TH-520, 147, (1965).

[3]   B. Alper et al., Nucl. Phys. B 87, 19, (1975).

[4]   B. I. Abelev et al., [STAR collaboration], Phys. Rev. C 75, 64901, (2007).

[5]   F. Arleo et al., Phys. Rev. Lett. 105, 062002, (2010).

[6]   S. Acharya et al., [ALICE Collaboration], Nature Physics, 13,535-539, (2017).

[7]   S. Acharya et al., [ALICE Collaboration], Eur. Phys. J. C 81, 256, (2021).

[8]   S. Acharya et al., [ALICE Collaboration], Phys. Rev. C 102, 024912, (2020).

[9]   E. Abbas et al., [ALICE Collaboration], J. Instrum. 8, P10016, (2013).

[10] B. Abelev et al., [ALICE Collaboration], Int. J. Mod. Phys. A 29, 1430044, (2014).

[11] A. Akindinov et al., Eur. Phys. J. Plus 128, 44, (2013).

[12] B. B. Abelev et al., [ALICE Collaboration], Eur. Phys. J. C72, 2183, (2012).

[13] S. Acharya et al.,[ALICE Collaboration], Phys. Lett. B 807, 135501, (2020).

[14] M. Tanabashi et al., Phys. Rev. D 98 3, 030001, (2018).

[15] T. Ullrich et al., arXiv:physics/0701199, (2000).

[16] Constantino Tsallis, Statist. Phys. 52, 479-487, (1988).

[17] J. Adam et al., [ALICE Collaboration], Phys. Rev. C 95, 064606, (2017).

[18] S. Acharya et al., [ALICE Collaboration], Eur. Phys. J. C 81, 256, (2021).

[19] B. Andersson et al., Nucl. Phys. B 197,1, 45-54, (1982).

[20] B. Andersson et al., Phys. Scripta 32, 574, (1985).

[21] K. Jiang, et al., Phys. Rev. C91 no. 2, 024910, (2015).

[22] S. Acharya et al., [ALICE Collaboration], Phys. Lett. B 802, 135225, (2020).

[23] J. Adams et al., [STAR Collaboration], Phys. Rev. C71, 064902,(2005).

[24] J. Stachel et al., J. Phys. Conf. Ser. 509, 012019, arXiv:1311.4662, (2014).

Spin alignment of vector mesons in heavy-ion collisions at $\sqrt{s_{\mathrm{NN}}}$ = 5.02 TeV

6.1 Motivation

Spin is one of the fundamental degrees of freedom of elementary particles. The study of spin-orbital angular momentum interaction is one of the important phenomena that describe the cause of fine structures in atomic physics, shell structures in nuclear physics, and spintronics in the branch of material sciences. Studying the spin-orbital angular momentum interaction in high-energy physics is crucial because that can provide information on the hadron production mechanism and the properties of strong interactions. Experimentally, heavy-ion collisions provide the opportunity to examine the characteristics of the QGP phase and initial conditions of the hot and dense medium produced in ultra-relativistic collisions. In non-central (i.e., impact parameter (b) between two colliding nuclei is non-zero) heavy-ion collisions, a large initial angular momentum of the order ($10^{6--7}\hbar$) and magnetic field O(10^{18} Gauss) are expected to be produced at LHC energies [1, 2, 3]. The angular momentum is a conserved quantity and could be felt throughout the evolution of a

system formed in heavy-ion collisions, whereas the magnetic field stays for a short time [3].

In the presence of large initial angular momentum, spin-orbit interaction of QCD leads to the polarization of quarks and anti-quarks in the produced QGP medium. The polarization of quarks and anti-quarks is translated to the polarization of produced hadrons with a non-zero spin during the process of hadronization [4]. Spin alignment measurements of vector mesons (spin =1) provide a unique opportunity to probe the initial condition of heavy-ion collisions. Spin alignment of vector meson is described by a spin-density matrix ρ, which is a 3×3 hermitian matrix having a unit trace. A deviation of the diagonal elements ρ_{mm} (m = -1, 0, 1) from 1/3 signal hints at the presence of net spin alignment. The diagonal elements $\rho_{-1,-1}$ and $\rho_{1,1}$ are degenerate, so the independent observable is ρ_{00}. The angular distribution of decay products of vector mesons is described by the Eq. 6.1 [5].

$$\frac{dN}{d\cos\theta^*} = N_0 \times [(1 - \rho_{00}) + (3\rho_{00} - 1)\cos^2\theta^*] \tag{6.1}$$

where N_0 is the normalization constant and θ^* is the angle between the quantization axis and the momentum direction of a daughter particle in the rest frame of the vector meson. In the absence of spin alignment, ρ_{00}= 1/3 that makes the angular distribution uniform. The ρ_{00} deviates from 1/3 and leads to a non-uniform angular distribution, which is considered as the experimental signature of the spin alignment. According to the different choices of quantization axes, spin alignment study can be divided into global polarization (quantization axis is parallel to $\vec{L}$ or $\vec{B}$) and local polarization (quantization axis is along the momentum direction of vector mesons). The quantization axis can be normal to the production plane (plane subtended by the vector mesons momentum and the beam axis) or normal to the reaction plane (defined by the impact parameter and the beam axis). The schematic view of the definition of θ^* using the production plane and event plane (a proxy for reaction plane) for vector mesons (K^{*0}, $K^{*\pm}$, and ϕ) is shown in Fig. 6.1. Recently, the spin alignment

measurement of vector mesons (K^{*0} and ϕ) were reported for Pb–Pb collisions at $\sqrt{s_{NN}}$ = 2.76 TeV [3]. It is found that spin alignment of vector mesons is observed at low p_T in mid-central collisions at 3 σ level and the value of ρ_{00} K^{*0} is lower than ϕ meson. The spin alignment of vector mesons is surprisingly larger than the results of Λ hyperon polarization measurement at both RHIC and LHC energies. The present study extends the spin alignment of vector mesons (K^{*0}, $K^{*\pm}$, ϕ) in Pb–Pb collisions at $\sqrt{s_{NN}}$ = 5.02 TeV which also has ten times higher statistics than previous measurements [3]. It provides a precise and energy dependence of the ρ_{00}. The first measurement of spin alignment of $K^{*\pm}$ also has been studied in Pb–Pb collisions at $\sqrt{s_{NN}}$ = 5.02 TeV. This measurement is sensitive to the initial magnetic field due to K^{*0}, and $K^{*\pm}$ having different magnetic moments.
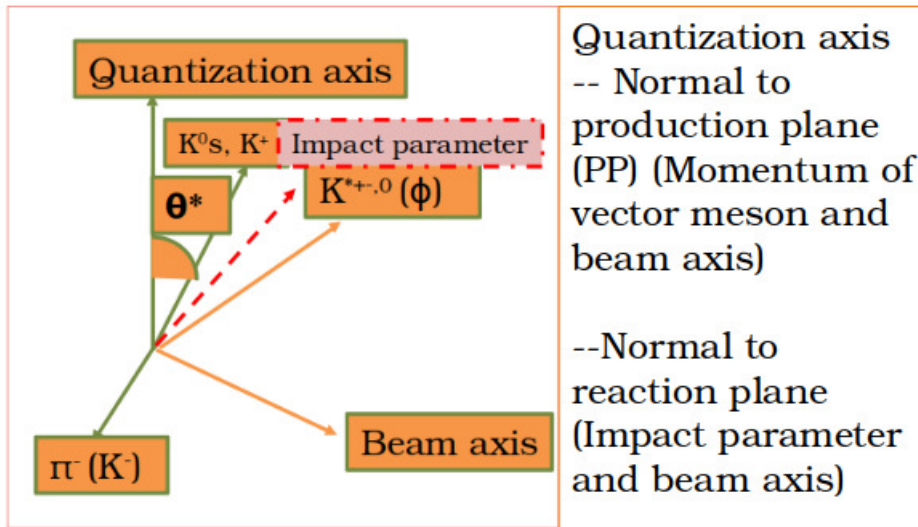
FIGURE 6.1: Definition of θ^* using production and reaction plane for global polarization of vector mesons.

Recent theoretical studies suggested that the spin alignment of vector mesons can arise from locally polarized quarks and anti-quarks. The quark and anti-quarks can be polarized due to helicity charge, and local vorticity generated from the anisotropic expansion of the

system created in non-central heavy-ion collisions [6, 7]. It is also interesting to extend such type measurements with different quantization axes that can help to understand the polarization coming due to global and local effect [6, 7]. We have discussed the spin alignment study of vector mesons (K^{*0} and ϕ) using a helicity frame (the quantization axis is taken along the momentum direction of vector mesons). It can act as a reference measurement compared to global spin alignment. The schematic view of the definition of helicity frame for vector mesons (K^{*0}, ϕ) is shown in Fig. 6.2, where the quantization axis is chosen as the vector mesons momentum direction. In this chapter, we have presented the
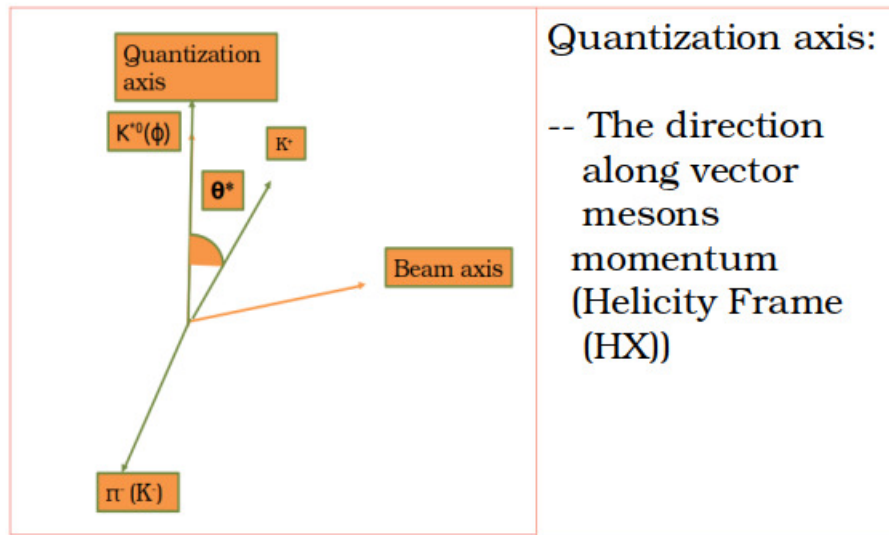
FIGURE 6.2: Definition angle θ^* using helicity frame (HX) is shown for K^{*0} and ϕ mesons.

results of spin alignment measurements for vector mesons (K^{*0}, $K^{*\pm}$ and ϕ) in Pb–Pb collisions at = 5.02 TeV using production plane (PP) and helicity frame (HX) for mid-centrality (10–50%) at midrapidity ($|y| < 0.5$) using ALICE detector [8]. Angular distribution of the decay products with respect to the production plane and helicity frame in the rest frame of vector mesons is measured to extract the ρ_{00}. The results are compared with the previous

measurements.

6.2 Analysis details

The study carried out here, were analyzed using the data from Pb–Pb collisions at $\sqrt{s_{NN}}$ = 5.02 TeV, collected in the year 2018. The analysis is performed based on data sample of 125 million minimum-bias trigger events after satisfying good event and track selection criteria. The spin alignment of vector mesons are reconstructed using the invariant mass technique from their hadronic decay channels of K^{*0} ($\overline{K^{*0}}$) $\rightarrow K^+\pi^-$ ($K^-\pi^+$) having branching ratio of 66.6% [9], K^{*+} (K^{*-}) $\rightarrow K_S^0\pi^+$ ($K_S^0\pi^-$) having branching ratio of 33.3% [10], and $\phi \rightarrow K^+K^-$ having with branching ratio of 49.2% [9] at the midrapidity ($|y| < 0.5$) in the Pb–Pb collisions at $\sqrt{s_{NN}}$ = 5.02 TeV using production plane (PP) and helicity frame (HX).

6.2.1 Event selection

Events are selected with a minimum bias trigger in which atleast one hit is considered simultanously in both V0A and V0C detectors. The minimum bias events are collected at a solenoidal magnetic field of B = 0.5 T. Beam-induced background events are removed by the timing information in the VZERO detectors [11]. Pile-up events are removed from the analysis by identifying events with multiple vertices reconstructed in the SPD detector. Events are selected, whose primary collision vertex is reconstructed in the SPD detector [12], and z position of primary vertex (v_z) within 10 cm from the nominal center of the detector.

6.3 Track selection and particle identification

Invariant mass reconstruction of vector mesons (K^{*0} and ϕ) are performed with charged π and K tracks, which are coming from the primary vertex of the collisions, known as primary tracks. The $K^{*\pm}$ is reconstructed from decay products of K^0_S and π. K^0_S is reconstructed using invariant mass method from opposite charged pair of pions, where pions are selected by V-shaped weak decay topological selection criteria [13]. A similar selection criteria used in in Ref. [10, 13] is taken for K^0_S. For this analysis, a set of high-quality track selection criteria is applied to maximize tracking efficiency, improve particle identification (PID) by optimizing the dE/dx resolution, and minimize the contamination due to secondary particles contribution from weak decay. Primary tracks are required to cross at least 70 out of 159 readout pad rows of the TPC. The tracks present at least one of the SPD layers. Primary tracks are selected within kinematic acceptance of $p_T > 0.15$ GeV/c to maintain a good momentum resolution. Tracks are selected within $|\eta| < 0.8$ to ensure uniform acceptance by avoiding the edge of the TPC. To reduce the contamination from the secondary particles coming from weak decays and the interaction with detector material, a selection criterion on the DCA of the primary track to the primary vertex in the DCA_{xy} is applied. The value of DCA_{xy} is required to be less than seven times its resolution: $DCA_{xy}(p_T) < 0.0105 + 0.035 \, p_T^{-1.1}$ cm (p_T in GeV/c) and the distance of closest approach of the track to the primary vertex in the longitudinal direction (DCA_z) is required to be less than 2 cm. In addition, the ratio of the number of crossed rows to the number of findable clusters in the TPC is larger than 0.8, and rejection of track with kink decay (a track that decays to muon and neutrino) is also applied to ensure the good quality tracks. The procedure of the PID is similar to that described in Section 3.2.3 of Chapter 3. The PID is done using Time Projection Chamber (TPC) and Time-Of-Flight (TOF). Both pions

and kaons are selected by applying selection criteria of $|n\sigma_{\text{TPC}}| < 2.0$ with a TOF $|n\sigma_{\text{TOF}}| < 3.0$ as a veto. TOF veto criteria are applied only if track information is available in TOF [14]. The event and track selection criteria used for this analysis is similar as used in Ref. [9]. The centrality selection is done, according to the total charge deposited in the forward V0 detector [11].

6.4 Signal extraction

For signal of vector mesons, K^{*0}, $K^{*\pm}$ and ϕ are extracted using invariant mass method from their decay products. The decay products are π^+K^- (π^-K^+) for K^{*0} ($\overline{K^{*0}}$), $K_S^0\pi^+$ ($K_S^0\pi^+$) for K^{*+} (K^{*-}) and K^+K^- for ϕ. The signal of K^{*0}, $K^{*\pm}$ and ϕ are obtained for various transverse momentum (p_T) and $\cos\theta^*$ intervals for a centrality class 10–50% in Pb–Pb collisions at $\sqrt{s_{\text{NN}}}$ = 5.02 TeV. The $\cos\theta^*$ bin is further divided into 5 bins (0.0, 0.2, 0.4, 0.6, 0.8, 1.0) having $\cos\theta^*$ bin gap ($\Delta\cos\theta^*$ = 0.2). The signals are extracted for p_T bins: 1.0, 1.2, 1.4, 1.6, 1.8, 2.0, 2.5, 3.0, 5.0, 7.0, 10.0 GeV/c for K^{*0} and 1.0, 1.2, 1.6, 2.0, 2.5, 3.0, 5.0, 7.0, 10.0 GeV/c for $K^{*\pm}$. The ϕ-meson signal extracted for p_T bins are 0.5, 0.8, 1.2, 1.6, 2.0, 2.5, 3.0, 4.0, 5.0, 7.0, 10.0 GeV/c. The combinatorial background distribution is estimated using the mixed-event method (details about the mixed-event method is described in Section 3.3 of Chapter3). An additional condition is used for event-mixing in Pb–Pb collisions; those events are selected for mixing, whose event plane angle difference is within 20°. The mixed-event background distributions are normalized 5 Γ (Γ is the full width half maxima of resonance distribution) away from mass peak of K^{*0}, $K^{*\pm}$ and ϕ, respectively. Figure 6.3 shows the invariant mass distribution of unlike charged πK pairs of same event before combinatorial background subtraction (left), whereas the invariant mass distribution of K^{*0} signal (right) after normalized-mixed event background subtraction is

fitted with Breit-Weigner function (blue line) for the transverse momentum (p_T) interval
($1.2 \leq p_T < 1.4$ GeV/c) in the $\cos\theta^*$ interval 0.6 to 0.8 for 10–50% centrality class in
Pb–Pb collisions at $\sqrt{s_{NN}}$ = 5.02 TeV using the production plane. After subtraction of
combinatorial background, a certain amount of backgrounds are left under the K^{*0} signal,
which are known as residual background. The residual background is described by the
polynomial function of the second order is shown by a dotted red line. Figure 6.4 shows
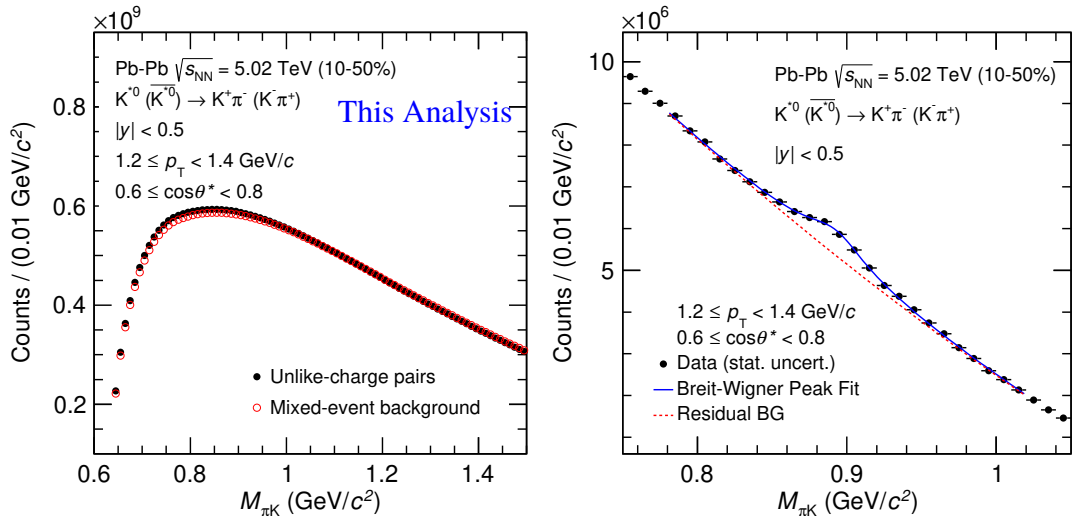
FIGURE 6.3: Left figure shows an invariant mass distribution of unlike charged πK same event pairs
(black markers) and mixed-event background pairs (red markers). Right panel shows
invariant mass distribution of unlike πK pairs after normalized mixed-event background
subtraction. The invariant mass distribution is fitted with Breit-Weigner distribution
function for signal (blue lines) and polynomial function of second order (red dotted
lines) for residual background function for the interval $1.2 \leq p_T < 1.4$ GeV/c in the
$\cos\theta^*$ interval 0.6 to 0.8 for 10-50% centrality class in Pb–Pb collisions at $\sqrt{s_{NN}}$ = 5.02
TeV. Quantization axis is normal to the production plane (PP).

the invariant mass distribution of $K^0_S\pi$ same event pairs (black markers) and mixed-event
background pairs (red markers) whereas the combinatorial background subtracted invariant
mass distribution is fitted with a Breit-Wigner distribution for signal and a exponential plus
second order polynomial function is used to describe the residual background (red dotted
lines) distribution for $1.6 \leq p_T < 2.0$ GeV/c in the $\cos\theta^*$ interval 0.6 to 0.8 for 10–50%

centrality class in Pb–Pb collisions at $\sqrt{s_{NN}}$ = 5.02 TeV using production plane.
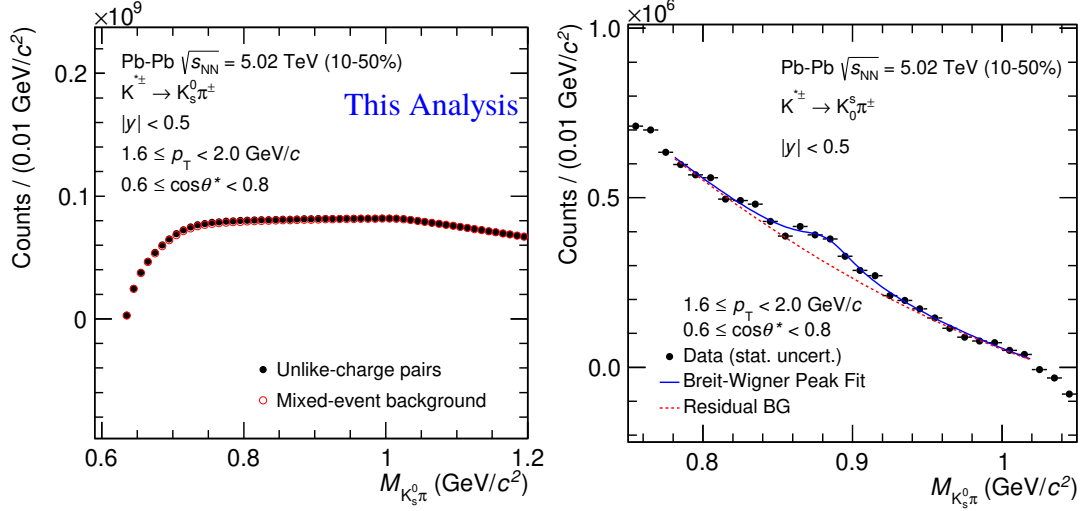
FIGURE 6.4: Left figure shows invariant mass distribution of $K_S^0\pi$ same event pairs (black markers) and mixed-event background pairs (red markers). Right panel shows invariant mass distribution of $K_S^0\pi$ pairs after normalized mixed-event background subtraction. The invariant mass distribution is fitted with Breit-Weigner distribution function (blue line) for signal and exponential plus polynomial function of second order for residual background function (red dotted lines) in the p_T interval $1.6 \leq p_T < 2.0$ *GeV*/c for $\cos\theta^*$ interval 0.6 to 0.8 in the 10–50% centrality class for Pb–Pb collisions at $\sqrt{s_{NN}}$ = 5.02 TeV. Quantization axis is normal to the production plane.

Figure 6.5 represents the invariant mass distribution of KK pairs from same events (black markers) and normalized-mixed event background distribution (red markers). The right panel of figure shows the normalized mixed-event background subtracted invariant mass distribution is fitted with Voigtian plus polynomial function of second order (blue lines) for $0.5 \leq p_T < 0.8$ GeV/c and $\cos\theta^*$ 0.6 to 0.8 in 10–50% collisions at $\sqrt{s_{NN}}$ = 5.02 TeV using quantization axis normal to the production plane. The Voigtian function describes the signal whereas the the polynomial function of the second order describes residual background distribution (red dotted lines). Similarly, the signal of K^{*0} and ϕ using quantization axis parallel to momentum direction of vector meson (HX) for invariant mass distributions before background subtraction and after subtraction of normalized background
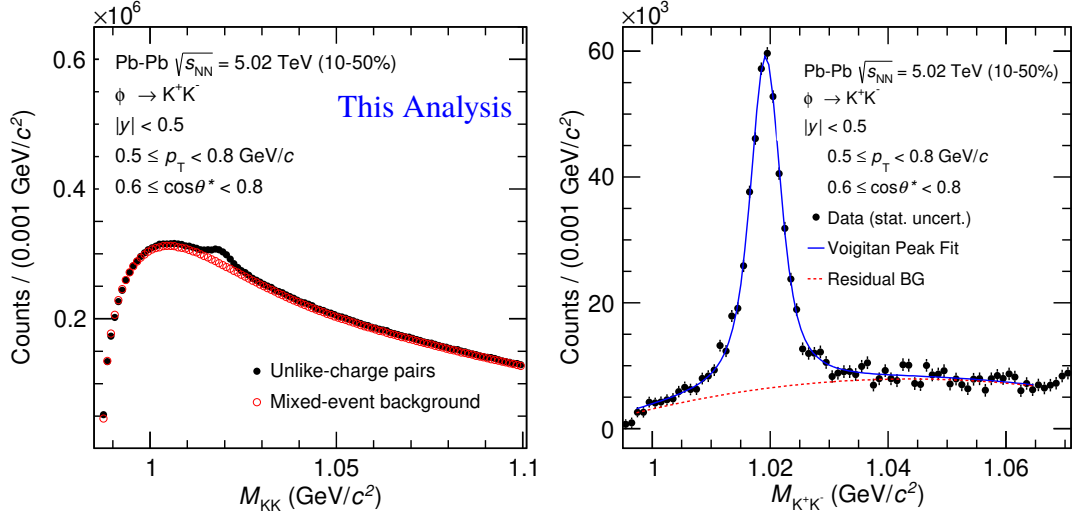
FIGURE 6.5: Left panel shows invariant mass distribution of unlike charged KK pairs from same events and normalized mixed event background for $0.5 \leq p_T < 0.8$ *GeV*/c and $\cos\theta^*$ 0.6 to 0.8 in 10–50% collisions at $\sqrt{s_{NN}}$ = 5.02 TeV. Right panel shows mixed-event background subtracted invariant mass distribution of KK pairs is fitted with the Voigtian function for signal (blue line) and the residual background distribution is described by the second order polynomial function. The Quantization axis is normal to the production plane.

distribution fitted with their corresponding fit functions for signal and residual background function are shown in Fig. D.7 and Fig. D.8 in the Appendix. During the extraction of yields for K^{*0} and $K^{*\pm}$, the width of resonances are kept as fixed to their PDG values, whereas mass resolution (σ_m) parameter obtained from Monte Carlo simulation is fixed during signal extraction due to its smaller width (4.26 fm/c) for ϕ meson. The σ_m as a function of p_T for various $\cos\theta^*$ interval for centrality class 10–50% is shown in Fig. 6.6. A $\cos\theta^*$ dependence in σ_m is seen and value varies from 1-1.5 MeV/c^2. After the residual background subtraction, the area under the Breit-Weigner distribution is known as the yield K^{*0} and $K^{*\pm}$ signal for given p_T and $\cos\theta^*$ interval for centrality class 10–50% at midrapidity in Pb–Pb collisions at $\sqrt{s_{NN}}$ = 5.02 TeV. The area under the Voigtian function after residual background subtraction is taken as the yield of ϕ meson for given p_T and
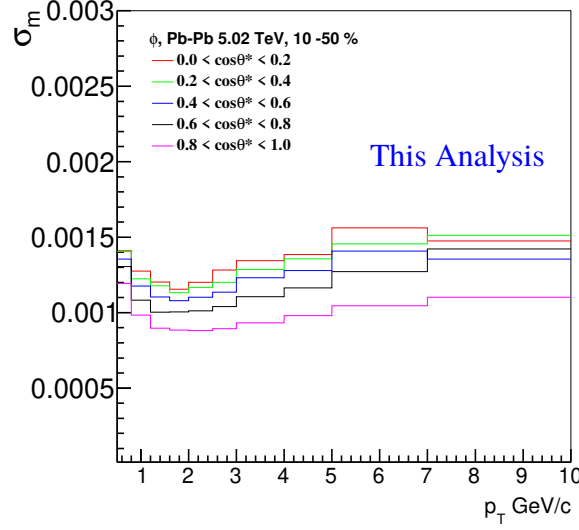
FIGURE 6.6: ϕ meson mass resolution as a function of p_T for various $\cos\theta^*$ in Pb–Pb collisions at $\sqrt{s_{NN}} = 5.02$ TeV. Results are obtained from MC simulation.

$\cos\theta^*$ interval in the centrality class 10–50% at midrapidity for Pb–Pb collisions at $\sqrt{s_{NN}} = 5.02$ TeV. The same procedure is repeated to extract the signal of vector mesons K^{*0}, $K^{*\pm}$ and ϕ for various p_T and $\cos\theta^*$ intervals for centrality class 10–50%. The average over K^{*0} and $\overline{K}^{*0}$ results is denoted as K^{*0} and the result of $K^{*\pm}$ is represented for average over K^{*+} and K^{*-}.

6.4.1 Raw transverse momentum (p_T) spectra

The raw yields of vector mesons (K^{*0}, $K^{*\pm}$ and ϕ) are calculated by using two different methods: bin counting and function integration method. The function integration is as the default whereas the bin counting method is used for systematic study. The yields are extracted as a function of p_T for various $\cos\theta^*$ intervals in the centrality class 10–50% for Pb–Pb collisions at $\sqrt{s_{NN}} = 5.02$ TeV. The left (for K^{*0}) and right(for $K^{*\pm}$) figures in Fig. 6.7 and Fig. 6.8 show the comparison of the raw p_T spectra for various $\cos\theta^*$ intervals

(upper panel) and their ratios with respect to the $\cos\theta^*$ bin 0.0 to 0.2 (lower panels) are shown. The raw p_T spectra are normalized to the total number of accepted events and results are shown using production plane analysis.
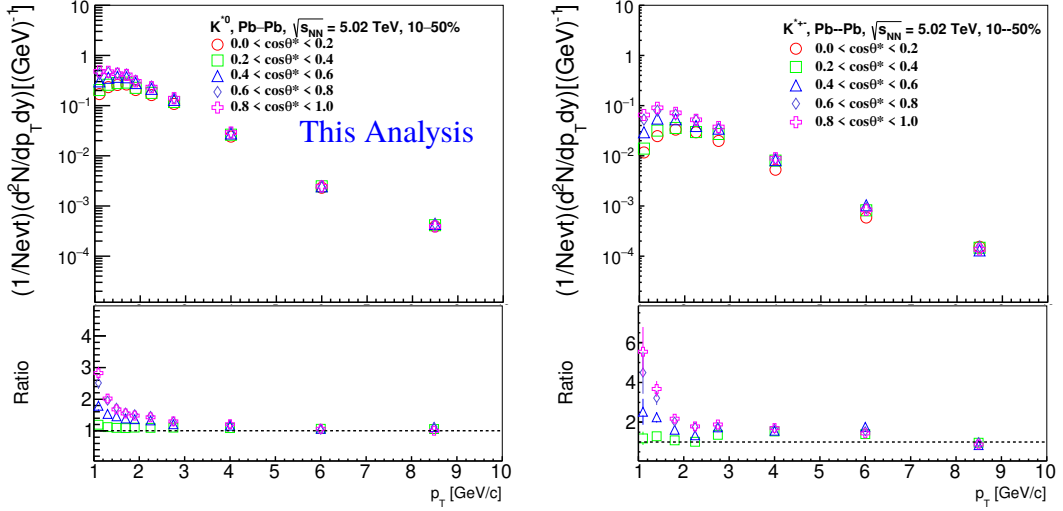
FIGURE 6.7: Left figure: Upper panel show the raw p_T spectra for different $\cos\theta^*$ intervals and lower panel show the ratio of raw p_T of different $\cos\theta^*$ interval to the raw p_T spectrum of the $\cos\theta^*$ bin 0.0 to 0.2 for K^{*0}. Right figure : Upper panel show the raw p_T spectra for different $\cos\theta^*$ intervals and lower panel show the ratio of raw p_T of different $\cos\theta^*$ interval to the raw p_T spectrum of the $\cos\theta^*$ bin 0.0 to 0.2 for $K^{*\pm}$. Results for 10–50% centrality class in Pb–Pb collisions at $\sqrt{s_{NN}}$ = 5.02 TeV. Results obtained from the quantization axis normal to the production plane. Statistical errors are considered only.

6.5   Efficiency × Acceptance

The reconstructed efficiency × acceptance for various p_T and $\cos\theta^*$ intervals are determined using Monte Carlo simulations. Particle production and resonance decays are simulated using HIJING [15] model. The ALICE detector response is incorporated by generated tracks information passes through the GEANT3 simulation. The same event and track selection criteria are used for real and simulated data. The number of accepted events used for Monet Carlo is about 3 Million minimum bias events. The reconstructed efficiency ×
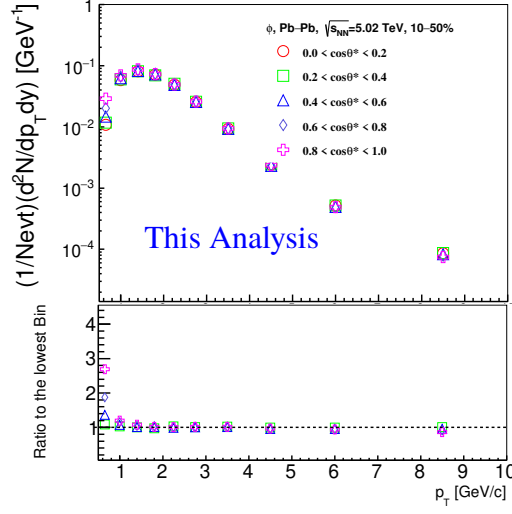
FIGURE 6.8: Upper panel show the raw p_T spectra for different $\cos\theta^*$ intervals and lower panel show the ratio of raw p_T of different $\cos\theta^*$ intervals to the raw p_T spectrum of the $\cos\theta^*$ bin 0.0 to 0.2 for ϕ. Results for 10-50% centrality class in Pb–Pb collisions at $\sqrt{s_{NN}}$ = 5.02 TeV. Results obtained from the quantization axis normal to the production plane. Statistical errors are considered only.

acceptance (detailed is discussed in Section 3.3.2 of Chapter 3) as a function of p_T for K^{*0} and $K^{*\pm}$ in various $\cos\theta^*$ intervals are shown in Fig. 6.9 and for ϕ is shown in Fig. 6.10. Lower panels in the same figures show the ratio of the efficiency × acceptance in different $\cos\theta^*$ intervals to the efficiency × acceptance of the $\cos\theta^*$ 0.0 to 0.2 interval for 10–50% centrality class in Pb–Pb collisions at $\sqrt{s_{NN}}$ = 5.02 TeV. It is found that a dependence in efficiency × acceptance on $\cos\theta^*$ is observed at low p_T for vector mesons (K^{*0}, $K^{*\pm}$ and ϕ) for the production plane analysis. Similar dependence in efficiency × acceptance as a function of p_T with reverse $\cos\theta^*$ trends are observed for K^{*0} and ϕ using helicity frame analysis. The results are shown in Fig. D.9 for K^{*0} (left) and ϕ (right) in the Appendix.
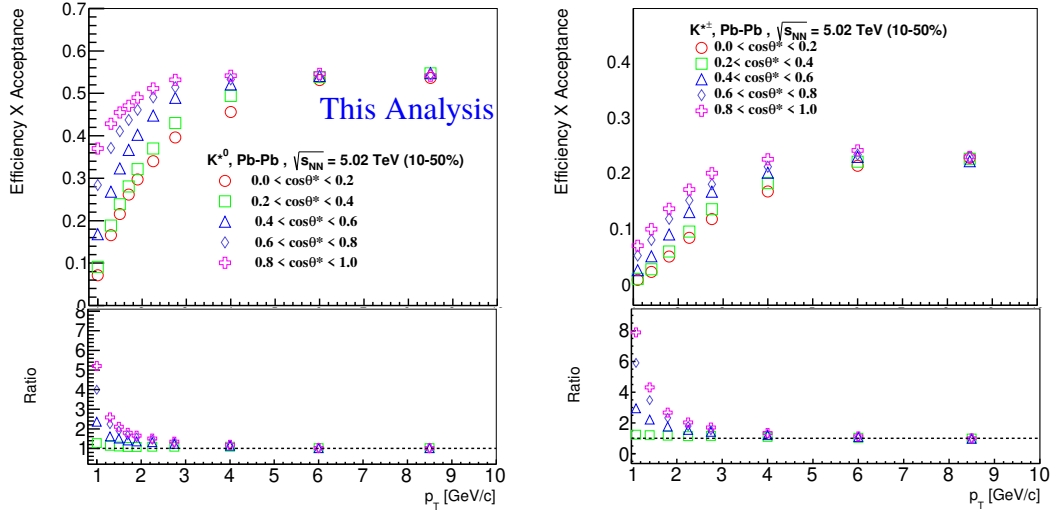
FIGURE 6.9: Upper panel: Efficiency × acceptance as a function of p_T for various $\cos\theta^*$ bins for K^{*0} (left) and for $K^{*\pm}$ (right). In lower panel, it is the ratio of efficiency × acceptance in different $\cos\theta^*$ bins to the efficiency × acceptance of the $\cos\theta^*$ bin 0.0 to 0.2 for 10–50 % centrality class in Pb–Pb collisions at $\sqrt{s_{NN}}$ = 5.02 TeV.

6.5.1   Re-weighted Efficiency × Acceptance

The shape of generated p_T spectra may have different from the p_T spectra of measurement. So, it is necessary to weight the generated and reconstructed p_T spectra of Monte Carlo simulation (a detailed procedure for calculating the re-weighted factor is discussed in the Section 3.3.3 of Chapter 3). The re-weighted factor on efficiency × acceptance as a function of p_T for K^{*0} (left) and $K^{*\pm}$ (right) in various $\cos\theta^*$ ranges is shown in Fig. 6.11 and for ϕ is shown in Fig. 6.12 for the centrality class 10–50% in Pb–Pb collisions at $\sqrt{s_{NN}}$ = 5.02 TeV using production plane. The re-weighted correction factor varies 1-2% for both K^{*0} and $K^{*\pm}$, whereas this correction factor varies 5-13 % for ϕ at low p_T region.
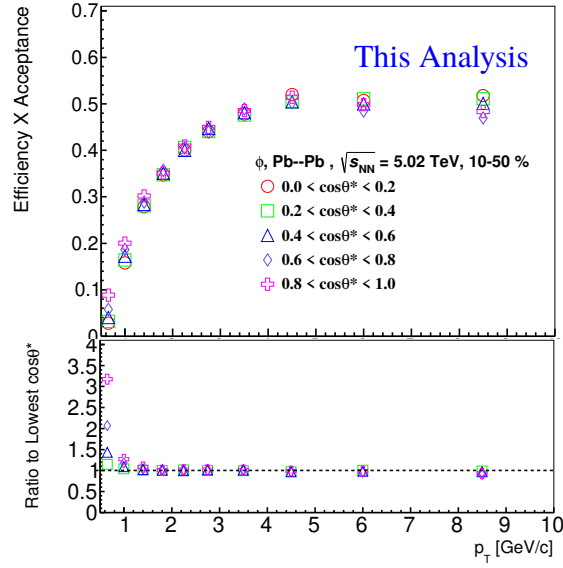
FIGURE 6.10: Upper panel: Efficiency × acceptance of ϕ meson as a function of p_T for various $\cos\theta^*$ bins and In lower panel, it is the ratio of efficiency × acceptance in different $\cos\theta^*$ bins to the efficiency × acceptance of the $\cos\theta^*$ bin 0.0 to 0.2 for 10-50 % centrality class in Pb–Pb collisions at $\sqrt{s_{NN}}$ = 5.02 TeV.
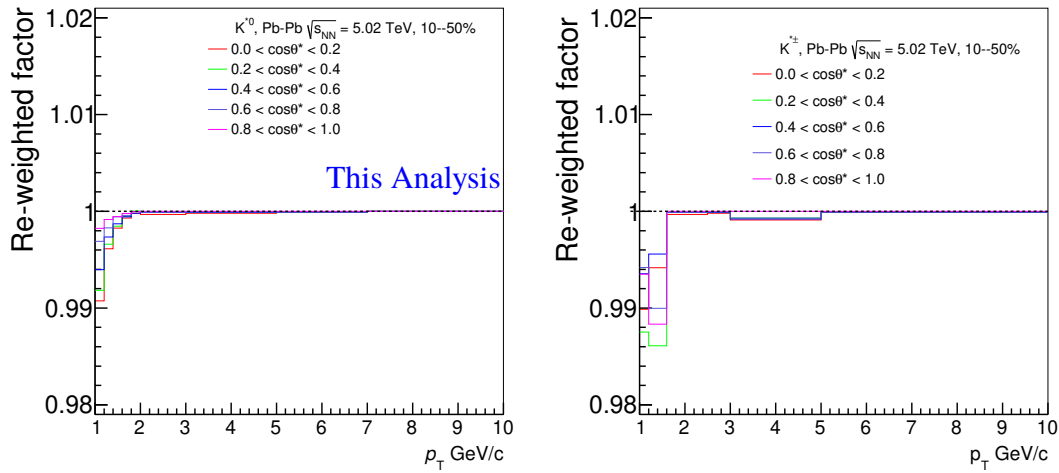
FIGURE 6.11: Re-weighted factor on efficiency × acceptance as a function of p_T for various $\cos\theta^*$ ranges for K^{*0} (left) and for $K^{*\pm}$ (right) in the centrality class 10–50 % for Pb–Pb collisions at $\sqrt{s_{NN}}$ = 5.02 TeV using production plane study.
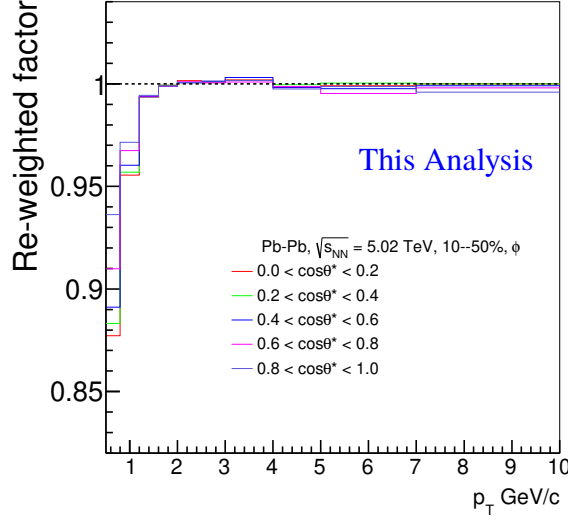
FIGURE 6.12: Upper panel: Efficiency × acceptance of ϕ meson as a function of p_T for various $\cos\theta^*$ bins. In the lower panel, it is the ratio of efficiency × acceptance in different $\cos\theta^*$ bins to the efficiency × acceptance of the $\cos\theta^*$ bin 0.0 to 0.2 for 10-50 % centrality class in Pb–Pb collisions at $\sqrt{s_{NN}}$ = 5.02 TeV.

6.6 Corrected p_T spectra

The extracted raw yield is corrected with efficiency ×acceptance and branching ratio. Corrected p_T spectra in different $\cos\theta^*$ ranges is shown the upper panel of the Fig. 6.13 for K^{*0} (left) and $K^{*\pm}$ (right) for centrality class 10–50% in Pb–Pb collisions at $\sqrt{s_{NN}}$ = 5.02 TeV. The the lower panels show the ratio of corrected p_T spectra in different $\cos\theta^*$ range to the p_T spectrum of the $\cos\theta^*$ in the interval 0.0 to 0.2 for 10–50% centrality class in Pb–Pb collisions at $\sqrt{s_{NN}}$ = 5.02 TeV. It is found that a strong $\cos\theta^*$ dependence is observed at low p_T region for both K^{*0} and $K^{*\pm}$. Upper panel of the Fig. 6.14 represents the corrected p_T spectra of ϕ for various $\cos\theta^*$ intervals. Lower panel shows the ratio of p_T spectra for various $\cos\theta^*$ interval to p_T spectra in the $\cos\theta^*$ interval 0 to 0.2 for centrality class 10–50% in Pb–Pb collisions at $\sqrt{s_{NN}}$ = 5.02 TeV. The results are presented here using production plane analysis. A $\cos\theta^*$ dependence is also observed for ϕ at low p_T (< 1
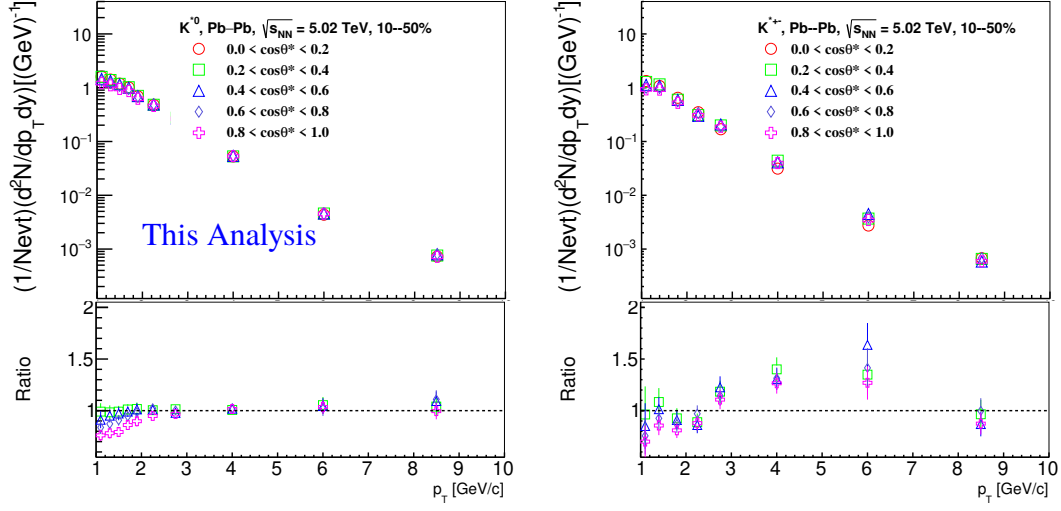
FIGURE 6.13: Left figure: Upper panel shows corrected transverse momentum spectra for different $\cos\theta^*$ and lower panel shows the ratio of corrected p_T in different $\cos\theta^*$ bins to the corrected p_T spectrum of the $\cos\theta^*$ bin 0.0 to 0.2 for K^{*0} and $K^{*\pm}$ (right). Results for 10–50% centrality class in Pb–Pb collisions at $\sqrt{s_{NN}}$ = 5.02 TeV. Statistical uncertainties are shown only.

GeV/c). Similarly, the $\cos\theta^*$ dependence is observed for K^{*0} and ϕ mesons in centrality class 10–50% for Pb–Pb collisions at $\sqrt{s_{NN}}$ = 5.02 TeV using helicity frame analysis shown in Fig. D.10 and Fig. D.11, respectively in the Appendix. The yield of vector mesons are summed over $\cos\theta^*$ bins for each p_T interval to get the $\cos\theta^*$ integrated p_T spectra. These measured p_T spectra are found to be consistent with the published results [9] within uncertainties for K^{*0}, and ϕ. The $\cos\theta^*$ integrated p_T of $K^{*\pm}$ is also consistent with the $K^{*\pm}$ spectra [16] in Pb–Pb collisions at $\sqrt{s_{NN}}$ = 5.02 TeV. Comparisons of consistency check of vector mesons (K^{*0}, $K^{*\pm}$ and ϕ) p_T spectra from $\cos\theta^*$ integrated and default p_T spectra measurement is shown in Fig. D.12 and Fig. D.13 in the Appendix.
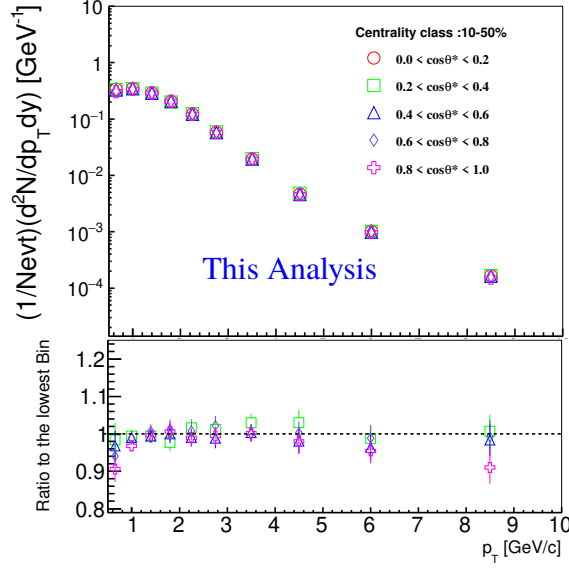
FIGURE 6.14: Upper panel show corrected transverse momentum spectra for different $\cos\theta^*$ and lower panel show the ratio of corrected p_T in different $\cos\theta^*$ bins to the corrected p_T spectrum of the $\cos\theta^*$ bin 0.0 to 0.2 for ϕ in 10–50% centrality class of Pb–Pb collisions at $\sqrt{s_{NN}}$ = 5.02 TeV. Statistical uncertainties are shown only.

6.6.1 Angular distributions and ρ_{00} for vector mesons

The angular distribution, one of the decay products of vector mesons are obtained from the corrected p_T spectra of various $\cos\theta^*$ bins. The corrected $\cos\theta^*$ distribution for p_T interval 1.0–1.2 GeV/c is shown in Fig. 6.15 for K^{*0} (left) and for K$^{*\pm}$ (right) in Pb–Pb collisions for centrality class 10–50% at $\sqrt{s_{NN}}$ = 5.02 TeV. The corrected $\cos\theta^*$ distribution for p_T bin 0.5–0.8 GeV/c is shown in Fig. 6.16 for ϕ in Pb–Pb collisions for 10–50% at $\sqrt{s_{NN}}$ = 5.02 TeV. The corrected $\frac{1}{N_{evt}}\frac{dN}{d\cos\theta^*}$ is fitted with the Eq. 6.1 to obtain ρ_{00}. The ρ_{00} values are obtained from various p_T bins for centrality class 10–50%. The non-uniform dependence in $\cos\theta^*$ distributions are observed at low p_T, whereas no angular dependence is seen at high p_T for vector mesons, consistent with no spin alignment criteria, ρ_{00} = 1/3.

The corrected $\cos\theta^*$ distribution for p_T bin 0.5 -0.8 (GeV/c) is shown in Fig. 6.17 for ϕ meson using helicity frame. The non-uniform $\cos\theta$ distribution is observed at low
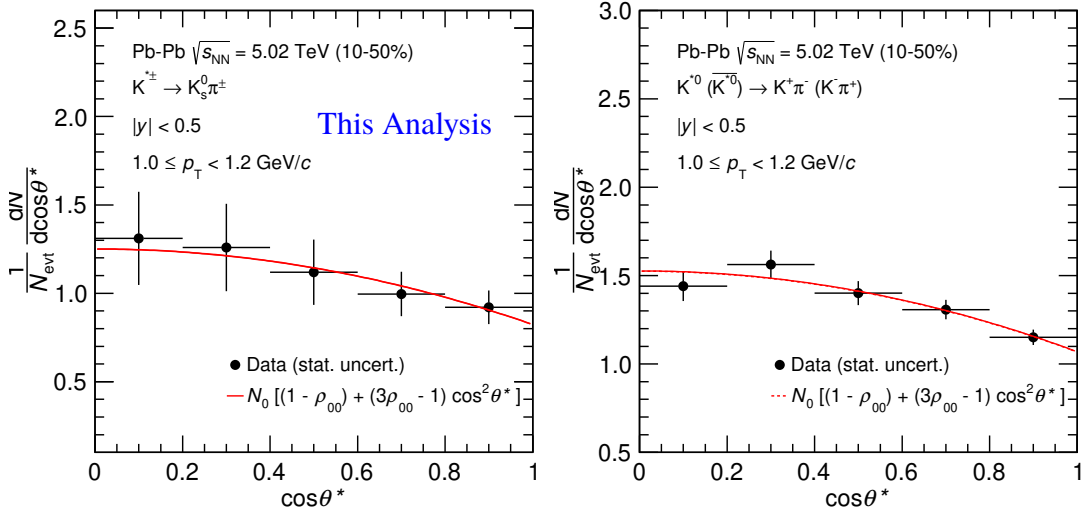
FIGURE 6.15: Corrected $\cos\theta^*$ distribution for the transverse momentum bins ($1.0 < p_T < 1.2$ GeV/c for $K^{*\pm}$ (left) and for K^{*0} (right) in Pb–Pb collisions for 10–50% centrality class at $\sqrt{s_{NN}} = 5.02$ TeV. The distribution is fitted with the Eq. 6.1. Statistical error is shown only.
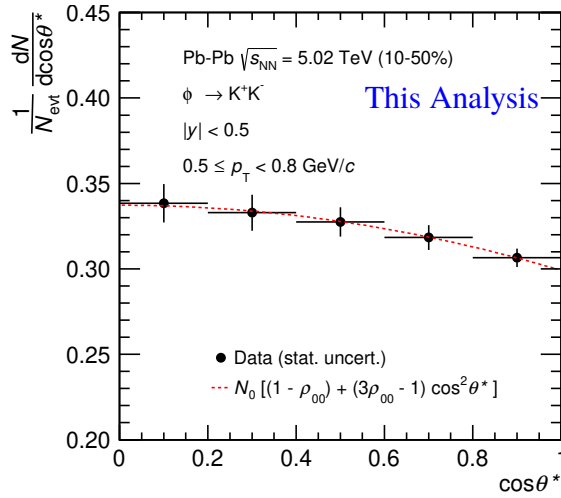
FIGURE 6.16: Corrected $\cos\theta^*$ distribution for the transverse momentum bins ($0.5 < p_T < 0.8$ GeV/c for 10–50% centrality class in Pb–Pb collisions at $\sqrt{s_{NN}} = 5.02$ TeV for ϕ. The distribution is fitted with the Eq. 6.1. Statistical error is shown only.

p_T. The distribution seems opposite to the trend observed in the production plane. The detail angular distribution of vector mesons for all p_T bins are shown in Fig. D.14 for K^{*0},
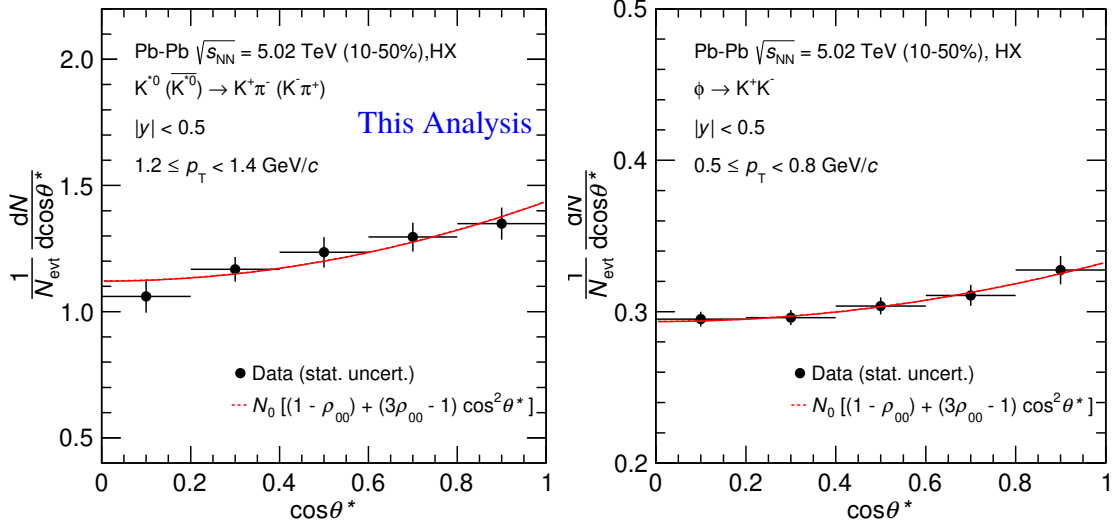
FIGURE 6.17: Corrected $\cos\theta^*$ distribution for the transverse momentum bins $(0.5 < p_T < 0.8$ (GeV/c) for 10–50% centrality class with helicity frame in Pb–Pb collisions at $\sqrt{s_{NN}}$ = 5.02 TeV. The distribution is fitted with the Eq. 6.1. Statistical error is shown only.

Fig. D.15 for $K^{*\pm}$, and Fig. D.16 for ϕ using the production plane study and similarly for

helicity frame analysis for K^{*0} and ϕ are shown in Fig. D.17 and Fig. D.18 in the Appendix.

6.7   Systematic uncertainties

Systematic uncertainties on ρ_{00} are calculated by varying the default selection criteria. A

similar method is adopted to calculate the systematic uncertainty on ρ_{00} used for previous

measurement [3]. A particular variation with respect to default selection criteria is taken

as a source of systematic uncertainties. The left panel of Fig. 6.18 shows the fractional

uncertainties on ρ_{00} as a function of p_T due to signal extraction for K^{*0} in Pb–Pb collisions

at $\sqrt{s_{NN}}$ = 5.02 TeV using production plane analysis. The source of signal extraction

includes variation in the signal peak fitting range, width variation, mixed-event background

normalization region, and choice of residual background function. The total uncertainty

due to signal extraction is calculated as the quadrature sum of an individual source of

variations. The total fractional uncertainty shown in the black line varies from 3–15% for K^{*0} in the centrality class 10–50% for Pb–Pb collisions at $\sqrt{s_{NN}}$ = 5.02 TeV. The right panel of Fig. 6.18 shows fractional uncertainties on ρ_{00} as a function of p_T due to source of signal extraction, track variable and particle identification (PID) for ϕ in centrality class 10–50% in Pb–Pb collisions at $\sqrt{s_{NN}}$ =5.02 TeV. The source of signal extraction variation is the same as discussed above for K^{*0}. For source of track variables, including the number of crossed rows in the TPC, the ratio of TPC crossed rows to findable clusters and the distance of the closest approach to the primary vertex of the collisions. For PID variation, the selection on the TPC dE/dx of $2\sigma_{TPC}$ only is used for systematic. The total systematic uncertainty
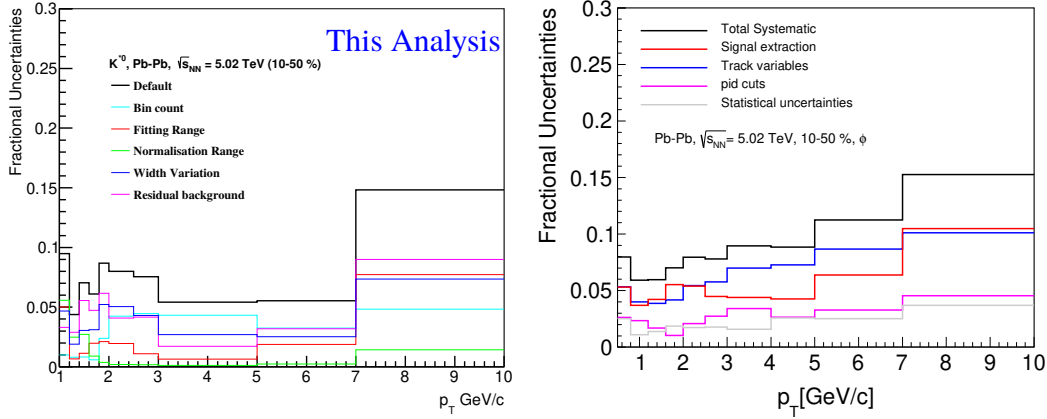
FIGURE 6.18: Left figure : Fractional uncertainties as a function of p_T for K^{*0} in the centrality class 10–50% for Pb–Pb collisions at $\sqrt{s_{NN}}$ = 5.02 TeV. Right figure : Fractional uncertainties as a function of p_T for ϕ in the centrality class 10–50% for Pb–Pb collisions at $\sqrt{s_{NN}}$ = 5.02 TeV.

shown in the black line varies from 5–15% for ϕ in the centrality class 10–50% in Pb–Pb collisions at $\sqrt{s_{NN}}$ = 5.02 TeV. Comparison of ρ_{00} as a function of p_T for various sources of systematic uncertainties and default selection criteria for signal extraction of K^{*0} is shown in Fig. D.19. The left of Fig. D.20 for signal extraction and the right of the Fig. D.20 for track variables along with PID are shown, respectively, for ϕ in Pb–Pb collisions at $\sqrt{s_{NN}}$

= 5.02 TeV in the Appendix.

6.8   Results

6.8.1   Transverse momentum dependence of ρ_{00}
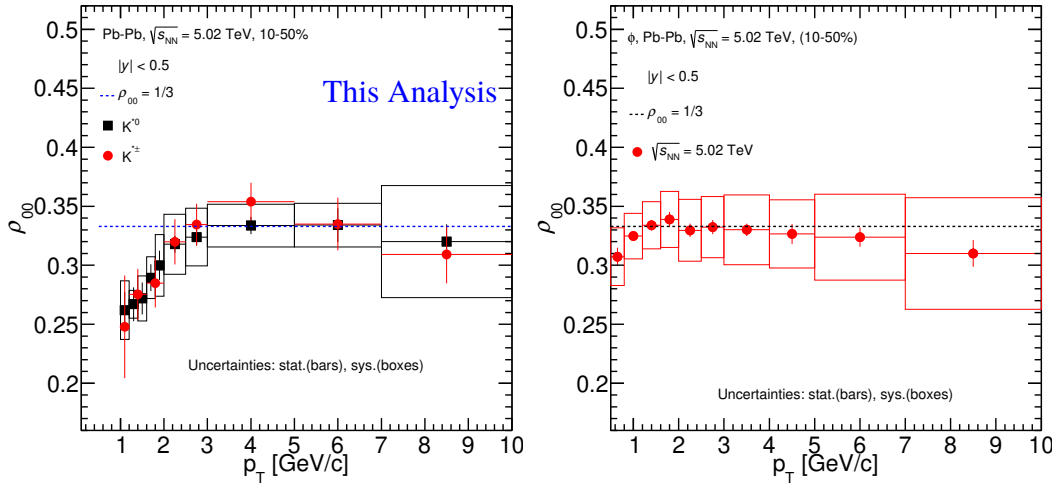
FIGURE 6.19: Left figure: ρ_{00} as a function of p_T for K^{*0} (black markers) and $K^{*\pm}$ (red markers) in
the centrality class 10–50% for Pb–Pb collisions at $\sqrt{s_{NN}}$ = 5.02 TeV. Right figure:
ρ_{00} as a function of p_T for ϕ in the centrality class 10–50% for Pb–Pb collisions at
$\sqrt{s_{NN}}$ = 5.02 TeV. Results are obtained using the quantization axis perpendicular to
the production plane.

Transverse momentum dependence of the ρ_{00} for vector mesons (K^{*0}, $K^{*\pm}$ and ϕ) have
been studied at midrapidity ($|y| < 0.5$) in the centrality class 10–50% for Pb–Pb collisions
at $\sqrt{s_{NN}}$ = 5.02 TeV using production plane and helicity frame analysis. The Left panel
of Fig. 6.19 for K^{*0} and $K^{*\pm}$, and right panel of Fig. 6.19 for ϕ show ρ_{00} as a function
of p_T for 10–50% in Pb–Pb collisions at $\sqrt{s_{NN}}$ = 5.02 TeV using production plane. It is
observed that ρ_{00} deviates from 1/3 (no spinalignment criteria) at low p_T (< 2–3 GeV/c),
whereas it consistent with 1/3 at high p_T. The ρ_{00} values of K^{*0} and $K^{*\pm}$ are consistent
with uncertainties. Similarly, ϕ shows slightly deviation from 1/3 at low p_T (< 1 GeV/c),

whereas consistent with 1/3 within uncertainties at high p_T (> 1 GeV/c). Measured spin alignment effect on ρ_{00} for K$^{*0,\pm}$ is higher than ϕ at low p_T. The observed p_T dependence of ρ_{00} are qualitatively described by quark-recombination model [4]. In quark polarization model predicts that the maximum deviation of ρ_{00} from 1/3 is expected at low p_T at mid-central collisions, whereas ρ_{00} consistent with 1/3 at high p_T. It also suggested that the effect of spin alignment is expected to be larger for K^{*0} than ϕ due to their different constituent quark composition. Even though the quark-recombination model describes qualitatively the measurements, but quantitatively the measured values of spin alignment are suppersingly larger compared to Λ polarization measurements at both RHIC and LHC energies [17, 18].

6.8.2 Energy dependence of ρ_{00}
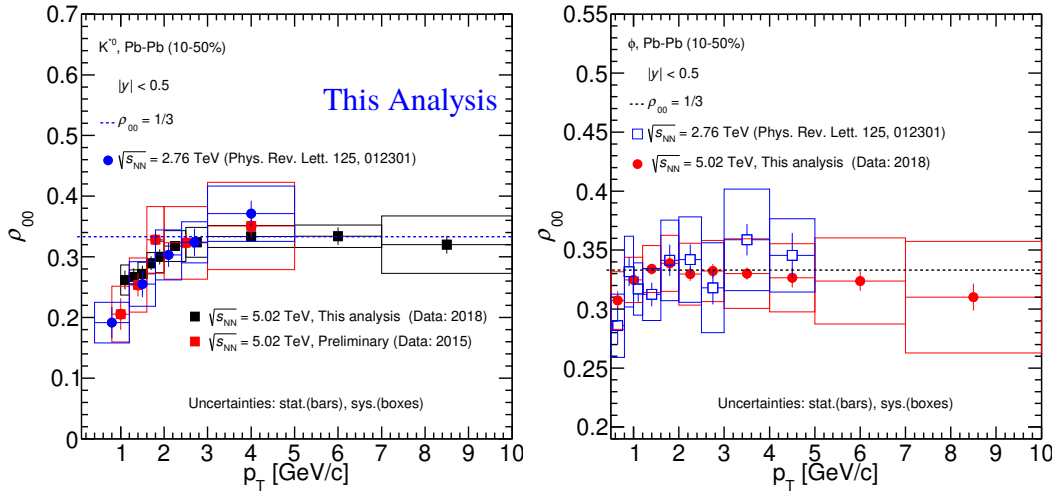
FIGURE 6.20: Left figure: ρ_{00} as a function of p_T for K^{*0} in the centrality class 10–50 % for Pb–Pb collisions at $\sqrt{s_{NN}} = 2.76$ and 5.02 TeV. Black marker stands for published results at $\sqrt{s_{NN}} = 2.76$ TeV [3]. Red marker represents the preliminary results (red marker) taken from [19] and black marker represents high statistics measurement for Pb–Pb collisions at $\sqrt{s_{NN}} = 5.02$ TeV. Right figure: Comparison of ρ_{00} as a function of p_T for ϕ in Pb–Pb collisions at $\sqrt{s_{NN}} = 2.76$ (blue) and 5.02 TeV (red).

Figure 6.20 (left) shows energy dependence comparison of ρ_{00} as a function of p_T for K^{*0} at midrapidity for centrality class 10–50% in Pb–Pb collisions at $\sqrt{s_{NN}}$ = 2.76 and 5.02 TeV. Figure 6.20 (right) shows ρ_{00} as a function of p_T at midrapidity for 10–50% centrality class in Pb–Pb collisions at $\sqrt{s_{NN}}$ = 2.76 and 5.02 TeV for ϕ. It is observed that ρ_{00} slightly deviates from 1/3 at low p_T whereas it is consistent with no spin alignment criteria at high p_T. The ρ_{00} values are similar and consistent with each other within uncertainties at $\sqrt{s_{NN}}$ = 2.76 and 5.02 TeV, suggesting no significant energy dependence is observed at LHC energy in heavy-ion collisions. Recent measurements from STAR
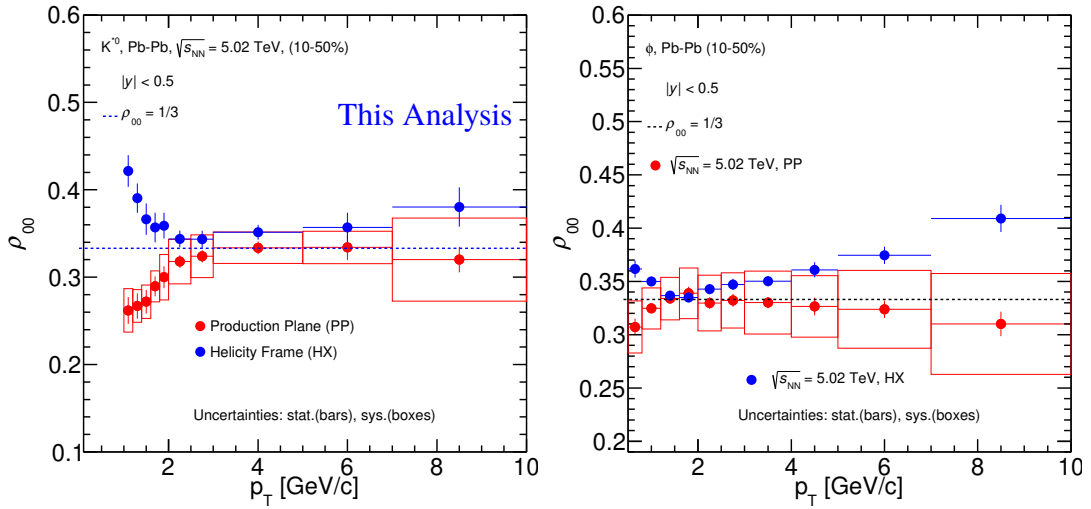
FIGURE 6.21: Left figure: ρ_{00} as a function of p_T for K^{*0} (left) and ϕ (right) at midrapidity for 10–50% centrality class in Pb–Pb collisions at $\sqrt{s_{NN}}$ = 5.02 TeV. Results are obtained form both production plane and helicity frame analysis.

experiments predict collisions energy dependence of spin alignment for vector mesons [20]. The strong-meson field which describes the trend of measurement for ϕ meson [20, 21]. The collision energy dependence of polarization order varies from 1% to 0.1% for the Λ hyperon from low to high beam energy [17]. The value of polarization is higher compared to vector meson polarization. According to quark recombination model [4], the ρ_{00} is

linearly related to polarization vector for Λ hyperon, whereas it is related to square of polarization vector for vector mesons. These assumptions do not yet provide a complete understanding of the measured polarization difference between vector mesons and lambda hyperons. Recent measurements from J/ψ measurements with helicity and event plane show non-zero longitudinal and transverse polarization [22]. It is also interesting to look at the spin alignment of vector mesons using different quantization axes that can help to disentangle local spin alignment effects from global spin alignment. Figure 6.21 shows comparison of ρ_{00} as a function p_T for K^{*0} (left) and ϕ (right) in the centrality class 10–50% for Pb–Pb collisions at $\sqrt{s_{NN}}$ = 5.02 TeV using both production plane and helicity frame. It is observed that ρ_{00} deviates from 1/3 at low p_T but the opposite trend is observed for both vector mesons. This result indicates that extraction of spin alignment of vector mesons depends on the quantization axis and also there is relation between production plane and helicity frame. In future, the different model predictions and numerical relations between both quantization axes will further provide a better understanding of local and global effects on ρ_{00}.

6.9 Summary

We report the spin alignment measurement of vector mesons (K^{*0}, $K^{*\pm}$, ϕ) at midrapidity ($|y|$ <0.5) for centrality class (10–50%) in Pb–Pb collisions at $\sqrt{s_{NN}}$ = 5.02 TeV. Spin alignment (a deviation of ρ_{00} from 1/3) of vector mesons is observed at low p_T for mid-central Pb–Pb collisions. It supports the quark recombination scenario of spin alignment due to the large initial angular momentum created in non-central heavy-ion collisions. The spin alignment of K^{*0} and $K^{*\pm}$ are similar, even though the difference in the magnetic moment between them suggests that initial magnetic field does not play a significant role.

The measurements are compared with previous measurements in Pb–Pb collisions at $\sqrt{s_{NN}}$ = 2.76 TeV; it is found that ρ_{00} values of both energies are consistent with each other within uncertainties. Spin alignment measurements of K^{*0} and ϕ using the quantization axis along the momentum direction of vector mesons show deviation from 1/3 at low p_T with the opposite trend as observed using the quantization axis normal to the production plane. In future measurements, spin alignment studies with different quantization axes, measurement of azimuthal angle and off-diagonal spin density matrix elements can be used to understand global and local vector mesons polarization.

Bibliography

[1] F. Becattini et al., Phys. Rev. C 77, 024906, (2008).

[2] D. E. Kharzeev et al., Nucl. Phys. A 803, (2008).

[3] S. Acharya et al., [ALICE Collaboration], Phys. Rev. Lett. 125. 012301, (2020).

[4] Z.T.Liang et al., Phys. Lett. B 629, 20, (2005).

[5] B.I. Abelev et al., [STAR Collaboration], Phys. Rev. C 77, 061902, (2008).

[6] X.L. Xia et al., Phys. Lett. B 817, 136325, (2021).

[7] J.H. Gao et al., Phys. Rev. D 104 7, 076016, (2021).

[8] D. mallick et al., [ALICE Collaboration], https://alice-notes.web.cern.ch/node/1340, (2022).

[9] S. Acharya et al., [ALICE Collaboration], Phys. Lett. B 802, 135225, (2020).

[10] S. Acharya et al., [ALICE Collaboration], Phys. Lett. B 828 137013, (2022).

[11] E. Abbas et al., [ALICE Collaboration], J. Instrum. 8, P10016, (2013).

[12] B. Abelev et al., [ALICE Collaboration], Int. J. Mod. Phys. A 29, 1430044, (2014).

[13] B.B. Abelev et al., [ALICE Collaboration], Phys. Rev. Lett. 111, 222301, (2013).

[14] A. Akindinov et al., [ALICE Collaboration], Eur.Phys.J.Plus 128, 44, (2013).

[15] M. Gyulassy et al., Comput.Phys.Commun. 83, 307, (1994).

[16] P. das et al., [ALICE Collaboration], https://alice-notes.web.cern.ch/node/1215, (2021).

[17] L. Adamczyk et al., [STAR Collaboration], Nature 548, 62-65, (2017).

[18] S. Acharya et al., [ALICE Collaboration], Phys. Rev. C 101, 044611, (2020).

[19] Bedanga et al., [ALICE Collaboration], https://alice-notes.web.cern.ch/node/636, (2017).

[20] X. Sun et al., [STAR Collaboration], https://arxiv.org/abs/2204.02302, (2022).

[21] Sheng, X.-L. et al.,Phys. Rev. D 101, 096005 (2020).

[22] S. Acharya et al., [ALICE Collaboration], arXiv:2204.10171, (2022).

Summary

Resonances are short-lived particles with a lifetime of a few fm/c and decay via the strong interaction. Due to their short lifetime, they are sensitive probe to characterize the hadronic phase. At the LHC energies, the hadronization temperature and chemical freeze-out temperature are very close. The phase between chemical freeze-out (when inelastic collisions among the constituents cease) and kinetic freeze-out (when elastic collisions ceases) is referred to as the hadronic phase. The decay products of resonances can elastically interact with other hadrons and change their momentum in the hadronic phase. As a result, the parent resonance can not be reconstructed experimentally, leading to a suppression in the final resonance yield. This process is known as the rescattering effect. Similarly, another process is that the hadrons inside the hadronic phase can regenerate a resonance via pseudo-elastic interaction (for example: $K\pi \rightarrow K^{*0} \rightarrow K\pi$). This effect is known as regeneration; it enhances the final measured resonance yield relative to primary production. The interplay between the rescattering and the regeneration effects are studied by measuring the ratio of the resonance yield to stable hadron yield with similar quark content. Modification of the resonance yields in the hadronic phase through rescattering

195

and regeneration processes, bulk properties and mechanism of high p_T particle production and parton energy loss in p–Pb collisions are discussed in this thesis. Rapidity dependence of K^{*0} production in p–Pb collisions is also discussed to understand the initial nuclear state effects and final multiplicity effect on resonance production at LHC energies. Considering the importance of spin-orbital interaction in various fields of physics (atomic, condensed matter, and spintronics), study of this interaction is also of great interest in the QCD matter created in ultra-relativistic heavy-ion collisions. A large initial angular momentum ($\vec{L}$) of the order (10^{6-7} $\hbar$), and magnetic field ($|\vec{B}|$) of the order (10^{18} Gauss) expected to be generated in non-central heavy-ion collisions, its interaction with vector mesons having non-zero spin can lead to the phenomena of spin-orbital coupling. The production of vector meson $K^{*0,\pm}$ and ϕ mesons are considered ideal candidates to study the spin-orbit interaction. The spin-orbit interaction provides information about the response of initial conditions of collisions to the medium created in such collisions and aid in understanding how the polarization of quarks translates to the final hadron produced such a study is presented in this thesis. . The detailed analysis and results presented in this thesis are summarized here. We have carried out several new measurements using pp, p–Pb and Pb–Pb collisions at LHC energies. In addition to the introduction and details about the experimental setup, the new results presented in various chapters of the thesis are discussed as follows:

- Multiplicity dependence of $K^{*0,\pm}$ production in p–Pb collisions at LHC energies.

- Rapidity dependence of K^{*0} production in p–Pb collisions at $\sqrt{s_{NN}}$ = 5.02 TeV.

- Production of K^{*0} in pp collisions at $\sqrt{s}$ = 7 TeV.

- Spin alignment of vector mesons ($K^{*0,\pm}$, ϕ) in Pb–Pb collisions at $\sqrt{s_{NN}}$ = 5.02 TeV.

Recent measurements of collective flow-like-effect, double ridge structure, strangeness enhancement, and suppression of resonance yields compared to minimum bias pp collisions show striking similarities between small systems and heavy-ion collisions. These observations initiate huge interest in understanding the underlying physics behind the high multiplicity study among experimental and theoretical physicists. The measurements in proton-nucleus (p–Pb) collisions also play a crucial role in disentangling initial cold nuclear matter effects from final state effects of hot dense matter produced in heavy-ion collisions. We have studied K^{*0} production at a center-of-mass energy per nucleon, $\sqrt{s_{NN}} = 8.16$ TeV and $K^{*\pm}$ at $\sqrt{s_{NN}} = 5.02$ TeV in p–Pb collisions for minimum bias and various multiplicity classes. We have found that the shape and slope of K^{*0} p_T spectra changes with charged-particle multiplicity. It is observed that the measured K^{*0} p_T spectrum in p–Pb collisions at $\sqrt{s_{NN}} = 8.16$ TeV have higher inverse slope compared to the K^{*0} p_T spectrum in p–Pb collisions at $\sqrt{s_{NN}} = 5.02$ TeV. The ratio of K^{*0} p_T spectrum between 5.02 and 8.16 TeV is consistent with unity within uncertainties at low p_T (< 1 GeV/c). This ratio increases with p_T and collision energies, indicating that the dominance of hard processes or high p_T particle production increases with collision energy in the Section 3.6.1. The dN/dy and $\langle p_T \rangle$ as a function of charged-particle multiplicity are reported and compared with previous results in pp, p–Pb and Pb–Pb collisions. It is observed that the event multiplicity mainly drives the resonance production. The $\langle p_T \rangle$ values increase with multiplicity, and the rise is steeper for small collisions compared to Pb-Pb collisions in the Section 3.6.2. To understand the hadronic phase effect in p–Pb collisions, we have measured K^{*0}/K as a function of charged particle multiplicity. The ratio K^{*0}/K shows a decreasing trend as a function of charged particle multiplicity similar to that observed in heavy-ion collisions. This observation suggests the possible finite hadronic phase in high multiplicity p–Pb colliding system at LHC energies in the Setion 3.6.3. Empirical x_T (= $2p_T/\sqrt{s_{NN}}$) scaling

is tested for K^{*0} in p–Pb collisions at LHC energies. The x_T scaling is observed and the exponent (n) value is ∼ 5. The value of exponent n at LHC energies is lower than at RHIC energies. Further, the n value of K^{*0} is similar to ϕ in p–Pb collisions and also compatible with the corresponding values obtained in pp collisions for $\pi^{\pm}$, $K^{\pm}$ and K^{*0}. This suggests that the high p_T particle production mechanism is similar in both pp and p–Pb colliding systems at LHC energies in the Section 3.6.4. To investigate the parton energy loss in p–Pb collisions, nuclear modification factors (R_{pPb}) are measured. The R_{pPb} as a function of p_T for K^{*0} at $\sqrt{s_{NN}}$ = 8.16 TeV are compared with the R_{pPb} measurements of K^{*0}, ϕ, Ξ, and Ω at $\sqrt{s_{NN}}$ = 5.02 TeV in the Section 3.6.5. At intermediate p_T (2 – 8 GeV/c), the R_{pPb} of Ξ, and Ω show a Cronin-like enhancement, while K^{*0} show no or little nuclear modification. At high p_T (> 8 GeV/c), the R_{pPb} values of all hadrons are consistent with unity within uncertainties in contrast to suppression in R_{AA} in heavy-ion collisions. The R_{pPb} of K^{*0} at $\sqrt{s_{NN}}$ = 5.02 and 8.16 TeV show no significant energy dependence. Measurements are also compared with model predictions such as HIJING, DPMJET, and EPOS-LHC. The EPOS-LHC model, which includes parameterized flow, gives a good quantitative description of energy dependence p_T spectra and the scaled p_T-integrated yields. It also qualitatively describes the increase in $\langle p_T \rangle$ values with multiplicity.

The p–Pb is an asymmetric and intermediate colliding system compared to the pp and Pb–Pb collisions. One expects the mechanism of particle productions are different in forward (p−going) and backward (Pb−going) rapidities. The partons from the p−going side are expected to undergo multiple scattering while traversing the Pb-nucleus. Those on the Pb−side, are likely to be affected by the properties of the nucleus. The various particle production mechanisms are expected to influence by different effects like nuclear modification of the parton distribution functions (nuclear shadowing) and possible parton saturation, multiple scattering, and radial flow in forward and backward rapidities. In

addition, the p−Pb collisions at Large Hadron Collider (LHC) energies enable probing the parton distribution functions in nuclei at very small values of the Bjorken x variable, where gluon saturation effects may occur. In this thesis, we have reported the first measurement of the rapidity dependence of K^{*0} meson production in p−Pb collisions at $\sqrt{s_{NN}}$ = 5.02 TeV by the ALICE experiment at the LHC. The large size of the data sample collected in 2016 and the excellent particle identification using ALICE detectors provided an opportunity to extend these measurements in a wider rapidity intervals and multiplicity classes. Further the results are compared to previous midrapidity measurements. The p_T spectra, dN/dy and $\langle p_T \rangle$ and their ratios have been studied in the rapidity range -1.2 < y < 0.3 and for four multiplicity classes. The rapidity and multiplicity dependence effects have been seen in the measured p_T spectra at low p_T, whereas no significant dependence is observed at high p_T (> 5 GeV/c) in the Section 4.5.1. The (dN/dy)/(dN/dy)$_{y=0}$ decreases with increasing rapidity in the measured interval -1.2 < y < 0.3, whereas the $\langle p_T \rangle$ and the $\langle p_T \rangle$/$\langle p_T \rangle_{y=0}$ ratios show a flat behavior as a function of y for all multiplicity classes in the Section 4.5.2. In addition, to understanding the asymmetry of particle production in forward and backward rapidity, a quantity known as rapidity asymmetry (Y_{asym}) is measured. The Y_{asym} is calculated as the ratio of the particle yield between Pb−and p-going directions in the Section 4.5.3. The Y_{asym} is measured as a function of p_T in the rapidity interval 0.0 < |y| < 0.3 for four multiplicity classes. Experimentally, it is a good observable because several systematic uncertainties cancel out in the ratio. Hence, it helps to discriminate rapidity-dependent effects by comparing the results from various models to the measurement. The Y_{asym} is observed at low p_T (< 5 GeV/c), more significant for higher multiplicity classes. At high p_T, no Y_{asym} is observed for all the multiplicity classes studied. The Y_{asym} is similar for K^{*0} and ϕ in the measured rapidity range in p–Pb collisions at $\sqrt{s_{NN}}$ = 5.02 TeV. Further, to investigate the evolution of the nuclear effect, the nuclear modification factor (Q_{CP}) of

K^{*0} as a function of p_T for various rapidity intervals is measured in the Section 4.5.4. The Q_{CP} is calculated as the ratio of yields of K^{*0} normalized to the corresponding number of binary collisions ($\langle N_{coll}\rangle$) in high multiplicity (central) and low multiplicity (peripheral) collisions. The Q_{CP} as a function of p_T shows a bump, with a maximum around p_T =3 GeV/c. It suggests the presence of Cronin-like enhancement. This Cronin-like enhancement is more pronounced for higher rapidity and high multiplicity classes. The measurements suggest that nuclear effects play an important role in particle production in p–Pb collisions at the LHC energies. Measurements are also compared with different model predictions. It is found that the EPOS-LHC model provides a good description of the dN/dy and $\langle p_T\rangle$, whereas HIJING predictions are closer to the measurements of the ratios (dN/dy)/(dN/dy)$_{y=0}$ and $\langle p_T\rangle$/$\langle p_T\rangle_{y=0}$ with rapidity.

In this thesis, we have studied K^{*0} production in minimum-bias pp collisions at $\sqrt{s}$ = 7 TeV. Compared to the previous study, it is an improved and extended measurement of the transverse momentum spectrum up to p_T = 20 GeV/c. It includes the p_T-distribution, dN/dy, $\langle p_T\rangle$, p_T-integrated particle ratios of inelastic pp collisions. The collision energy dependence in p_T spectrum is observed at high p_T. It increases with p_T and collision energy due to increasing the hard-scattering contribution with collision energy in the Section 5.4.1. Empirical m_T and x_T-scaling are tested for K^{*0} resonance along with identified hadrons in pp collisions at LHC energies in the Section 5.4.2. At p_T > 2 GeV/c, breaking of m_T scaling behavior is observed for mesons and baryons. The m_T spectrum of pion deviates at low m_T or low p_T from the universal m_T scaling of other mesons; it is likely due to feed-down from resonance decays. The x_T-scaling holds fairly well for K^{*0} resonance and other identified hadrons (π, K and p) produced in pp collisions at the LHC energies. The exponent value is $\sim$ 5 and the value for baryon is slightly higher than for meson. At low p_T, no collision energy dependence is seen in the p_T-spectrum, where soft processes govern particle production.

No collision energy dependence in the p_T-integrated particle ratios (K^{*0}/K, ϕ/K, ϕ/K^{*0}) are observed in inelastic pp collisions in the Section 5.4.3. The pp measurements act as a reference for the measurements in p–Pb and Pb–Pb collisions.

In ultra-relativistic high energy collisions, spin polarization studies have drawn much attention in both theory and experiment to understand the initial condition of collisions, as spin degree of freedom provides us a unique opportunity to probe the QGP at a quantum level. In non-central relativistic heavy-ion collisions, when two nuclei collide with nonzero impact parameters, a large orbital angular momentum ($\vec{L}$) of O(10^{6-7} $\hbar$), and magnetic field ($|\vec{B}|$) of O(10^{18} Guass) are expected to be created. As the angular momentum is a conserved quantity, its effect could be present throughout the evolution of the system, whereas the magnetic field is transient. In the presence of large initial angular momentum, vector mesons (spin = 1) can be polarized due to the spin-orbital interaction of QCD. The spin-orbit coupling could lead to a polarization of quarks that is succeeded by a net polarization of vector mesons along the direction of angular momentum. Subsequently, it is transferred to hadronic degrees of freedom through recombination. Recently, the measured spin alignment of vector mesons at LHC energy at $\sqrt{s_{NN}}$ = 2.76 TeV is surprisingly large compared to the polarization measured for hyperons at RHIC and LHC energies. Present theoretical studies have suggested that local polarization (i.e., longitudinal polarization where polarization axes are chosen as beam momentum direction or direction along the momentum of vector meson) can also lead to the polarization of vector mesons and hyperons. The quark and anti-quarks can be polarized due to helicity charge and local vorticity generated from the anisotropic expansion of the system created in non-central heavy-ion collisions. It is also interesting to extend such measurements to understand the contribution of global and local polarization. Experimentally, the effects of spin-orbit interactions have been studied by measuring the angular distribution of decay daughters of vector mesons.

Spin alignment of vector meson is described by a spin-density matrix ρ, which is a 3×3 hermitian matrix having a unit trace. A deviation of the diagonal elements ρ_{mm} (m = -1, 0, 1) from 1/3 signals hints at the presence of net spin alignment. The diagonal elements $\rho_{-1,-1}$ and $\rho_{1,1}$ are degenerate and so the independent observable is ρ_{00}. The angular distribution of decay products of vector mesons is described by the equation given below.

$$\frac{dN}{d\cos\theta^*} = N_0 \times [(1 - \rho_{00}) + (3\rho_{00} - 1)\cos^2\theta^*] \qquad (7.1)$$

Where N_0 is the normalization constant and θ^* is the angle between the quantization axis and the momentum direction of a daughter particle in the rest frame of the vector meson. This quantization axis can be the normal to the production plane (plane subtended by the momentum vector of resonance and the beam axis) or normal to the reaction plane (defined by the impact parameter and the beam axis) of the system. In the absence of spin alignment, $\rho_{00} = 1/3$, which makes the angular distribution uniform. The ρ_{00} deviates from 1/3 and leads to a non-uniform angular distribution, which is considered as the experimental signature of the spin alignment. In this thesis, we have presented the measurement of spin alignment of vector mesons ($K^{*0,\pm}$, ϕ) in Pb-Pb collisions at $\sqrt{s_{NN}}$ = 5.02 TeV using ALICE detector at the LHC. The present study focuses energy dependence measurement of ρ_{00} with high precision. The spin alignment of $K^{*\pm}$ may be sensitive to the initial magnetic field due to the different magnetic moments between K^{*0} and $K^{*\pm}$. In addition to that, the local spin alignment of vector mesons (K^{*0}, ϕ) is explored using the helicity frame (quantization axis is taken as momentum vector of resonance) in Pb–Pb collisions at $\sqrt{s_{NN}}$ = 5.02 TeV. The spin density matrix element (ρ_{00}) measurements are carried out in midrapidity ($|y|$ < 0.5) as a function of transverse momentum (p_T) with the ALICE detector in Pb-Pb collisions at $\sqrt{s_{NN}}$ = 5.02 TeV. The ρ_{00} values are extracted from the angular distribution of the vector meson's decay daughter with respect to the production plane and helicity frame.

Spin alignment of vector mesons is observed at low p_T for midcentral collisions, whereas no spin alignment is seen at high p_T. Similar p_T dependence in the ρ_{00} is observed for K^{*0} and $K^{*\pm}$ at mid central in Pb–Pb collisions at $\sqrt{s_{NN}}$ = 5.02 TeV in the Section 6.8.1. No significant energy dependence of ρ_{00} is observed for vector mesons in the Section 6.8.2. The ρ_{00} measurement of vector mesons shows an opposite trend between the production plane and the helicity frame. The ρ_{00} of K^{*0} and ϕ are compared with the previous measurements and found to be consistent within the uncertainties.

A.0.1 Particle identification using TPC and TOF

The Fig. A.1 and Fig. A.2 shows for the comparison of the PID efficiency from data and MC in different momentum range for decay daughter of resonances (both pion and kaon) using TPC and TOF detector. The PID efficiency is defined as, Efficiency = $\frac{\int_{-n}^{n} GaussFit(M_i, \sigma_i)}{\int_{-10}^{10} GaussFit(M_i, \sigma_i)}$, Here n, M_i, σ_i are given sigma range, the mean and standard deviation of Gaussian fits. The PID criteria is chosen so that the PID efficiency is above 99% in different p_T intervals for both DATA and MC.

TPC and TOF particle identification selection criteria are illustrated in Fig. A.3 and Fig. A.4 in p–Pb collisions at $\sqrt{s_{NN}}$ = 8.16 TeV.
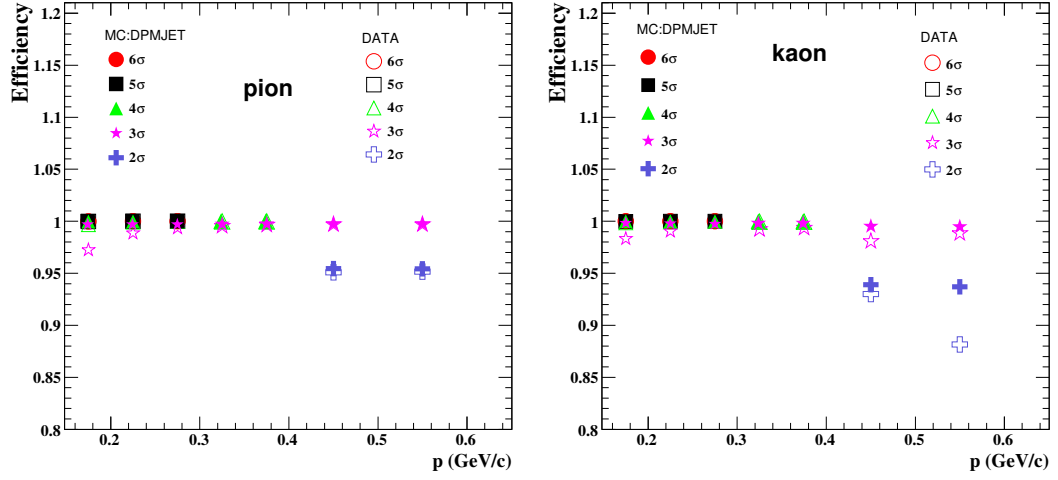
FIGURE A.1: Efficiency of TPC Nσ distribution for pion (left) and kaon (right) as function of momentum (p) in p–Pb collisions at $\sqrt{s_{NN}}$ = 8.16 TeV.
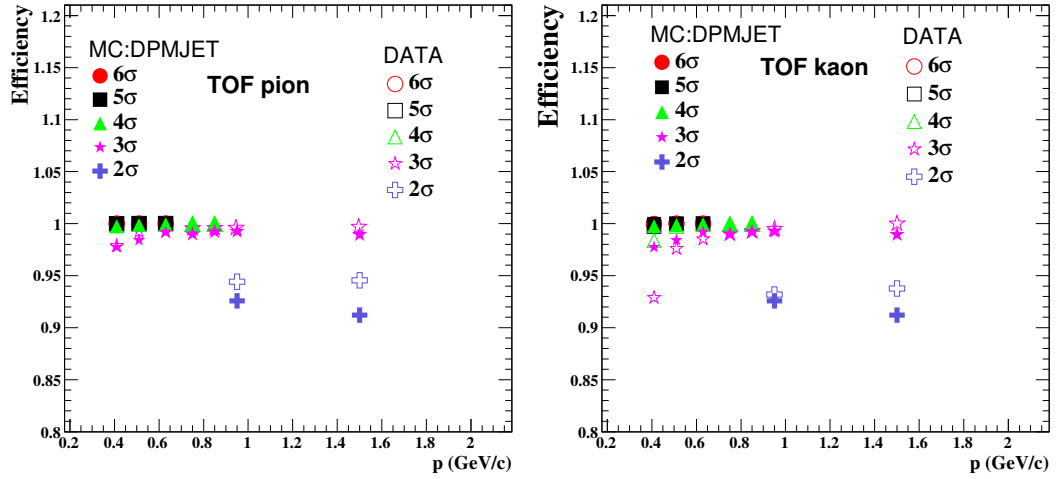
FIGURE A.2: Efficiency of TOF Nσ distribution for pion (left) and kaon (right) as function of momentum (p) in p–Pb collisions at $\sqrt{s_{NN}}$ = 8.16 TeV.

A.0.2 Invariant mass distributions

Invariant mass distributions of πK pair before combinatorial background subtraction in the p_T intervals 0 to 3 GeV/c and 3 to 20 GeV/c are shown in
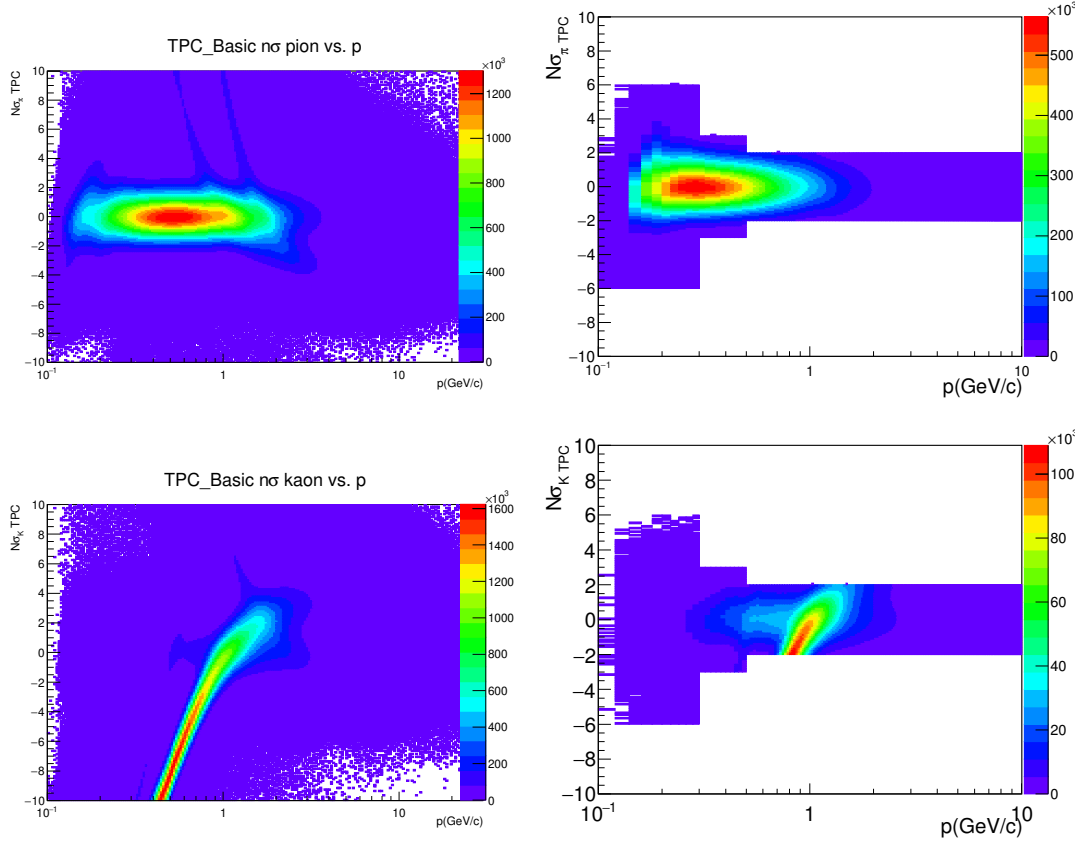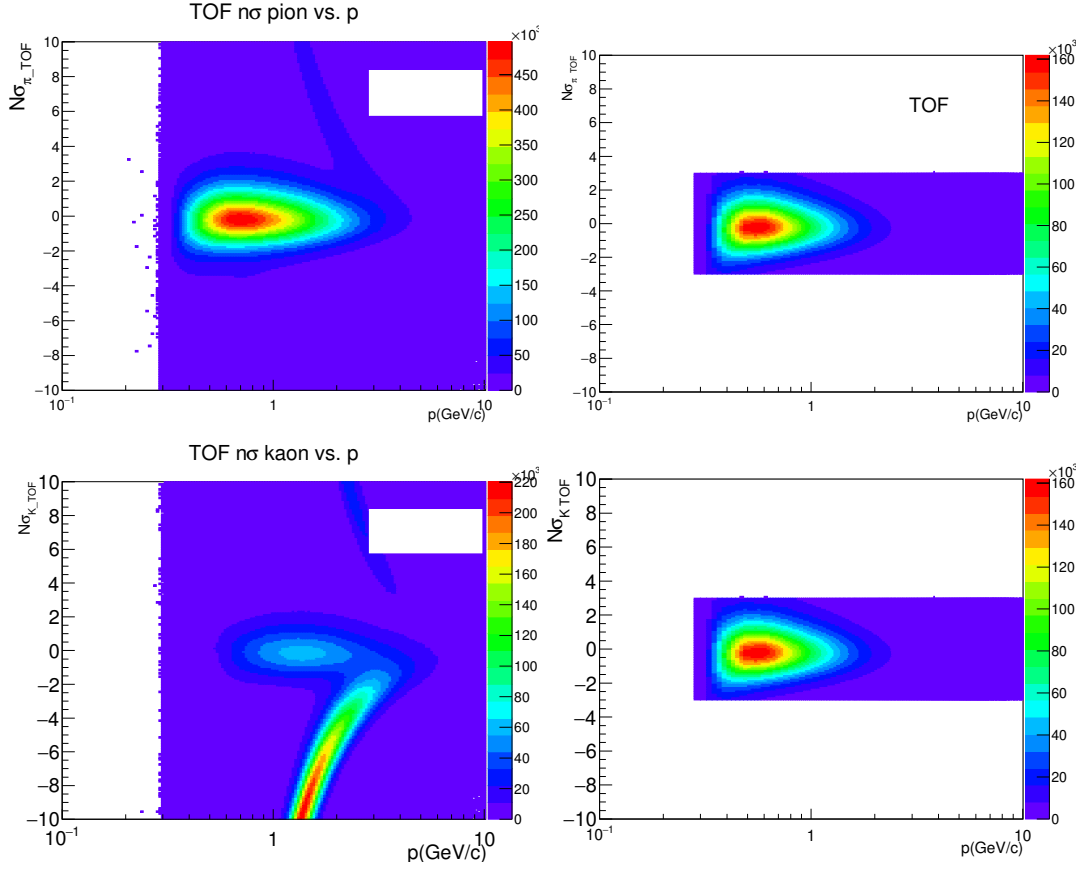
FIGURE A.3: Upper left panel shows $|N\sigma_{TPC}|$ distribution for pion without any PID cut and upper right panel shows $|N\sigma_{TPC}|$ distribution for pion after PID cut as function of momentum (p). $|N\sigma_{TPC}|$ distribution for kaon without PID cut and with PID cut as function of momentum are shown in lower left and right panel in p–Pb collisions at $\sqrt{s_{NN}}$ = 8.16 TeV.

Fig A.5 and Fig A.6, respectively for minimum bias(0–100%).

The signal distributions are fitted with the Breit-Wigner + pol2 function after background subtraction, as shown in Fig A.7 and Fig A.8.

Fig.A.9 shows mass of K^{*0} as a function of p_T obtained from data and Monte-Carlo simulation for p–Pb collisions at $\sqrt{s_{NN}}$ = 8.16 TeV.

The invariant mass distributions of πK pairs after mixed event back-

FIGURE A.4: Upper left panel shows $|N\sigma_{TOF}|$ distribution for pion without any PID cut and upper right panel shows $|N\sigma_{TOF}|$ distribution for pion after PID cut as function of momentum. $|N\sigma_{TOF}|$ distribution for kaon without PID cut and with PID cut as function of momentum are shown in lower left and right panel in p–Pb collisions at $\sqrt{s_{NN}} = 8.16$ TeV.

ground subtraction for multiplicity 0–5% is shown in Fig A.10.

The invariant mass distributions of πK pairs after mixed event background subtraction for multiplicity 80-100% is shown in Fig A.11.
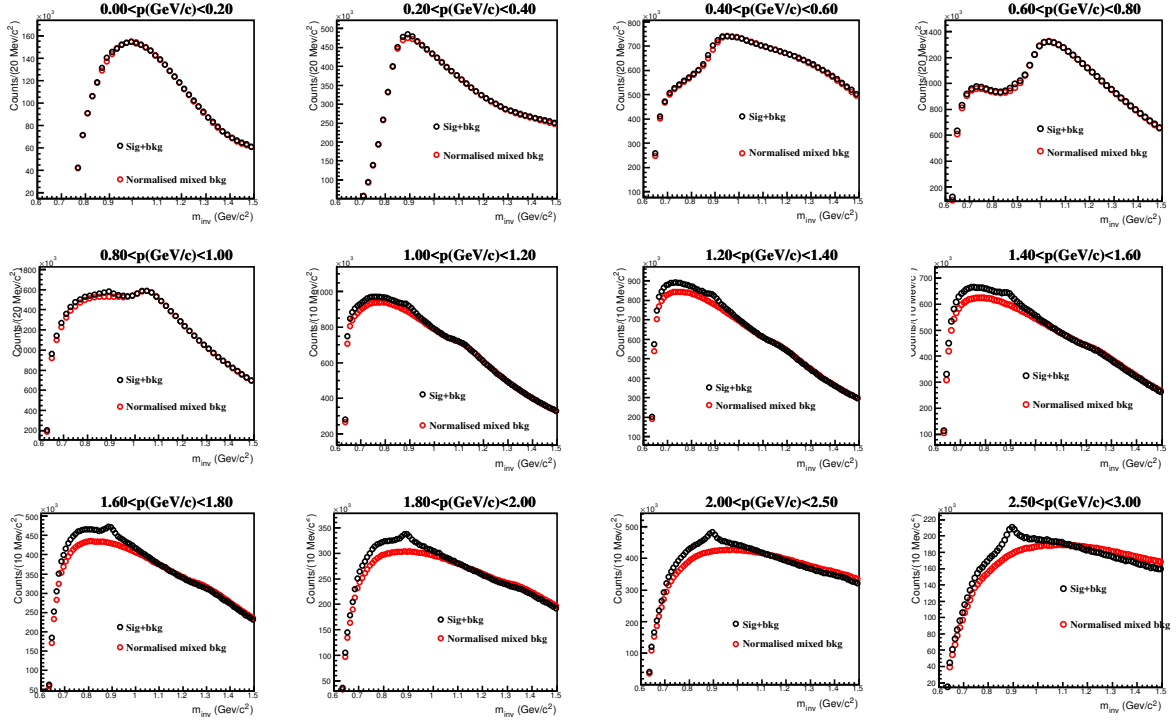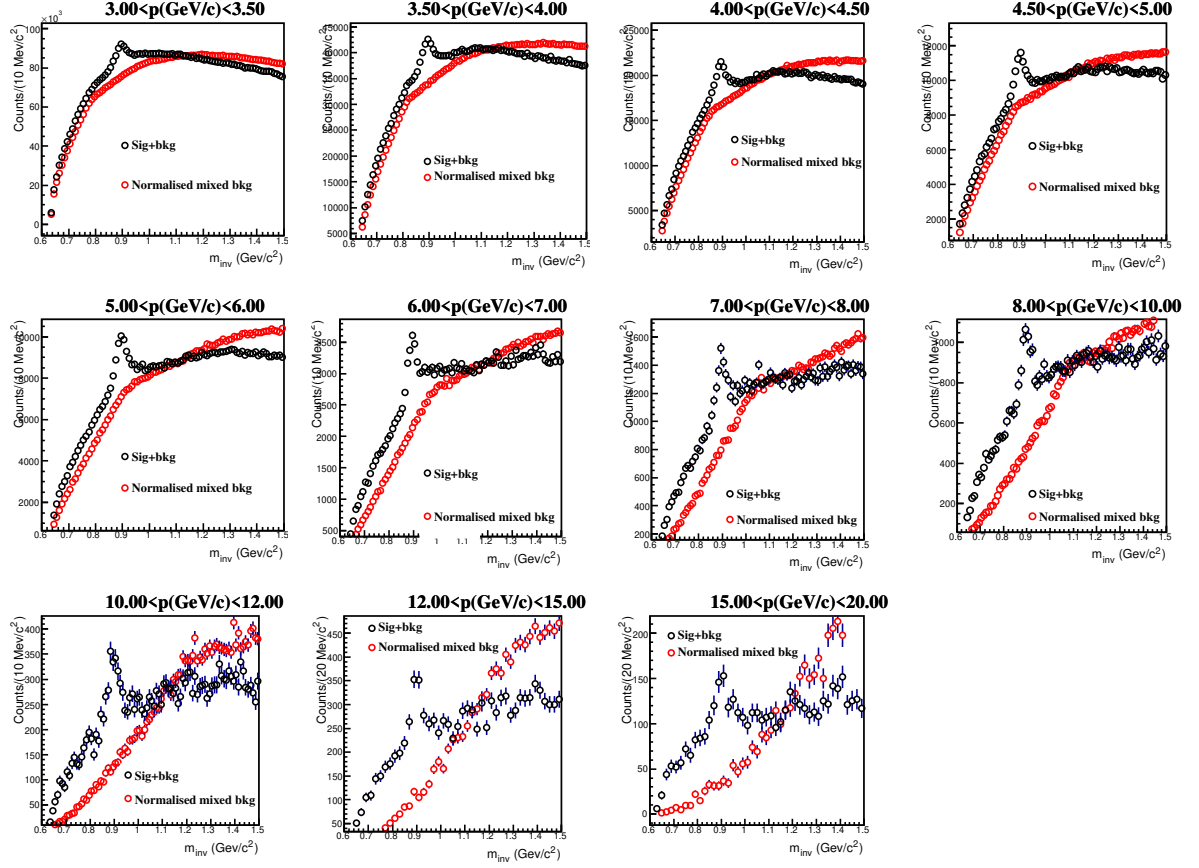
FIGURE A.5: Invariant mass distributions of both same event (black marker) and mixed event (red marker) of πK after normalization for p_T range 0 to 3 GeV/c is shown here.

A.0.3 Efficiency × acceptance for various multiplicity classes

Figure A.12 shows efficiency × acceptance as a function of p_T for various multiplicity classes for K^{*0} (left) at $\sqrt{s_{NN}}$ = 8.16 TeV and for K$^{*\pm}$ (right) at $\sqrt{s_{NN}}$ = 5.02 TeV in the rapidity interval -0.5 < y < 0 for p–Pb collisions. It is observed that no significant multiplicity dependence is observed for both K^{*0} and K$^{*\pm}$, respectively.

FIGURE A.6: Invariant mass distributions of both same event (black marker) and mixed event (red marker) of πK after normalization for p_T range 3 to 20 GeV/c is shown here.

A.0.4 Signal loss correction for various multiplicity classes

Figure A.13 shows signal loss correction factor as a function of p_T for various multiplicity classes in p–Pb collisions at $\sqrt{s_{NN}}$ = 8.16 TeV. A constant fit function is shown in red lines. No multiplicity dependence correction factors is observed.
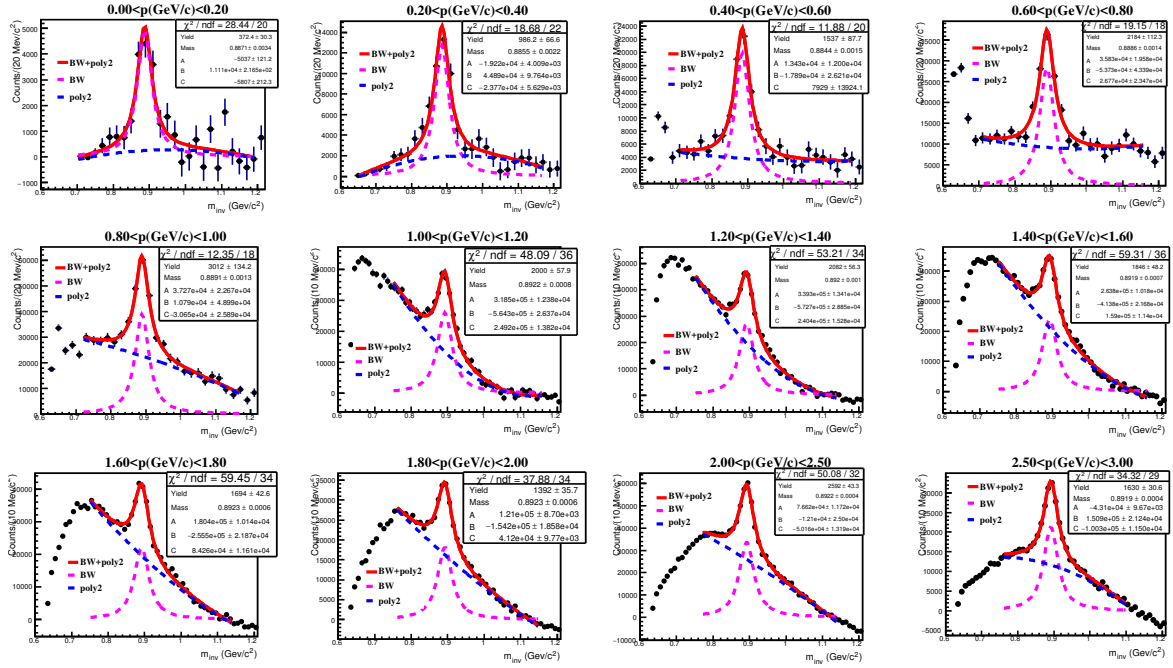
FIGURE A.7: K^{*0} signal for mixed event background, where signals are fitted with Breit-Wigner + pol2 function for MB (0-100)%. Where the red line shows the signal + residual background and blue line shows the residual background. In low the p_T, like sign describes better background shape. Like sign background is used for p_T up to 1.0 GeV/c. Invariant mass distributions of πK after background subtraction for p_T range 0 to 3 GeV/c is shown here.

A.0.5 Barlow Criteria

Barlow criteria have applied for various source systematics, the distribution of n or Δ/σ is shown in Fig. A.14 for K^{*0} in p–Pb collisions at $\sqrt{s_{NN}}$ = 8.16 TeV.
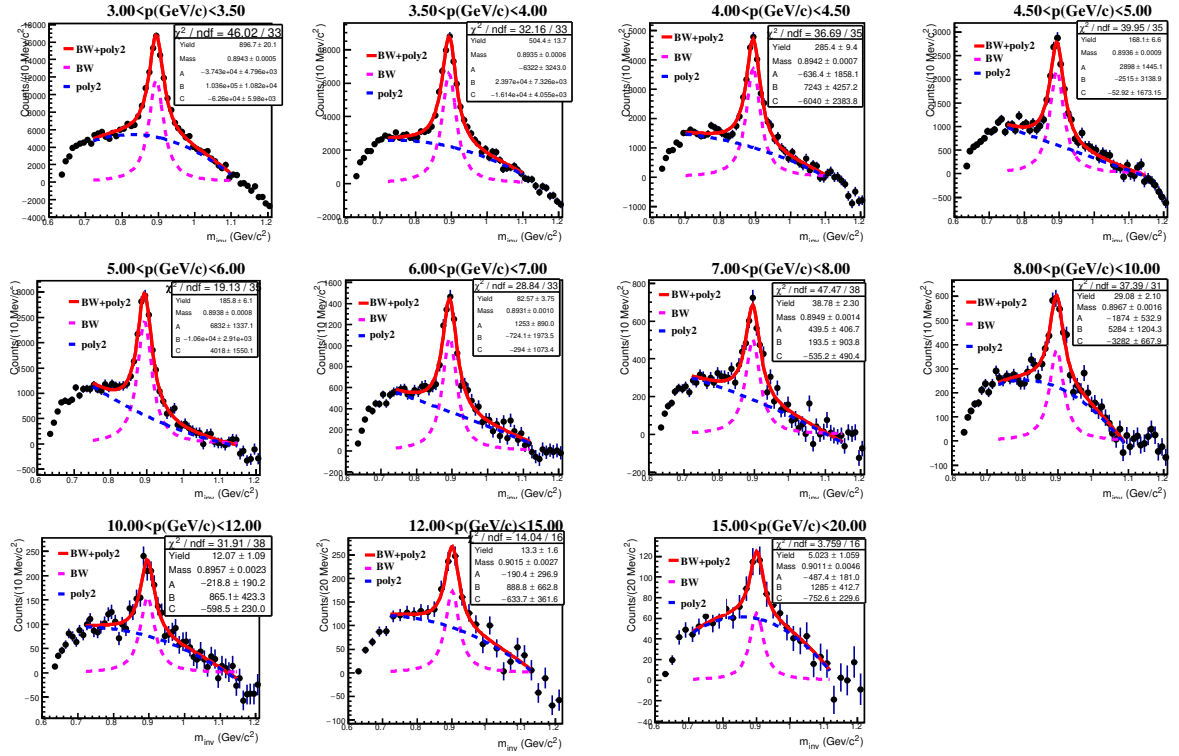
FIGURE A.8: Invariant mass distributions of πK after background subtraction for p_T range 3 to 20 GeV/c is shown here.

A.0.6 Systematic uncertainties for various multiplicity classes

The summary of systematic uncertainties of K^{*0} for various multiplicity classes is shown in the Fig. A.15.
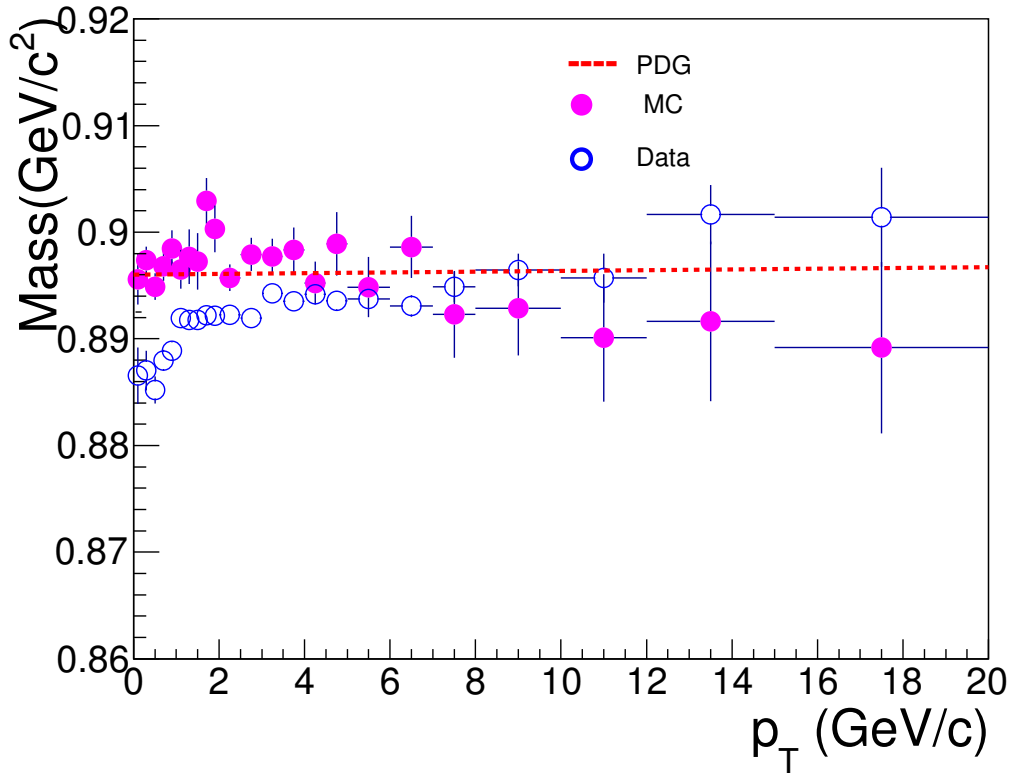
FIGURE A.9: K^{*0} mass as a function of p_T for p–Pb collisions at $\sqrt{s_{NN}}$= 8.16 TeV. The red dashes line represents the PDG value for mass. Mass shift in data at low p_T is not reproduced by reconstructed MC data. The errors shown are statistical only.
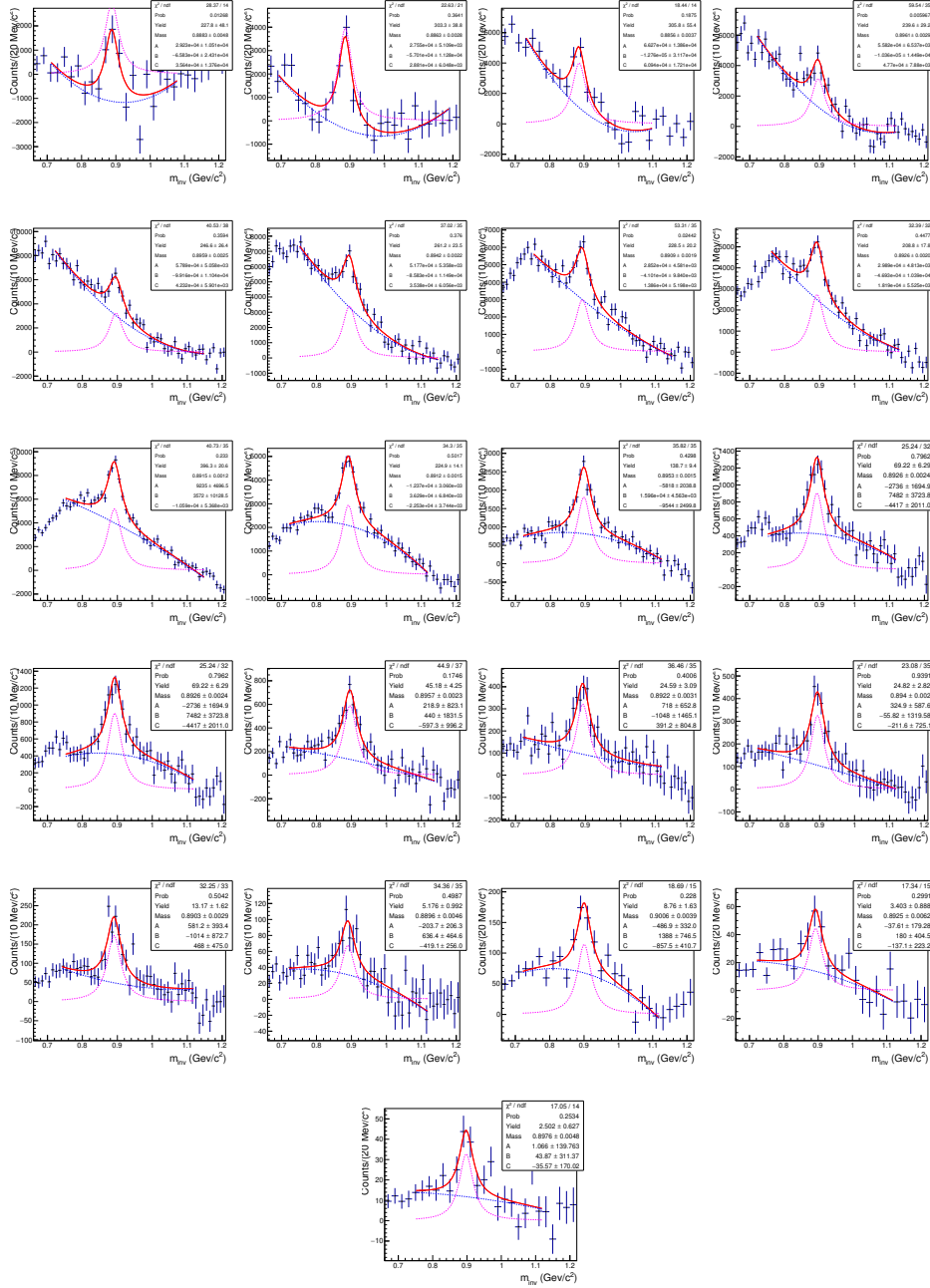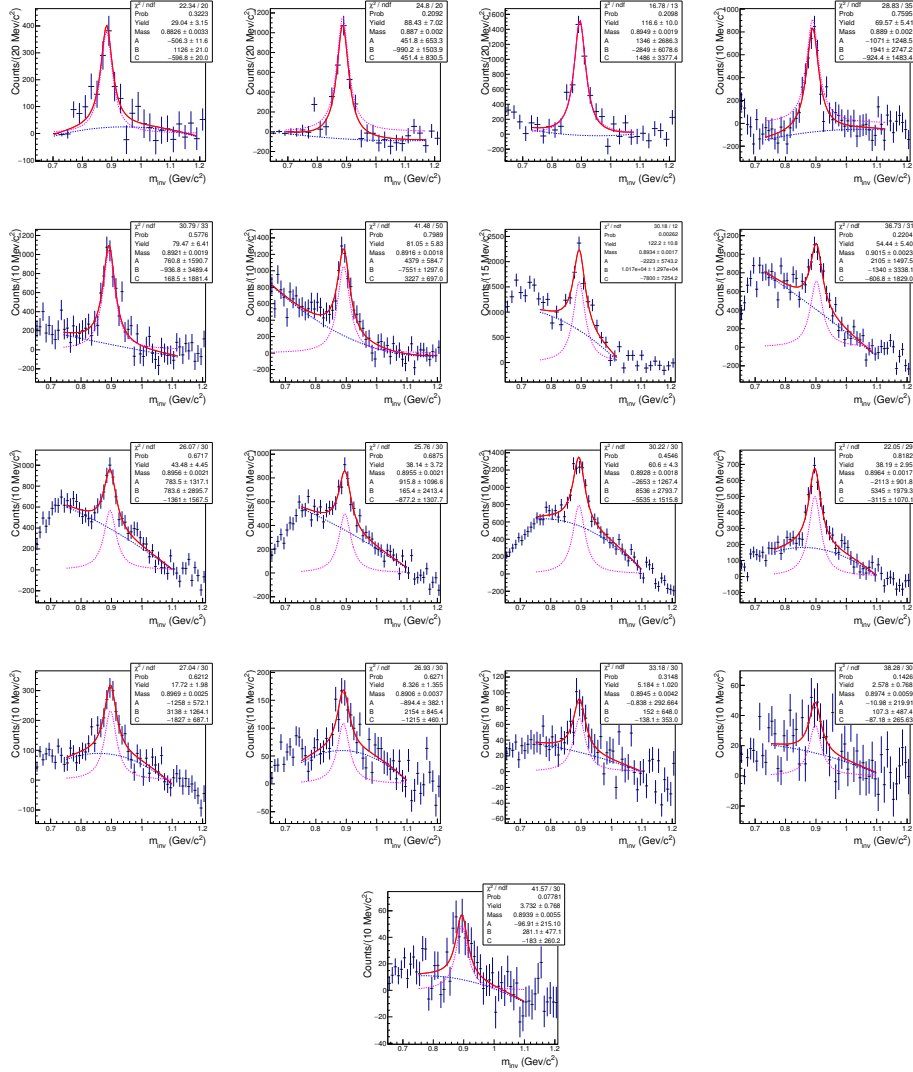
FIGURE A.10: K^{*0} signal for mixed event background, where signals are fitted with Breit-Wigner + pol2 function for multiplicity event class, 0–5%. Where the red line shows the signal + residual background and blue line shows the residual background in p_T bin range $0.0 < p_T < 15$ GeV/c.
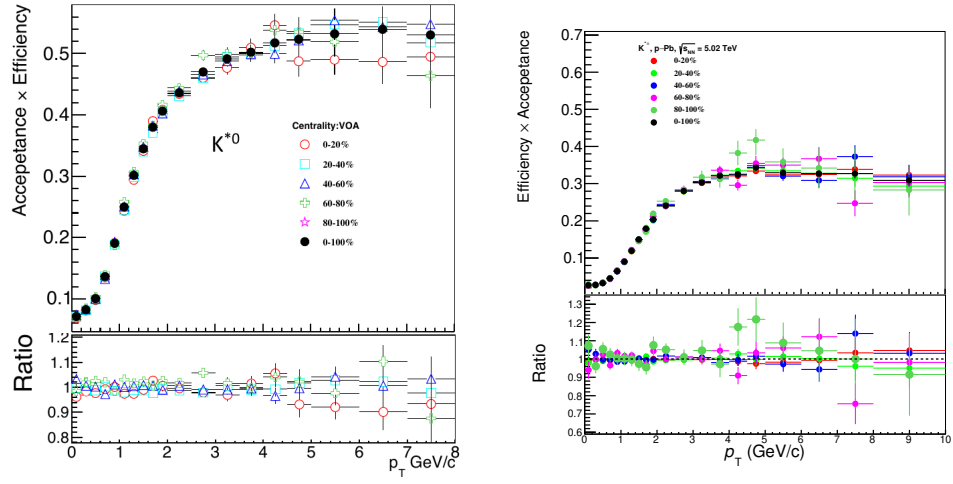
FIGURE A.11: K^{*0} signal for mixed event background, where signals are fitted with Breit-Wigner + pol2 function for multiplicity event class, 80–100%. Where the red line shows the signal + residual background and blue line shows the residual background in p_{T} bin range $0.0 < p_{\mathrm{T}} < 10.0$ GeV/c.

FIGURE A.12: Efficiency × acceptance as a function of p_T in various multiplicity classes for K^{*0} (left) at $\sqrt{s_{NN}}$ = 8.16 TeV and for K$^{*\pm}$ (right) at $\sqrt{s_{NN}}$ = 5.02 TeV in the rapidity interval -0.5 < y < 0 for p–Pb collisions.
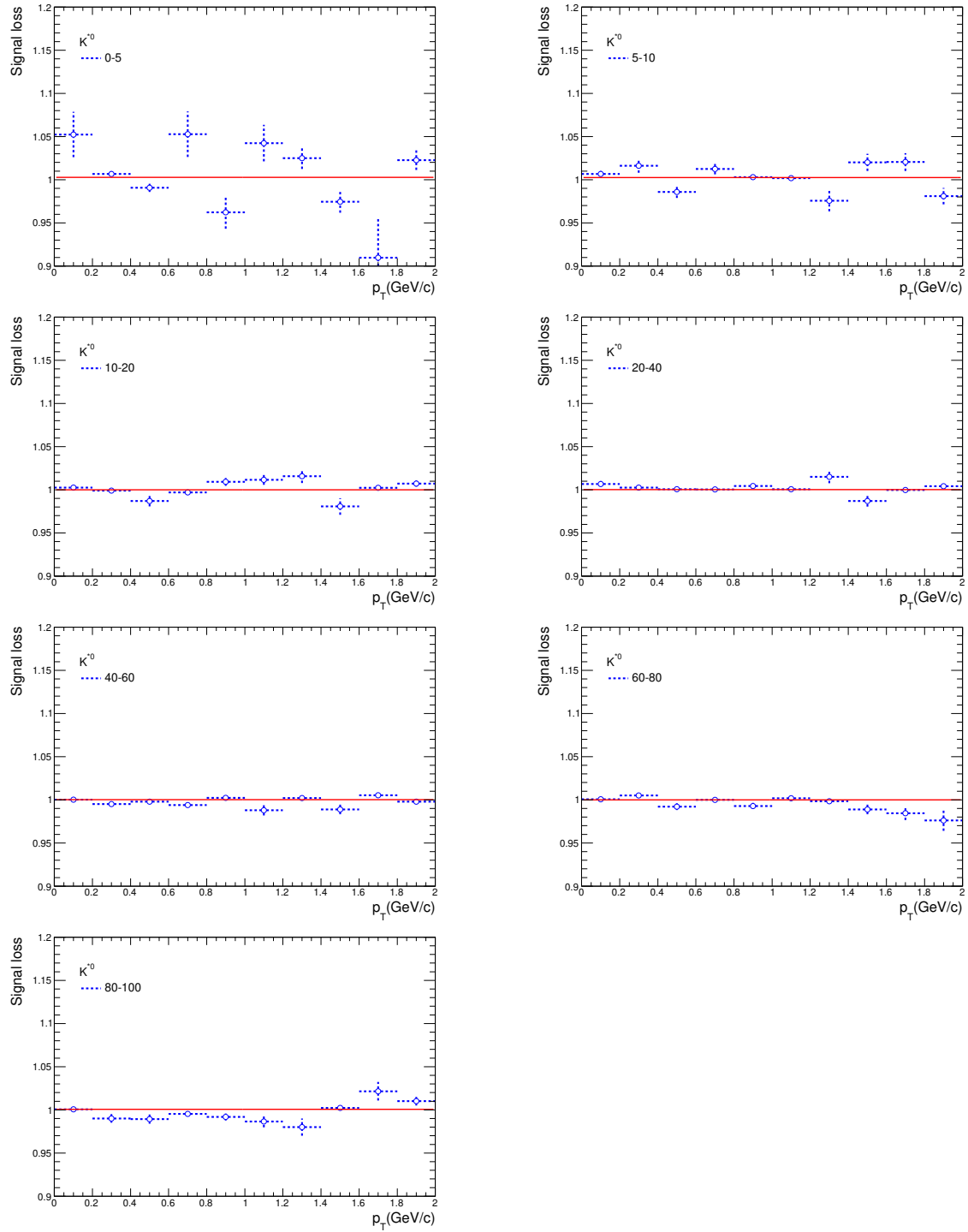
FIGURE A.13: Signal loss corrections as a function of p_T for various multiplicity classes in p–Pb collisions at $\sqrt{s_{NN}}$ = 8.16 TeV. The red line represents the a constant fit function.
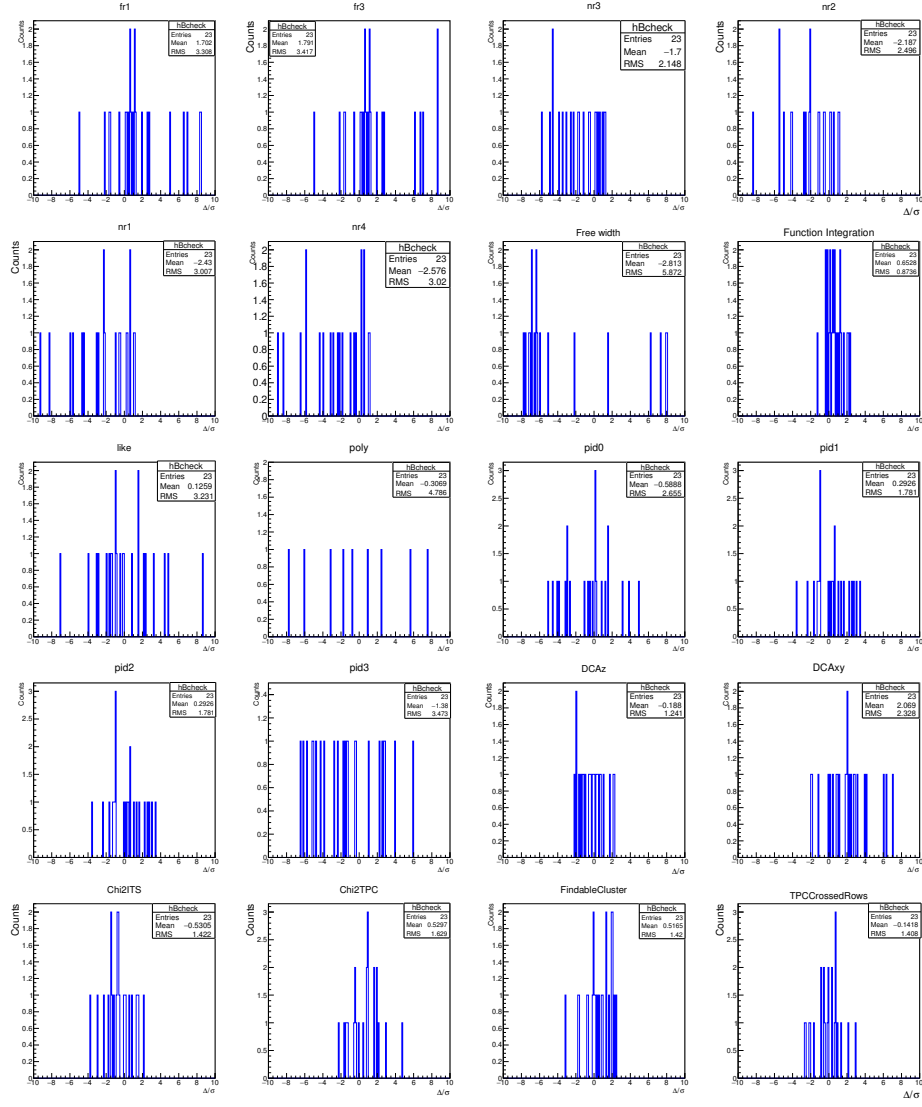
FIGURE A.14: Barlow checks for various source of systematics are shown here for K^{*0} in p–Pb collisions at $\sqrt{s_{\mathrm{NN}}}$ = 8.16 TeV.
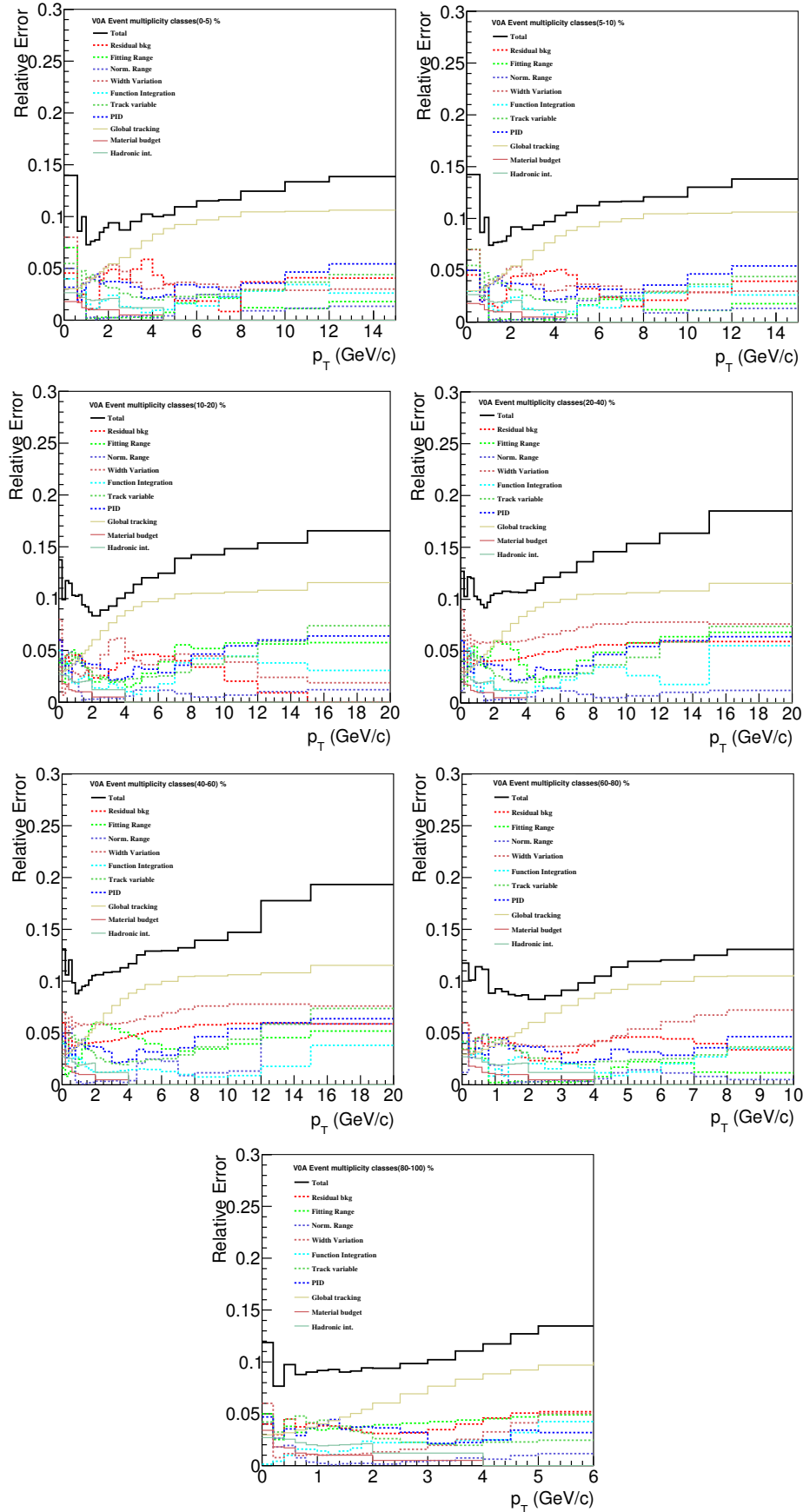
FIGURE A.15: Summary of relative uncertainties of K^{*0} for various multiplicity classes in p–Pb collisions at $\sqrt{s_{NN}}$ = 8.16 TeV. Different sources are shown by lines of different colors.

B.0.1 Mass as a function of p_T

Figure B.1 shows mass as a function of p_T for various rapidity interval in p–Pb collisions at $\sqrt{s_\mathrm{NN}} = 5.02$ TeV. No rapidity dependence on mass is seen for K^{*0} in the p–Pb collisions at $\sqrt{s_\mathrm{NN}} = 5.02$ TeV.

B.0.2 Multiplicity and rapidity dependence p_T spectra of K^{*0} production in p–Pb collisions

Figure B.2 shows the corrected p_T spectra for various rapidity and multiplicity classes of K^{*0} in p–Pb collisions at $\sqrt{s_\mathrm{NN}} = 5.02$ TeV.
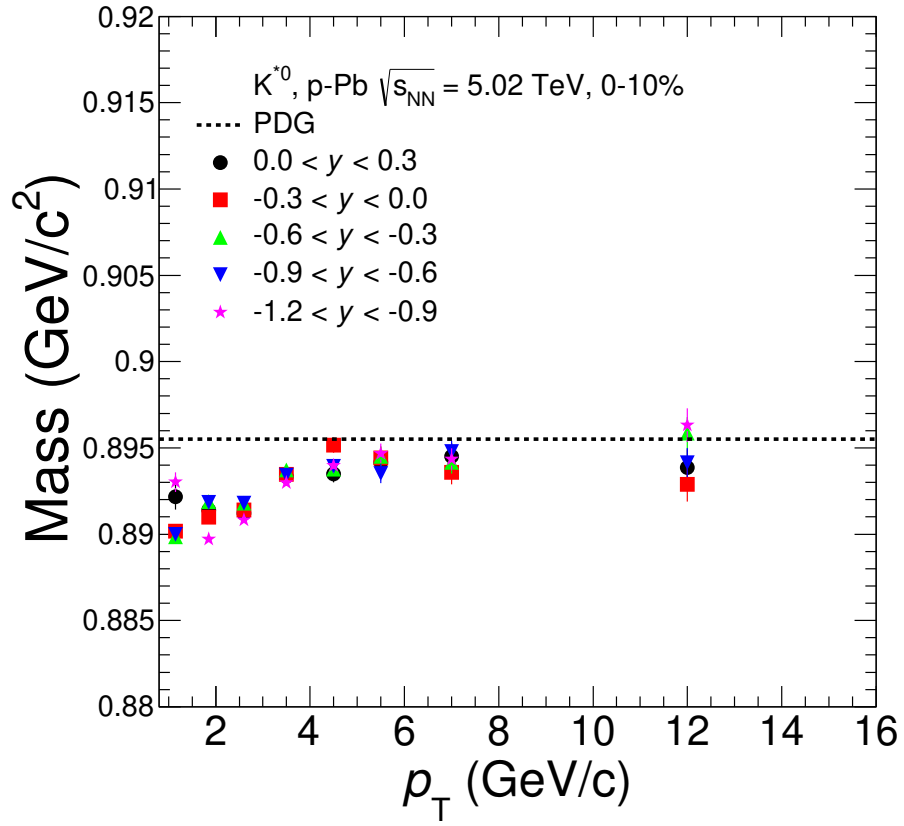
FIGURE B.1: Extracted mass peak of πK invariant-mass distribution as a function of p_T for various rapidity interval in p–Pb collisions for 0–10% at $\sqrt{s_{NN}}$= 5.02 TeV. The red dashes line represents the PDG value of K^{*0} mass. The error is shown statistical only.
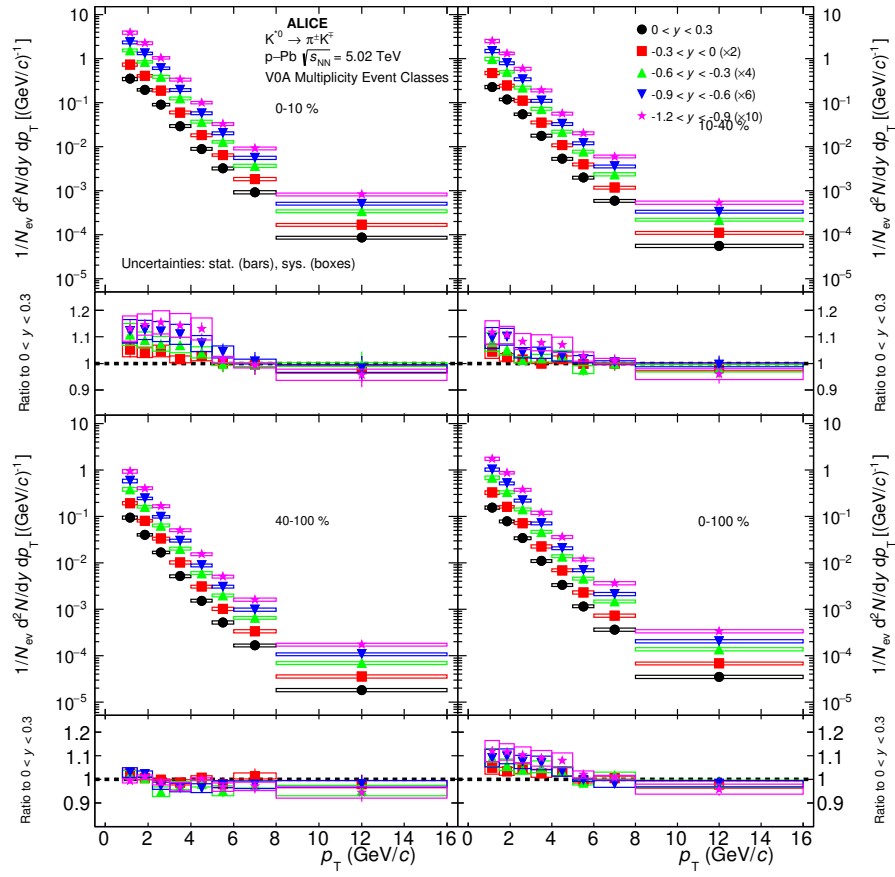
FIGURE B.2: Transverse momentum (p_T) spectra of K^{*0} measured in the rapidity interval -1.2< y < 0.3 for various multiplicity classes in p–Pb collisions at $\sqrt{s_{NN}}$ = 5.02 TeV.

C.0.1 Invariant mass distributions

Invariant mass distribution of πK pairs after subtraction of combinatorial background and the distributions are fitted with the Breit-Wigner + pol2 function for various p_{T} intervals are shown in Fig C.1 and Fig C.2 in pp collisions at $\sqrt{s}$ = 7 TeV.
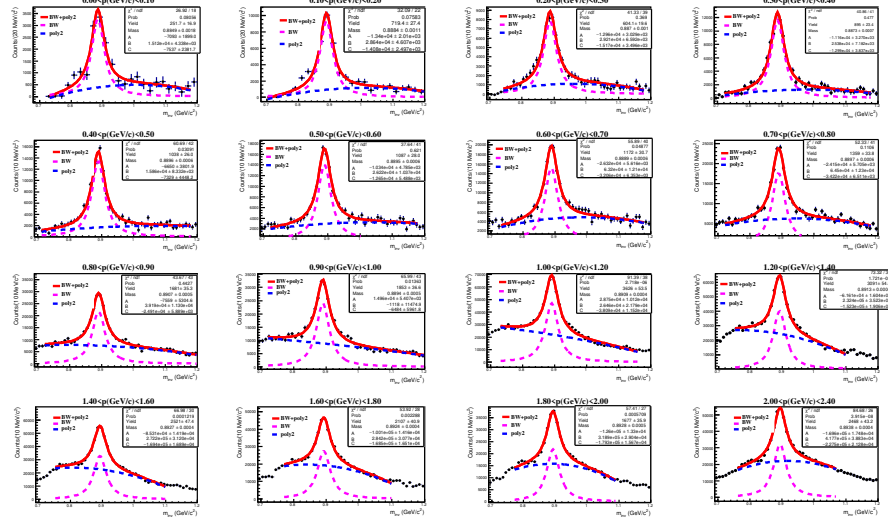
FIGURE C.1: Invariant mass distribution of πK pair after mixed event background subtraction for $0.0 < p_T < 2.4$ GeV/c interval inelastic minimum bias pp collisions at $\sqrt{s} = 7$ TeV in $|y| < 0.5$. Distributions are fitted with Breit-Wigner + 2nd order polynomial function, where red, magenta and blue lines describe the signal + residual background, signal and residual background, respectively.
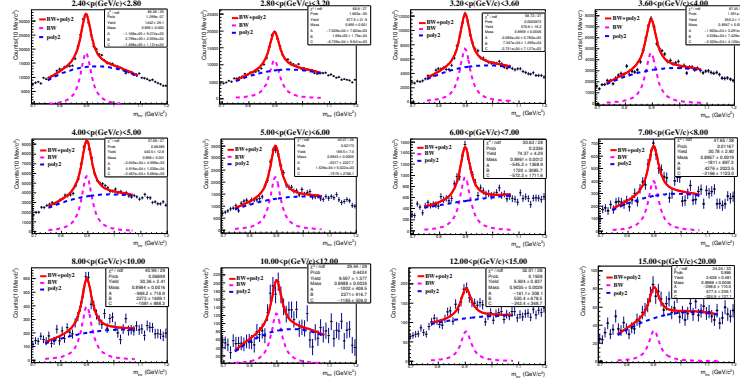

FIGURE C.2: Invariant mass distribution of πK pair after mixed event background subtraction for $2.4 < p_T < 20.0$ GeV/c interval inelastic minimum bias pp collisions at $\sqrt{s} = 7$ TeV in $|y| < 0.5$. Distributions are fitted with Breit-Wigner + 2nd order polynomial function, where red, magenta and blue lines describe the signal + residual background, signal and residual background, respectively.

D.0.1 Invariant mass distributions

Figure D.1 shows invariant mass distributions $M_{\pi K}$ pairs after mixed event background subtraction and fitted with Breit-Wigner plus residual background function in centrality class 10–50% for various p_T bins in $\cos\theta^*$ bin $0.0 < \cos\theta^* < 0.2$ in Pb–Pb collisions at $\sqrt{s_{NN}} = 5.02$ TeV.

Figure D.2 shows invariant mass distributions $M_{\pi K}$ pairs after mixed event background subtraction and fitted with Breit-Wigner plus residual background function in centrality class 10–50% for various p_T bins in $\cos\theta^*$ bin $0.8 < \cos\theta^* < 1.0$ in Pb–Pb collisions at $\sqrt{s_{NN}} = 5.02$ TeV.
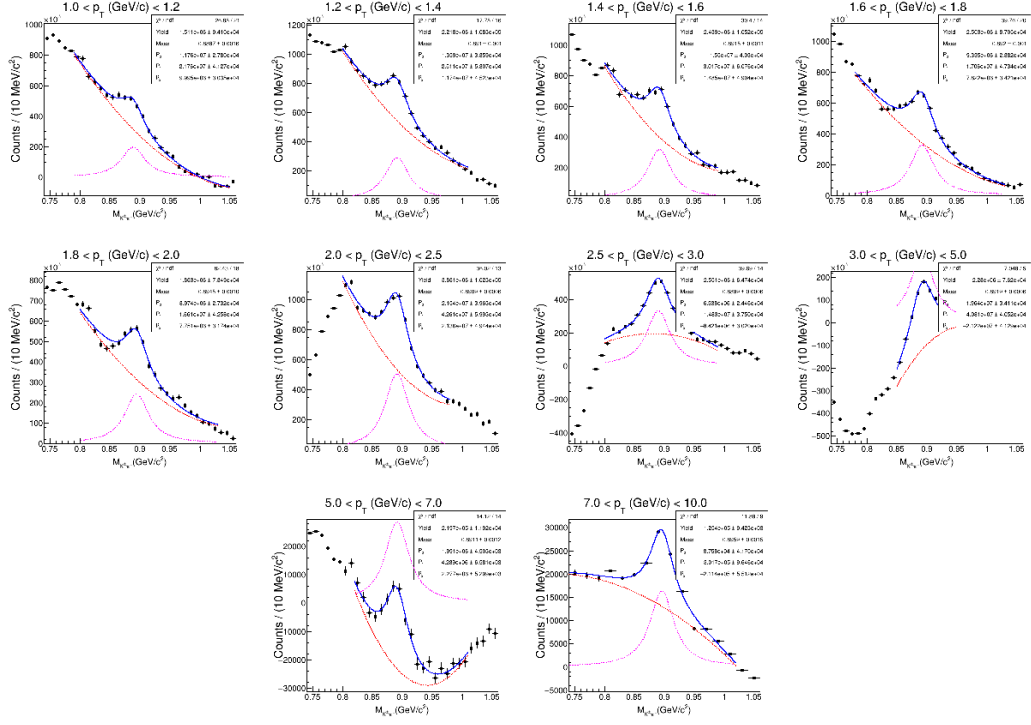
Figure D.3 shows invariant mass distributions $M_{K_S^0 \pi^\pm}$ pairs after mixed event background subtraction and fitted with Breit-Wigner plus residual background function in centrality class 10–50% for various p_T bins in $\cos\theta^*$ bin $0.0 < \cos\theta^* < 0.2$ in Pb–Pb collisions at $\sqrt{s_{NN}} = 5.02$ TeV.
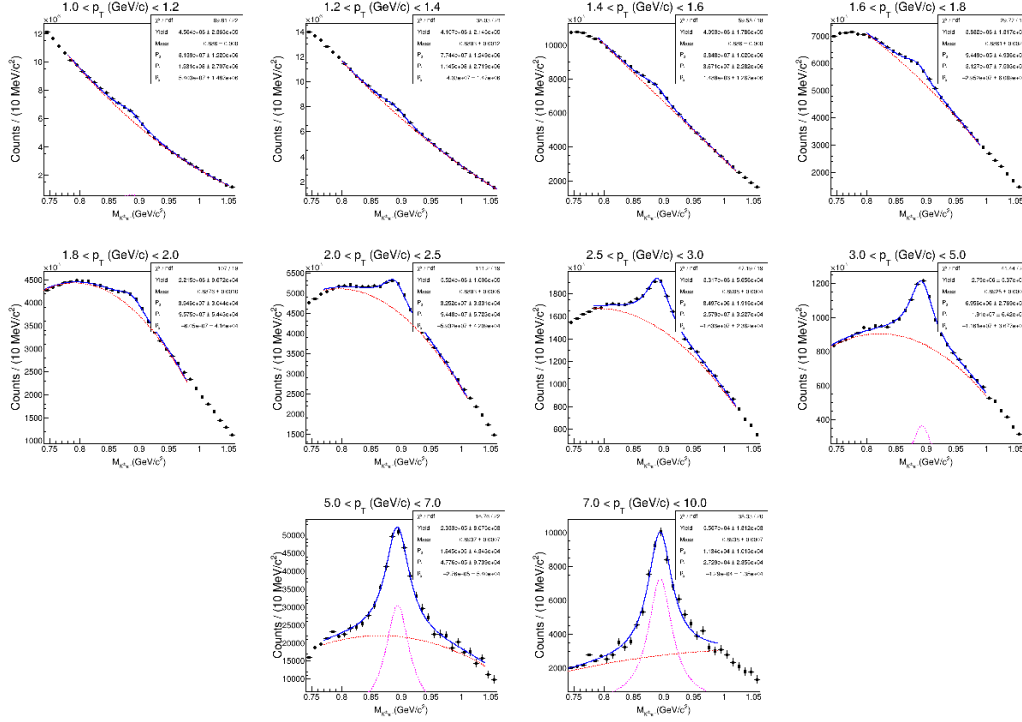
FIGURE D.1: Invariant mass distributions $M_{\pi K}$ pairs after mixed event background subtraction and fitted with Breit-Wigner plus residual background function in centrality class 10–50% for various p_T bins in $\cos\theta^*$ bin $0.0 < \cos\theta^* < 0.2$ in Pb–Pb collisions at $\sqrt{s_{NN}} = 5.02$ TeV. Quantization axis is perpendicular to the production plane (PP).

Figure D.4 shows invariant mass distributions $M_{K_S^0 \pi^\pm}$ pairs after mixed event background subtraction and fitted with Breit-Wigner plus residual background function in centrality class 10–50% for various p_T bins in $\cos\theta^*$ bin $0.8 < \cos\theta^* < 1.0$ in Pb–Pb collisions at $\sqrt{s_{NN}} = 5.02$ TeV. Figure D.5 invariant mass distributions M_{KK} pairs after mixed event background subtraction and fitted with Voigtian plus residual background function in centrality class 10–50% for various p_T bins in $\cos\theta^*$ bin $0.0 < \cos\theta^* < 0.2$ in Pb–Pb collisions at $\sqrt{s_{NN}} = 5.02$ TeV. Figure D.6 invariant mass distributions M_{KK}

FIGURE D.2: Invariant mass distributions $M_{\pi K}$ pairs after mixed event background subtraction and fitted with Breit-Wigner plus residual background function in centrality class 10–50% for various p_T bins in cosθ^* bin 0.8 < cosθ^* < 1.0 in Pb–Pb collisions at $\sqrt{s_{NN}}$ = 5.02 TeV. Quantization axis is perpendicular to the production plane (PP).

pairs after mixed event background subtraction and fitted with Voigtian plus residual background function in centrality class 10–50% for various p_T bins in cosθ^* bin 0.8 < cosθ^* < 1.0 in Pb–Pb collisions at $\sqrt{s_{NN}}$ = 5.02 TeV.

D.0.2 Invariant mass distributions of K^{*0} and ϕ using helicity frame

Figure D.7 represents the invariant mass distribution of πK pairs for the p_T interval 1.2 ≤ p_T < 1.4 GeV/c and KK pairs for 0.5 ≤ p_T < 0.8 GeV/c from same events (black markers),respectively for cosθ^* interval 0.6 to 0.8
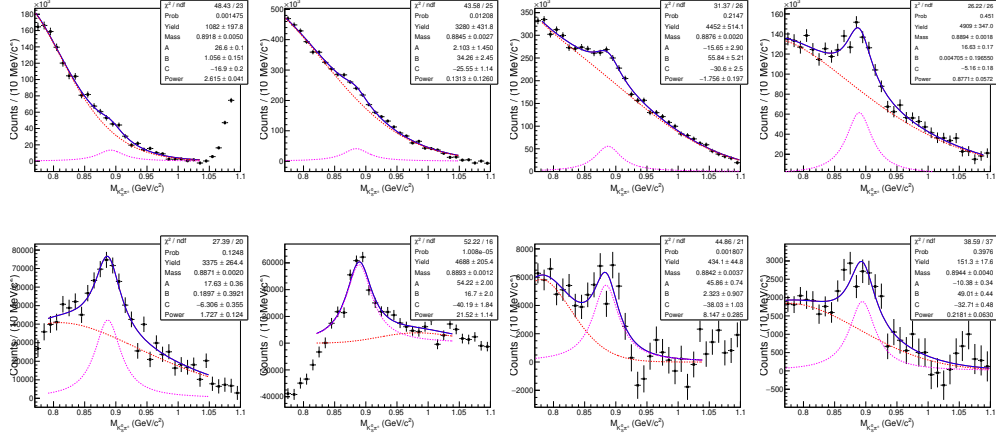
FIGURE D.3: Invariant mass distributions $M_{K_S^0 \pi^\pm}$ pairs after mixed event background subtraction and fitted with Breit-Wigner plus residual background function in centrality class 10–50% for various p_T bins in $\cos\theta^*$ bin $0.0 < \cos\theta^* < 0.2$ in Pb–Pb collisions at $\sqrt{s_{NN}} = 5.02$ TeV. Quantization axis is perpendicular to the production plane (PP).
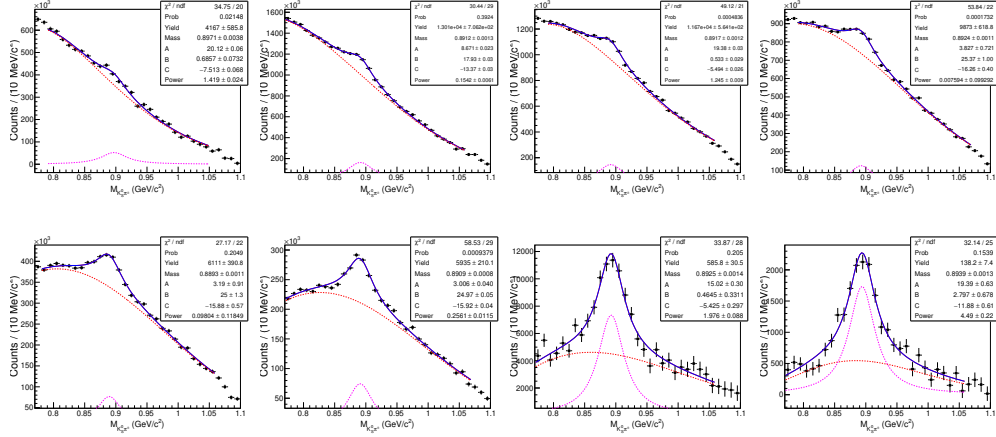

FIGURE D.4: Invariant mass distributions $M_{K_S^0 \pi^\pm}$ pairs after mixed event background subtraction and fitted with Breit-Wigner plus residual background function in centrality class 10–50% for various p_T bins in $\cos\theta^*$ bin $0.8 < \cos\theta^* < 1.0$ in Pb–Pb collisions at $\sqrt{s_{NN}} = 5.02$ TeV. Quantization axis is perpendicular to the production plane (PP).
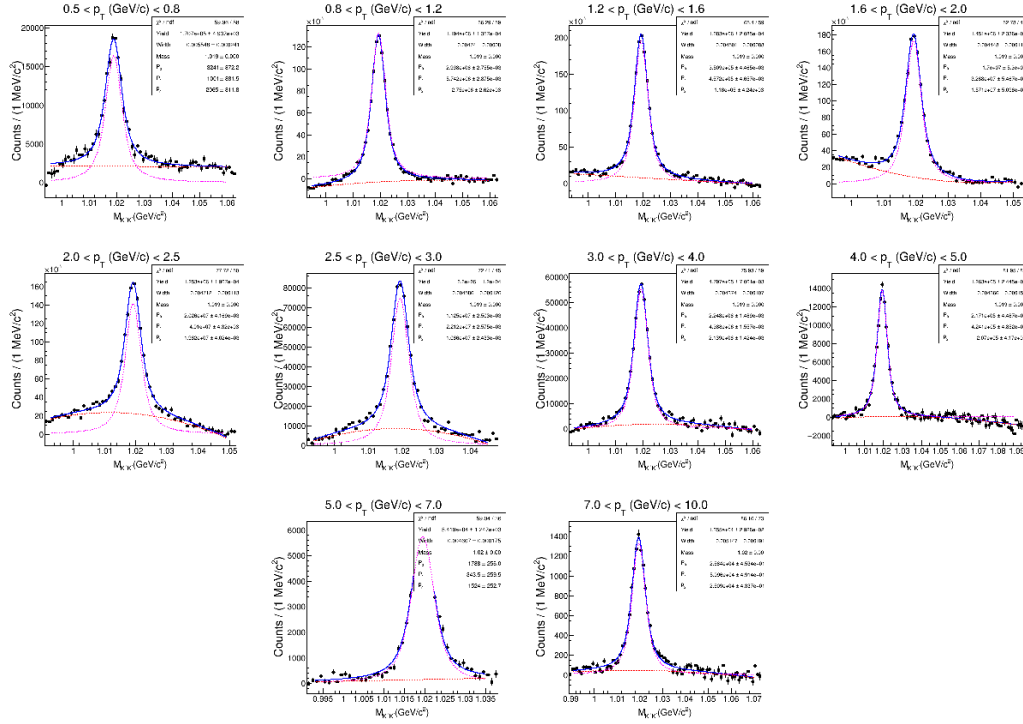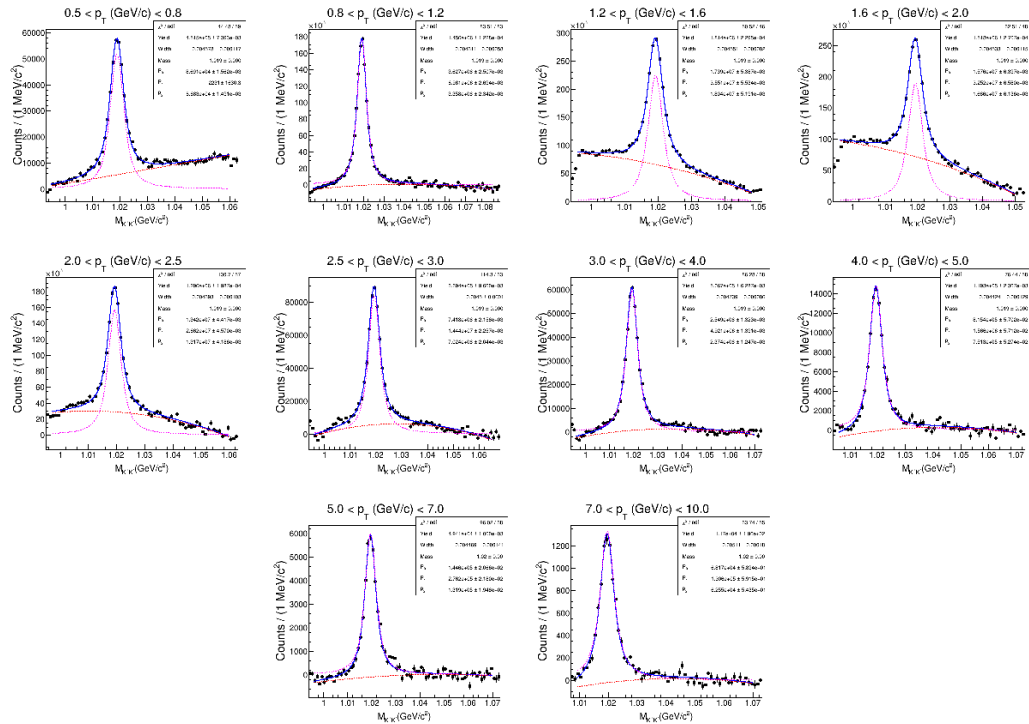
FIGURE D.5: Invariant mass distributions M_{KK} pairs after mixed event background subtraction and fitted with Voigtian plus residual background function in centrality class 10–50% for various p_T bins in $\cos\theta^*$ bin $0.0 < \cos\theta^* < 0.2$ in Pb–Pb collisions at $\sqrt{s_{NN}} = 5.02$ TeV. Quantization axis is perpendicular to the production plane (PP).

in the 10–50% centrality class in Pb–Pb collisions at $\sqrt{s_{NN}} = 5.02$ TeV. The normalized-mixed event background distributions are shown in red markers. Figure D.8 represents the invariant mass distribution of πK pairs for the p_T interval $1.2 \leq p_T < 1.4$ GeV/c and KK pairs for $0.5 \leq p_T < 0.8$ GeV/c after normalized-mixed event background subtraction fitted with Breit-Wigner distribution function (blue line) for signal and exponential plus polynomial function of second order (red dotted line) for residual background function for $\cos\theta^*$ interval 0.6 to 0.8 in the 10–50% centrality class in Pb–Pb collisions

FIGURE D.6: Invariant mass distributions M_{KK} pairs after mixed event background subtraction and fitted with Voigtian plus residual background function in centrality class 10–50% for various p_T bins in $\cos\theta^*$ bin $0.8 < \cos\theta^* < 1.0$ in Pb–Pb collisions at $\sqrt{s_{NN}} = 5.02$ TeV. Quantization axis is perpendicular to the production plane (PP).

at $\sqrt{s_{NN}} = 5.02$ TeV. The normalized-mixed event background distributions are shown in red markers.

D.0.3 Efficiency × acceptance, corrected spectra of K^{*0} and ϕ using helicity frame

Figure D.9 shows efficiency × acceptance as a function of p_T for various $\cos\theta^*$ bins for K^{*0} (left) and for ϕ (right). Lower panel shows the ratio of efficiency × acceptance in different $\cos\theta^*$ bins to that in the $\cos\theta^*$ bin 0.0
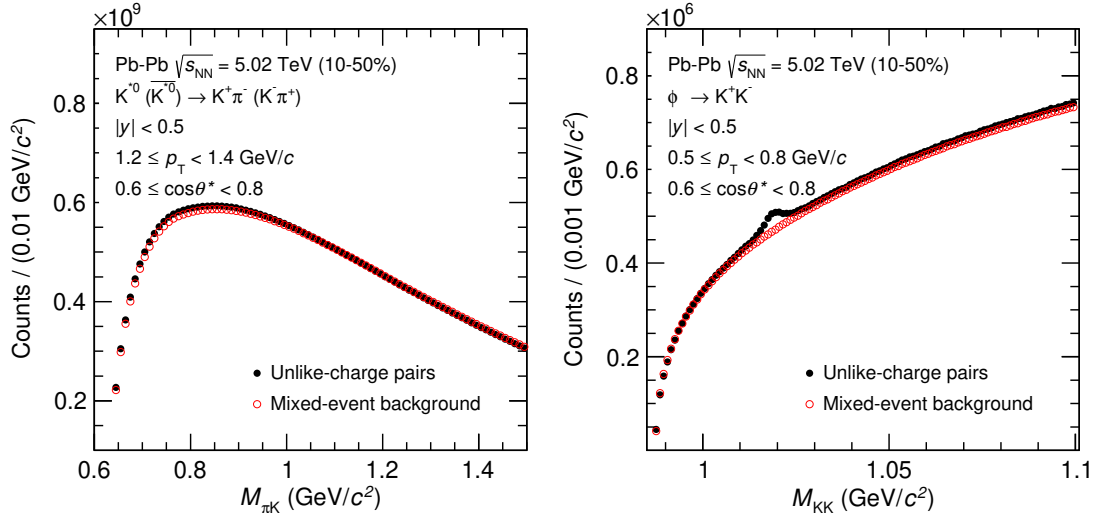
FIGURE D.7: Left panel shows invariant mass distribution of unlike charged πK pairs from same event (black markers) and normalized-mixed event background distribution in red markers in the p_T interval $1.2 \leq p_T < 1.4$ GeV/c for $\cos\theta^*$ interval 0.6 to 0.8 in the 10–50% centrality class for Pb–Pb collisions at $\sqrt{s_{NN}} = 5.02$ TeV. Right panel shows the invariant mass distribution of unlike charged KK pairs from same events and normalized mixed event background for $0.5 \leq p_T < 0.8$ GeV/c and $\cos\theta^*$ 0.6 to 0.8 in 10–50% collisions at $\sqrt{s_{NN}} = 5.02$ TeV. Quantization axis is along the momentum direction of vector mesons i.e., helicity frame (HX).

to 0.2 for 10–50% centrality class in Pb–Pb collisions at $\sqrt{s_{NN}} = 5.02$ TeV. Figure D.10 (for K^{*0}) and Fig. D.11 (for ϕ) shows the corrected p_T spectra for various $\cos\theta^*$ for centrality class 10–50% in Pb–Pb collisions at $\sqrt{s_{NN}} = 5.02$ TeV using helicity frame.

D.0.4 Consistency check: Transverse momentum spectrum

The comparison of transverse momentum spectra of vector mesons from p_T spectra and transverse momentum spectra measured from spin alignments are shown in Fig. D.12 (for K^{*0} and K$^{*\pm}$) and Fig. D.13 (for ϕ) in Pb–Pb
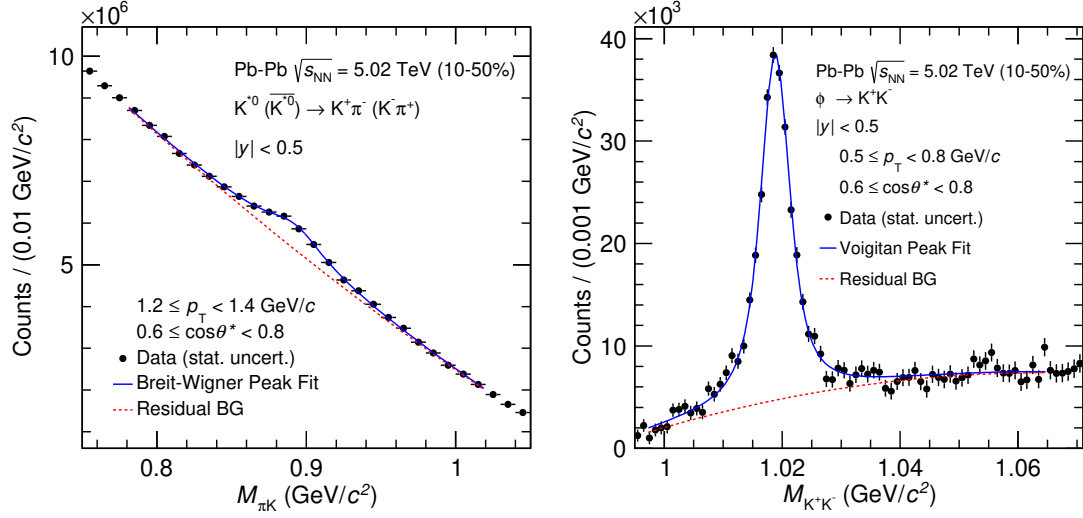
FIGURE D.8: Left panel shows invariant mass distribution of unlike charged πK pairs after normalized-mixed event background subtraction fitted with Breit-Wigner distribution function (blue line) for signal and exponential plus polynomial function of second order (red dotted line) for residual background function in the p_T interval $1.2 \leq p_T$ < 1.4 GeV/c for $\cos\theta^*$ interval 0.6 to 0.8 in the 10–50% centrality class for Pb–Pb collisions at $\sqrt{s_{NN}} = 5.02$ TeV. Right panel shows mixed-event background subtracted invariant mass distribution of KK pairs fitted with the Voigtian function for signal (blue line) and the residual background distributions is described by the polynomial second order function for p_T interval $0.5 \leq p_T < 0.8$ GeV/c for $\cos\theta^*$ interval 0.6 to 0.8 in the 10–50% centrality class for Pb–Pb collisions at $\sqrt{s_{NN}} = 5.02$ TeV. Quantization axis is along the momentum direction of vector mesons i.e., helicity frame (HX).

collisions at $\sqrt{s_{NN}} = 5.02$ TeV.

D.0.5 Angular momentum distributions and extracting ρ_{00} for vector mesons

The comparison of angular distributions of decay daughter of vector mesons for all p_T bins are shown in Fig. D.14, Fig. D.15 and Fig. D.16, respectively using quantization axis normal to production plane. Similarly, angular distribution of vector mesons, K^{*0} and ϕ using quantization axis along
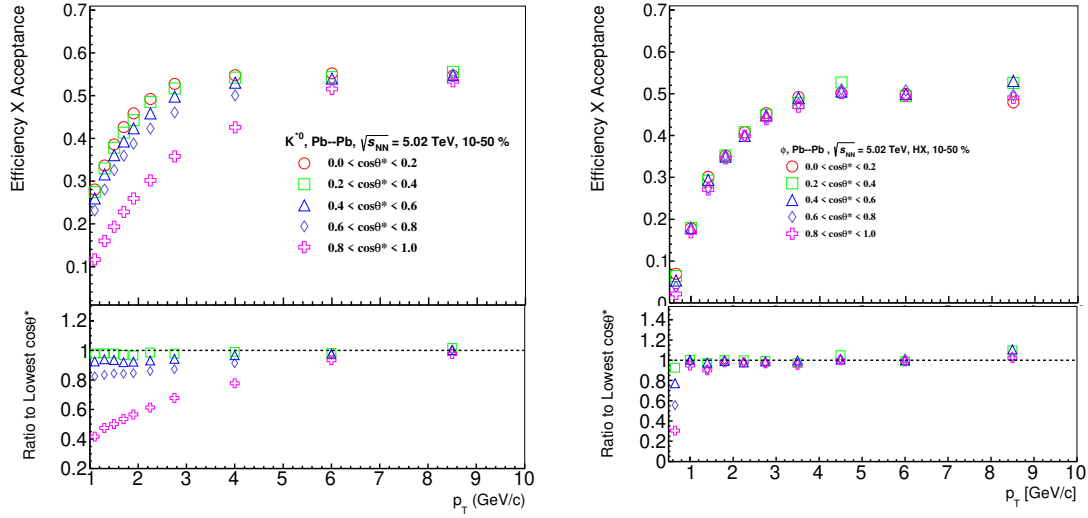
FIGURE D.9: Upper panel: Efficiency × acceptance as a function of p_T for various $\cos\theta^*$ bins for K^{*0} (left) and for ϕ (right). In lower panel, it is the ratio of efficiency × acceptance in different $\cos\theta^*$ bins to the efficiency × acceptance of the $\cos\theta^*$ bin 0.0 to 0.2 for 10–50% centrality class in Pb–Pb collisions at $\sqrt{s_{NN}}$ = 5.02 TeV. Results are obtained from helicity frame study.
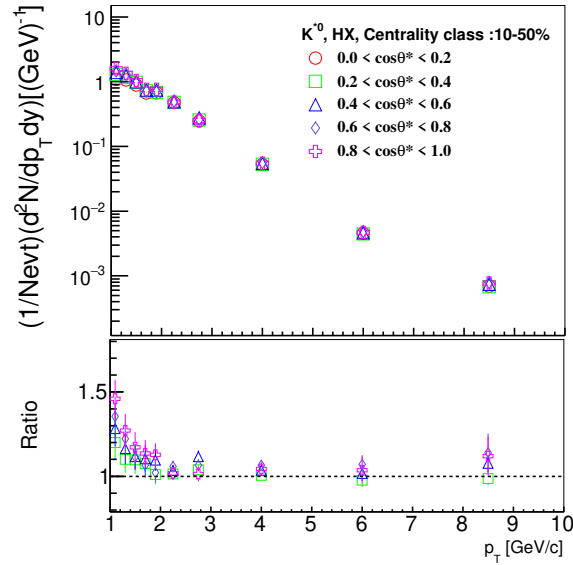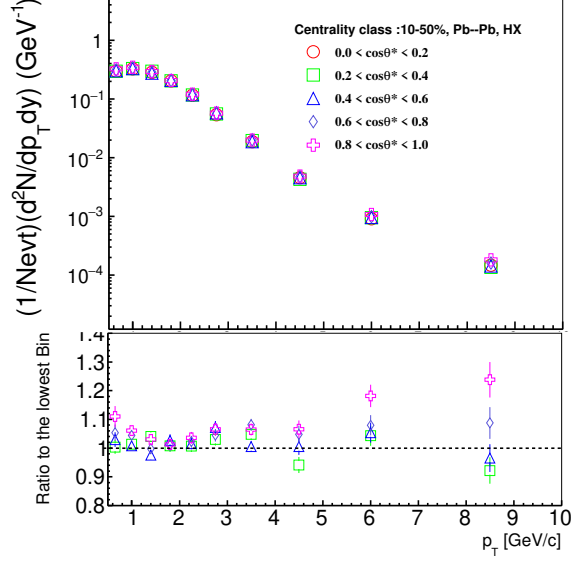

FIGURE D.10: Upper panel show corrected transverse momentum spectra for different $\cos\theta^*$ and lower panel show the ratio of corrected p_T in different $\cos\theta^*$ bins to the corrected p_T spectrum of the $\cos\theta^*$ bin 0.0 to 0.2 for K^{*0} in 10–50% centrality class of Pb–Pb collisions at $\sqrt{s_{NN}}$ = 5.02 TeV. Statistical uncertainties are shown only.
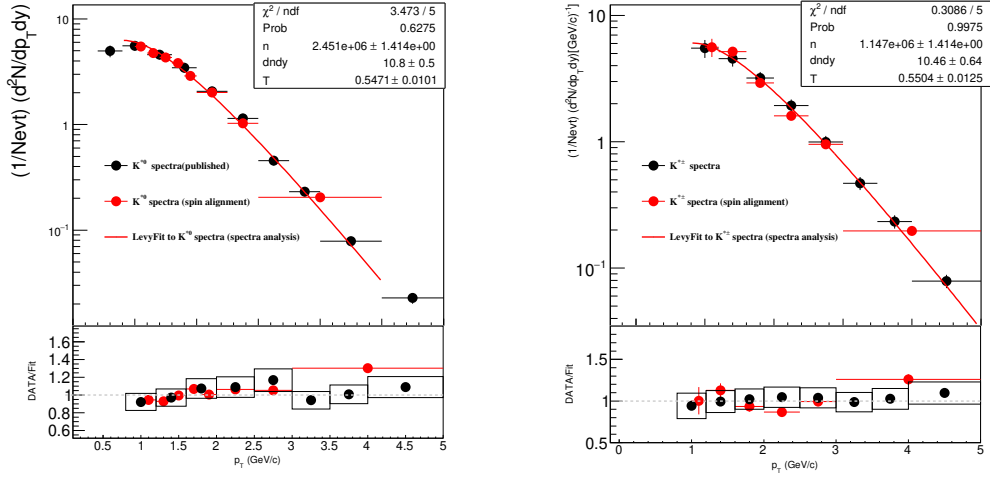
FIGURE D.11: Upper panel shows corrected transverse momentum spectra for different $\cos\theta^*$ and lower panel show the ratio of corrected p_T in different $\cos\theta^*$ bins to the corrected p_T spectrum of the $\cos\theta^*$ bin 0.0 to 0.2 for ϕ in 10–50% centrality class of Pb–Pb collisions at $\sqrt{s_{NN}}$ = 5.02 TeV. Statistical uncertainties are shown only.

FIGURE D.12: Upper panels: Comparison of transverse momentum spectra of K^{*0} and $K^{*\pm}$, respectively with the published measurements of K^{*0} and preliminary results of $K^{*\pm}$ for centrality class 10–50% in Pb–Pb collisions at $\sqrt{s_{NN}}$ = 5.02 TeV. The distributions are fitted with Lévy-Tsallis function. Below panels: Ratio of data to fit function. The error in ratios are quadrature sum of statistical and systematic uncertainties.
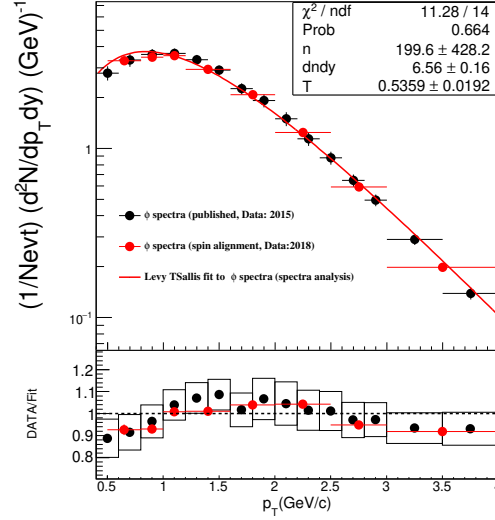
FIGURE D.13: Upper panel: Comparison of transverse momentum spectra of ϕ with published measurement for centrality class 10–50% in Pb–Pb collisions at $\sqrt{s_{NN}}$ = 5.02 TeV. The distributions are fitted with Lévy-Tsallis function. Below panel: Ratio of data to fit function. The error in ratios are quadrature sum of statistical and systematic uncertainties.

the momentum direction of vector mesons (helicity frame) are shown in Fig. D.17 and Fig.D.18, respectively.

D.0.6 Comparison of spin density matrix element (ρ_{00}) with different source of systematic variations

The comparison of ρ_{00} as a function of p_T for default and different source of systematic variations are shown in Fig. D.19 for K^{*0} and Fig. D.20 for ϕ in centrality class 10–50% for Pb–Pb collisions at $\sqrt{s_{NN}}$ = 5.02 TeV.
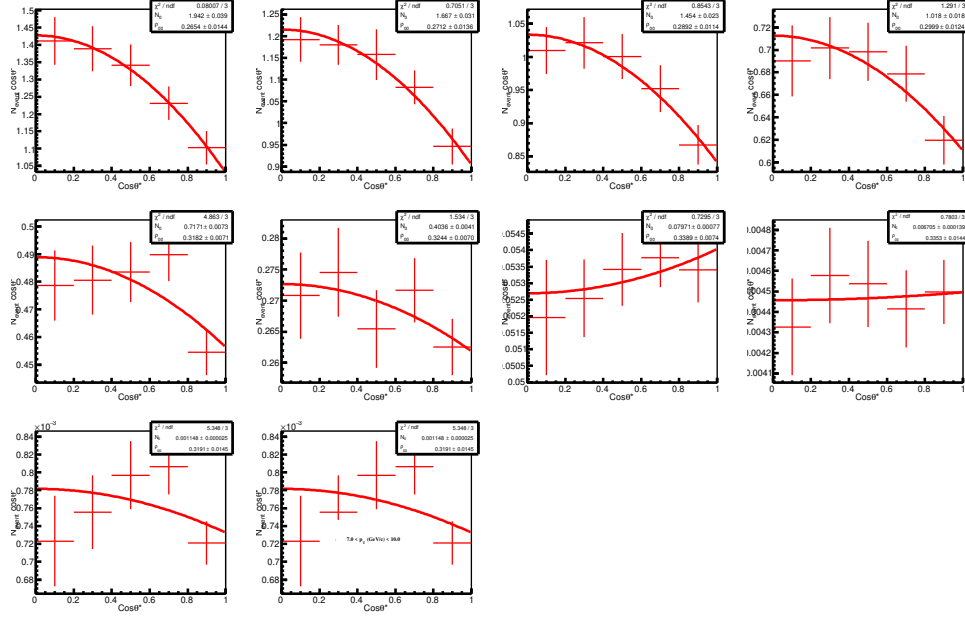
FIGURE D.14: Angular distribution of decay daughter of K^{*0} for 10–50% centrality class in Pb–Pb collisions at $\sqrt{s_{NN}}$ = 5.02 TeV.
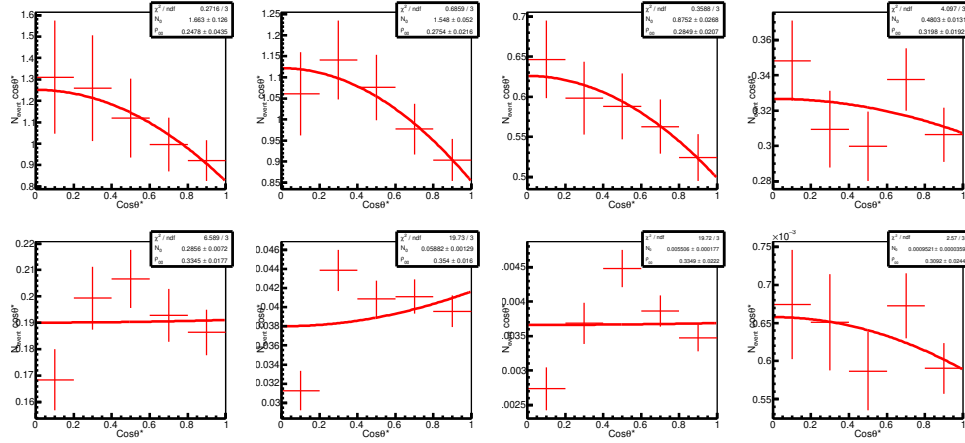

FIGURE D.15: Angular distribution of decay daughter of K$^{*\pm}$ for 10–50% centrality class in Pb–Pb collisions at $\sqrt{s_{NN}}$ = 5.02 TeV.
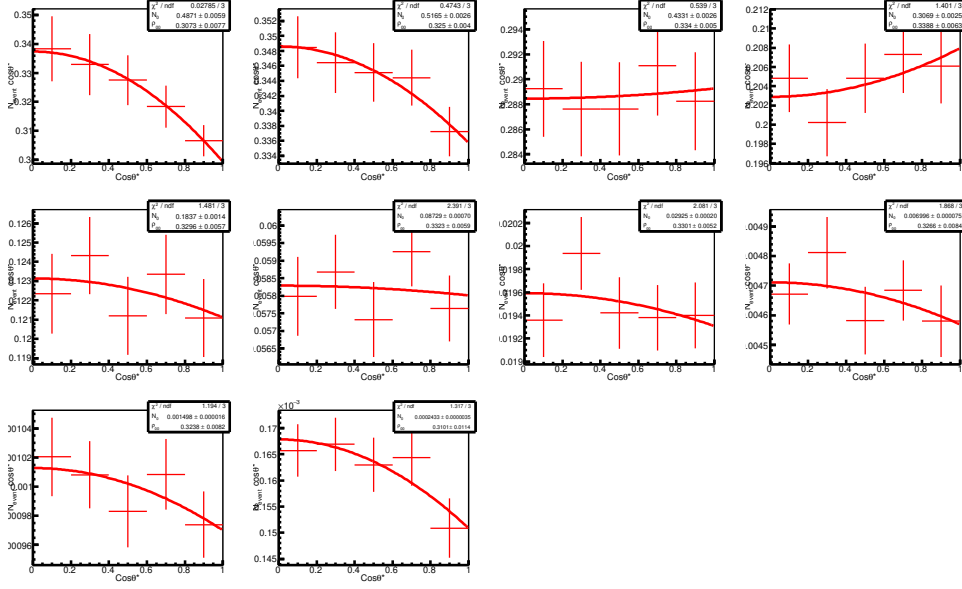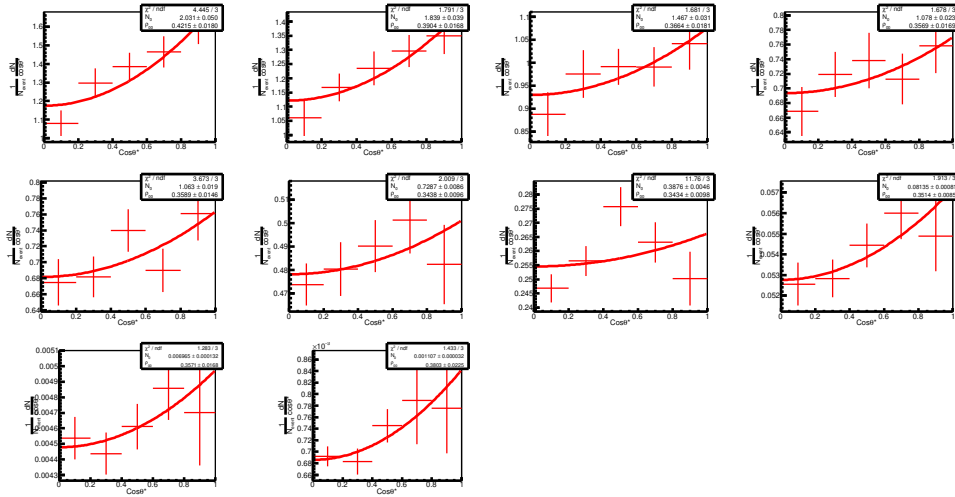
FIGURE D.16: Angular distribution of decay daughter of ϕ for 10–50% centrality class in Pb–Pb collisions at $\sqrt{s_{NN}}$ = 5.02 TeV.

FIGURE D.17: Angular distribution of decay daughter of K^{*0} for 10–50% centrality class in Pb–Pb collisions at $\sqrt{s_{NN}}$ = 5.02 TeV using helicity frame analysis.
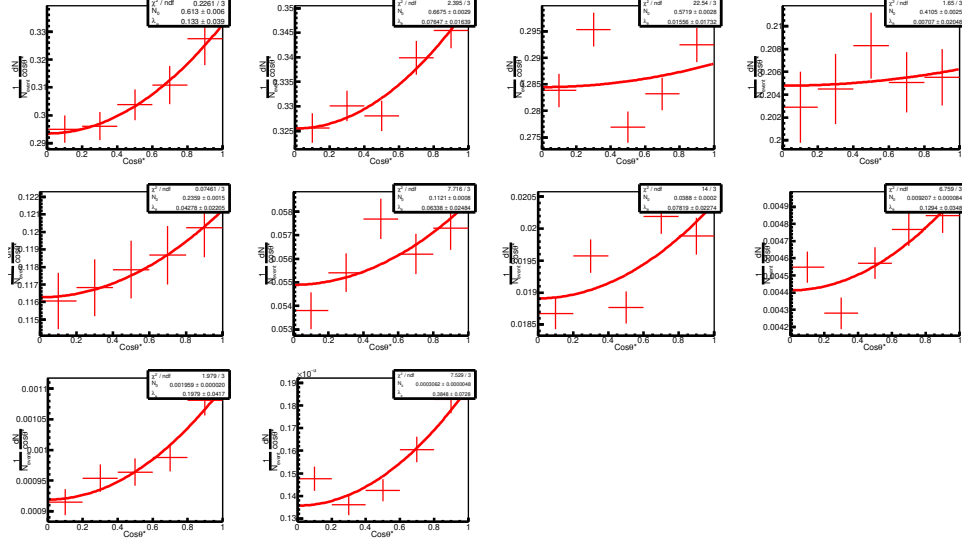
FIGURE D.18: Angular distribution of decay daughter of ϕ for 10–50% centrality class in Pb–Pb collisions at $\sqrt{s_{NN}}$ = 5.02 TeV using helicity frame analysis.
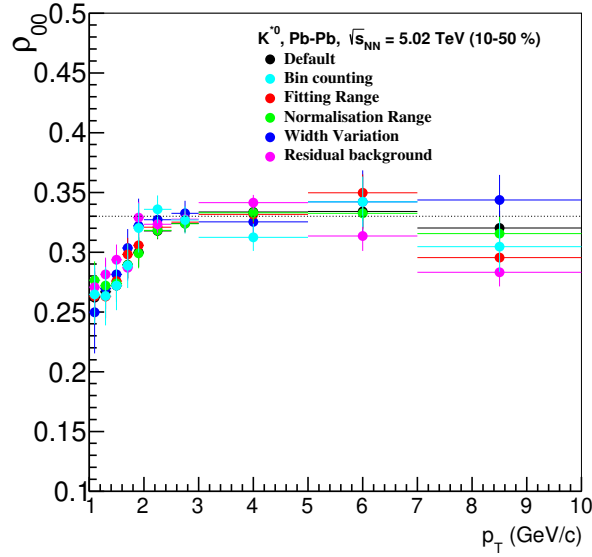

FIGURE D.19: Comparison of ρ_{00} values as a function of p_T for default and variation due to signal extraction for K^{*0} in the centrality class 10–50% for Pb–Pb collisions at $\sqrt{s_{NN}}$ = 5.02 TeV using production plane analysis.
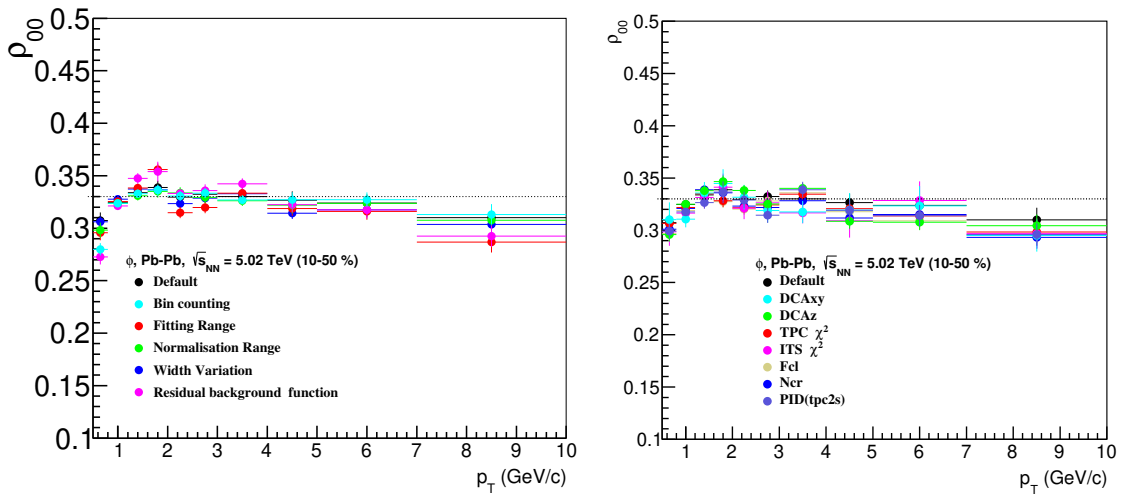
FIGURE D.20: Comparison of ρ_{00} as a function of p_T for source of signal extraction (left) and source of track variable along with PID (right) for ϕ in the centrality class 10–50% for Pb–Pb collisions at $\sqrt{s_{NN}}$ = 5.02 TeV using production plane analysis .